



Bilim, Teknoloji ve Mühendislik Araştırmaları Dergisi

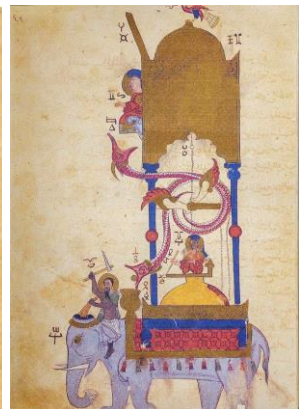
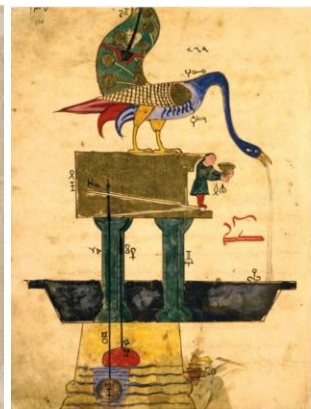
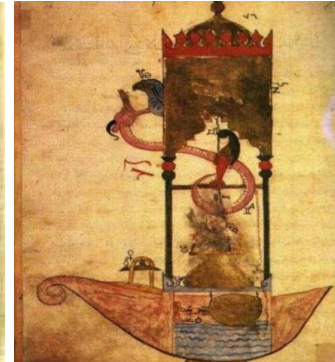
ISSN: 2717-8404

Cilt/Volume: 5 Sayı/Issue: 1-2 Yıl/Year: 2024

JOURNAL

SCIENCE | TECHNOLOGY | ENGINEERING

Bilim ⊕ Teknoloji ⊕ Mühendislik



Every science that is not converted into practice remains somewhere between right and wrong.

El Cezeri



CONTENTS / İÇİNDEKİLER

Research Article / Araştırma Makalesi

1. *A Novel Method for Measuring the Performance of Decision Alternatives in Multi-Criteria Decision Making: Proportional Superiority Approach (PSA)*, Furkan Fahri Altıntaş, **Page: 102-126**

2. *Drone Swarm Classification from ISAR Imaging*, Remziye Büşra Çoruk , Ali Kara , Elif Aydın, **Page: 127-134**
Research Article

4. *Bulanık K-En Yakın Komşuluk Algoritmasında Lempel-Ziv Mesafe Ölçütünün Etkisi: Büyüme Faktörlerinin Sınıflandırılması Örneği*, Berk Tolga Çifci , Ramazan Kabadayı , Çağın Kandemir Çavaş **Page: 148-162**
Research Article

5. *Investigation of the effects of laser power and gas pressure on the top and bottom HAZ widths in AISI 1040 steels*, Mehmet Şükrü Adin, **Page: 163-175**
Research Article

6. *Farklı serbest yağ asidi oranlarına sahip yağlardan elde edilen biyodizel yakutlarının, dizel motorlardaki kullanılabilirliğinin kimyasal özellikler açısından değerlendirilmesi*, Mahmut Uyar, **Page: 176-185**
Research Article

7. *Evaluating the Educational Effectiveness of Radar Systems Laboratory Sessions in the Undergraduate Curriculum*, Bengisu Yalçinkaya , Mohamed Benzaghta , Remziye Büşra Çoruk , Ali Kara, **Page: 186-198**
Research Article

9. *The Analysis of Water Losses and Leakages in Drinking Water Networks Using Scada System: A Case Study from Yozgat*, Yunus Görkem , Muhammet Furkan Karaman , Şekip Esat Hayber, **Page: 223-243**

Review Article / İnceleme Makalesi

3. *Review of Grid-Connected Solar PV Systems With Decoupled Control*, Abdulkadir Özcan , Ahmed Saadon Mahmood Algburi , Omar Ali Khaleel , Hanaa Hussein Lafta, **Page: 135-147**
Review Article

8. *Hydrogen generation from sodium borohydride solutions using different catalysts for the survival of living beings in the long-time space flights*, Erk İnger, **Page: 199-222**





RESEARCH ARTICLE

A Novel Method for Measuring the Performance of Decision Alternatives in Multi-Criteria Decision Making: Proportional Superiority Approach (PSA)

* Furkan Fahri ALTINTAŞ

*Aydın Provincial Gendarmerie Command, Aydın, Türkiye
furkanfahrialtintas@yahoo.com, Orcid. 0000-0002-0161-5862

Citation:

Altıntaş, F. F. (2024). *A Novel Method for Measuring the Performance of Decision Alternatives in Multi-Criteria Decision Making: Proportional Superiority Approach (PSA)*, Journal of Science Technology and Engineering Research, 5(2):102-126. DOI: 10.53525/jster.1501506

HIGHLIGHTS

- Effect and important of this article in literature
- Exchange between sources in related subjects of this article
- Contribution and strongest impact on the related subject of this article
- Examined study and obtained results why is important

Article Info

Received : 14 June 2024

Accepted : 06 August 2024

DOI:

10.53525/jster.1501506

***Corresponding Author:**

Furkan Fahri Altıntaş
furkanfahrialtintas@yahoo.com

Phone: +90 506 9765411

ABSTRACT

In the face of increasing complexity and uncertainty, new multi-criteria decision making (MCDM) methods facilitate making informed and rational decisions by enhancing problem-solving skills. Therefore, the discovery of new MCDM methods is of great importance. In this context, this study introduces a new MCDM model (Proportional Superiority Approach-PSA) based on the fundamental logic of measuring the performance of decision alternatives, which relies on the proportional increase of decision alternatives to each other, aiming to expand the modeling logic of MCDM and enrich MCDM literature. Initially, a comparative analysis of the proposed method was conducted. According to the findings, although the relationship of PSA with other MCDM methods included in the study was high. Therefore, based on the results of the comparative analysis, it was observed that the proposed method is credible and reliable. In the scope of the simulation analysis, 10 scenarios were obtained, and it was found that as the number of scenarios increased, the relationship levels of the PSA method with other methods differed. Furthermore, the PSA method was found to be capable of discriminating between the performances of decision alternatives through variance measurement. Finally, in the analysis, the level of variance of the PSA method was measured within the scenarios, and it was found that the variances of the PSA method were homogeneous within the scenarios. Therefore, according to the results of the simulation analysis, it was evaluated that the PSA method is robust and stable.

Keywords: Rate of increase, proportional increase superiority, proportional superiority approach-PSA, MCDM

I. INTRODUCTION

Multi-criteria decision-making (MCDM) methods are a critical tool for making informed decisions in complex situations. They enable decision-makers to consider multiple, often conflicting, criteria simultaneously, leading to more comprehensive and effective choices (Puška, 2013). MCDM methods are powerful tools that can significantly enhance the decision-making process. By providing a structured framework for considering multiple criteria, integrating diverse perspectives, and enhancing transparency, MCDM methods enable decision-makers to navigate the complexities of real-world decisions and make more informed, effective, and defensible choices (Triantaphyllou, 2010).

When examining the MCDM literature, it is possible to encounter many methods that measure the performances or optimality of decision alternatives. The most significant feature of these methods is that each has its own unique calculation method (Behl, 2020). Developing original and new MCDM methods is important to provide more specific and accurate solutions to problems, offer new perspectives and solution approaches, expand the application areas of MCDM, and benefit from scientific and technological advancements (Amor et al., 2021).

In this context, to contribute to, enrich, and provide a new perspective to the MCDM literature, the Proportional Superiority Approach (PSA) method, which is new and original in selection problems or measuring the performances of decision alternatives, is presented in the research. The motivation of the study is determined as the method's reliance on more realistic values for assessing the quantitative superiority of decision alternatives, compared to other MCDM methods that measure the performance of decision alternatives. This is because, except for the TODIM method, other MCDM methods are based on the idea that the decision-maker is always seeking a solution corresponding to the maximum value (Ecer, 2020). However, in the proposed method, as in the TODIM method, decision alternatives are compared with each other based on criteria, and those with quantitative superiority are ranked. Therefore, in this case, the true superiority value of the decision alternatives is determined by comparing the values corresponding to each criterion for each decision alternative. The basis of the proposed method lies in the increase rate of values of decision alternatives for each criterion. Accordingly, some commonly used MCDM methods in the literature and the proposed method are mentioned in the study. In the conclusion section, implications regarding the proposed method are provided based on the findings of the research.

II. MATERIAL AND METHOD

A. *Some MCDM Methods in the Literature and Their Characteristics*

When examining the MCDM literature, it is evident that numerous techniques are employed for the selection of decision alternatives or the measurement of their performances (Lopez et al., 2023; Van Thanh, 2020). Accordingly, when evaluating MCDM research, it is observed that many researchers utilize techniques such as SAW (Simple Additive Weighting), WPM (Weighted Product Method), WASPAS (Weighted Aggregated Sum Product Assessment), COPRAS (Complex Proportional Assessment), EDAS (Evaluation Based on Distance from Average Solution), ARAS (Additive Ratio Assessment), TOPSIS (Technique for Order Preference by Similarity to Ideal Solution), MAUT (Multiple Attribute Utility Theory), PSI (Preference Selection Index), and TODIM (Tornado de Decisao Interativa Multicriterio) for selection problems (Karende et al., 2016; Mousavi-Nasab and Sotoudeh-Anvari, 2017; Biswas et al., 2019; Chourabi et al., 2019; ; Yadav et al., 2019; Goswami et al., 2021; Karakış, 2021; Tiwari and Kumar, 2021; Dhanalakshmi et al., 2022). SAW is also described as a weighted linear combination or scoring method. For the method to be correctly applied, data must be numerical and comparable (Al Khoiry and Amelia, 2023; Taherdoost, 2023). In the method, the first step in calculating the performance of decision alternatives or solving selection problems is to create a decision matrix. Subsequently, the values in the decision matrix are normalized. In the third step, a weighted normalized decision matrix is obtained. In the final step, the normalized decision matrix values for each decision alternative are summed, and the summed values are sorted from highest to lowest (Sotoudeh-Anvari et al., 2018; Dinçer, 2019; Demirci, 2020).

WPM compares each decision alternative with others by multiplying several ratios for each criterion, one for each decision alternative. Due to the method's exponential nature, it is important for the sum of criterion weights to be equal to 1 (Chinnasamy et al., 2023). In this method, the first step involves creating a decision matrix. In the second step, the values in the decision matrix are normalized. In the third step, the exponential structure of the normalized values is assigned criterion weights. Finally, new values specific to decision alternatives are determined by multiplying criterion-wise values, and the resulting performance scores are ranked from highest to lowest (Demir et al., 2021; Onajite and Oke, 2021). WASPAS is a method provided by combining the SAW and WPM techniques. In this method, the combined optimality coefficient and total relative importance quantity are calculated. The total relative importance value explains the performance of decision alternatives or the preferred alternative in decision problems (Handayani et al., 2023). The first step of the WASPAS method involves preparing the decision matrix. In the second step, the normalization process of the decision matrix values is carried out. In the third step, the relative importance value of alternatives is determined according to the SAW and WPM methods. Finally, the combined optimal value of decision alternatives is calculated, and the calculated values are ranked from highest to lowest (Ayçin, 2019; Stanujkić and Karabašević, 2023).

COPRAS method places importance on whether criteria are benefit-oriented or cost-oriented. In this method, the comparison of decision alternatives can be achieved with percentage values (Varatharajulu et al., 2022). The first step of the method involves creating a decision matrix. In the second step, the values in the decision matrix are normalized. In the third step, the normalized decision matrix values are weighted. The fourth step takes into account benefit-oriented and cost-oriented criteria by separately summing them in the weighted normalized decision matrix. In the fifth step, the relative importance value of each decision alternative is calculated based on the benefit-oriented and cost-oriented weighted normalized values. In the final step of the method, the performance index value of each decision alternative is measured, and the measured values are ranked from highest to lowest (Paksoy, 2017; Hezer et al., 2021).

In the EDAS method, the best decision alternative is determined based on its distance from the average solution rather than positive (ideal) or negative (anti-ideal) solutions. In this context, calculating the positive and negative distances from the average solution is crucial. Accordingly, an increase in positive values and a decrease in negative distances from the average solution enhance the preference or performance of the decision alternative (Sudha, 2019). The first step of the method involves creating a decision matrix. In the second step, the average solution value is measured according to the criteria. In the third step, the positive (PDA) and negative distances (NDA) from the average solution are calculated for each criterion corresponding to each decision alternative. In the fourth step, PDA and NDA values are weighted, and the weighted values are summed for PDAs and NDAs separately on a decision alternative basis to calculate the weighted total of positive alternatives (SP) and negative alternatives (SN), respectively. In the fifth step, normalized SP values (NSP) are calculated by dividing SP values by the maximum SP value. Conversely, normalized SN values (NSN) are measured by subtracting SN values from 1 divided by the maximum SN values. Finally, the performance scores of decision alternatives are measured by averaging NSP and NSN values, and the ranked scores are sorted from highest to lowest (Özbek, 2019; Yıldırım et al., 2020; Trung, 2021).

In the ARAS method, the performance and selection of decision alternatives are determined based on the assessment of the benefit degrees of decision alternatives. For this purpose, the optimality value of each decision alternative needs to be compared with the optimality function value of the reference alternative (Vijayakumar, 2020). Accordingly, in the method, the first step involves obtaining a decision matrix. In the second step, the values in the decision matrix are standardized. In the third step, the standardized decision matrix values are weighted. In the fourth step, the optimality function value for each decision alternative is calculated based on the weighted standardized decision matrix values. In the final step of the method, the benefit degrees or performances of decision alternatives are measured by comparing the optimality function value of each decision alternative to the optimality function value of the best alternative, and the measured values are ranked from highest to lowest (Karabašević et al., 2015; Uludağ and Doğan, 2021).

In the TOPSIS method, the selection or performance of decision alternatives varies based on their proximity to the positive ideal and the distance from the negative ideal. In this context, the positive ideal solution comprises the best values obtained from the criteria, while the negative ideal solution consists of the worst values obtained from the criteria. Therefore, for a decision alternative to be selectable, it needs to be closest to the positive ideal or possess the maximum quantity derived from the criteria compared to other alternatives (Kabir and Hasin, 2012; Ciardiello and Genovese, 2023). In this method, the first step involves obtaining a decision matrix. In the second step, the values in the decision matrix are standardized. The third step of the method involves weighting the standardized decision matrix values. In the fourth step, the positive and negative ideal values for each decision alternative are determined. In the fifth step, the distance values from the positive and negative ideal solutions for each criterion are calculated. Finally, the relative closeness values for each decision alternative are measured, and the calculated values are ranked from highest to lowest (Aktaş et al., 2015; Çelikkilek, 2018; Kaya and Karaşan, 2018; Azad, 2019; Tepe, 2021).

The MAUT method is a technique based on a real-valued function or utility that needs to be maximized in any decision problem. In other words, this method is used to find the solution that maximizes utility in decision problems with multiple conflicting criteria. In the method, decision maker preferences are formulated as utility functions defined over the criteria (Maharani et al., 2021). Accordingly, the first step of the method involves providing a decision matrix. In the second step, normalization of the decision matrix values is carried out. In the third step of the method, for each decision alternative, the normalized value corresponding to the criterion is multiplied by the criterion weights, and then the new criterion values corresponding to the decision alternatives are summed to calculate the weighted total utility values for each decision alternative, and the calculated values are ranked from highest to lowest (Atan and Altan, 2020; Taufik et al., 2020; Öztel and Alp, 2020). Additionally, Ecer (2020) has described the standardization process of the decision matrix and the utility values differently in the MAUT method. According to this, for the standardization process of cost-oriented criteria in particular, it has been stated that 1 is added to the standard value of cost-oriented criteria in the classical MAUT method. Furthermore, the utility functions of decision alternatives are calculated by comparing the value derived from the score standardized as the power of the natural logarithm base 'e' minus 1 to the score standardized as the square of the value, minus 1, compared to the value of 1.71.

The PSI method relies on basic statistical knowledge, and its greatest advantage, unlike other MCDM methods, lies in not requiring assigning relative importance degrees among criteria or weighting criteria during the comparison of criteria. In this sense, the method is quite useful in situations where there is disagreement about assigning weights to the problem criteria (Tuş and Adalı, 2018). The method fundamentally relies on calculating preference variance, overall preference, and preference index. In this regard, the first step of the method involves providing a decision matrix. In the second step, normalization of the decision matrix values is achieved. In the third step, the average value of each criterion is calculated. Then, the sum of the squares of the differences between the normalized value and the normalized average value is calculated for each criterion. This way, the preference variance values for each criterion are determined. In the fourth step of the method, initially, the deviation scores of preference values are calculated by subtracting 1 from the preference values for each criterion. Then, the deviation scores of preference values for each criterion are divided by the sum of deviation scores of preference values for the criteria to obtain overall preference values for the criteria. In the final stage of the method, the normalized decision matrix values are multiplied by the overall preference values for each criterion corresponding to the decision alternatives, and the multiplied values are summed to calculate the preference index values for the decision alternatives (Petković et al., 2017; Ulutaş and Topal, 2020).

TODIM utilizes a global preference value measure that can be calculated using the expectation theory paradigm. The method's core principle is based on the dominance of decision alternatives over each other. In the TODIM method, the first step is to construct the decision matrix. The second step involves normalizing the values of the decision matrix. The third step of the method involves identifying the reference criterion, while the fourth step involves calculating the dominance values of the decision alternatives. Finally, the overall dominance level of the decision alternatives relative to each other is computed (Ecer, 2020).

B. Theoretical Background of Proposed Method: Proportional Superiority Approach (PSA)

In the MCDM literature, many methods have been developed with unique mathematical models or logic for measuring the performance of decision alternatives or solving selection problems (Ecer, 2020). Within the scope of MCDM, these mathematical models, obtained according to the respective method, demonstrate the quantitative superiority of decision alternatives and, consequently, their optimality or selectability. In this context, in the SAW method, the normalization of any decision alternative's criterion values and the corresponding criterion weight being higher indicate its quantitative superiority compared to other decision alternatives. This is because in the SAW method, the performances of decision alternatives are determined by the sum of the products of all normalized criterion values and their corresponding criterion weights (Churchman and Ackoff, 1954).

In the WPM method, the quantitative superiority of any decision alternative arises from the exponential structure of the WPM method, where criterion values and their weights in the decision matrix are higher compared to other decision alternatives (Bridgman, 1922). The WASPAS method, being a combination of the SAW and WPM methods, ensures the superiority of any decision alternative over others, as described in the SAW and WPM methods (Zawadskas et al., 2012). In the COPRAS method, the quantitative superiority of any decision alternative is achieved by the increase/decrease of the total weighted standardized indexes for each decision alternative in terms of benefit/cost direction (Zawadskas and Kaklauskas, 1996). In the EDAS method, the superiority of any decision alternative is ensured by the positive/negative direction of the values corresponding to benefit-oriented criteria for the respective decision alternative in the decision matrix being greater/less than the positive/negative direction average value. Conversely, for cost-oriented criteria, the superiority of any decision alternative is determined by the values corresponding to cost-oriented criteria for the respective decision alternative in the decision matrix being less/greater than the negative/positive direction average value (Ghorabae et al., 2015).

In the ARAS method, the optimality of each decision alternative is measured by the total of the normalized weighted values for each criterion in the decision matrix, including the optimal values (the highest benefit-oriented value for each criterion and the lowest cost-oriented value). This is because for any decision alternative to be optimal, the ratio of the total of the normalized weighted values corresponding to the criteria for that decision alternative to the total of the optimal normalized weighted values is expected to be high (Zawadskas et al., 2010). In the TOPSIS method, the optimality of decision alternatives is determined by their distances to the ideal points. In this regard, if the negative distance value (negative ideal proximity) of any decision alternative in the normalized weighted matrix with respect to the criteria increases and the positive distance value (positive ideal proximity) decreases, the optimality level of that decision alternative increases. This is because a greater difference between the weighted normalized value of any decision alternative and the negative ideal solution value (the lowest value) implies a greater proximity of that decision alternative to the ideal solution. Conversely, a greater difference between the weighted normalized value of any decision alternative and the positive ideal solution value (the highest value) implies a lesser proximity of that decision alternative to the ideal solution (Hwang and Yoon, 1981). In the MAUT method, the higher the normalized values of any decision alternative, the higher its preference. This is because in this method, the optimality of decision alternatives is calculated by the sum of the products of criterion weights and normalized values for each decision alternative (Keeney and Raiffa, 1976).

In the PSI method, the optimal decision alternative can be determined by having low variance values for each criterion's preference variance (variability) after normalization. This is because in the PSI method, if the decision alternative values for each criterion in the normalized decision matrix are greater than the average criterion value, it will reduce the total variance (variability) of the criteria. Furthermore, to achieve the best optimal value for decision alternatives, it is necessary for the difference between the total variance (variability) value and 1 to be maximized (Maniya and Bhatt, 2010). The core idea of the TODIM method is to measure the dominance degree of each alternative over the others using the expected value function. Essentially, in this method, if an alternative has the highest overall dominance value over the other alternatives, then the quantitative superiority of that alternative is greater (Ecer, 2020).

In conclusion, SAW, WPM, WASPAS, and COPRAS methods focus solely on the mathematical model-based quantitative superiority of decision alternatives over each other without considering their relative dominance. On the other hand, EDAS, ARAS, and TOPSIS methods determine the performance of alternatives based on the

mathematical model's consideration of the quantitative values that should be taken into account for each alternative. Unlike other MCDM methods, the TODIM method identifies the quantitative superiority of each alternative by comparing it to each other alternative based on the mathematical model. The fundamental logic of the proposed method's mathematical model relies on the increase ratio among criteria for each decision alternative. Therefore, in this method, the optimality of any decision alternative is sought based on the proportional increase of its criterion values compared to those of other decision alternatives. Therefore, it can be considered that the fundamental structure of the proposed method is based on the logic of the TODIM method. In this context, the implementation steps of the proposed method are outlined below:

Step 1: Obtaining the Decision Matrix

$i: 1, 2, 3, \dots, n$, where n represents the number of decision alternatives

$j: 1, 2, 3, \dots, m$, where m represents the number of criteria

D : Decision matrix

C : Criterion

d_{ij} : The decision matrix is constructed according to Equation 1, where " i_j " represents the i – th decision alternative on the j -th criterion.

$$D = [d_{ij}]_{m \times n} = \begin{bmatrix} C_1 & C_2 & \dots & C_n \\ x_{11} & x_{12} & \dots & x_{1n} \\ x_{21} & x_{22} & \dots & x_{2n} \\ \vdots & \vdots & \vdots & \vdots \\ x_{m1} & x_{m2} & \dots & x_{mn} \end{bmatrix} \tag{1}$$

Step 2: Normalization of Decision Matrix (r_{ij}^*)

The normalization of the decision matrix is conducted through the utilization of the subsequent equation. Benefit criteria undergo normalization using Equation 2, whereas cost criteria are subjected to normalization employing Equation 3.

$$r_{ij}^* = \frac{x_{ij}}{x_j^{max}} \tag{2}$$

$$r_{ij}^* = \frac{x_j^{min}}{x_{ij}} \tag{3}$$

The generated normalized decision matrix is shown in Equation 4.

$$D = [r_{ij}^*]_{m \times n} = \begin{bmatrix} x_{11}^* & x_{12}^* & \dots & x_{1n}^* \\ x_{21}^* & x_{22}^* & \dots & x_{2n}^* \\ \vdots & \vdots & \vdots & \vdots \\ x_{m1}^* & x_{m2}^* & \dots & x_{mn}^* \end{bmatrix} \tag{4}$$

Step 3: Calculation of Proportional Increases in Criteria for Decision Alternatives (RI)

In this step, the proportional increases of each criterion for decision alternatives are calculated in two cases.

Case 1: When the normalized value of the criterion for the normalized decision alternative is numerically greater than that of the other decision alternative:

For the first criterion and the first alternative:

$$x_{11}^* > x_{21}^* \\ RI_{x_{11}^* \rightarrow x_{21}^*}^+ = \frac{(x_{11}^* - x_{21}^*) \cdot 100}{x_{21}^*} \tag{5}$$

$$x_{11}^* > x_{31}^* \\ RI_{x_{11}^* \rightarrow x_{31}^*}^+ = \frac{(x_{11}^* - x_{31}^*) \cdot 100}{x_{31}^*} \tag{6}$$

\vdots
 \vdots
 \vdots
 \vdots
 \vdots

$$x_{11}^* > x_{m1}^* \\ RI_{x_{11}^* \rightarrow x_{m1}^*}^+ = \frac{(x_{11}^* - x_{m1}^*) \cdot 100}{x_{m1}^*} \tag{7}$$

For the first criterion and the second alternative:

$$x_{21}^* > x_{11}^*$$

$$RI_{x_{21}^* \rightarrow x_{11}^*}^+ = \frac{(x_{21}^* - x_{11}^*) \cdot 100}{x_{11}^*} \tag{8}$$

$$x_{21}^* > x_{31}^*$$

$$RI_{x_{21}^* \rightarrow x_{31}^*}^+ = \frac{(x_{21}^* - x_{31}^*) \cdot 100}{x_{31}^*} \tag{9}$$

$$\vdots$$

$$\vdots$$

$$\vdots$$

$$\vdots$$

$$RI_{x_{21}^* \rightarrow x_{m1}^*}^+ = \frac{(x_{21}^* - x_{m1}^*) \cdot 100}{x_{m1}^*} \tag{10}$$

For the first criterion, regarding the mth alternative:

$$x_{m1}^* > x_{11}^*$$

$$RI_{x_{m1}^* \rightarrow x_{11}^*}^+ = \frac{(x_{m1}^* - x_{11}^*) \cdot 100}{x_{11}^*} \tag{11}$$

$$x_{m1}^* > x_{21}^*$$

$$RI_{x_{m1}^* \rightarrow x_{21}^*}^+ = \frac{(x_{m1}^* - x_{21}^*) \cdot 100}{x_{21}^*} \tag{12}$$

$$\vdots$$

$$\vdots$$

$$\vdots$$

For the nth criterion, concerning the first alternative:

$$x_{1n}^* > x_{2n}^*$$

$$RI_{x_{1n}^* \rightarrow x_{2n}^*}^+ = \frac{(x_{1n}^* - x_{2n}^*) \cdot 100}{x_{2n}^*} \tag{13}$$

$$x_{1n}^* > x_{3n}^*$$

$$RI_{x_{1n}^* \rightarrow x_{3n}^*}^+ = \frac{(x_{1n}^* - x_{3n}^*) \cdot 100}{x_{3n}^*} \tag{14}$$

$$\vdots$$

$$\vdots$$

$$\vdots$$

$$x_{1n}^* > x_{mn}^*$$

$$RI_{x_{1n}^* \rightarrow x_{mn}^*}^+ = \frac{(x_{1n}^* - x_{mn}^*) \cdot 100}{x_{mn}^*} \tag{15}$$

For the nth criterion, concerning the second alternative:

$$x_{2n}^* > x_{1n}^*$$

$$RI_{x_{2n}^* \rightarrow x_{1n}^*}^+ = \frac{(x_{2n}^* - x_{1n}^*) \cdot 100}{x_{1n}^*} \tag{16}$$

$$x_{2n}^* > x_{3n}^*$$

$$RI_{x_{2n}^* \rightarrow x_{3n}^*}^+ = \frac{(x_{2n}^* - x_{3n}^*) \cdot 100}{x_{3n}^*} \tag{17}$$

$$\vdots$$

$$\vdots$$

$$\vdots$$

$$x_{2n}^* > x_{mn}^*$$

$$RI_{x_{2n}^* \rightarrow x_{mn}^*}^+ = \frac{(x_{2n}^* - x_{mn}^*) \cdot 100}{x_{mn}^*} \tag{18}$$

For the nth criterion, concerning mth alternative:

$$x_{mn}^* > x_{1n}^*$$

$$RI_{x_{mn}^* \rightarrow x_{1n}^*}^+ = \frac{(x_{mn}^* - x_{1n}^*) \cdot 100}{x_{1n}^*} \tag{19}$$

$$x_{mn}^* > x_{2n}^*$$

$$RI_{x_{mn}^* \rightarrow x_{2n}^*}^+ = \frac{(x_{mn}^* - x_{2n}^*) \cdot 100}{x_{2n}^*} \tag{20}$$

⋮
⋮
⋮

$$x_{mn}^* > x_{(m-1)n}^*$$

$$RI_{x_{mn}^* \rightarrow x_{(m-1)n}^*}^+ = \frac{(x_{mn}^* - x_{(m-1)n}^*) \cdot 100}{x_{(m-1)n}^*} \tag{21}$$

Case 2: When the normalized value of the criterion for decision alternative is numerically smaller than that of the other decision alternative:

For the first criterion and the first alternative:

$$x_{11}^* < x_{21}^*$$

$$RI_{x_{11}^* \rightarrow x_{21}^*}^- = \frac{(x_{21}^* - x_{11}^*) \cdot 100}{x_{11}^*} \tag{22}$$

$$x_{11}^* < x_{31}^*$$

$$RI_{x_{11}^* \rightarrow x_{31}^*}^- = \frac{(x_{31}^* - x_{11}^*) \cdot 100}{x_{11}^*} \tag{23}$$

⋮
⋮
⋮

$$x_{11}^* < x_{m1}^*$$

$$RI_{x_{11}^* \rightarrow x_{m1}^*}^- = \frac{(x_{m1}^* - x_{11}^*) \cdot 100}{x_{11}^*} \tag{24}$$

For the first criterion and the second alternative:

$$x_{21}^* < x_{11}^*$$

$$RI_{x_{21}^* \rightarrow x_{11}^*}^- = \frac{(x_{11}^* - x_{21}^*) \cdot 100}{x_{21}^*} \tag{25}$$

$$x_{21}^* < x_{31}^*$$

$$RI_{x_{21}^* \rightarrow x_{31}^*}^- = \frac{(x_{31}^* - x_{21}^*) \cdot 100}{x_{21}^*} \tag{26}$$

⋮
⋮
⋮

$$x_{21}^* < x_{m1}^*$$

$$RI_{x_{21}^* \rightarrow x_{m1}^*}^- = \frac{(x_{m1}^* - x_{21}^*) \cdot 100}{x_{21}^*} \tag{27}$$

For the first criterion, regarding the mth alternative:

$$x_{m1}^* < x_{11}^*$$

$$RI_{x_{m1}^* \rightarrow x_{11}^*}^- = \frac{(x_{11}^* - x_{m1}^*) \cdot 100}{x_{m1}^*} \tag{28}$$

$$x_{m1}^* < x_{21}^*$$

$$RI_{x_{m1}^* \rightarrow x_{21}^*}^- = \frac{(x_{21}^* - x_{m1}^*) \cdot 100}{x_{m1}^*} \tag{29}$$

⋮
⋮
⋮

For the nth criterion, concerning the first alternative:

$$x_{1n}^* < x_{2n}^* \\ RI_{x_{1n}^* \rightarrow x_{2n}^*}^- = \frac{(x_{2n}^* - x_{1n}^*) \cdot 100}{x_{1n}^*} \tag{30}$$

$$x_{1n}^* < x_{3n}^* \\ RI_{x_{1n}^* \rightarrow x_{3n}^*}^- = \frac{(x_{3n}^* - x_{1n}^*) \cdot 100}{x_{1n}^*} \tag{31}$$

$$\vdots \\ \vdots \\ \vdots \\ \vdots \\ \vdots \\ x_{1n}^* < x_{mn}^* \\ RI_{x_{1n}^* \rightarrow x_{mn}^*}^- = \frac{(x_{mn}^* - x_{1n}^*) \cdot 100}{x_{1n}^*} \tag{32}$$

For the nth criterion, concerning the second alternative:

$$x_{2n}^* < x_{1n}^* \\ RI_{x_{2n}^* \rightarrow x_{1n}^*}^- = \frac{(x_{1n}^* - x_{2n}^*) \cdot 100}{x_{2n}^*} \tag{33}$$

$$x_{2n}^* < x_{3n}^* \\ RI_{x_{2n}^* \rightarrow x_{3n}^*}^- = \frac{(x_{3n}^* - x_{2n}^*) \cdot 100}{x_{2n}^*} \tag{34}$$

$$\vdots \\ \vdots \\ \vdots \\ \vdots \\ \vdots \\ x_{2n}^* < x_{mn}^* \\ RI_{x_{2n}^* \rightarrow x_{mn}^*}^- = \frac{(x_{mn}^* - x_{2n}^*) \cdot 100}{x_{2n}^*} \tag{35}$$

For the nth criterion, concerning the mth alternative:

$$x_{mn}^* < x_{1n}^* \\ RI_{x_{mn}^* \rightarrow x_{1n}^*}^- = \frac{(x_{1n}^* - x_{mn}^*) \cdot 100}{x_{mn}^*} \tag{36}$$

$$x_{mn}^* < x_{2n}^* \\ RI_{x_{mn}^* \rightarrow x_{2n}^*}^- = \frac{(x_{2n}^* - x_{mn}^*) \cdot 100}{x_{mn}^*} \tag{37}$$

$$\vdots \\ \vdots \\ \vdots \\ \vdots \\ \vdots \\ x_{mn}^* < x_{(m-1)n}^* \\ RI_{x_{mn}^* \rightarrow x_{(m-1)n}^*}^- = \frac{(x_{(m-1)n}^* - x_{mn}^*) \cdot 100}{x_{(m-1)n}^*} \tag{38}$$

Step 4: Calculation of Proportional Increase Superiority (PIS) Values for Decision Alternatives

PIS values of the first decision alternative relative to each decision alternative (PIS_{DA₁})

$$\text{For the second decision alternative: } PIS_{DA_1 \rightarrow DA_2} = \overbrace{\left[\sum_{j=1}^n RI_{1j}^+ \right]}^{\text{First Group}} - \overbrace{\left[\sum_{j=1}^n RI_{1j}^- \right]}^{\text{Second Group}} \tag{39}$$

$$\text{For the third decision alternative: } PIS_{DA_1 \rightarrow DA_3} = \overbrace{\left[\sum_{j=1}^n RI_{2j}^+ \right]}^{\text{First Group}} - \overbrace{\left[\sum_{j=1}^n RI_{2j}^- \right]}^{\text{Second Group}} \tag{40}$$

$$\vdots \\ \vdots \\ \vdots \\ \vdots \\ \vdots$$

$$\text{For the mth decision alternative: } PIS_{DA_1 \rightarrow DA_m} = \overbrace{\left[\sum_{j=1}^n RI_{mj}^+ \right]}^{\text{First Group}} - \overbrace{\left[\sum_{j=1}^n RI_{mj}^- \right]}^{\text{Second Group}} \tag{41}$$

PIS values of the second decision alternative relative to each decision alternative (PIS_{DA_2})

$$\text{For the first decision alternative: } PIS_{DA_2 \rightarrow DA_1} = \overbrace{\left[\sum_{j=1}^n RI_{1j}^+ \right]}^{\text{First Group}} - \overbrace{\left[\sum_{j=1}^n RI_{1j}^- \right]}^{\text{Second Group}} \quad (42)$$

$$\text{For the third decision alternative: } PIS_{DA_2 \rightarrow DA_3} = \overbrace{\left[\sum_{j=1}^n RI_{2j}^+ \right]}^{\text{First Group}} - \overbrace{\left[\sum_{j=1}^n RI_{2j}^- \right]}^{\text{Second Group}} \quad (43)$$

⋮
⋮
⋮

$$\text{For the } m\text{th decision alternative: } PIS_{DA_2 \rightarrow DA_m} = \overbrace{\left[\sum_{j=1}^n RI_{mj}^+ \right]}^{\text{First Group}} - \overbrace{\left[\sum_{j=1}^n RI_{mj}^- \right]}^{\text{Second Group}} \quad (44)$$

PIS values of the m th decision alternative relative to each decision alternative (PIS_{DA_m})

$$\text{For the first decision alternative: } PIS_{DA_m \rightarrow DA_1} = \overbrace{\left[\sum_{j=1}^n RI_{1j}^+ \right]}^{\text{First Group}} - \overbrace{\left[\sum_{j=1}^n RI_{1j}^- \right]}^{\text{Second Group}} \quad (45)$$

$$\text{For the second decision alternative: } PIS_{DA_m \rightarrow DA_2} = \overbrace{\left[\sum_{j=1}^n RI_{2j}^+ \right]}^{\text{First Group}} - \overbrace{\left[\sum_{j=1}^n RI_{2j}^- \right]}^{\text{Second Group}} \quad (46)$$

⋮
⋮
⋮

$$\text{For the } (m-1)\text{th decision alternative: } PIS_{DA_m \rightarrow DA_{m-1}} = \overbrace{\left[\sum_{j=1}^n RI_{mj}^+ \right]}^{\text{First Group}} - \overbrace{\left[\sum_{j=1}^n RI_{mj}^- \right]}^{\text{Second Group}} \quad (47)$$

Step 5: Calculating the Total PIS Values of Decision Alternatives (TPSI)

$$TPIS_{DA_1} = PIS_{DA_1 \rightarrow DA_2} + PIS_{DA_1 \rightarrow DA_3} + \dots + PIS_{DA_1 \rightarrow DA_m} = \sum_{i=1}^{m-1} PIS_{DA_1 \rightarrow DA_{i+1}} \quad (48)$$

$$TPIS_{DA_2} = PIS_{DA_2 \rightarrow DA_1} + PIS_{DA_2 \rightarrow DA_3} + \dots + PIS_{DA_2 \rightarrow DA_m} = \sum_{i=0, i \neq 1}^{m-1} PIS_{DA_2 \rightarrow DA_{i+1}} \quad (49)$$

⋮
⋮
⋮

$$TPIS_{DA_m} = PIS_{DA_m \rightarrow DA_1} + PIS_{DA_m \rightarrow DA_3} + \dots + PIS_{DA_m \rightarrow DA_{m-1}} = \sum_{j=1}^{m-1} PIS_{DA_m \rightarrow DA_j} \quad (50)$$

Step 6: Calculating the Proportional Superiority Performance PSP Values of Decision Alternatives

Case 1: The situation where all TPSI values of decision alternatives are positive

$$PSP = \frac{TPIS_j}{\sum_1^m TPIS_j} \quad (51)$$

Case 2: The situation where any of the TPSI values of decision alternatives is negative

In this case, firstly, Z-Score transformation is applied to the TPSI values. This ensures that the negative TPSI values become positive. The Z-Score formula is shown in Equation 52 (Zhang et al., 2014).

$$z_j = \frac{x_j - \bar{x}_j}{\sigma_j} \quad (52)$$

The values \bar{x}_j and σ_j shown in Equation 52 represent the mean and standard deviation values of the j th criterion, respectively. By applying the transformations indicated in Equations 53 and 54, the data in the decision matrix are ensured to be positively oriented (Zhang et al., 2014).

$$z'_j = z_j + A \quad (53)$$

$$A > |\min Z_j| \quad (54)$$

The value A is the value closest to the smallest z_{ij} value that is planned to be assigned. In this context, the equations related to TPSI provided by Z-Score are shown below.

$$TPSI_{z_j} = \frac{TPSI_j - \overline{TPSI_j}}{\sigma_j} \tag{55}$$

$$TPSI_{z'_j} = TPSI_{z_j} + A \tag{56}$$

After calculating the $TPSI_{z'_j}$ values for decision alternatives, Equation 57 is used to measure the *PSP* values of decision alternatives.

$$PSP = \frac{TPSI_{z'_j}}{\sum_1^m TPSI_{z'_j}} \tag{57}$$

One of the most distinctive features of the PSA method is the absence of assigning criterion weights. This is because the method explicitly demonstrates, especially in its third step, the calculation of proportional increases in criteria for decision alternatives (*RI*), how much each alternative increases proportionally compared to others for each criterion, thereby indirectly calculating the strength of the criterion. Similarly, in the PSI method, the absence of criterion weights is due to the determination of the criterion's influence within the scope of the method's implementation steps, based on the deviation and overall (total) preference values of the criteria. Thus, in both methods, the true power of decision alternatives is determined not from their values on different criteria but rather from calculations made on different values of decision alternatives for each criterion. Moreover, when examining the MCDM literature, as explained in many MCDM methods, the evaluation of criterion weights is achieved through normalized decision matrix values. Even if weights are assigned to normalized decision matrix values in this method, there will be no change in the calculation of proportional increases of criteria (*RI*), as explained previously, since the true power of decision alternatives in the method is revealed through calculations made on different values of decision alternatives for each criterion. On the other hand, in some MCDM methods (MAUT, OWA operator), criterion weights are assigned during or after the specific calculation logic of the method. Because the main mathematical model in this method is the proportional increase calculated based on different values of decision alternatives for each criterion, applying weighting to these increase rates would result in the loss of logic of the method. In this context, as in the PSI method, no weight value is assigned to the proposed method.

The method has various advantages. Firstly, as previously mentioned, one of the advantages is the absence of assigning criterion weights in the method. Because the absence of criterion weight assignment can be quite useful in cases where there is disagreement regarding assigning weights to the criteria of the problem (Madic et al., 2017 cited in Tuş and Aytaç Adalı, 2018: 248). Secondly, the method clearly demonstrates which alternatives perform better than others based on the proportional increases of decision alternatives in each criterion. This is because in many MCDM methods, the superiority of decision alternatives to each other is generally calculated based on common values such as the optimal (maximum or minimum) values, mean value, standard deviation, etc., of decision alternatives' criteria. Therefore, by calculating the impact of each criterion on different decision alternatives in the method, it can make the decision-making process more objective. This, in turn, further increases the optimality of decision alternatives. Another advantage of the method is that, since the proportional superiority of decision alternatives is clearly calculated for each criterion, the method provides a good discrimination of performance scores of decision alternatives.

The method has both advantages and disadvantages. One of the disadvantages is that if the decision matrix takes on values of 0 or negative, it requires the calculation of Z-Score values to achieve a positive transformation of the decision matrix. Another disadvantage is that when the number of criteria and decision alternatives increases, it becomes more challenging to calculate the optimal values of decision alternatives in the method. However, complex calculations can be facilitated with various software programs such as Microsoft Excel.

C. Data Set and Analysis of the Study

The dataset of the research consists of values related to selected 10 criteria of the Economic Freedom Index (EFI) developed by the Heritage Foundation for the G7 countries for the year 2023. In this context, the performance of G7 countries has been measured using the PSA method based on selected EFI criteria values in the research. These 10 criteria were chosen to have different numerical ranges for each country. In the EFI literature, all criteria are utility-oriented. To better understand the characteristics of the proposed method, the EFI12 criterion has been transformed into a cost-oriented quantity. This transformation activity was calculated by subtracting the country's EFI12 value

from 100. This is because, according to the EFI literature, considering that the maximum value of EFI criteria for countries is 100, the cost-oriented criterion value of any country can be calculated by subtracting the utility-oriented performance of the criterion from the 100 value of the criterion. Aside from these, the weight coefficients of all criteria are of equal quantity (Heritage Foundation, 2023). Additionally, in terms of methodology, the weight coefficients of the criteria used in comparative and simulation analyses with MCDM methods have been calculated as equal quantities ($1/10 = 0,100$). In this context, abbreviations of EFI criteria are explained in Table 1 for convenience in the research.

Table 1. EFI Criteria and Abbreviations

Criteria	Abbreviations
Property Rights	EFI1
Government Integrity	EFI2
Judicial Effectiveness	EFI3
Tax Burden	EFI4
Business Freedom	EFI7
Labor Freedom	EFI8
Monetary Freedom	EFI9
Trade Freedom	EFI10
Investment Freedom	EFI11
Financial Freedom	EFI12

III. THE CASE STUDY

A. Computational Analysis

In the study, firstly, decision matrix was constructed with Equality 1. The decision matrix values pertaining to this are shown in Table 2.

Table 2. Decision Matrix

Countries	EFI1	EFI2	EFI3	EFI4	EFI7	EFI8	EFI9	EFI10	EFI11	EFI12
Criteria	Max.	Max.	Max.	Max.	Max.	Max.	Max.	Max.	Max.	Min.
Canada	88.5	95.1	83.1	75.0	87.9	69.0	74.8	83.4	80	20
France	93.0	83.9	75.5	52.9	78.2	59.2	76.9	78.6	75	30
Germany	94.8	93.1	89.4	60.2	79.7	52.8	75.3	78.6	80	30
Italy	81.2	77.9	61.1	57.3	73.8	70.6	82.6	78.6	80	50
Japan	94.1	94.7	80.7	68.1	78.3	66.8	87.1	75.2	60	40
UK	95.1	84.8	86.4	65.4	79.1	62.2	80.8	81.8	80	20
USA	94.7	76.1	73.4	75.4	83.8	76.3	78.0	75.4	85	20
Minimum	81.2	76.1	61.1	52.9	73.8	52.8	74.8	75.2	60.0	20.0
Maximum	95.1	95.1	89.4	75.4	87.9	76.3	87.1	83.4	85.0	50.0

Reference: Heritage Foundation. 2023

In the second step of the proposed method in the research, benefit-oriented normalization was conducted with Equality 2, while cost-oriented normalization was achieved with Equality 3. Subsequently, a normalized decision matrix was formed with Equality 4. The normalized values calculated based on the decision matrix values are explained in Table 3.

Table 3. Normalized Decision Matrix

Criteria	Canada	France	Germany	Italy	Japan	UK	USA
EFI1	0.930599	0.977918	0.996845	0.853838	0.989485	1	0.995794
EFI2	1	0.882229	0.97897	0.819138	0.995794	0.891693	0.80021
EFI3	0.92953	0.844519	1	0.683445	0.902685	0.966443	0.821029
EFI4	0.994695	0.701592	0.798408	0.759947	0.903183	0.867374	1
EFI7	1	0.889647	0.906712	0.83959	0.890785	0.899886	0.953356

EFI8	0.904325	0.775885	0.692005	0.925295	0.875491	0.815203	1
EFI9	0.858783	0.882893	0.864524	0.948335	1	0.927669	0.895522
EFI10	1	0.942446	0.942446	0.942446	0.901679	0.980815	0.904077
EFI11	0.941176	0.882353	0.941176	0.941176	0.705882	0.941176	1
EFI12	1	0.666667	0.666667	0.4	0.5	1	1

The calculation method for normalization is demonstrated below, taking into account the benefit-oriented EFI1 and cost-oriented EFI12 decision matrix values for Canada.

In the third step, the rates of increase (*RI*) of each decision alternative over other decision alternatives on a criterion basis were measured based on the normalized decision matrix values, considering their quantitative magnitudes and directions relative to each other. The relevant calculations were made using the pertinent equations from Equation 5 to Equation 38. The resulting values are presented in Table 4.

Table 4. Rates of Increase of Decision Alternatives (Countries) Over Each Other

CANADA						
Criteria	France	Germany	Italy	Japan	UK	USA
EFI1	5.084746	7.11864407	8.990148	6.327684	7.457627	7.00565
EFI2	13.34923	2.14822771	22.07959	0.422386	12.14623	24.96715
EFI3	10.06623	7.58122744	36.00655	2.973978	3.971119	13.21526
EFI4	41.77694	24.5847176	30.89005	10.13216	14.6789	0.533333
EFI7	12.40409	10.2885822	19.10569	12.26054	11.12516	4.892601
EFI8	16.55405	30.6818182	2.318841	3.293413	10.93248	10.57971
EFI9	2.807487	0.6684492	10.42781	16.44385	8.02139	4.278075
EFI10	6.10687	6.10687023	6.10687	10.90426	1.95599	10.61008
EFI11	6.666667	0	0	33.33333	0	6.25
EFI12	50	50	150	100	0	0
FRANCE						
Criteria	Canada	Germany	Italy	Japan	UK	USA
EFI1	5.084746	1.935484	14.53202	1.182796	2.258064516	1.827957
EFI2	13.34923	10.96544	7.702182	12.87247	1.072705602	10.24967
EFI3	10.06623	18.4106	23.56792	6.887417	14.43708609	2.861035
EFI4	41.77694	13.79962	8.31758	28.73346	23.6294896	42.53308
EFI7	12.40409	1.918159	5.96206	0.127877	1.150895141	7.161125
EFI8	16.55405	12.12121	19.25676	12.83784	5.067567568	28.88514
EFI9	2.807487	2.124834	7.412224	13.26398	5.071521456	1.430429
EFI10	6.10687	0	0	4.521277	4.071246819	4.244032
EFI11	6.666667	6.666667	6.666667	25	6.666666667	13.33333
EFI12	50	0	66.66667	33.33333	50	50
GERMANY						
Criteria	Canada	France	Italy	Japan	UK	USA
EFI1	7.118644	1.935484	16.74877	0.743889	0.316456	0.105597
EFI2	2.148228	10.96544	19.5122	1.718582	9.787736	22.33903
EFI3	7.581227	18.4106	46.31751	10.78067	3.472222	21.79837
EFI4	24.58472	13.79962	5.061082	13.12292	8.637874	25.24917
EFI7	10.28858	1.918159	7.99458	1.787995	0.758534	5.144291
EFI8	30.68182	12.12121	33.71212	26.51515	17.80303	44.50758
EFI9	0.668449	2.124834	9.694555	15.67065	7.304117	3.585657
EFI10	6.10687	0	0	4.521277	4.071247	4.244032
EFI11	0	6.666667	0	33.33333	0	6.25
EFI12	50	0	66.66667	33.33333	50	50
ITALY						
Criteria	France	Germany	Italy	Japan	UK	USA
EFI1	8.990148	14.53202	16.74877	15.8867	17.11823	16.62562
EFI2	22.07959	7.702182	19.5122	21.56611	8.85751	2.365309
EFI3	36.00655	23.56792	46.31751	32.07856	41.40753	20.13093

EFI4	30.89005	8.31758	5.061082	18.84817	14.13613	31.58813
EFI7	19.10569	5.96206	7.99458	6.097561	7.181572	13.55014
EFI8	2.318841	19.25676	33.71212	5.688623	13.50482	8.073654
EFI9	10.42781	7.412224	9.694555	5.447942	2.227723	5.897436
EFI10	6.10687	0	0	4.521277	4.071247	4.244032
EFI11	0	6.666667	0	33.33333	0	6.25
EFI12	150	66.66667	66.66667	25	150	150
JAPAN						
Criteria	France	Germany	Italy	Japan	UK	USA
EFI1	6.327684	1.182796	0.743889	15.8867	1.062699	0.63762
EFI2	0.422386	12.87247	1.718582	21.56611	11.67453	24.44152
EFI3	2.973978	6.887417	10.78067	32.07856	7.063197	9.945504
EFI4	10.13216	28.73346	13.12292	18.84817	4.12844	10.71953
EFI7	12.26054	0.127877	1.787995	6.097561	1.021711	7.024266
EFI8	3.293413	12.83784	26.51515	5.688623	7.395498	14.22156
EFI9	16.44385	13.26398	15.67065	5.447942	7.79703	11.66667
EFI10	10.90426	4.521277	4.521277	4.521277	8.776596	0.265957
EFI11	33.33333	25	33.33333	33.33333	33.33333	41.66667
EFI12	100	33.33333	33.33333	25	100	100
UK						
Criteria	Canada	France	Germany	Italy	Japan	USA
EFI1	7.457627	2.258065	0.316456	17.11823	1.062699	0.422386
EFI2	12.14623	1.072706	9.787736	8.85751	11.67453	11.43233
EFI3	3.971119	14.43709	3.472222	41.40753	7.063197	17.71117
EFI4	14.6789	23.62949	8.637874	14.13613	4.12844	15.29052
EFI7	11.12516	1.150895	0.758534	7.181572	1.021711	5.941846
EFI8	10.93248	5.067568	17.80303	13.50482	7.395498	22.66881
EFI9	8.02139	5.071521	7.304117	2.227723	7.79703	3.589744
EFI10	1.95599	4.071247	4.071247	4.071247	8.776596	8.488064
EFI11	0	6.666667	0	0	33.33333	6.25
EFI12	0	50	50	150	100	0
USA						
Criteria	Canada	France	Germany	Italy	Japan	UK
EFI1	7.00565	1.827957	0.105597	16.62562	0.63762	0.422386
EFI2	24.96715	10.24967	22.33903	2.365309	24.44152	11.43233
EFI3	13.21526	2.861035	21.79837	20.13093	9.945504	17.71117
EFI4	0.533333	42.53308	25.24917	31.58813	10.71953	15.29052
EFI7	4.892601	7.161125	5.144291	13.55014	7.024266	5.941846
EFI8	10.57971	28.88514	44.50758	8.073654	14.22156	22.66881
EFI9	4.278075	1.430429	3.585657	5.897436	11.66667	3.589744
EFI10	10.61008	4.244032	4.244032	4.244032	0.265957	8.488064
EFI11	6.25	13.33333	6.25	6.25	41.66667	6.25
EFI12	0	50	50	150	100	0

To provide a better explanation of the proposed method and to illustrate an example calculation, in the fourth step, the rate of increase between Canada and France under the criterion EFI1 is computed using Equation 22 for Case 2 and Equation 8 for Case 1.

For Case 2, since $r_{EFI1:Canada \rightarrow France}^* = 0.930599 < 0.977918$, Equation 22 is considered.

$$RI^-_{EFI1:Canada \rightarrow France} = \frac{(0.977918 - 0.930599) \cdot 100}{0.930599} = 5.084746$$

For Case 1, since $r_{EFI1:France \rightarrow Canada}^* = 0.977918 > 0.930599$, Equation 8 is considered.

$$RI^+_{EFI1:France \rightarrow Canada} = \frac{(0.977918 - 0.930599) \cdot 100}{0.930599} = 5.084746$$

In the 5th step of the method, first, utilizing the relevant equations from Equation 39 to Equation 47, the Proportional Increase Superiority (PIS) values of each decision alternative over the other decision alternatives are calculated. In the 6th step of the method, the Total Proportional Increase Superiority (TPIS) values of the countries are determined using Equation 48, Equation 49, and Equation 50. The calculated values regarding this process are presented in Table 5.

Table 5. The PIS and TPIS Values of the Countries

Canada		France		Germany		Italy	
Countries	PIS	Countries	PIS	Countries	PIS	Countries	PIS
France	149.03184	Canada	-149.03184	Canada	-108.44190	Canada	-260.43225
Germany	108.44190	Germany	19.30215	France	39.44992	France	-76.77762
Italy	260.43225	Italy	61.37326	Italy	118.89413	Germany	-118.89413
Japan	150.54853	Japan	-12.79547	Japan	30.91035	Japan	-81.38181
UK	31.38861	UK	-113.42524	UK	-74.11423	UK	-227.03966
USA	25.03832	USA	-113.49407	USA	-86.24967	USA	-233.71169
TPIS	724.88144	TPIS	-308.07122	TPIS	-79.55140	TPIS	-998.23716
Japan		UK		USA			
Countries	PIS	Countries	PIS	Countries		PIS	
Canada	-149.70375	Canada	-31.38861	Canada		-25.03832	
France	-12.69371	France	113.42524	France		127.81632	
Germany	-30.91035	Germany	74.11423	Germany		86.24967	
Italy	38.24959	Italy	227.03966	Italy		193.44983	
UK	-143.61110	Japan	120.26204	Japan		148.37291	
USA	-163.31642	USA	-8.50748	UK		8.50748	
TPIS	-461.98575	TPIS	494.945081	TPIS		539.357898	

In the fifth step, as an example to illustrate the calculation of the relevant values of the method, Canada's PIS values are determined using Equation 39, Equation 40, and Equation 41, while the TPIS value of the countries is computed using Equation 48, Equation 49, and Equation 50, as shown below. For this purpose, it is necessary to first compare Canada's normalized values with those of other countries.

for PIS_{Canada} :

Since $r_{EF1:Canada}^*(0.930599) < r_{EF1:France}^*(0.977918)$, the value of $RI_{EF1:Canada \rightarrow France}^- (5.084746)$ belongs to the second group.

Since $r_{EF2:Canada}^*(1) > r_{EF2:France}^*(0.882229)$, the value of $RI_{EF2:Canada \rightarrow France}^+ (13.34923)$ belongs to the first group.

Since $r_{EF3:Canada}^*(1) > r_{EF3:France}^*(8.44519)$, the value of $RI_{EF3:Canada \rightarrow France}^+ (10.06623)$ belongs to the first group.

Since $r_{EF4:Canada}^*(0.994695) > r_{EF4:France}^*(0.701592)$, the value of $RI_{EF4:Canada \rightarrow France}^+ (41.77694)$ belongs to the first group.

Since $r_{EF7:Canada}^*(1) > r_{EF7:France}^*(0.889647)$, the value of $RI_{EF7:Canada \rightarrow France}^+ (12.40409)$ belongs to the first group.

Since $r_{EF8:Canada}^*(1) > r_{EF8:France}^*(0.904325)$, the value of $RI_{EF8:Canada \rightarrow France}^+ (16.55405)$ belongs to the first group.

Since $r_{EF9:Canada}^*(0.858783) < r_{EF9:France}^*(0.882893)$, the value of $RI_{EF9:Canada \rightarrow France}^- (2.80749)$ belongs to the second group.

Since $r_{EF10:Canada}^*(1) > r_{EF10:France}^*(0.942446)$, the value of $RI_{EF10:Canada \rightarrow France}^+ (6.10687)$ belongs to the first group.

Since $r_{EF11:Canada}^*(0.941176) > r_{EF11:France}^*(0.882353)$, the value of $RI_{EF11:Canada \rightarrow France}^+ (6.666667)$ belongs to the first group.

Since $r_{EF12:Canada}^*(1) > r_{EF12:France}^*(0.666667)$, the value of $RI_{EF12:Canada \rightarrow France}^+ (50)$ belongs to the first group.

$$PIS_{Canada \rightarrow France} = (13.34923 + 10.06623 + 41.77694 + 12.40409 + 16.55405 + 6.10687 + 6.666667 + 50) - (5.084746 + 2.80749) = 149.031839$$

$TPIS_{Canada} = 149.03184 + 108.44190 + 260.43225 + 150.54853 + 31.38861 + 25.03832 = 724.88144$
 In the final step, to measure the proportional superiority performance (PSP) of decision alternatives based on their TPIS values, Equation 51 is utilized in Case 1 (where all countries' TPIS values are positive). However, in Case 2, where some countries' TPIS values are negative according to Table 5, Equations 51 to 57 are employed to assess the PSP values of decision alternatives. Within this framework, the PSP values for each country are presented in Table 6.

Table 6. Z-Scores, Std. Z-Scores, and PSP Values of Countries

Countries	TPIS	Z-Score	Z-Score Std. (Z')	PSP	Ranking
Canada	724.881444	1.17318763	2.773188	0.247606	1
France	-308.071219	-0.4698897	1.13011	0.100903	5
Germany	-79.5514023	-0.1063922	1.493608	0.133358	4
Italy	-998.237165	-1.5677097	0.03229	0.002883	7
Japan	-461.985746	-0.7147155	0.885284	0.079043	6
UK	494.945081	0.80743686	2.407437	0.21495	3
USA	539.357898	0.87808259	2.478083	0.221257	2
Mean	-12.6658728				
Std. Dev.	628.669532				
Minimum		-1.5677097			
Sum			11.2		

Upon examination of Table 6, countries' PSP or economic freedom performances are ranked as Canada, USA, UK, Germany, France, Japan, and Italy. To illustrate the calculation method, the calculation processes of Canada's Z-Score, Std. Z-Score, and PSP values are presented below.

$$Z - Score_{Canada} = \frac{(724.881444 - (-12.665873))}{628.669532} = 1.17318763$$

$$A_i = 1.6 > |-1.5677097|$$

$$Z - Score Std. Canada = (Z')_{Canada} = 1.17318763 + 1.6 = 2.773188$$

In the calculation of the Z-Score std. the value of A_i is determined to be 1.5. This is because Zwang et al. (2014) calculated the transformation of a Z value to its Z standard value by adding 0,1 to the decimal value of the smallest magnitude of Z values in the respective series (-1.5677097).

$$PSP_{Canada} = \frac{2.773188}{11.2} = 0.247606$$

B. Comparative Analysis

The proposed method's credibility and reliability are assessed by comparing its relationship and position with other objective weight coefficient calculation methods. In this comparison, we expect the new method to be consistent with existing methods, showing a close alignment and a positive, significant correlation with their weight coefficients (Keshavarz-Ghorabae et al., 2021). In this context, the countries' economic freedom performances calculated using the ARAS, COPRAS, EDAS, TOPSIS, MUT, SAW, and PSI methods are described in Table 7.

Table 7. Economic Freedom Performances Calculated Using the ARAS, COPRAS, EDAS, TOPSIS, MUT, SAW, and PSI Methods for Countries

Countries	ARAS		COPRAS		WASPAS		EDAS	
	Score	Rank	Score	Rank	Score	Rank	Score	Rank
Canada	0.995254	1	0.876253	1	0.955297	1	0.904122	1
France	0.685522	5	0.794085	6	0.841768	6	0.186509	6
Germany	0.689209	4	0.829318	5	0.874631	4	0.391865	5
Italy	0.444018	7	0.788778	7	0.800635	7	0.088996	7
Japan	0.539237	6	0.835338	4	0.858717	5	0.46174	4
UK	0.992253	3	0.847422	3	0.928109	3	0.73254	2

USA	0.993261	2	0.857283	2	0.935475	2	0.712476	3
Countries	TOPSIS		MAUT		SAW		PSI	
	Score	Rank	Score	Rank	Score	Rank	Score	Rank
Canada	0.762192	1	0.777415	1	0.385482	1	0.954273	1
France	0.458788	6	0.420471	6	0.340626	6	0.852864	6
Germany	0.579839	4	0.553799	4	0.377422	3	0.88758	4
Italy	0.349307	7	0.289652	7	0.311637	7	0.82783	7
Japan	0.515877	5	0.552337	5	0.379115	2	0.880999	5
UK	0.681661	2	0.677601	2	0.372551	4	0.927058	3
USA	0.663196	3	0.639962	3	0.361703	5	0.934461	2

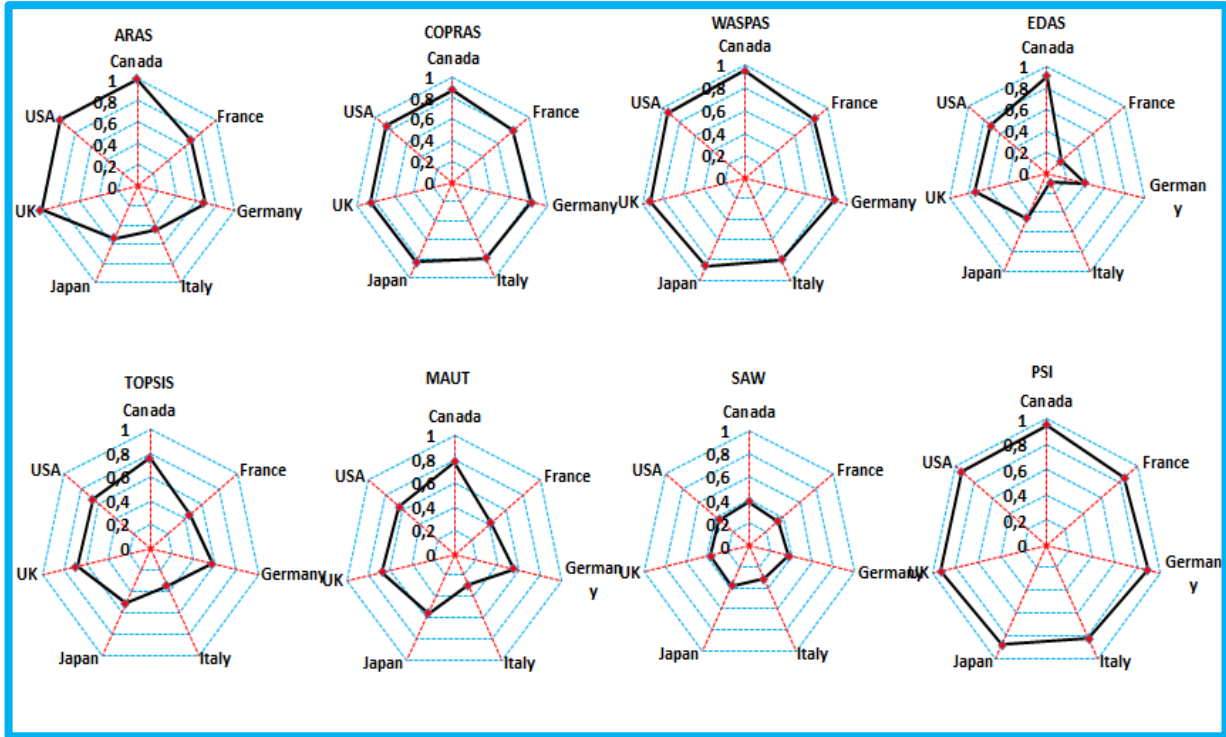


Figure 1. Positions of the ARAS, COPRAS, WASPAS, EDAS, TOPSIS, MAUT, SAW and PSI Methods
Note: The axes is graduated in increments of 0, 0.20, 0.4, 0.6, 0.8 and 1

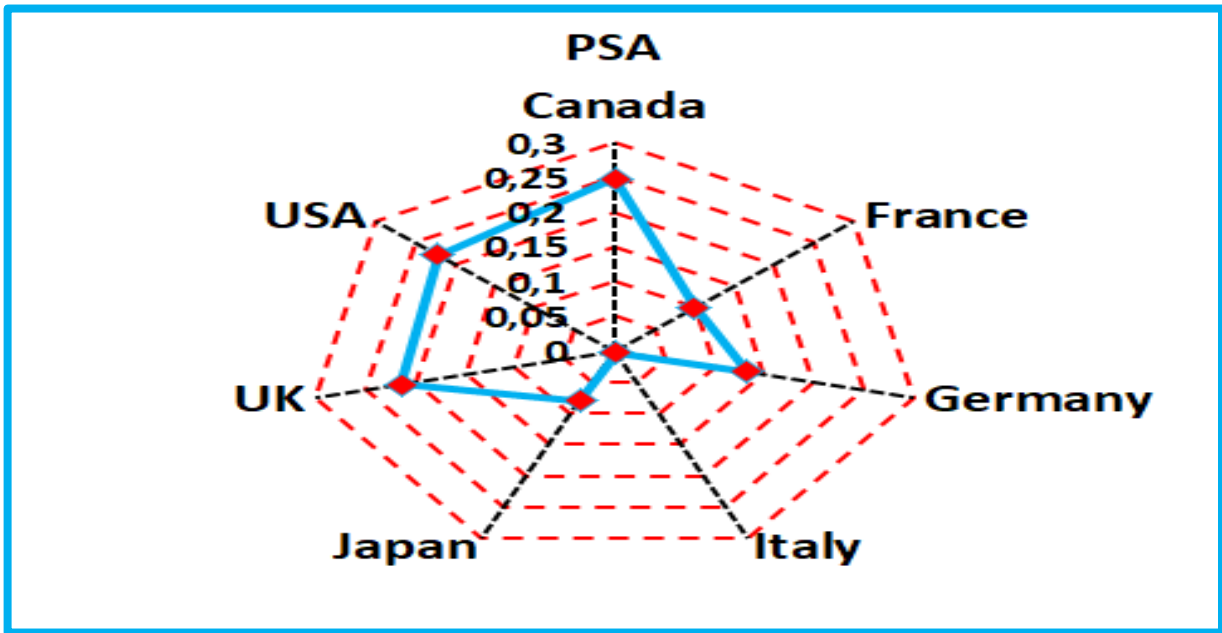


Figure 2. Position of PSA
Note: The axes is graduated in increments of 0, 0.05, 0.1, 0.15, 0.2, 0.25, 0.3

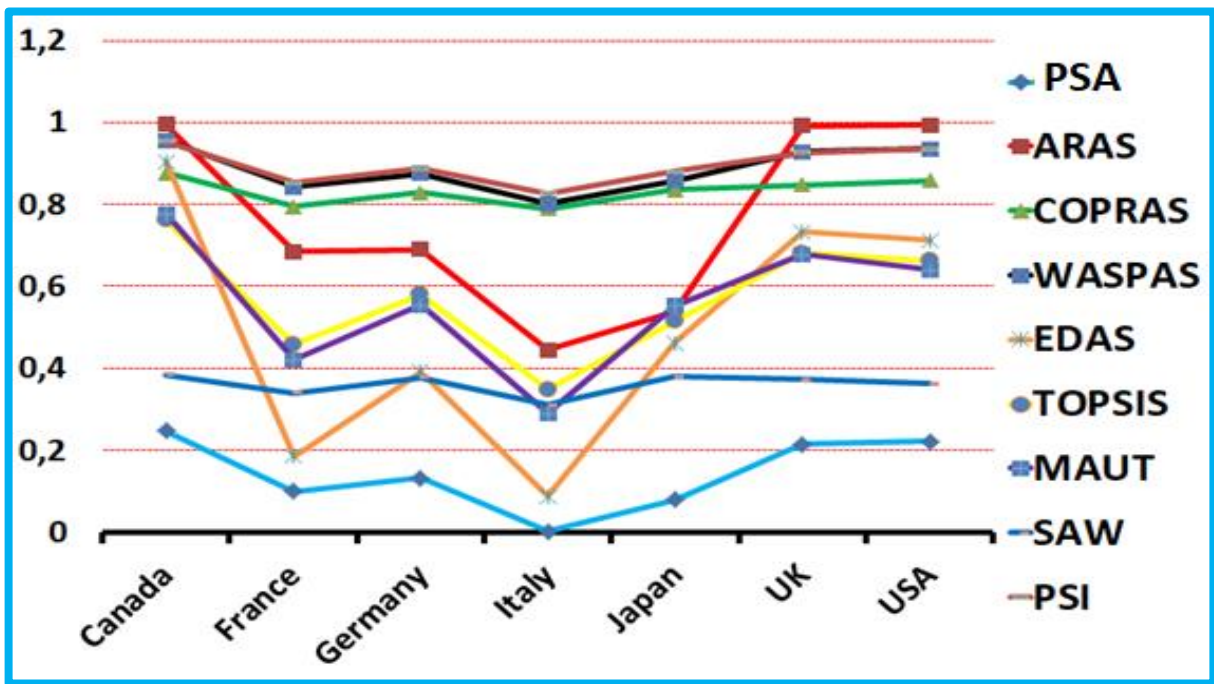


Figure 3. Positions of the PSA, ARAS, COPRAS, WASPAS, EDAS, TOPSIS, MAUT, SAW, and PSI Methods

When Table 7 and Figure 3 are examined together, it is observed that the fluctuations in the performance scores of countries according to the PSA method are generally consistent with the MCDM methods. Therefore, based on this visual structure, it is believed that there is a significant relationship between the performance values of countries calculated by the PSA method and those calculated by other MCDM methods. Accordingly, the correlation values of the PSA method with other MCDM methods are shown in Table 8.

Table 8. Pearson Correlation Values of the PSA Method with Other MCDM Methods

Methods	ARAS	COPRAS	WASPAS	EDAS	TOPSIS	MAUT	SAW	PSI
Score	0.980**	0.885**	0.986**	0.930**	0.974**	0.934**	0.700**	0.966**

p<.01. p*<.05**

Keshavarz-Ghorabae (2021) citing the findings of Walters (2009), noted that when measuring the Pearson correlation among the MEREC method and other techniques (such as SD, ENTROPY, and CRITIC), a positive and significant correlation falling within the range of 0,400-0,600 indicates a moderate level of association between variables. Moreover, if the correlation exceeds 0,600, it signifies a substantial relationship. Accordingly, when Table 8 is examined, it is observed that the PSA method has a positive, significant, and very high-level correlation with all MCDM methods except for the SAW method, with which it has a significant and high-level correlation. Therefore, based on these results, it is evaluated that the PSA method's methodology shows more differences compared to the SAW method than other MCDM methods and that the PSA method is credible and reliable.

C.Simulation Analysis

To assess robustness and stability of the proposed method's results under various conditions, a simulation analysis is conducted using different scenarios represented by diverse decision matrices. Firstly, as the number of scenarios increases, the proposed method is expected to exhibit a greater degree of differentiation from other methods in terms of the resulting performance scores. This suggests that the proposed method is more sensitive to the specific context of each scenario. Secondly, on average, the variance of the performance scores obtained using the proposed method across different scenarios should be demonstrably greater than the variance observed with at least one or more alternative weight calculation methods. This indicates that the proposed method is more effective in differentiating the relative importance of different criteria. Thirdly, homogeneity of variances within scenarios: Within each individual scenario, the variances of the weights obtained using different methods should exhibit a degree of homogeneity. This implies that the proposed method, along with other methods, consistently captures the inherent variability of the weights within each specific scenario (Keshavarz-Ghorabae, 2021). During the simulation analysis, the correlation coefficients of the PSA method with other methodologies were computed using the initial 10 scenarios, and these findings are outlined in Table 9.

Table 9. Correlation Values of the PSA Method with Other Methods under Different Scenarios

Scenarios	ARAS	COPRAS	WASPAS	EDAS	TOPSIS	MAUT	SAW	PSI
1. Sce.	0.985**	0.889**	0.989**	0.945**	0.981**	0.941**	0.725**	0.975**
2. Sce.	0.975**	0.883**	0.985**	0.935**	0.977**	0.935**	0.710**	0.966**
3. Sce.	0.970**	0.885**	0.990**	0.921**	0.965**	0.928**	0.685*	0.955**
4. Sce.	0.981**	0.887**	0.975**	0.923**	0.969**	0.915**	0.679*	0.949**
5. Sce.	0.967**	0.867**	0.973**	0.901**	0.958**	0.889**	0.677*	0.936**
6. Sce.	0.965**	0.869**	0.967**	0.885**	0.945**	0.885**	0.669*	0.941**
7. Sce.	0.967**	0.977**	0.965**	0.888**	0.949**	0.884**	0.683*	0.901**
8. Sce.	0.959**	0.961**	0.971**	0.887**	0.952**	0.988**	0.671*	0.885**
9. Sce.	0.963**	0.955**	0.975**	0.889**	0.963**	0.881**	0.668*	0.873**
10. Sce.	0.961**	0.951**	0.962**	0.883**	0.953**	0.879**	0.663*	0.865**

p<.01. p*<.05**

Upon examination of Table 9, it was observed that the PSA method exhibits positive and significant correlations with other MCDM methods in each scenario. Subsequently, scenarios 1, 2, and 3 were grouped as the first group, while the remaining 7 scenarios were grouped as the second group, and the correlation positions of these two groups were compared separately. Accordingly, a visual representation showing the encounter analysis between correlation groups under scenarios is presented in Figure 4.

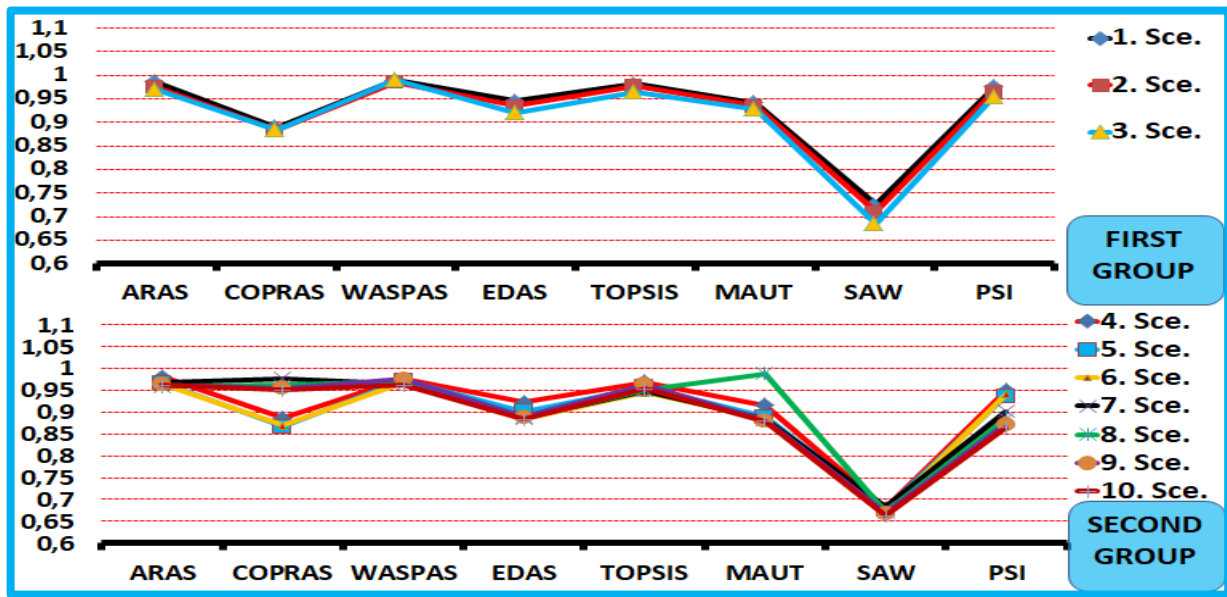


Figure 4. The Correlation Status of The PSA Method with Other Approaches within Various Scenarios

When Table 9 and Figure 4 are considered together, it is observed that as the scenarios increase, the correlation values of the PSA method with other MCDM methods diverge and decrease. As a consequence, it has been noted that the distinctive characteristics of the methodologies become increasingly conspicuous with the expansion of scenarios, leading to more pronounced disparities between them. Throughout the simulation analysis, the variance values of the methodologies were computed across various scenarios, and the resulting values are elaborated. The variance values of the performance scores determined for each scenario with respect to the mentioned scenarios, along with the mean variance values, are presented in Table 10.

Table 10. Variability in Methodologies Across Scenarios

Methods	ARAS	COPRAS	WASPAS	EDAS	
1.Sce	0.054313	0.001498	0.004313	0.092318	
2.Sce	0.053921	0.001201	0.004218	0.091921	
3.Sce	0.055433	0.001324	0.004519	0.093027	
4.Sce	0.054765	0.001465	0.004356	0.094156	
5.Sce	0.055187	0.001389	0.004478	0.093781	
6.Sce	0.054123	0.001527	0.004191	0.092519	
7.Sce	0.054929	0.001372	0.004587	0.094011	
8.Sce	0.055842	0.001438	0.004397	0.092878	
9.Sce	0.054621	0.001289	0.004245	0.095011	
10.Sce	0.055296	0.001503	0.004514	0.093687	
Mean	0.054842	0.001401	0.004382	0.093331	
Methods	TOPSIS	MAUT	SAW	PSI	PSA
1.Sce	0.023218	0.030218	0.000789	0.002523	0.008423
2.Sce	0.022991	0.028991	0.000852	0.002357	0.008212
3.Sce	0.021987	0.029987	0.000734	0.002568	0.008342
4.Sce	0.024156	0.028156	0.000916	0.002432	0.008476
5.Sce	0.022781	0.030781	0.000827	0.002497	0.008536
6.Sce	0.023519	0.029519	0.000895	0.002374	0.008489
7.Sce	0.024011	0.031011	0.000768	0.002586	0.008278
8.Sce	0.022878	0.029878	0.000912	0.002491	0.008355
9.Sce	0.025011	0.030011	0.000845	0.002425	0.008491
10.Sce	0.022687	0.028687	0.000781	0.002518	0.008578
Mean	0.023324	0.029724	0.000832	0.002477	0.008418

According to Table 10, within the scope of scenarios, the average variance value of the PSA method is higher compared to the PSI, SAW, WASPAS, and COPRAS methods, while it is lower compared to other MCDM methods. In this regard, it can be evaluated that the PSA method is more effective in distinguishing the performance of decision alternatives compared to the PSI, SAW, WASPAS, and COPRAS methods. It can be considered that the proposed method has capacity in distinguishing the performance of decision alternatives.

In the continuation of the simulation analysis, the consistency of variances in the criterion weights of the PSA method was assessed using ADM (Analysis of Means for variances with Levene) analysis across various scenarios. This analytical method offers a visual representation for evaluating the equality of variances. The visual representation consists of three elements: the overall mean ADM acts as the central line, accompanied by the upper decision limits (UDL) and lower decision limits (LDL). If the standard deviation of a group (cluster) surpasses the decision limits, it indicates a notable deviation from the general mean ADM, suggesting heterogeneity in variances. Conversely, if the standard deviations of all clusters lie within the LDL and UDL, it confirms the uniformity of variances. The graphical depiction of the ADM analysis is showcased in Figure 5.

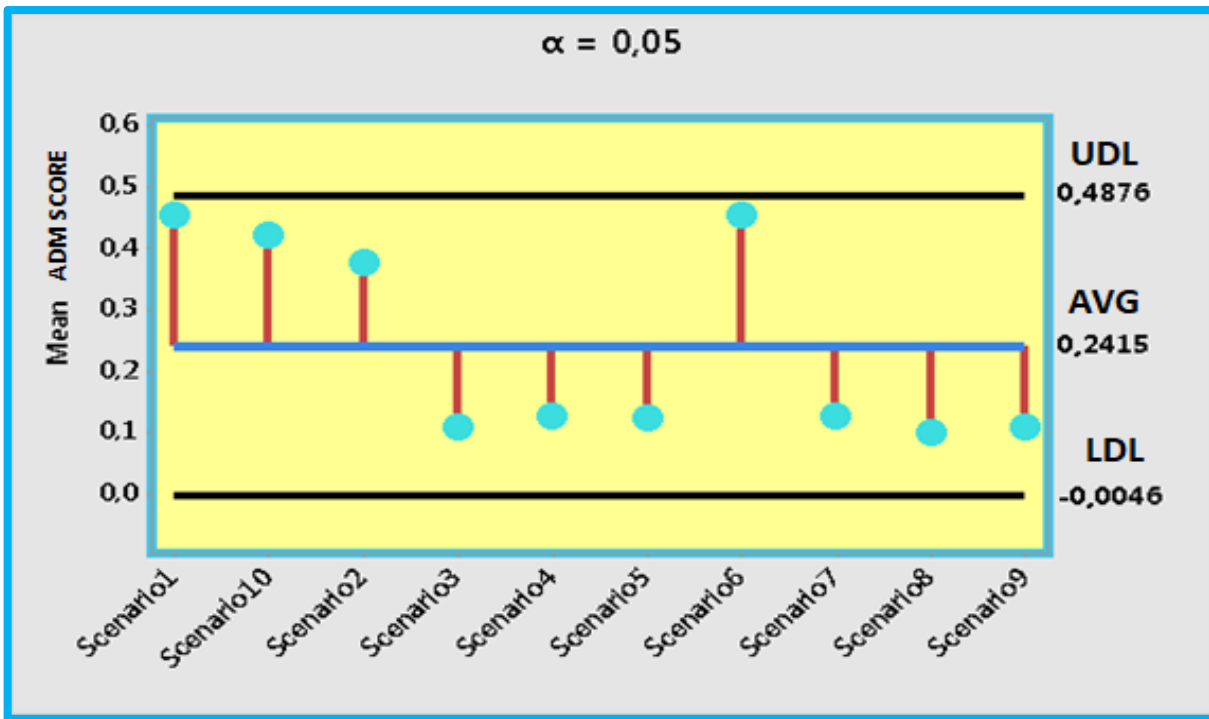


Figure 5. ADM Visual

Based on the information in Figure 5, the ADM analysis confirms that the variances in the identified performance for each scenario exhibit homogeneity. This means that the variations in the performance values across different scenarios are statistically similar. In simpler terms, the performance score are consistent across the scenarios. This finding is further corroborated by the results of the Levene Test, which are likely presented in Table 11.

Table 11. Levene Test

Levene Statistic	df1	df2	Sig.
0.268	2	10	0.124

p**<.05

The Levene Test is a statistical test specifically designed to assess the equality of variances between groups. Table 11 further corroborates the aforementioned conclusion. The p-value obtained from the Levene Test is 0,212, which is greater than the significance threshold of 0,05. This outcome statistically confirms the homogeneity of variances in the performance value of decision alternatives across different scenarios. Overall, the ADM analysis and Levene Test together provide strong evidence that the variances in the criterion weights are consistent across the different

scenarios investigated in the simulation analysis. In conclusion, the findings of the simulation analysis provide compelling evidence regarding the robustness and stability of the PSA method. The consistent performance of the method across diverse scenarios demonstrates its the robustness, stability and potential for practical applications.

IV. CONCLUSION

The complex problems of today necessitate a systematic and consistent decision-making process that considers multiple criteria. This is because novel approaches can render the decision-making process more transparent and enable better coping with uncertainties. Therefore, developing new approaches and methods in multi-criteria decision-making is crucial for solving complex problems more effectively and making more informed decisions. In this context, this research proposes a new method (PSA) that can be used in measuring the performance of decision alternatives or in selection problems. The fundamental principle of the PSA method is based on the proportional increase in values assigned to each criterion across different decision alternatives. Therefore, any decision alternative whose increase in criterion values is higher compared to other decision alternatives enhances its performance. The most significant advantage of the method lies in enabling a clear and objective evaluation of decision alternatives' performances by comparing the increase rates in different criteria within the method. The method's most distinctive feature is the absence of weighting criteria. This is because by clearly indicating which alternatives perform better than others for each criterion, the strength of the criterion is implicitly calculated.

The research dataset consists of Economic Freedom Index criterion values for G7 countries. Initially, the results of the proposed method were compared with ARAS, COPRAS, WASPAS, EDAS, TOPSIS, MAUT, SAW, and PSI methods using the same dataset values. According to the findings, it was observed that the PSA method had a positive, significant, and very high correlation with the ARAS, COPRAS, WASPAS, EDAS, TOPSIS, MAUT, and PSI methods, and a high correlation with the SAW method. Based on all these results, the proposed method was evaluated as credible and reliable.

In the simulation analysis, initially, 10 different scenarios were created, and the relationship between the PSA method and other MCDM methods was evaluated according to these 10 scenarios. The results indicated that as the number of scenarios increased, the relationships between the PSA method and other MCDM methods decreased, making its characteristic feature more pronounced. Continuing with the simulation analysis, the average variance values of the methods were measured across the 10 scenarios. Upon examining the results, it was found that the PSA method had higher average variance values compared to the COPRAS, WASPAS, SAW, and PSI methods. Based on this result, it was evaluated that the PSA method has a capability to distinguish the performance of decision alternatives. Finally, an ADM analysis was conducted with 10 different scenarios for the PSA method. As a result, it was found that the homogeneity of variances was achieved. Considering all these results of the simulation analysis, it was concluded that the proposed method is robust and stable.

In future studies, decision-making problems concerning the superiority of decision alternatives based on criteria values can be addressed using different mathematical models to calculate or solve the selection problem of decision alternatives. The superiority, weaknesses, and contributions to the literature of models constructed by comparing different mathematical models explaining the performance of said decision alternatives can be discussed more comprehensively.

STATEMENT OF CONTRIBUTION RATE

Authors' contribution rates to the study are 100%

CONFLICTS OF INTEREST

They stated that no conflict of interest existed between the authors and their respective institutions.

RESEARCH AND PUBLICATION ETHICS

In the studies carried out within the scope of this article, the rules of research and publication ethics were followed.

REFERENCES

- [1] Aktaş, R., Doğanay, M. M., Gökmen, Y., Gazibey, Y., & Türen, U. (2015). Sayısal karar verme yöntemleri. İstanbul: Beta Yayıncılık.
- [2] Al Khoiry, I., & Amelia, D. R. (2023). Exploring simple additive weighting (SAW) for decision making. *Jurnal Inovtek Polbeng - Seri Informatika*, 8(2), 281-290. DOI: 10.35314/isi.v8i2.3433.
- [3] Amor, S. B., De Almedia, A. T., De Miranda, J. L., & Aktas, E. (2021). *Advanced studies in multi-criteria decision making*. Oxfordshire: Taylor & Francis.
- [4] Atan, M., & Altan, Ş. (2020). Örnek uygulamalarla çok kriterli karar verme yöntemleri. Ankara: Gazi Kitabevi.
- [5] Ayçin, E. (2019). Çok kriterli karar verme . Ankara: Nobel Yayın.
- [6] Azad, T. (2019). Implementation of TOPSIS method for multi criteria decision making of supplier selection. *European Journal of Advances in Engineering and Technology*, 6(11), 22-27.
- [7] Behl, A. (2020). *Multi-Criteria Decision Analysis in Management*. Hershey, PA : Business Science Reference.
- [8] Biswas, T. K., Chaki, S., & Das, M. C. (2019). MCDM technique application to the selection of an Indian institute of technology. *Operational Research in Engineering Sciences: Theory and Applications*, 2(3), 65-76. DOI: 10.31181/10.31181/oresta1903065b.
- [9] Bridgman, P. W. (1922). *Dimensional analysis*. New Haven: Yale University Press.
- [10] Chinnasamy, S., Ramachandran, M., Rajkumar, S., & Sivaji, C. (2023). A survey on transportation system using the WPM method. *Building Materials and Engineering Structures*, 1(2), 37-44. DOI: 10.46632/bmes/1/2/5.
- [11] Chourabi, Z., Khedher, F., Babay, A., & Cheikhrouhou, M. (2019). Multi criteria decision making in workforce choice using AHP, WSM and WPM. *The Journal of The Textile Institute*, 110(7), 1092-1101. DOI: 10.1080/00405000.2018.1541434.
- [12] Churchman, C. W., & Ackoff, R. L. (1954). An approximate measure of value. *Journal of Operation Research Society of America*, 2(2), 172-187.
- [13] Ciardiello, F., & Genovese, A. (2023). A comparison between TOPSIS and SAW methods. *Annals of Operations Research*, 325, 967–994. DOI: 10.1007/s10479-023-05339-w.
- [14] Çelikbilek, Y. (2018). Çok kriterli karar verme yöntemleri. Ankara: Nobel Akademik Yayıncılık.
- [15] Demir, G., Özyalçın, A. T., & Bircan, H. (2021). Çok kriterli karar verme yöntemleri ve ÇKKV yazılımı ile problem çözümü. Ankara: Nobel.
- [16] Demirci, A. (2020). Sağlık hizmetleri yönetiminde çok kriterli karar verme teknikleri. Ankara: Gazi Kitabevi.
- [17] Dhanalakshmi, C. S., Madhu, P., Karthick, A., Mathew, M., & Kumar, R. V. (2022). A comprehensive MCDM-based approach using TOPSIS and EDAS as an auxiliary tool for pyrolysis material selection and its application. *Biomass Conv. Bioref*, 12, s. 5845–5860. DOI: 10.1007/s13399-020-01009-0.
- [18] Dinçer, S. E. (2019). Çok kriterli karar alma. Ankara: Gece Akademi.
- [19] Ecer, F. (2020). Çok kriterli karar verme. Ankara: Seçkin Yayıncılık.
- [20] Ghorabae, M. K., Zavadskas, E. K., Olfat, L., & Turskis, Z. (2015). Multi criteria inventory classification using a new method of evaluation based on distance from avarege solution (EDAS). *Informatica*, 26(3), 435-451. DOI: 10.15388/Informatica.2015.57
- [21] Goswami, S. S., & Behera, D. K. (2021). Solving material handling equipment selection problems in an industry with the help of Entropy integrated COPRAS and ARAS MCDM techniques. *Process Integr. Optim. Sustain.*, 5, 947–973. DOI: 10.1007/s41660-021-00192-5.
- [22] Handayani, N., Heriyani, N., Septian, F., & Alexander, A. D. (2023). Multi-criteria decision making using The WASPAS method for online English course selection. *Jurnal Teknoinfo*, 17(1), 260-270.
- [23] Heritage Foundation (2023). *Economic Freedom Index. Country Scores*: Retrieved from <https://www.heritage.org/index>.
- [24] Hezer, S., Gelmez, E., & Özceylan, E. (2021). Comparative analysis of TOPSIS, VIKOR and COPRAS methods for the COVID 19 regional safety assessment. *Journal of Infection and Public Health*, 14, 775–786. DOI: 10.1016/j.jiph.2021.03.003
- [25] Hwang, C. L., & Yoon, K. (1981). *Multiple attribute decision making: Methods and applications*. New York: Springer-Verlag.
- [26] Kabir, G., & Hasin, M. A. (2012). Comparative analysis of TOPSIS and FUZZY TOPSIS for the evaluation of travel website service quality. *International Journal for Quality Research*, 6(3), 169-185.
- [27] Karabašević, D., Stanujkić, D., & Urošević, S. (2015). The MCDM model for personnel selection based on SWARA and ARAS methods. *Management*, 77, 43-51.
- [28] Karakiş, E. (2021). Machine selection for a textile company with CRITIC and MAUT methods. *Avrupa Bilim ve Teknoloji Dergisi*(27), 842-848. DOI: 10.31590/ejosat.994697
- [29] Karande, P., Zavadskas, E. K., & Chakraborty, S. (2016). A study on the ranking performance of some MCDM methods for industrial robot selection problems. *International Journal of Industrial Engineering Computations*, 7(3), 399-422. DOI: 10.5267/j.ijiec.2016.1.001
- [30] Kaya, İ., & Karaşan, A. (2020). Çok kriterli karar verme. İstanbul: Umuttepe Yayınları.
- [31] Keeney, R. L., & Raiffa, H. (1976). *Decision with multiple objectives: Preferences and value trade off*. New York: John Wiley & Sons .

- [32] Keshavarz-Ghorabae, M., Amiri, M., Zavadskas, E. K., Turskis, Z., & Antucheviciene, J. (2021). Determination of objective weights using a new method based on the removal effects of criteria (MERECE). *Symmetry*, 13, 1-20. DOI: 10.3390/sym13040525
- [33] Lopez, L. M., Ishizaka, A., & Qin, J. (2023). *Multi criteria decision making sorting methods: applications to real world*. Cambridge-Massachusetts: Academic Press.
- [34] Maharani, S., Ridwanto, H., Hatta, H. R., Khairina, D. M., & Ibrahim, M. R. (2021). Comparison of TOPSIS and MAUT methods for recipient determination home surgery. *IAES International Journal of Artificial Intelligence (IJ-AI)*, 10(4), 930-937. DOI: 10.11591/ijai.v10.i4.pp930-937.
- [35] Maniya, K., & Bhatt, M. G. (2010). A selection of material using a novel type decision-making method: Preference selection index method. *Materials and Design*(31), 1785-1789.
- [36] Mousavi-Nasab, S. H., & Sotoudeh-Anvari, A. (2017). A comprehensive MCDM based approach using TOPSIS, COPRAS and DEA as an auxiliary tool for material selection problems. *Materials & Design*, 121, 237-253. DOI: 10.1016/j.matdes.2017.02.041
- [37] Onajite, O., & Oke, S. A. (2021). The application of WSM, WPM and WASPAS multicriteria methods for optimum operating conditions selection in machining operations. *Jurnal Rekayasa Sistem Industri*, 10(1), 1-15. DOI: 10.26593/jrsi.v10i1.4271.1-14.
- [38] Özbek, A. (2019). Çok kriterli karar verme yöntemleri ve excel ile problem çözümü kavram-teori-uygulama (2. b.). Ankara: Seçkin Yayıncılık.
- [39] Öztel, A., & Alp, İ. (2020). Çok kriterli karar verme yöntemi seçiminde yeni bir yaklaşım. İstanbul: Kriter Yayınevi.
- [40] Paksoy, S. (2017). Çok kriterli karar vermede güncel yaklaşımlar. Adana: Karahan Kitabevi.
- [41] Petković, D., Madić, M., Radovanović, M., & Gečevska, V. (2017). Application of the performance selection index method for solving machining MCDM problems. *FACTA Universitatis-Series: Mechanical Engineering*, 15(1), 97-106. DOI: 10.22190/FUME151120001P.
- [42] Puška, A. (2013). *Comparative analysis of MCDM methods in investment decision*. London: LAP LAMBERT Academic Publishing.
- [43] Sotoudeh-Anvaria, A., Sadjadi, S. J., Molanaa, S. M., & Sadi-Nezhad, S. (2018). A new MCDM-based approach using BWM and SAW for optimal search model. *Decision Science Letters*, 7, 395-404. DOI: 10.5267/j.dsl.2018.2.001
- [44] Stanujkić, D., & Karabašević, D. (2018). An extension of the decision making problems with intuitionistic fuzzy numbers: A case of web site evaluation. *Operational Research in Engineering Sciences: Theory and Applications*, 7(1), 29-39. DOI: 10.31181/oresta19012010129s
- [45] Sudha, S. (2019). Application of EDAS method on water requirement in agriculture. *International Journal of Engineering Research & Technology (IJERT)*, 8(12), 558-561. DOI: 10.17577/IJERTV8IS120283
- [46] Taherdoost, H. (2023). Analysis of Simple Additive Weighting Method (SAW) as a Multi-Attribute Decision-Making Technique: A Step-by-Step Guide. *Journal of Management Science & Engineering Research*, 6(1), 21-24. DOI: 10.30564/jmser.v6i1.5400
- [47] Taufik, I., Alam, C. N., Mustofa, Z., Rusdiana, A., & Uriawan, W. (2020). Implementation of multi-attribute utility theory (MAUT) method for selecting diplomats. *The 5th Annual Applied Science and Engineering Conference (AASEC 2020)* (pp. 1-7). Bandung Barat: AASEC.
- [48] Tepe, S. (2021). Örnek uygulamalarla çok kriterli karar verme yöntemleri. Ankara: Akademisyen Kitabevi.
- [49] Tiwari, R. K., & Kumar, R. (2021). A robust and efficient MCDM based framework for cloud service selection using modified TOPSIS. *International Journal of Cloud Applications and Computing*, 11(1), 21-50. DOI: 10.4018/IJCAC.2021010102.
- [50] Triantaphyllou, E. (2010). *Multi-Criteria Decision Making Methods: A Comparative Study*. New York: Springer.
- [51] Trung, D. (2021). Application of EDAS, MARCOS, TOPSIS, MOORA AND PIV Methods For Multi-Criteria Decision Making In Milling Process. *Journal of Mechanical Engineering*, 71(2), 69-84. DOI: 10.2478/scjme-2021-0019
- [52] Tuş, A., & Adalı, E. A. (2018). Personel assessment with CODAS and PSI methods. *Alphanumeric Journal*, 6(2), 243-255. DOI: 10.17093/alphanumeric.432843
- [53] Uludağ, A. S., & Doğan, H. (2021). Üretim yönetiminde çok kriterli karar verme. Ankara: Nobel.
- [54] Ulutaş, A., & Topal, A. (2020). Bütünleştirilmiş çok kriterli karar verme yöntemlerinin üretim sektörü uygulamaları. Ankara: Akademisyen Kitabevi.
- [55] Van Thanh, N. (2020). *Multi Criteria Decision Making (MCDM) Model for Supplier Evaluation and Selection in the Supply Chain Management*. Moscova: Eliva Press.
- [56] Varatharajulu, M., Duraiselvam, M., Kumar, M. B., Jayaprakash, G., & Baskar, N. (2022). Multi criteria decision making through TOPSIS and COPRAS on drilling parameters of magnesium AZ91. *Journal of Magnesium and Alloys*, 10, 2857-2874. DOI: 10.1016/j.jma.2021.05.006
- [57] Vijayakuma, A. (2020). Comparison of multi criteria decision making methods SAW and ARAS: An application to performance of Indian pharmaceutical companies. *Journal of Economics and Technology Research*, 1(2), 23-46. DOI: 10.22158/jetr.v1n2p23

- [58] Walters, S. J. (2009). *Quality of life outcomes in clinical trials and health-care evaluation: A practical guide to analysis and interpretation*. New York: Wiley.
- [59] Yadav, S., Pathak, V. K., & Gangwar, S. (2019). A novel hybrid TOPSIS-PSI approach for material selection in marine applications. *Sādhanā*, 44(58), 1-12. DOI: 10.1007/s12046-018-1020.
- [60] Yıldırım, B. F., & Çiftçi, H. N. (2020). Çok kriterli karar verme yöntemleri ile finansal performans analizi ve tahmin modeli. İstanbul: Türkmen Kitapevi.
- [61] Zavadskas, E. K., & Kaklauskas, A. (1996). *Systemotechnical evaluation of buildings (pastatu sistemotechninis ivertinimas)*. Vilnius: Technika.
- [62] Zavadskas, E. K., Turskis, Z., & Vilutiene, T. (2010). Multiple criteria analysis of foundation instalment alternatives by applying additive ration assessment (ARAS) method. *Archives of Civil and Mechanical Engineering*, 10(3), 123-141. DOI: 10.1016/S1644-9665(12)60141-1
- [63] Zavadskas, E. K., Turskis, Z., Antucheviciene, J., & Zakarevicius, A. (2012). Optimization of weighted aggregated sum product assessment. *elektronika ir electrotechnika*, 122(6), 3-6. DOI: 10.5755/j01.eee.122.6.181
- [64] Zhang, X., Wang, C., Li, E., & Xu, C. (2014). Assessment model of ecoenvironmental vulnerability based on improved entropy weight method. *Scientific World Journal*, 2014, s. 1-7. DOI: 10.1155/2014/797814.



RESEARCH ARTICLE

Drone Swarm Classification from ISAR Imaging

*¹Remziye Busra Coruk, ¹Ali Kara, and ²Elif Aydin

*Atılım University, Faculty of Engineering, Electrical and Electronics Engineering Department, Ankara, Turkey
rbusratezel@gmail.com, [Orcid.0000-0002-9466-3862](https://orcid.org/0000-0002-9466-3862)

¹Gazi University, Faculty of Engineering, Electrical and Electronics Engineering Department, Ankara, Turkey
akara@gazi.edu.tr, [Orcid.0000-0002-9739-7619](https://orcid.org/0000-0002-9739-7619)

²Cankaya University, Faculty of Engineering, Electrical and Electronics Engineering Department, Ankara, Turkey
elif.aydin@cankaya.edu.tr, [Orcid.0000-0001-6878-1796](https://orcid.org/0000-0001-6878-1796)

Citation:

Coruk, R. B., Kara, A., Aydin, E. (2024). *Drone Swarm Classification from ISAR Imaging*, Journal of Science Technology and Engineering Research, 5(2): 127-134. DOI: 10.53525/jster.1529575

HIGHLIGHTS

- ISAR images of drone swarms are created based on various formation types
- Radar and simulation parameters are adjusted to achieve high resolution
- Formation types of drone swarm are classified with deep learning algorithm
- The developed method can be used for anti-drone technologies

Article Info

Received : August 7, 2024

Accepted : September 23, 2024

DOI:

10.53525/jster.1529575

*Corresponding Author:

Remziye Busra Coruk
rbusratezel@gmail.com

ABSTRACT

The use of drones has become increasingly popular as they can be easily purchased over the Internet. As drones find applications in a variety of fields, drone swarms have also gained significance. However, this popularity has introduced some challenges, particularly in the realm of drone detection, which is crucial for preventing the uncontrolled use of drone swarms in airspace. Drone swarm detection is essential to avoid dangerous accidents or criminal acts. This paper presents an inverse synthetic aperture radar (ISAR) imaging-based approach for identifying the formation types of drone swarms. The ISAR images of drone swarms are generated by using commercial EM tools including ANSYS. High frequency structural simulator (HFSS) - shooting bouncing ray (SBR+) solver is used for fast computation. The radar operation, as well as simulation configuration necessary for generating usable ISAR images, are quantified. In particular, the down-range and cross-range resolutions are evaluated to achieve high resolution images. The ISAR images are classified based on pre-defined swarm formations using deep learning. To this end, a convolutional neural network (CNN) model is employed. The model consists of training, validation, and testing phases. The swarm formation classes include Line, Square, Cross, and Triangle. The results demonstrate high accuracy in classification performance. The developed method can be utilized in anti-drone technologies.

Keywords: Radar Systems, Inverse synthetic aperture radar imaging, Drone, Classification, Convolution neural network

I. INTRODUCTION

Drones are defined as one of the Unmanned Aerial Vehicles (UAVs) that can be controlled remotely and automatically. Nowadays, they are widely used due to their easily accessible features. With the widespread use of drones, some rules and regulations have emerged to prevent the uncontrolled use of drones in the airspace. And, detecting drones that do not comply with these rules has become important. In addition, the use of drones in the military along with civil has become prevalent today. Thus, drone detection has also gained popularity in both civil and military fields [1]. By operating in a group, drones can combine their individual capabilities to deliver superior capabilities and tackle defined missions. Moreover, even if they are within the herd, they can also undertake different tasks individually defined for themselves. With these versatile capabilities, drone swarms have become popular nowadays [2].

Radar, electro-optical, and camera systems among the developing world technologies, are used for reconnaissance and surveillance purposes. The ability of radar systems to detect objects at long distances even in bad weather conditions makes them more selectable in recently developed systems. Consequently, the usage of radar systems to detect drones flying in the airspace is more common in the literature [3]. To detect the targets, there are two methods of radar systems. These are the frequency measurement method [4] and the range (time) measurement method [5]. While the frequency measurement method measures the micro-doppler of drones, the range (time) measurement method creates imaging of a drone by synthetic aperture radar (SAR) or the inverse-SAR (ISAR). SAR allows obtaining high-resolution images of the earth's surface even in bad weather conditions [6]. ISAR, on the other hand, provides information about targets such as ships, aircraft, and UAVs by obtaining images of moving targets [7]. SAR/ISAR systems are used by deploying to ground stations or manned/unmanned aerial platforms such as aircraft or satellites.

ISAR imaging is a topic that has attracted much attention in radar imaging technology in recent years. In ISAR technology, there is target movement, and this movement changes the direction of the target relative to the radar system, resulting in different aspect angles of viewing the target. Afterward, the backscatter signal of each reflection point of the target undergoes a phase change. Coherent data processing, as in SAR, provides high spatial resolution even in the azimuthal direction [8]. ISAR images for drone targets have been investigated in the literature. In [9], drone types of different sizes are detected by radar. Drones are made to rotate according to the radar by using a turntable. Thus, the radar data is processed to obtain an ISAR image of the target. In ISAR results, images of the drone at different frequency values, viewing angles, and also various polarization modes are analyzed and interpreted. In the other work [10], the authors present radar cross section (RCS) and ISAR image results of the fixed-wing drone. Experiments are carried out in an anechoic chamber using fully polarimetric radar. The authors show the effects of different parts of the drone based on four polarization modes. In [11], 2D and 3D ISAR images are reconstructed to identify flying drones. Sparse recovery techniques are used to create 2D ISAR images. Finally, 3D ISAR image of the drone is created using interferometry. The study includes measurement results. In [12], the authors emphasize the importance of ISAR imaging for the classification of drone targets. High-resolution images are reconstructed using multi-band radar. Both theoretical and experimental analyses are conducted on drones, and the results are analyzed and compared. In [13], the authors propose a method that uses ISAR images to classify drone targets. The polar mapping procedure is important to obtain the features of targets for the classifier. Experimental results are presented to show the differences between distorted and undistorted images. In [14], the authors propose a new algorithm to classify drone types (a commercial quadcopter and its explosive-loaded version). The authors propose an approach in security-sensitive environments for drones. On the other hand, the detection and recognition of drone swarms have not been studied much. In [15], the drone formation types are classified based on navigation data. The machine learning classification is employed. In today's technology, the usage of drone swarm structures has increased considerably in both civilian and military fields. With the increase in the use of drone swarm structures, it has become important to develop drone swarm detection algorithms to prevent their illegal use and to ensure that they are moved in the airspace in a controlled manner. However, the detection of drone swarms especially using ISAR images is limited in the literature. Additionally, the classification of drone swarms using ISAR images with a deep learning

algorithm with high accuracy and a small dataset is not available at all in the literature.

This paper presents an approach, based on ISAR images, to the problem of classification of drone swarms. The ISAR images are reconstructed using commercially available software tools, including ANSYS. Imaging radar configuration and simulation parameters are analyzed to achieve higher resolution. ISAR images are created based on several formations of drone swarms including Line, Square, Cross, and Triangle. A convolutional neural network (CNN) is proposed for the classification of drone swarms. Some preliminary results of the classification performance are presented.

The remainder of this paper is organized as follows; Section II presents the proposed method including a review of image formation concepts, radar configuration, and simulation parameters as well as the classification process. Section III presents the results of the classification of drone swarm formations, and finally, Section IV draws some conclusions.

II. METHOD

A. ISAR Image Formation

The reflected radio frequency signals from the target to the radar are processed with the ISAR technique. The Inverse Fourier Transform (IFT) is applied to the signal and the reflectivity density function which express the ISAR image of the target is generated by the following equation

$$\rho(x, y) = IFT\{S_R(t) \exp\left[-j4\pi f \frac{R(t)}{c}\right]\} \quad (1)$$

$S_R(t)$ is the return signal to radar from the target, $R(t)$ is the distance from the radar to the point target at time t (sn), f (Hz) is the frequency, and c (m/sn) is the speed of light [16].

B. Radar and Simulation Parameters

Millimeter wave (mmWave) radars are widely used for high resolution imaging applications. Obtaining high-resolution ISAR images of targets is important for detecting objects with high accuracy. High resolution depends on accurate calculation of the mmWave radar's down-range and cross-range resolution. Considering the synthetic aperture created by the radar on the target, the component in the direction of the radar is called down-range, and the component parallel to the flight line is called cross-range. While down-range resolution is dependent on bandwidth ($\frac{c}{2B}$) while cross-range is dependent on both the synthetic antenna aperture and the range ($\frac{\lambda R}{2D_s}$) [16].

High frequency structural simulator (HFSS) within ANSYS software platform is utilized in this study. HFSS-SBR+ which is an asymptotic high-frequency electromagnetic (EM) simulator is used for generating ISAR images. The shooting and bouncing ray (SBR+) technique is preferred due to its highly efficient and an accurate computation of complex EM scattering mechanisms. Here, the configuration of the radar and simulation parameters are important for high resolution ISAR imaging [17]. Frequency (MHz) and angle steps (degree) are formulated, respectively, as follows

$$\Delta f = \frac{c}{2 x_{max}} \quad (2)$$

$$\Delta\phi = \frac{\lambda}{2 y_{max}} \quad (3)$$

where x_{max} (m) is the down range extent while y_{max} (m) is the cross range extent, and λ (m) is the wavelength. Also, bandwidth (MHz) and aspect angle (degree) parameters are formulated, respectively, as follows

$$B = \Delta f N_x \quad (4)$$

$$\Delta\phi = \Delta\phi N_y \quad (5)$$

where N_x is the number of samples in x-axis and N_y is the number of samples in y-axis.

C. Classification of images

Deep learning has attracted a lot of attention in recent years and occupies a large place in the literature. Deep learning methods are also used for image classification in the literature. One of the most common is CNN in image classification, and it is utilized in this research. When briefly reviewing, CNN is a specialized neural network for processing and classification of image data. CNN processes the image with several layers [18]. CNN layers are listed below:

1) Convolutional Layer

This layer of the CNN model is the most important and indispensable layer. It is responsible for extracting the features of the image. It applies filtering techniques to extract low and high-level features in the image.

2) Pooling (Down-sampling) Layer

A pooling layer is added between successive convolutional layers. It takes on the task of reducing parameters and computational complexity. Max pooling, average pooling, and L2-norm pooling methods are frequently used, but the most popular one is max pooling.

3) Flattening Layer: This layer of the CNN prepares the data for the input of the last layer, the fully connected layer. The data are the matrixes coming from the convolutional and pooling layers converted into a one-dimensional array.

4) Fully-Connected Layer: Fully-connected layer is the most important layer of the CNN model. It performs the process of learning the data prepared by the flattening layer through the neural network.

III. RESULTS

ISAR images are reconstructed based on various scenarios of swarms using ANSYS software. Five bounces are used to simulate the ISAR images. For the physical theory of diffraction (PTD), the edge density of 20 edge segments/wavelength is considered. Radar parameter values are important for high-resolution ISAR images. Radar is operated at mmWave frequency band (77 GHz). ISAR image size is adjusted as 5 m×5 m. Additionally, down-range and cross-range resolution parameters are selected as 0.05 m. Based on the radar configuration, the simulation parameters are estimated including frequency step, angle step, bandwidth, and aspect angle. The drone type is specified as a quadcopter in the swarm. Computer aided design (CAD) model of drone is created as in Fig.1.

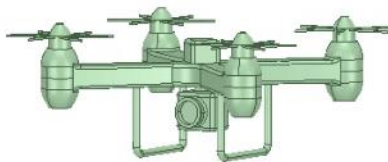


Figure. 1. CAD model of drone

Drones follow the rules of swarm structures and fly synchronously with other drones by following the same formation in the swarm structure. A drone swarm is composed of a static structure with a generally adopted geometric shape [19-21]. Drone swarm scenarios are designed by considering several formation types (Line, Square, Cross, and Triangle). Formation types of drone swarms at various look angles can be examined in Fig. 2.

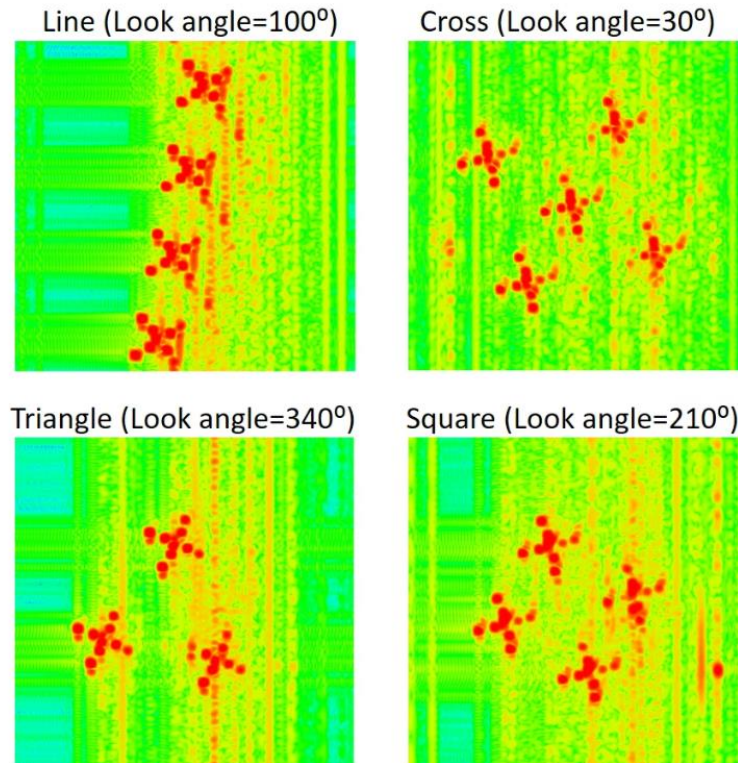


Figure. 2. Formation types of drone swarm

Due to the deep learning algorithm requirements, it is important to study large data sets to solve the classification problem with high accuracy without the need for deep networks. Therefore, it is important to expand the high-resolution ISAR image data, obtained for the drone swarms, for use in the deep learning algorithm. CNN model is used to classify ISAR images of drone swarms, because it is the most useful model for the image classification problem. The basic CNN model is selected for the classification part to avoid computational complexity. The dataset is extended by creating ISAR images between 0° and 350° with 10° intervals. A total of 140 ISAR images are used. The dataset is divided into training, validation, and testing phases to increase performance (80% training, 10% validation, 10% testing). ISAR images of drone swarms are trained with 30 epochs. The convolutional layers in the model use 3×3 kernel filters. Rectified linear units (ReLU) are used as the activation function in the convolutional layers, while the softmax activation function is applied in the last layer of the CNN model. Additionally, the batch size is set to 32. Google Colab environment, which allows to write python code, is used to create CNN algorithms. CNN model is given in Fig. 3.

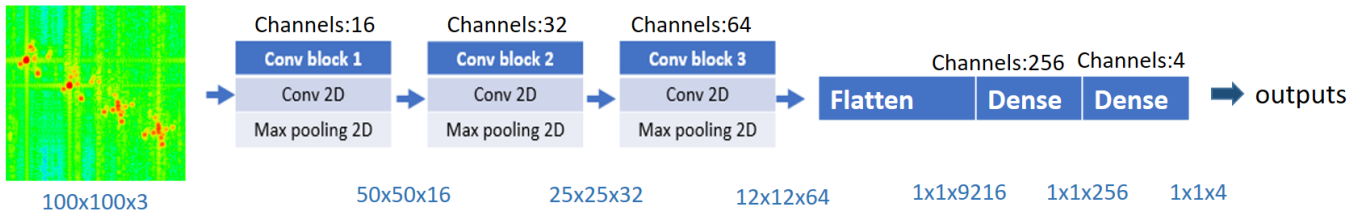


Figure. 3. Layers of the CNN algorithm

ISAR images are trained using CNN model. The plotting of the accuracy results versus epoch is given in Fig. 4.

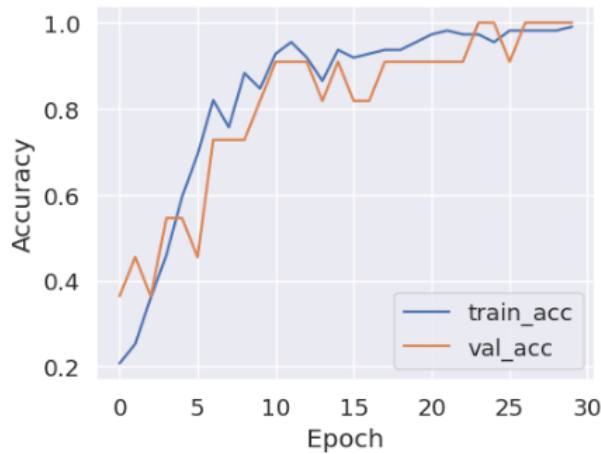


Figure. 4. Accuracy Results versus epoch

Training and validation performances improve as the number of epochs increases, reaching the highest at the end. To test the model's performance, the four ISAR images shown in Figure 2 are used. The test results are provided with confusion matrix given in Figure 5.

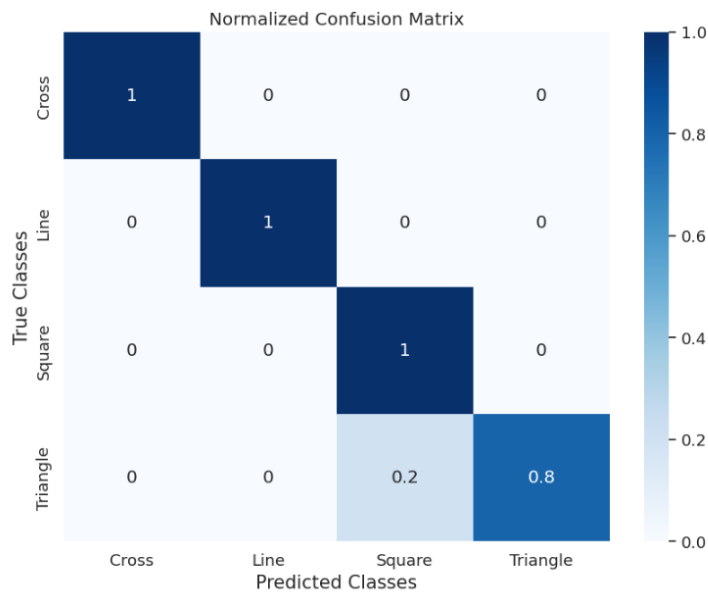


Figure. 5. Confusion matrix for test step

As a result, the classification performance of the model, which is trained with ISAR images based on various formation swarm types, is presented. Based on the confusion matrix, test accuracy is 95%. Triangle-Square formation types are confused for one image. Promising results have been obtained for future drone swarm classification studies.

IV. CONCLUSION

The classification of the formation of drone swarms remains a challenging problem when datasets created from ISAR images are used. This paper presents an approach for detecting drone swarm formations using ISAR images. Drone swarms are created based on several formation types including Line, Square, Cross, and Triangle. The dataset includes reconstructed ISAR images of scenarios from different look angles (ranging from 0° to 350° in 10° intervals) to ensure angular diversity. Radar and simulation parameters are quantified in image reconstruction in order to achieve high-resolution imaging. ISAR image dataset is divided into training, validation, and testing phases (80%-10%-10%) to prevent overfitting. The model is trained using a CNN algorithm, and an acceptable classification performance is demonstrated. The developed method can be used for anti-drone technologies.

As the paper presents some preliminary results of ongoing research, the future work will focus on extending the ISAR image dataset to include diverse scenarios (such as various drone sizes and with and without payload configurations) to further improve performance for more realistic operations. Furthermore, some more complex classification methods will be developed, and comparative results will be presented.

CONFLICTS OF INTEREST

They reported that there was no conflict of interest between the authors and their respective institutions.

RESEARCH AND PUBLICATION ETHICS

In the studies carried out within the scope of this article, the rules of research and publication ethics were followed.

REFERENCES

- [1] Coluccia, A., Parisi, G., & Fascista, A. (2020). Detection and classification of multirotor drones in radar sensor networks: A review. *Sensors*, 20(15), 4172. doi: 10.3390/s20154172
- [2] Tang, J., Duan, H., & Lao, S. (2023). Swarm intelligence algorithms for multiple unmanned aerial vehicles collaboration: A comprehensive review. *Artificial Intelligence Review*, 56(5), 4295-4327. doi: 10.1007/s10462-022-10281-7
- [3] Ciattaglia, G., Temperini, G., Spinsante, S., & Gambi, E. (2021, June). mmWave Radar Features Extraction of Drones for Machine Learning Classification. In *2021 IEEE 8th International Workshop on Metrology for AeroSpace (MetroAeroSpace)* (pp. 259-264). IEEE. doi: 10.1109/MetroAeroSpace51421.2021.9511703
- [4] Chen, V. C. (2019). *The micro-Doppler effect in radar*. Artech house.
- [5] Franceschetti, G., & Lanari, R. (2018). *Synthetic aperture radar processing*. CRC press.
- [6] Gökdoğan, B. Y., Çoruk, R. B., Aydın, E., & Kara, A. 2D Millimeter-Wave SAR Imaging with Automotive Radar. *Journal of Science, Technology and Engineering Research*, 5(1), 68-77.
- [7] Borkar, V. G., Ghosh, A., Singh, R. K., & Chourasia, N. (2010). Radar cross-section measurement techniques. *Defence Science Journal*, 60(2), 204-212. doi: 10.14429/dsj.60.341
- [8] Yang, Y., Wang, X. S., Li, Y. Z., & Shi, L. F. (2019, September). RCS measurements and ISAR images of fixed-wing UAV for fully polarimetric radar. In *2019 International Radar Conference (RADAR)* (pp. 1-5). IEEE. doi: 10.1109/RADAR41533.2019.171361
- [9] Li, C. J., & Ling, H. (2016). An investigation on the radar signatures of small consumer drones. *IEEE Antennas and Wireless Propagation Letters*, 16, 649-652.
- [10] Yang, Y., Wang, X. S., Li, Y. Z., & Shi, L. F. (2019, September). RCS measurements and ISAR images of fixed-wing UAV for fully polarimetric radar. In *2019 International Radar Conference (RADAR)* (pp. 1-5). IEEE.
- [11] Hamad, A., & Berens, P. (2024, July). 3D ISAR Imaging of an in-Air Rotating Drone Using Sparse Recovery and Multi-Channel Interferometry. In *2024 International Radar Symposium (IRS)* (pp. 358-362). IEEE.
- [12] Lee, W. K., & Song, K. M. (2018, August). Enhanced ISAR imaging for surveillance of multiple drones in urban areas. In *2018 International Conference on Radar (RADAR)* (pp. 1-4). IEEE.
- [13] Kim, K. T., Seo, D. K., & Kim, H. T. (2005). Efficient classification of ISAR images. *IEEE Transactions on Antennas and Propagation*, 53(5), 1611-1621.

- [14] Sayed, A. N., Ramahi, O. M., & Shaker, G. (2024). In the Realm of Aerial Deception: UAV Classification via ISAR Images and Radar Digital Twins for Enhanced Security. *IEEE Sensors Letters*.
- [15] Barbeau, M. (2019). Recognizing drone swarm activities: Classical versus quantum machine learning. *Digitale Welt*, 3(4), 45-50.
- [16] Chen, V., & Martorella, M. (2014). Inverse synthetic aperture radar imaging: principles, algorithms and applications. *IET*. doi: 10.1049/SBRA504E
- [17] “ANSYS HFSS SBR+” <https://www.ansys.com/content/dam/resource-center/application-brief/ansys-sbr-plus.pdf> (accessed: Dec 18, 2023).
- [18] Ketkar, N., Moolayil, J., Ketkar, N., & Moolayil, J. (2020). *Deep Learning with Python: Learn Best Practices of Deep Learning Models with PyTorch*. Apress LP.
- [19] Alkouz, B., Abusafia, A., Lakhdari, A., & Bouguettaya, A. (2022). In-flight energy-driven composition of drone swarm services. *IEEE Transactions on Services Computing*, 16(3), 1919-1933.
- [20] Adoni, W. Y. H., Lorenz, S., Fareedh, J. S., Gloaguen, R., & Bussmann, M. (2023). Investigation of autonomous multi-UAV systems for target detection in distributed environment: Current developments and open challenges. *Drones*, 7(4), 263.
- [21] Alkouz, B., & Bouguettaya, A. (2020, December). Formation-based selection of drone swarm services. In *MobiQuitous 2020-17th EAI International Conference on Mobile and Ubiquitous Systems: Computing, Networking and Services* (pp. 386-394). doi: 10.1145/3448891.3448899



REVIEW ARTICLE

Review of Grid-Connected Solar PV Systems With Decoupled Control

*^{id} Abdulkadir OZCAN, ¹^{id} Ahmed Saadon ALGBURI, ²^{id} Omar Ali NUAIMI, ³^{id} Hanaa Hussein LAFTA

*College of Engineering and Natural Sciences, Department of Electrical Electronics Engineering, KTO Karatay University, Konya, Turkey
abdulkadir.ozcan@karatay.edu.tr, [Orcid. 0009-0009-7224-1798](https://orcid.org/0009-0009-7224-1798)

¹Department Electrical-Computer Engineering, College of Engineering, University of KTO Karatay University, Konya, Turkey
Eng.ahmet.shkur@gmail.com, [Orcid. 0009-0006-0969-6878](https://orcid.org/0009-0006-0969-6878)

²Department of Electrical - Electronic Engineering, college of Engineering, Istanbul Gelisim University, Istanbul, Turkey
Omar.ali.khaleel1@gmail.com, [Orcid. 0009-0004-2210-0931](https://orcid.org/0009-0004-2210-0931)

³Department of Mechatronics Engineering, College of Engineering, University of KTO Karatay University, Konya, Turkey
Hanaa.hussein.lafta@gmail.com, [Orcid. 0009-0001-1838-1951](https://orcid.org/0009-0001-1838-1951)

Citation:

Özcan, A., Algburi, A.S., Nuaimi, O.A., Lafta H.H., (2024). *Review of Grid-Connected Solar PV Systems With Decoupled Control*, Journal of Science Technology and Engineering Research, 5(2): 135-147. DOI: 10.53525/jster.1533727

HIGHLIGHTS

- Filling knowledge gaps in optimizing power management in renewable energy systems.
- Exploring methods like vector control, direct power control, and model predictive control.
- By showcasing the importance of decoupled control, it emphasizes solutions for stabilizing power flows in modern grids
- Enhanced understanding of active/reactive power decoupling methods.

Article Info

Received : 15 August 2024

Accepted : 14 November 2024

DOI:

10.53525/jster.1533727

*Corresponding Author:

Abdulkadir OZCAN

abdulkadir.ozcan@karatay.edu.tr

Phone: +90 555 878 88 76

ABSTRACT

This paper presents a decoupled control for grid-connected solar photovoltaic (PV) system. The control framework used in this paper aims not to track the changing maximum power point (MPP) for extracting power at MPP, hence blocking the MPP tracking issue against the effect of solar radiation and temperature. Real power is produced by tracking the control voltage with a zero-dynamics-based controller. A cascaded loop controller with inner loop to regulate the control voltage is incorporated to ensure the produced real power follows the reference power in the presence of power disturbance. The proposed control scheme with the consideration of the inverter's rated voltage shows improved system dynamics. Simulations in various conditions are conducted to prove the effectiveness of the proposed control strategies. CIGRE 13-node benchmark system is used as the case study to evaluate the results of the PV system connected to a more complex power system. It has been shown that the proposed controller allows the total production of the energy under maximum power point conditions and also improves the overall stability of distributed generation connected to the grid. Therefore, it can be implemented to increase the capacity of renewable inverter-based power generation and the power system quality.

Keywords: solar power, power generation, solar energy, decoupled control

I. INTRODUCTION

Furthermore, the distribution static compensation (DSTATCOM) and the uninterruptible power supply (UPS) need to be operated during a grid-connected mode and a grid blackout condition while the solar PV system is disconnected from the grid. The energy storage system, such as a battery, a supercapacitor, and a flywheel system, is used for compensating the solar power quality problem by the energy storage system and the DSTATCOM during grid-connected mode and grid overvoltage condition. The energy management system based on the state of charge of the storage system is developed for the storage system efficiency. However, the solar energy system profitability is increased if the battery energy is designed with a better payback period of the investment [1].

The control algorithms are developed for maximum power point tracking and inverter control method for the conventional grid-connected solar PV system. However, in the conventional solar PV system, the solar PV system cannot be operated during a grid blackout condition. On the other hand, the solar PV system should be disconnected from the grid when the grid voltage is over the specified operating range. Because the solar PV system cannot supply the load, the disconnection of the solar PV system from the grid is used for voltage and frequency regulation in one-second control in autonomous mode or grid-connected mode [2].

To improve the efficiency of the solar power generation system and reduce the cost of the system, many research have been done in power electronic devices, control algorithms, and the configuration of the power conversion circuit connected between the solar PV system and the grid. In the conventional solar PV system, the control algorithms are developed for a maximum power point tracking method and a unity power factor operation of the inverter via a direct power control method to improve the efficiency of the solar PV system [3].

The solar power generation system is one of the promising sources of renewable energy. Nowadays, the solar photovoltaic (PV) system is the most attractive power generation source because it generates power at the point of usage, has high reliability, low maintenance cost, and a reasonable payback time. The solar power generation also has self-consumption and self-dispatch characteristics. These characteristics can be supported for stabilizing grid instability due to intermittent power generation by the self-consumption of solar power [1].

II. FUNDAMENTALS OF SOLAR PHOTOVOLTAIC SYSTEMS INTRODUCTION

An inverter is a power electronic device, converting DC to AC. The conversion is typically accomplished by the boost inverter, voltage source inverter, current source inverter, and multilevel inverter. A pure sine wave output of an inverter is the achievement. These inverters have two output filters, in which the presence of separate control is allowed so that the power can be distributed by a given mode. In grid-connected SPV systems, a multimode inverter can define the different functions that can contribute [4]. To make the consumption of energy easy, other functionalities such as filtering, reactive power compensation, and Ride Through Mode are viewed by the multimode inverter. In the absence of a power connection, a standalone system can also be running. The inverter multimode is driven CE, PE, and ES, to express the association. A functional enhancement of the grid allows the presence of other functionalities, CE, and PE. In the case of a strategy, the top level of the inverter deserves a certain strategy. The PV device allows a constant DC card to be sent to the motor drive in the output [5]. Moreover, after step-up connected by a DC-DC, the photovoltaic system at the other end is constructed. Finally, the connected switch is a DC-DC converter, to charge the battery or indeed support the grid to stabilize [6].

PV photovoltaic systems can generally be classified into three different types, i.e., standalone PV systems, grid-connected PV systems, and hybrid PV systems. In standalone PV systems, solar PV modules usually supply power to DC loads, and DC loads sometimes convert to AC loads by using an inverter. The charging of the battery is carried

out by the PV system after the loads are satisfied [7]. The inverter supplies the AC supply to the AC loads. In grid-connected PV systems, the power is used not only by the loads, but the excess power is fed back to the grid. In hybrid PV systems, it is the combination of standalone PV systems and grid-connected PV systems. It is a good form of electrification in underdeveloped, distant areas and largely isolated from the national grid. They provide electricity by means of renewable energy sources, and the power is stored in the battery for a 24-hour power supply. In this work, grid-connected PV systems and DC-coupled solar PV generate a constant DC voltage for a battery bank at the load. This is followed by the AC grid, offering power support [8]. Another output from the multimode inverter is fed into the traction motor through an LC filter circuit, converting the DC power to the AC source required to run the traction [9].

As the energy demand is rapidly increasing, researchers are looking for eco-friendly, renewable energy sources such as hydropower, solar energy, wind, and biogas. Among these sources, solar energy is one of the most promising sources because of its abundance and free availability [10]. There are two types of solar power systems: solar photovoltaic and solar thermal systems. Solar cells are the basic building block of a solar photovoltaic system. Solar PV systems have advantages of silent operation, low maintenance cost, low payback period, fast installation, and no carbon emissions. Efficiencies and cost per KW of solar PV systems have been rapidly improved. Most of the modern technologies for infrared generation are based on photonic processes, for instance, incandescent, fluorescent, and light-emitting diodes [11].

A. Basic Principle of Solar Pv Systems

The sun is the ultimate source of energy for our planet. The energy from the sun reaches the earth in two forms: light and heat [12]. The electromagnetic radiation from the sun that reaches the earth is composed of both light and heat, known as thermal radiation. The thermal part of the radiation is absorbed by the atmosphere, and the light part is incident on the earth's surface [13]. However, it should be noted that heat is responsible for the greenhouse effect. The light incident on the earth's surface is the necessary element for the photosynthesis process in plants [14].

With the increase in power demand and depletion of fossil fuels, photovoltaic (PV) power generation is gaining substantial attention and is one of several promising alternate sources of energy. A solar photovoltaic system harnesses solar energy through PV modules to generate electricity in the form of DC power [15]. The generated DC power is later used as is or converted into AC power using an inverter. Conversion of electrical energy from sunlight can provide significant benefits to society, both in reducing environmental pollution and enhancing energy security for a nation [16].

B. Types of Solar Pv Systems

The implementation of grid-connected photovoltaic (GCPV) systems for renewable energy has been rising. GCPV systems are clean, quiet, and have many other advantages. Also, it is easy for a GCPV system to be downscaled or upscaled in size, making it very flexible in its application. As an inverter is a very important device for GCPV systems, grid-connected inverters must have the most advanced technology for inverting DC power into AC power [17]. An efficient inverter is capable of greatly increasing the amount of power that is injected into the grid. When the phase-locked loop (PLL) performs its task, it uses a Pure Generalized Integrator (PGI) to increase its speed. When the grid frequency suddenly changes, the PLL synchronizes with the grid frequency. With traditional GCPV systems, the electronic interface contains two DC-DC converters, and the voltage used to feed the inverter-aligned voltage bus structure. This kind of process causes voltage increases. It is harder to control the interface to stabilize the voltage without power regulation [18].

III. GRID-CONNECTED SOLAR PV SYSTEMS

Solar irradiance typically ranges from about 1361 to 1362 W/m² at the top of Earth's atmosphere (known as the solar constant) under Air Mass 0 (AM0) conditions. However, at ground level, under clear sky conditions and Air Mass

1.5 (AM1.5), which is commonly used for photovoltaic testing, the irradiance usually does not exceed 1000 W/m^2 , while the operating temperature of solar PV panels changes in the range of $15\text{--}65 \text{ }^\circ\text{C}$. This wide range of fluctuation offers a particularly complicated problem in the design of the controller. Maximum power must be tracked to overcome the solar irradiation unit and temperature, even during partial shades or quick changes in operating points of the interconnected solar panel [19]. However, to accomplish the proper condition of the solar module, procedures to decouple P (Active power) and Q (Reactive power) are essential. Indeed, solar inverters should not generate reactive power at night, as this can drain the grid network power lines and present power factor problems, potentially damaging a power grid's stability [20].

The output current of solar photovoltaic inverters is associated with solar irradiation. Output voltage relies on solar panel temperature primarily and changes as any dependence on the solar panel transposition line. The inverter should compensate precisely for output variations due to solar radiation and module temperature. The control system must ensure this for maximum energy harvesting [21].

A grid-connected solar PV system employs solar panels to convert sunlight into electricity before feeding it directly into the electricity grid. The system consists of several modules and a power conditioning unit (inverter). In general, a photovoltaic array requires an inverter and feedback with grid voltage to supply power to a three-phase grid-connected inverter [22].

Grid-connected solar photovoltaic (PV) power systems convert light energy directly into electrical energy through the photoelectric effect and the use of a semiconductor material, for example, silicon wafers. Without any disturbance to environmental conditions such as cloud cover, this renewable source can provide useful energy. Large potential exists in most areas globally for the deployment of grid-connected solar photovoltaic systems to supply a significant part of the energy demand with relatively low environmental impact [22].

A. Components of A Grid-Connected Solar Pv System

- Grid-Connected Solar PV System with Decoupled Control
- Filters: The low-frequency harmonics need to be reduced to maintain a high-power quality of the grid-side current and voltage.
- DC-AC Panel Converter: In a solar power plant, large arrays can be built. To avoid shading, mounting, and size-related losses, the array is divided into a set of independent smaller modules. A panel converter can be utilized to convert the modules at the DC end itself [23].
- Inverter: It converts the DC power from the solar PV array to a precisely defined AC power output form suitable for interfacing with the utility grid [24].
- DC-DC Boost Converter: It boosts the DC power generated by the solar PV array to the DC power level necessary for the inverter to create a grid-compliant AC output voltage [25].
- Solar Array: It is the combination of solar cells that absorbs the energy from the sun in the form of solar radiation and converts it into electrical energy.

A grid-connected solar PV system is a power generation plant operating in parallel with the utility grid. Generation and distribution of electrical power is taken care of by the utility grid, while the utility grid supplies the required power for the connected loads. The basic configuration of a solar PV array consists of solar panels, a PV module junction box, and a combiner box, as shown in Figure 1. The various components of a grid-connected solar PV system are [26].

B. Benefits and Challenges Of Grid-Connected Systems

The main challenges of grid-connected solar PV are its high installation cost. However, it is specific to small-scale and incremental installation process. There is also a reduction in solar power output caused by system voltage increases above a certain level. Such a reduction should also be attributed to the increase in voltage, which causes the reverse power of the PV cell [27]. In this context, the installed photovoltaic capacity exceeds the threshold. Both

might increase the reverse of the solar module of the photovoltaic system, which reduces the current supply of the PV and further decreases the inverter's power output. Apart from when the voltage is too high, the reliability of the power point-speed tracking mechanism is not great. In-scale grid-connected power utilizing inverter energy, some products have a rate of heading reaction. And user operations are less stable because the intrinsic capacity of the grid is increasingly differentiated from the solar PV operation point [28]. Furthermore, overloaded, overheated, and advanced aging PV equipment are often triggered by slow malfunction. This means that real and reactive power control in the PV system is thus necessary.

The main benefits of grid-connected solar PV include:

The most solar PV systems are grid-connected and located at residential houses, commercial, and industrial customers. The grid-connected solar PV system is a synchronous system with high definition and allows customers to inject surplus generated power into the grid-connected busbar. They are constructed normally by connecting solar PV cells in series and parallel to form a system of practically established output voltage and current. They include a solar array, command, control, stability protection, equalization for voltage or current, storage-based power processing, and power quality [29]. It operates as a single source with enough injection of real power. When grid-connected, the inverter interface is synchronized to the grid voltage. The inverter and grid must match the amplitude, phase angle, and frequency of the voltage. It should be at a particular level of the reactive power [30].

C. Advantages and Disadvantages Of Grid-Connected Solar Pv Systems

- Improved Grid Stability: Decoupled control provides independent management of active and reactive power, helping to stabilize grid voltage and frequency.
- Compliance with Grid Codes: Many regions require PV systems to provide reactive power support for voltage regulation; decoupled control helps meet these regulatory demands.
- Maximized Power Output: Allows the PV system to operate at maximum power point tracking (MPPT) for active power, maximizing energy production while handling reactive power separately.
- Enhanced Power Quality: Controls reactive power to help address voltage sags, swells, and harmonics, which can improve overall power quality on the grid.
- Fast Response to Grid Fluctuations: Decoupled control enables quick adaptation to changing grid conditions, which is beneficial in managing grid disturbances.
- Complex Control System: Decoupled control requires advanced algorithms and tuning, which can increase the complexity and technical expertise needed for the system.
- Higher Costs: Requires advanced hardware and computing power, potentially increasing overall system costs.
- Potential Trade-offs in Power Output: Prioritizing reactive power during grid disturbances may slightly reduce active power output, impacting efficiency in some situations.
- Increased Wear on Components: Frequent power adjustments can wear out components like inverters faster, leading to higher maintenance needs over time.
- Dependence on Accurate Measurements: The control system relies on precise measurements of grid voltage and frequency; poor data quality can lead to ineffective control and instability.

IV. DECOUPLED CONTROL IN SOLAR PV SYSTEMS

Also, the improvement of the power quality at the connection points has motivated the study of power electronic equipment which contributes in this direction. Inverters have become a means for connecting solar power plants to the public utility grid, allowing for energy produced by the power plant to be injected into the network. The installation of inverters that are collectively installed at a medium voltage level and are connected to the public utility grid at a higher voltage level [22]. Because the inverters are power electronic devices connected to the medium voltage grid and power is being injected into the system, the grid is exposed to the distortion effects caused by the

inverters. The electrical system undergoes voltage wave distortion and transients in addition to oscillating at a frequency different from that of the standard. The grid's current and voltage distortions caused by the inverters are directly related to the control used by the power plants [31].

Renewable energy and distributed power generation systems are of great interest for modern power systems. Among these systems, solar photovoltaic (PV) systems have the advantage that they do not have rotating parts and that they generate electricity from sunlight, making them easy to install and fuel cost-free [32]. Furthermore, research and development in solar cells have reduced the cost of electricity production to levels closer to conventional energy resources. This has triggered the interest in implementing large generation systems. Both research reports and projects exist that require the connection of a solar power plant to the power system at medium and high voltages. This type of large generation is usually intended to be connected to high voltage levels. In order to implant the large power stations, it is necessary to install devices at the connection points which ensure that the power quality indexes are within the limits established by the standard and, if possible, are as close as possible to the levels assigned by the buyer [33].

A. Concept and Importance Of Decoupled Control

In a grid-connected system, a higher current, which is three times the input, is allowed to flow into the DC bus. This cannot be possible when the system is directly connected to the BLDC motor. The proposed decoupled controller comprises of the dump controller, which aids the solar PV array in feeding more power into the DC bus and to the grid without providing additional burden to the DC bus, thereby providing maximum power to feed into the grid [26]. Decoupled control allows the power flowing from the solar PV array to be independent of the speed of the BLDC motor and some portion of the power to flow inside the DC bus. When coupled systems are used, there is a possibility that 85% of the solar power would remain unutilized when solar power is higher in a standalone system. Decoupled control allows the system to pump water even if the BLDC motor runs at only a fraction of the speed. Moreover, in a standalone operation, the power harvested from the solar radiation is triple the input power [34].

The proposed scheme, apart from pumping water and injecting excess power to the grid, also allows the photovoltaic array to deliver a high current regardless of the solar radiation. Maximum power is extracted from the solar PV array and is proposed to be injected simultaneously into the grid and into the DC bus by means of a bidirectional coupled switched inductor voltage doubler. The number of power converters is reduced by $2/3$ when the proposed system is used for both grid-interfaced and standalone systems [35].

The efficiency of a PMSG-based water pumping system gets drastically reduced when connected directly to a solar PV array due to the intermittent associated with solar radiation, which is uncontrollable. In order to counter the drawback of this system and to achieve uninterrupted water discharge when solar radiation is unavailable, the system is proposed to be interfaced to the grid [36].

B. Other Alternatives to Grid-Connected Solar Pv Systems And Separate Control

There are alternative control strategies that offer different advantages and may be more suitable for specific applications or grid conditions.

- **Droop Control:** Droop control is a widely-used method, especially in microgrids and islanded systems, that adjusts the active and reactive power output based on frequency and voltage deviations. In droop control, a slight change in frequency corresponds to active power adjustment, while a change in voltage level affects reactive power.
- **Direct Power Control (DPC):** DPC controls the active and reactive power directly without using current control loops. Instead, it selects appropriate inverter voltage vectors to control power in real-time.
- **Field-Oriented Control (FOC):** Also known as vector control, FOC is a technique used primarily in motor control and PV inverters. It involves transforming the current into a d-q reference frame, where the d-axis is aligned with the stator flux (or a similar reference frame) and controls active power, while the q-axis controls reactive power.

- Model Predictive Control (MPC): MPC uses a model of the PV system to predict future behavior and selects control actions that minimize a cost function, often related to power output, stability, or power quality.
- Hysteresis Control: This technique operates by keeping the system variables (like current) within predefined hysteresis bands. The inverter switches are controlled to keep the current within these bands, indirectly controlling the active and reactive power.
- Resonant Control: Resonant controllers are tuned to respond to specific frequencies, usually the fundamental grid frequency, making them suitable for applications with strong grid frequency components. They work well in managing harmonics and specific frequency components of power.

V. INTEGRATION OF DECOUPLED CONTROL IN GRID-CONNECTED SOLAR PV SYSTEMS

Grid-connected solar PV systems became increasingly popular and are widely used. These systems are directly connected to the utility grid; therefore, two of the main functions required from the solar PV inverters are the maximum power point tracking and the grid current synchronization. In most of the conventional control strategies, a phase-locked loop (PLL) is used for the grid current synchronization, and the grid current, active and reactive power references are generated based on the PV inverter role, being it operated as the grid-connected current source (GSC) when there is a need to inject or consume the real power from the grid, or as a voltage source (VSC), to guarantee the grid-connected power factor and provide enough push-pull for the maximum power obtainment from the photovoltaic generator [37].

To achieve the objectives, a single-phase solar photovoltaic (PV) inverter is developed. The proposed control strategy gives double benefits for the users. It helps to maximize the power production as well as to compensate for the reactive power. This saves equipment, reduces energy losses, and improves system performance. The control strategy is used to provide a very small positive sequence reference current under normal operation mode to transfer maximum real power and to compensate for the reactive power required by the size of the inverter. When there is a need to control the three-phase load voltage, the inverter control changes to the traditional GSC mode [38]. The control strategy takes over the power exchange mode under the transition in every power cycle from the traditional GSC. The fast transition capability of the proposed control is highlighted with the simulation results under different operating conditions. The results verify the capability of the proposed control under different operating conditions and transitions [39].

A. Advantages of Decoupled Control In Grid-Connected Systems

Researchers have focused on enhancing the performance and reducing active losses in grid-connected inverter-based systems using static compensators. However, the solar PV source can allocate power flow in both buck and boost modes. The proposed Q–Z source converter with a unique Q–Z network aims to improve power flow and provide buck and boost capabilities for the DC voltage. The solar PV arrays, Q–Z source network, and grid are considered in various modes. The Q and Z transformer ratios are used to satisfy the Q–Z converter's operating modes as an inductor or capacitor. Consequently, the current-proportional voltage regulation strategy is applied to control the power flow in the Q–Z source inverter-based systems [18].

Grid-connected solar PV systems with Q–Z source converters and a decoupled power control strategy are designed to improve power flow and meet the standards set by grid codes. The power conditioning units (PCUs) are responsible for ensuring power quality and implementing maximum power point tracking (MPPT) and current-proportional voltage regulation. Various control algorithms are used to control active power, reactive power, and harmonic contents [40].

In this chapter, a decoupled power control strategy is proposed for grid-connected solar PV systems with Q–Z source converters. The Z source network is utilized to provide a better power flow in buck and boost modes. The advantages of the Q–Z source network are the two independent control loops for voltage proportional current regulation and

effectively utilize the power flow in voltage variations. The MATLAB/Simulink models with the proposed decoupled power control strategy are implemented for various scenarios relating to switching functions, efficiency, and grid reliability [41].

Grid-connected solar photovoltaic (PV) systems are gaining popularity in modern power systems. The power conditioning units (PCUs) play a crucial role in power quality assurance and satisfy the standards based on grid codes. The fast control of PCUs blending maximum power point tracking (MPPT) and current-proportional voltage regulation abilities is essential for the longevity of the inverter and high-power quality.

VI. CONTROL STRATEGIES FOR GRID-CONNECTED SOLAR PV SYSTEMS

Solar PV power generation rate, voltage, power, and current can be controlled in a more coordinated manner. The suggested control scheme is simulated. The outputs demonstrate the potential of the presented scheme under various conditions of variation in solar radiation, line voltage, grid frequency, and load power. The output of this simulation presents a reasonable tracking of the P-V characteristic of a PV panel. It is shown that the cancellation of the AC ripples in the interconnected system during the variation of environmental effects of solar radiation makes the coordinate control strategy more flexible and efficient under different loading conditions [42].

In a grid-connected solar PV system, the solar cell output is connected in parallel with the load, whereas the generated power is fed to the utility grid through the pulse width modulated (PWM) inverter. Because of the fluctuating solar irradiance and temperature, the solar PV system output will momentarily fluctuate, causing voltage and current waveform distortion. The decoupled control of the solar PV system is achieved using Proportional Resonant (PR) controller, including the integral control loop. The PR controller uses the positive and negative sequence of synchronous reference frame theory to linearize the solar PV system. These controllers allow the implementation of a high-performance, robust linear controller that completely removes AC ripple without requiring a bandwidth that's in the range of megahertz. These controllers provide an additional benefit to the grid side. Even more, they could directly inject the fundamental positive and negative sequence current without considering to impose a fixed phase current value [43].

A. Traditional Control Strategies

The most straight-forward regulation can be provided with this control which relates the output to the reference. The developed control takes both the reference and the measured values, which can fit the system to the utility grid or an external application. Both conventional integration and passivity-based controllers are widely used. The error signal is denoted as the voltage bode controller. To obtain good stability and dynamic response, an output filter with a proper quality factor Q is employed. Rapid response time is enabled by taking into account both the system and load properties. State feedback control, involving the scaled estimation error, yields a wide range of dynamic performance. Due to guidance for a proper Q , feasibility for different harmonic reduction strategies is provided. The state feedback control with the error minimizing to zero yields the desired station keeping accuracy. What local control designed for the fault is lacking [44].

This section first details traditional control strategies employed in a grid-connected PV system. Inside section Category, the General classification gives a fundamental instruction, providing current level information to the controller. Voltage-Concerned classification is capable of extracting complete fundamental phase. In the Frequency-Concerned classification, varying gains without the logarithmic state estimation cost are exploited. Signal-Decomposition classification is composed of the Frequency and Harmonic-Concerned classifications to utilize decoupled control strategies. Using the modulation index, high precision is ensured. The output current with reduced number of switching is shown to produce better harmonic and unbalanced current in UPS and IPSP. In the absence of LCL filter, the traditional parallel DC is simpler with the same function. The soft commutated switches, tolerating a wide range of modulation and L are employed. Centralized modulation with balanced DC-link capacitor voltages

can increase output power and complete the reactive power compensation. Inductive load increase reduces LSPR, and phase shift control leads to a widely used modulation method with reduced phase taken [45].

B. Decoupled Control Strategies

In this chapter, by integrating the synchronous dq reference frame and the tripartite timescale with the zero-frequency decoupling characteristic, a current-compensated-decoupled power-balance equivalent inverter is introduced to replace the traditional grid-tied inverters, thereby obtaining unified, stable, and flexible grid-connected performance. Then, the presented decoupled control is derived according to the described H-type inverter, as a complementation of Chapter 5. The purposes of this chapter are to 1) establish the equivalent background for a standalone inverter; 2) introduce the characteristic, operation principles, and key analysis methods of the novel inverter; and 3) develop an independent, unified, and rational decoupled control, as a complementation of the tightly coupled control in Chapter 5. It is noteworthy that the presented H-type inverter can address the intrinsic contradiction of the traditional grid-tied inverters and implement many grid-friendly functions with good economy [45].

Chapter 5 describes the operation and control methods of several types of grid-connected PV systems. However, all these methods are tightly coupled, and inadequate parameter design may lead to poor performance or even instability. A novel H-type inverter with a simpler structure and reduced number of switches is thus introduced in this chapter. The operation and control methods of the presented decoupled approach are detailed to establish a unified and rational control framework. All control methods and regulatory structures can be realized with decoupled, independent, and consistent control strategies, which are thus simplified and more flexible [45].

VII. CASE STUDIES AND APPLICATIONS

The proposed Three-Phase Neutral Point Clamped (3P-NPC) solar photovoltaic system based on the designed decoupled control method is validated through two distinct simulations. The simulation results illustrate that the hybrid decoupled control ensures stable and improved performance of the system when compared with the existing systems that use a single DC-DC converter along with PWM modulation and MPPT individual controller for better output power. The efficiency of the entire system is also enhanced by including the proposed battery energy storage system. The graphical results for individually controlling the renewable energy using the designed energy storage system in the proposed system are also discussed to state the effectiveness of the present research work. The only limitation of the current work is that the control method designed is checked on to the transformer less converter. The decoupled control to this type of PV has to be designed and the augmented controller behavior have to obtain [46].

The hybrid decoupled controller design has been tested extensively on a large-scale grid-connected 2x2 multilevel converter-based solar photovoltaic system. The individual components of the solar photovoltaic system are modeled in MATLAB/Simulink environment. The operation of the complete system is carried out in different operation modes, namely PWM modulation, MPPT with decoupled control, MPPT with individual controller, and grid-connected mode of operation. The validation of the entire simulation is carried out on the USB-connected DSPACE DS1103 controller. The graphical results and the efficiency of the proposed system are analyzed thoroughly for adapting the proposed components in large-scale solar photovoltaic power conversion systems. The complete simulation results for the selected case study will also be made available for the further comparative analysis of the proposed controllers [47].

A. Real-World Implementations of Decoupled Control

The feedforward controller utilized during start-up processes is often a parameter of the perms-mode vdc/vac. Inverter contractors offered ready-made designs of solar inverter grid-feeding systems. The solar inverter systems were the most integrated and compact available. The most typical agglomerations of the safety, renewable and smart grid functions were – isolated or grid-interactive could systems, PV and battery storage inverters and converters, multi-

parallel grid-inverters, multi-parallel grid-inverters with transformer less matrix converter input bridge and multi-feed DC-to-AC converters. The solar inverter included a range of discrete packaging components, digital micro controller unit evaluation kit, digital PWM generation board evaluation kit with the resolution of 0.1ns based on field programmable gate array, mold inspection and packing inspection with thorough examination and improvement of the long-term reliability, stability and performance. Market-standard industry tools and devices could be used for regression test and prototype grids. Small scale versions or scaled solution were popular in academic tests and laboratories [48].

The synchronous decoupled control for single-phase grid-connected inverter is probably the simplest control variant for the case recursion on the current component. Another recursive synchronous control was proposed that handled the difficult case when the reference harmonic component should be pole close to the current. The modified version of this recursive controller was proposed in and was used in the single-phase solar PV system. It was more than two times faster and more than two times cheaper in terms of computational resources than the brick wall filter-based algorithm. Related improvements obtained from the theoretical point of view were addressed respectively on the noise level and reference current renewal. Many grid interfacing systems used proportional integration controller. Community of the software developers published the software design patterns related to the contemporary and future proofed power electronics controller architecture in the open-source repositories. The open organizations sponsored the research works related to the hardware implementation of the solar inverter where motion of the machine learning was used for development of the actual control [49].

B. Quantitative Comparisons Of Control Strategies In Grid-Connected Pv Systems

Quantitative comparisons of control strategies in grid-connected PV systems, focusing on performance metrics like response time, accuracy, complexity, and harmonic distortion, provide valuable insights into their suitability for different applications. Here's a numerical comparison of key control strategies, based on typical ranges from recent studies

Response Time: Droop Control generally has a slower response time, making it suitable for distributed energy systems with gradual load changes. Direct Power Control and Sliding Mode Control provide very fast response times (1-10 MS), making them highly responsive for applications with rapid grid changes. Model Predictive Control has the fastest response time due to its predictive nature (1-5 MS), ideal for high-performance grids.

Total Harmonic Distortion (THD): Resonant Control and Model Predictive Control have the lowest THD (<2%), as they focus on harmonic suppression and precise power control, respectively. Hysteresis Control has relatively high THD due to its variable switching frequency, which makes it less ideal for applications requiring strict power quality.

Computational Complexity: Droop Control and Hysteresis Control have the lowest computational requirements, making them suitable for simpler or smaller PV systems. ANN, Fuzzy Logic, and MPC require significant computing power, as they involve real-time calculations and often need high-performance processors or digital signal processors (DSPs).

Grid Stability Contribution: MPC, ANN, FOC, and Resonant Control provide strong support for grid stability, as they manage reactive power and respond well to grid variations. Droop Control offers moderate stability support, as it passively adjusts output based on frequency and voltage but lacks precise power control.

VIII. FUTURE TRENDS AND DEVELOPMENTS

The system/prototype should be installed and verify its operation with the electrical distribution network. Prior to the prototype development, concept implementation needs to be developed and tested initially. The impacts of the solar PV system on the distribution grid need proper attention for robust and reliable grid operation. Sound protection

systems, grid ground fault detection can prevent hazardous grounding fault occurrence due to inverter leakage current. The earth grid should be effectively designed and properly maintained. The earthing network set-up to evaluate needs significant attention since it is the major contributor to the total cost deployment of the system. Economic development and its advantages for the economic-based PV system are crucial for its rapid growth and success. Also, areas of remote/off-grid areas are also expected to have good growth potential [50].

Several future trends and significant developments are expected in the area of grid-connected solar PV systems, innovation, research, and development. The advancement in power electronics, control methodologies, microcontrollers, microprocessors, development of a new power transformer, development of a new power system analysis, design and simulation software, transformers and structures, cooling systems, thermal management systems, battery systems, fuel cell developments, the use of single-stage inverters or multi-port transformer-based inverters, etc., are some of the important future directions and future developments to do significant research and development. A significant effort is needed in I-V characteristic improvement. Various electronic components and their life models result in failure installations need to explore and investigate more about it. The low-power PF compensation at the grid side on the power-injection network (low-power network which is below 2 MW), and harmonic reduction methods to be developed are a few more advancements [51].

IX. CONCLUSION

The laboratory prototype of the proposed power conditioning system has been developed to validate the effectiveness of the power conditioning system under different environmental conditions, for example, changes in PV array irradiation, sudden changes in power demand, etc. Simulated and experimental results demonstrate the effectiveness of the proposed power conditioning system under different operating conditions. With the successful achievement of the maintenance and control of the constant DC-link voltage even during the closed-loop faults and the enhanced ability of the power quality, the proposed power conditioning system can also be effectively employed for microgrids. This paper deals with a grid-connected solar photovoltaic (PV) power system with a decoupled boost half-bridge (BHB) converter for single-phase operation. The proposed decoupled BHB converter ensures that only the utilized power is supplied from the PV array, and the inverter is only operated within the peak power constraints on the PV array. The double-loop control strategy, along with PV array state estimation, provides better dynamic performance. The inherent perturbation negation property of the BHB converter ensures good power quality at the output. The decoupled control approach for the BHB converters in the dc-link voltage regulation is also employed during the DC-side fault.

CONFLICTS OF INTEREST

They reported that there was no conflict of interest between the authors and their respective institutions.

RESEARCH AND PUBLICATION ETHICS

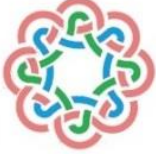
In the studies carried out within the scope of this article, the rules of research and publication ethics were followed.

REFERENCES

- [1] T. Sutikno, W. Arsadiando, A. Wangsupphaphol, "A review of recent advances on hybrid energy storage system for solar photovoltaics power generation," IEEE, 2022. ieeexplore.ieee.org
- [2] AS Aziz, MFN Tajuddin, MR Adzman, MF Mohammed, "Feasibility analysis of grid-connected and islanded operation of a solar PV microgrid system: A case study of Iraq," Energy, Elsevier, 2020. [\[HTML\]](#)
- [3] ZMS Elbarbary, MA Alranani, "Review of maximum power point tracking algorithms of PV system," in *Frontiers in Engineering and Built Environment*, 2021, emerald.com. [emerald.com](https://www.emerald.com/)
- [4] V. K. Goyal and A. Shukla, "Two-stage hybrid isolated DC–DC boost converter for high power and wide input voltage range applications," IEEE Transactions on Industrial Electronics, 2021. [\[HTML\]](#)
- [5] O. K. Albasri and E. Ercelebi, "Multilevel cascaded three-phase inverter with low-voltage ride-through flexible control capability for photovoltaic systems.," Proceedings of the Estonian Academy of Sciences, 2020. kirj.ee

- [6] S. P. Litrán, E. Durán, J. Semião, and R. S. Barroso, "Single-switch bipolar output DC-DC converter for photovoltaic application," *Electronics*, 2020. [mdpi.com](https://doi.org/10.3390/e11071107)
- [7] M. A. Khan, A. Haque, V. S. B. Kurukuru, et al., "Advanced control strategy with voltage sag classification for single-phase grid-connected photovoltaic system," *IEEE Journal of ...*, 2020. [\[HTML\]](#)
- [8] W. Jean and ACP. Brasil Junior, "Solar model for Rural Communities: Analysis of Impact of a Grid-Connected Photovoltaic System in the Brazilian semi-arid region," in *Energy, Water and Environment Systems*, 2022. [srce.hr](https://www.srce.hr)
- [9] V. Kumar, R. K. Behera, D. Joshi, and R. Bansal, "Power electronics, drives, and advanced applications," 2020. [\[HTML\]](#)
- [10] CMS Kumar, S Singh, MK Gupta, YM Nimdeo, "Solar energy: A promising renewable source for meeting energy demand in Indian agriculture applications," *Sustainable Energy Technologies and Assessments*, vol. 53, Elsevier, 2023. [\[HTML\]](#)
- [11] ISF Gomes, Y Perez, E Suomalainen, "Coupling small batteries and PV generation: A review," *Renewable and Sustainable Energy Reviews*, Elsevier, 2020. [sciencedirect.com](https://www.sciencedirect.com)
- [12] X. Sun, S. Jiang, H. Huang, H. Li, B. Jia, et al., "Solar energy catalysis," *Angewandte Chemie*, vol. 2022. Wiley Online Library. [wiley.com](https://www.wiley.com)
- [13] M. Zhang, M.S. Cao, J.C. Shu, W.Q. Cao, L. Li, et al., "Electromagnetic absorber converting radiation for multifunction," *Materials Science and Engineering*, Elsevier, 2021. [\[HTML\]](#)
- [14] R. Jovine, "How Light Makes Life: The Hidden Wonders and World-Saving Powers of Photosynthesis," 2022. [\[HTML\]](#)
- [15] D. Hao, L. Qi, A. M. Tairab, A. Ahmed, A. Azam, D. Luo, et al., "Solar energy harvesting technologies for PV self-powered applications: A comprehensive review," *Renewable Energy*, vol. 2022, Elsevier, 2022. [sciencedirect.com](https://www.sciencedirect.com)
- [16] T. Adefarati, R.C. Bansal, T. Shongwe, R. Naidoo, et al., "Optimal energy management, technical, economic, social, political and environmental benefit analysis of a grid-connected PV/WT/FC hybrid energy system," *Energy Conversion and Management*, vol. 2023, Elsevier, 2023. [\[HTML\]](#)
- [17] D. Dey and B. Subudhi, "Design, simulation and economic evaluation of 90 kW grid connected Photovoltaic system," *Energy Reports*, 2020. [sciencedirect.com](https://www.sciencedirect.com)
- [18] M. S. Aygen and M. İnci, "Zero-sequence current injection based power flow control strategy for grid inverter interfaced renewable energy systems," *Energy Sources, Part A: Recovery, Utilization, and Environmental Effects*, vol. 2022. Taylor & Francis, 2022. [\[HTML\]](#)
- [19] K Hasan, SB Yousuf, MSHK Tushar, "Effects of different environmental and operational factors on the PV performance: A comprehensive review," *Energy Science & Engineering*, vol. 2022, Wiley Online Library. [wiley.com](https://www.wiley.com)
- [20] Y. Lavi and J. Apt, "Using PV inverters for voltage support at night can lower grid costs," *Energy Reports*, 2022. [sciencedirect.com](https://www.sciencedirect.com)
- [21] M. Bhavani, K.V. Reddy, K. Mahesh, "Impact of variation of solar irradiance and temperature on the inverter output for grid connected photo voltaic (PV) system at different climate conditions," *Materials Today Proceedings*, vol. 2023, Elsevier. [\[HTML\]](#)
- [22] TEK Zidane, AS Aziz, Y Zahraoui, H Kotb, "Grid-connected Solar PV power plants optimization: A review," in *IEEE Transactions*, 2023. [ieee.org](https://www.ieee.org)
- [23] M. Uno and K. Honda, "Panel-to-substring differential power processing converter with embedded electrical diagnosis capability for photovoltaic panels under partial shading," *IEEE Transactions on Power Electronics*, 2021. [\[HTML\]](#)
- [24] I. Jamal, M.F. Elmorshedy, S.M. Dabour, E.M. Rashad, et al., "A comprehensive review of grid-connected PV systems based on impedance source inverter," in *IEEE*, 2022. [ieee.org](https://www.ieee.org)
- [25] R. Palanisamy, S. Usha, D. Selvabharathi, et al., "SVPWM Based Transformerless Z-Source Five Level Cascaded Inverter with Grid Connected PV System," in *Energy and ...*, vol. 2024, Springer, 2024. [\[HTML\]](#)
- [26] M. Morey, N. Gupta, M. M. Garg, and A. Kumar, "A comprehensive review of grid-connected solar photovoltaic system: Architecture, control, and ancillary services," *Renewable Energy Focus*, 2023. [\[HTML\]](#)
- [27] R. J. Mustafa, M. R. Gomaa, M. Al-Dhaifallah, and H. Rezk, "Environmental impacts on the performance of solar photovoltaic systems," *Sustainability*, 2020. [mdpi.com](https://www.mdpi.com)
- [28] C. Mokhtara, B. Negrou, N. Settou, A. Bouferrouk, et al., "Optimal design of grid-connected rooftop PV systems: An overview and a new approach with application to educational buildings in arid climates," *Renewable Energy Technologies and Assessments*, vol. 42, Elsevier, 2021. [\[HTML\]](#)
- [29] AAF Husain, MHA Phesal, MZA Ab Kadir, et al., "Techno-economic analysis of commercial size grid-connected rooftop solar pv systems in malaysia under the nem 3.0 scheme," *Applied Sciences*, vol. 2021. [mdpi.com](https://www.mdpi.com)

- [30] M.Z. Islam, M.S. Reza, M.M. Hossain, et al., "Accurate estimation of phase angle for three-phase systems in presence of unbalances and distortions," *IEEE Transactions on ...*, 2021. [\[HTML\]](#)
- [31] A. Lunardi, E. Conde, J. Assis, L. Meegahapola, "Repetitive predictive control for current control of grid-connected inverter under distorted voltage conditions," in *IEEE Transactions on Industrial Electronics*, 2022. [ieee.org](#)
- [32] M. Shafiullah, S. D. Ahmed, and F. A. Al-Sulaiman, "Grid integration challenges and solution strategies for solar PV systems: a review," *IEEE Access*, 2022. [ieee.org](#)
- [33] S. Alotaibi and A. Darwish, "Modular multilevel converters for large-scale grid-connected photovoltaic systems: A review," *Energies*, 2021. [mdpi.com](#)
- [34] AK Udayakumar, RRV Raghavan, MA Houran, "Three-port bi-directional DC–DC converter with solar PV system fed BLDC motor drive using FPGA," in *Energies*, 2023. [mdpi.com](#)
- [35] S. Rezazadeh, A. Moradzadeh, K. Pourhossein, et al., "Photovoltaic array reconfiguration under partial shading conditions for maximum power extraction: A state-of-the-art review and new solution method," *Energy Conversion and Management*, vol. 2022, Elsevier, 2022. [aau.dk](#)
- [36] SK Gautam, R Kumar, "Synchronisation of solar PV-wind-battery-based water pumping system using brushless DC motor drive," *International Journal of Power ...*, vol. 2023, inderscienceonline.com, 2023. [\[HTML\]](#)
- [37] B. Saleh, A.M. Yousef, F.K. Abo-Elyousr, et al., "Performance analysis of maximum power point tracking for two techniques with direct control of photovoltaic grid-connected systems," *Energy Sources, Part A: Recovery, Utilization, and Environmental Effects*, vol. 2022, Taylor & Francis, 2022. [\[HTML\]](#)
- [38] M.A. Khan, A. Haque, K.V.S. Bharath, et al., "Single phase transformerless photovoltaic inverter for grid connected systems-an overview," *International Journal of Power Electronics*, vol. 2021, inderscienceonline.com, 2021. [\[HTML\]](#)
- [39] TS Babu, KR Vasudevan, et al., "A comprehensive review of hybrid energy storage systems: Converter topologies, control strategies and future prospects," in *IEEE Transactions*, 2020. [ieee.org](#)
- [40] A. Lunardi, L. F. Normandia Lourenço, E. Munkhchuluun, et al., "Grid-connected power converters: An overview of control strategies for renewable energy," *Energies*, 2022. [mdpi.com](#)
- [41] N. Mohammed and M. Ciobotaru, "Adaptive power control strategy for smart droop-based grid-connected inverters," *IEEE Transactions on Smart Grid*, 2022. [\[HTML\]](#)
- [42] S. Mahdavi, H. Panamtash, et al., "Predictive coordinated and cooperative voltage control for systems with high penetration of PV," in **Proc. IEEE Trans. on Industry Applications**, 2021. [osti.gov](#)
- [43] M.H. Rezaei and M. Akhbari, "Power decoupling capability with PR controller for Micro-Inverter applications," *International Journal of Electrical Power & Energy Systems*, vol. 133, pp. 107090, 2022, Elsevier. [\[HTML\]](#)
- [44] W. Zheng, Y. Luo, Y. Q. Chen, and X. Wang, "Synthesis of fractional order robust controller based on Bode's ideas," *ISA transactions*, 2021. [\[HTML\]](#)
- [45] X. Wang, M. Chen, B. Li, G. Zhu, L. Chen, et al., "Control and modulation of a single-phase AC/DC converter with smooth bidirectional mode switching and symmetrical decoupling voltage compensation," in **Transactions on Power Electronics**, 2021. [\[HTML\]](#)
- [46] P. R. Martinez-Rodriguez, G. Vazquez-Guzman, et al., "Analysis and Improved Behavior of a Single-Phase Transformerless PV Inverter," *Machines*, vol. 2023, mdpi.com, 2023. [mdpi.com](#)
- [47] M. A. Ghasemi, S. F. Zarei, S. Peyghami, and F. Blaabjerg, "A theoretical concept of decoupled current control scheme for grid-connected inverter with LCL filter," *Applied Sciences*, 2021. [mdpi.com](#)
- [48] S. Mehta and V. Puri, "A review of different multi-level inverter topologies for grid integration of solar photovoltaic system," *Renewable energy focus*, 2022. [researchgate.net](#)
- [49] M. Bhunia and B. Subudhi, "A self-tuning adaptive control scheme for a grid-connected three-phase PV system," in *IEEE Journal of Emerging and Selected Topics in Power Electronics*, 2022. [\[HTML\]](#)
- [50] D. Sarathkumar, M. Srinivasan, A.A. Stonier, et al., "A technical review on classification of various faults in smart grid systems," *IOP Conference Series*, 2021. [iop.org](#)
- [51] DK Mishra, MJ Ghadi, L Li, MJ Hossain, J Zhang, "A review on solid-state transformer: A breakthrough technology for future smart distribution grids," *Journal of Electrical Power & Energy Systems*, vol. 125, 2021, Elsevier. [\[HTML\]](#)



RESEARCH ARTICLE

The Impact of Lempel-Ziv Distance Metric in Fuzzy K-Nearest Neighbor Algorithm: A Case Study on Classification of Growth Factors

¹ Berk Tolga Çiftçi, ¹ Ramazan Kabadayı, ^{1*} Çağın Kandemir Çavaş

¹Dokuz Eylül Üniversitesi, Fen Fakültesi, Bilgisayar Bilimleri Bölümü, İzmir, Türkiye

berktolga.ciftci@ogr.deu.edu.tr, Orcid.0000-0001-9779-270X

ramazan.kabadayi@ogr.deu.edu.tr, Orcid. 0000-0002-5114-291X

cagin.kandemir@deu.edu.tr, Orcid.0000-0003-2241-3546

Citation:

Çiftçi, B.T., Kabadayı, R., Çavaş, Ç.K. (2024). *The Impact of Lempel-Ziv Distance Metric in Fuzzy K-Nearest Neighbor Algorithm: A Case Study on Classification of Growth Factors*, Journal of Science, Technology and Engineering Research, 5(2):148-162. DOI: 10.53525/jster.1573661

HIGHLIGHTS

- The functions of growth factors in cellular processes and their analysis using bioinformatics methods
- The use of the Lempel-Ziv distance metric in the FKNN algorithm and the evaluation of classification success
- Presentation of the results of the classification method using the Lempel-Ziv distance and its advantages over the traditional Euclidean distance

Article Info

Received : 25.10.2024

Accepted : 25.11.2024

DOI:

10.53525/jster.1573661

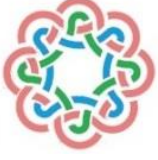
***Corresponding Author:**

Çağın Kandemir Çavaş
cagin.kandemir@deu.edu.tr
Phone: +90 232 3019512

ABSTRACT

Cellular events occur as a result of the activities of proteins. Different amino acid sequences create distinct protein structures, which in turn affect the activities in cellular events. Therefore, classifying protein sequences structurally or functionally is valuable for gaining insights into their roles in cellular events. Growth factors are proteins involved in processes such as cell proliferation, differentiation, repair, and maintenance. The bioinformatics study of growth factors can provide faster results at a lower cost. Neurotrophins are a family of growth factors that influence the growth, proliferation, differentiation, and functions of nerve cells. In this study, the fuzzy classification of NGF and BDNF, which share a common ancestor and have highly similar protein structures, as well as NT-3, is performed. The performance of the k-Nearest Neighbors (KNN) algorithm, widely used in bioinformatics, significantly depends on the distance measure used. For the Fuzzy KNN (FKNN) algorithm, the distance measurements are important for calculating the degree of fuzziness. In this study, Lempel-Ziv Complexity is proposed as a new distance measure to improve the classification success of the FKNN algorithm. When the Lempel-Ziv distance metric is used in the Fuzzy k-Nearest Neighbors Algorithm, and with data obtained from the Uniprot database, the classification performance reaches 83% when the number of neighbors (K) is 12. The highest classification performance obtained using Euclidean Distance was 75%. At the point where maximum accuracy was achieved, the algorithm's processing time using Euclidean Distance was 0.0054 ms, while it was 0.0038 ms when using the Lempel-Ziv distance. The results show that using Lempel-Ziv distance in the Fuzzy K-Nearest Neighbors Algorithm not only provides faster processing time compared to Euclidean distance but also significantly improves classification performance. In this context, it is believed that our approach could contribute significantly to bioinformatics research.

Keywords: Fuzzy K-nearest Neighbor Algorithm, Growth Factor, Lempel-Ziv Complexity, Neurotrophin, Protein Sequence



ARAŞTIRMA MAKALESİ

Bulanık K-En Yakın Komşuluk Algoritmasında Lempel-Ziv Mesafe Ölçütünün Etkisi: Büyüme Faktörlerinin Sınıflandırılması Örneği

Berk Tolga Çiftçi, Ramazan Kabadayı, ^{1*} Çağın Kandemir Çavaş

¹Dokuz Eylül Üniversitesi, Fen Fakültesi, Bilgisayar Bilimleri Bölümü, İzmir, Türkiye

berktolga.ciftci@ogr.deu.edu.tr, Orcid.0000-0001-9779-270X

ramazan.kabadayi@ogr.deu.edu.tr, Orcid. 0000-0002-5114-291X

cagin.kandemir@deu.edu.tr, Orcid.0000-0003-2241-3546

Alıntı / Citation :

Çiftçi, B.T., Kabadayı, R., Çavaş, Ç.K. (2024). *The Impact of Lempel-Ziv Distance Metric in Fuzzy K-Nearest Neighbor Algorithm: A Case Study on Classification of Growth Factors*, Journal of Science, Technology and Engineering Research, 5(2):148-162. DOI: 10.53525/jster.1573661

ÖNE ÇIKANLAR / HIGHLIGHTS

- Büyüme faktörlerinin hücresel süreçlerdeki işlevleri ve biyoenformatik yöntemlerle incelenmesi
- FKNN algoritmasının Lempel-Ziv mesafe metriğinin kullanılması ve sınıflandırma başarılarının değerlendirilmesi
- Lempel-Ziv uzaklığının kullanıldığı sınıflandırma yönteminin sonuçlarının ve geleneksel Öklid uzaklığına göre avantajlarının ortaya konulması.

Makale Bilgileri / Article Info

Geliş Tarihi : 25.10.2024

Kabul Tarihi : 25.11.2024

DOI: 10.53525/jster.1573661

*** Sorumlu Yazar:**

Çağın Kandemir Çavaş

cagin.kandemir@deu.edu.tr

Phone: +90 232 3019512

ÖZET / ABSTRACT

Hücreyel olaylar, proteinlerin aktiviteleri sonucunda gerçekleşir. Amino asitlerin farklı dizimleri farklı protein yapılarının oluşmasına neden olur. Yapılarına göre hücreyel olaylardaki aktiviteleri de değişiklik gösterir. Bu nedenle protein dizilerinin yapısal veya işlevsel olarak sınıflandırılması hücreyel olaylardaki rolleri hakkında bilgi edinmek için oldukça değerlidir. Büyüme faktörleri; hücreler üzerinde çoğalma, farklılaşma, onarım ve bakım gibi birçok süreçte yer alan proteinlerdir. Büyüme faktörlerinin biyoenformatik alanında incelenmesi, düşük maliyetle daha hızlı sonuçlara ulaşılmasını sağlayabilir. Nörotrofinler; sinir hücrelerinin büyümesi, çoğalması, farklılaşması ve fonksiyonları üzerinde etkili olan büyüme faktörü ailelerinden biridir. Çalışmamızda, ortak bir atadan gelen ve çok benzer yüksek dereceli protein yapısına sahip olan NGF ve BDNF'nin, ayrıca NT-3'ün bulanık sınıflandırılması yapılmaktadır. Biyoenformatik alanında yaygın olarak kullanılan k-En Yakın Komşuluk (KNN) algoritmasının performansı önemli ölçüde kullanılan mesafeye bağlıdır. Bulanık KNN (FKNN) algoritması için de mesafe ölçümleri, bulanıklık derecesini hesaplamak için önemlidir. Bu çalışmada, FKNN algoritmasının sınıflandırma başarısını artırmak amacıyla yeni bir mesafe ölçütü olarak Lempel-Ziv Karmaşıklığı önerilmiştir. Bulanık K-En Yakın Komşuluk Algoritması'nda Lempel-Ziv mesafe metriği kullanıldığında, Uniprot veri tabanından alınan verilerle birlikte FKNN algoritmasında K komşu sayısının 12 olması durumunda, sınıflandırma performansı %83 olarak elde edilmiştir. Öklid Uzaklığı kullanıldığında elde edilen en yüksek sınıflandırma performansı ise %75'tir. Maksimum doğruluk oranını elde ettiğimiz noktada Öklid uzaklığını kullandığımızda algoritmamızın çalışma süresi 0.0054 ms iken Lempel-Ziv uzaklığı kullandığımızda 0.0038 ms'dir. Elde edilen sonuçlara göre, Bulanık K-En Yakın Komşuluk Algoritması'nda Lempel-Ziv mesafesinin kullanılması, Öklid mesafesine kıyasla daha hızlı bir işlem süresi sağlamakla kalmamış, aynı zamanda sınıflandırma performansını da önemli ölçüde iyileştirmiştir. Bu bağlamda, önerdiğimiz yaklaşımın biyoenformatik çalışmalarına önemli katkılar sunabileceği düşünülmektedir.

Anahtar Kelimeler: Bulanık k-en yakın komşu algoritması, büyüme faktörü, Lempel-Ziv karmaşıklığı, nörotrofinler, protein sekansı.

I. GİRİŞ [INTRODUCTION]

Organizmaların incelenmesi üzerine yapılan araştırma ve projeler sonucunda zengin biyolojik veriler elde edildi ve artan bir şekilde elde edilmeye devam ediliyor. Deneysel yöntemler, oldukça fazla yoğun iş gücü, uzun zaman ve maliyet gerektirdiği için elde edilen yeni verilerin incelenmesi, yorumlanması maliyetli ve zaman alıcıdır. Biyoenformatik, deneysel yöntemlere göre daha az zaman ve maliyetle verileri incelemeye ve sonuçlar elde etmeye olanak sağlar. Biyoenformatik, bilgisayar bilimi yöntemleriyle biyolojik verileri depolamak, analiz etmek, modellemek için yöntemler geliştiren disiplinler arası bir alandır. Biyoenformatik; veri madenciliği teknikleri, görselleştirme, makine öğrenimi teknikleri gibi yöntemleri kullanarak verileri verimli bir şekilde analiz etmeyi amaçlar. Bu alanda verilerin sınıflandırılması da önemli bir konu olarak yer alır.

Hücre içerisinde gerçekleşen çoğunlukla birçok olay, proteinlerin aktiviteleri sonucu gerçekleşir. Ayrıca vücuttaki organ ve dokuların yapı ve işlevlerinde etkilidirler. Proteinlerin dört farklı yapısı bulunmaktadır. Bunlardan birincil yapısı, amino asitlerin doğrusal dizisinden oluşur [1]. Proteinler, birçok bileşenden oluşsa da farklılaşmasını sağlayan yan zincir olarak adlandırılan amino asitlerdir. Amino asitlerin bir araya gelmesiyle beraber aynı zamanda farklı bağlarla bir araya gelmeleri çeşitli üç boyutlu yapıları katlanmalarına neden olur. Katlanan yapılar da proteinin doğrusal amino asit dizisine bağlıdır ve bu yapılar da proteinin işlevini belirler [2]. Dolayısıyla yapısal veya işlevsel olarak yapılacak sınıflandırma o proteinin hangi hücreyel olaylarda nasıl görev aldığı anlamak açısından büyük öneme sahiptir. Sınıflandırmanın diğer bir önemli yanı da homolojiyi bulmaktır. Homoloji, dizilerin ortak bir atadan geldiklerini dolayısıyla ortak işlevsel yönlerinin olduğunu gösterir.

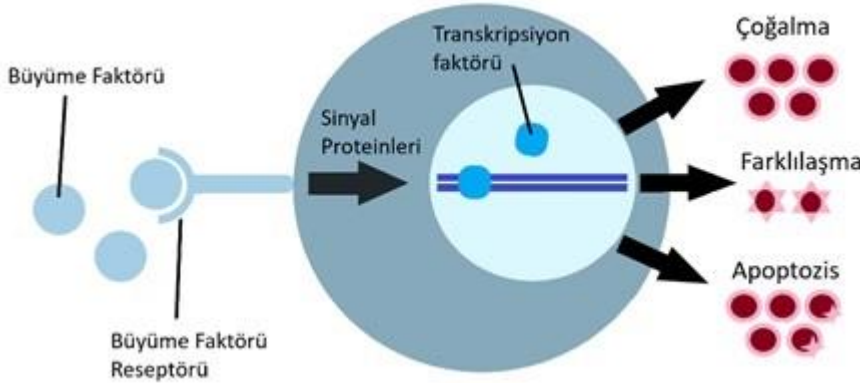
Biyoenformatik çalışmalarında k-en yakın komşu algoritması (KNN) yaygın olarak kullanılmaktadır. KNN, etiketli olmayan verileri, mesafe ölçümü kullanarak en yakın k adet etiketli verilerin sınıflarına göre sınıflandıran makine öğrenmesi algoritmalarından biridir. K adet en yakın komşudan çoğunluk hangi sınıf ise yeni değer o sınıfa atanır. Ancak KNN algoritması, her komşuya aynı önemi verir [3]. Klasik KNN algoritmasında bir veri, bir sınıfa atandığında verilerin arasındaki uzaklık durumuna göre bu atama gerçekleşir. Bu durumda o sınıfa üyeliğin gücünün hiçbir etkisi yoktur. Etkili olan yalnızca mesafedir. Bu noktada KNN algoritmasına bulanıklığın eklenmesi gerekmektedir. Bulanık KNN algoritması, en başta sınıfı bilinmeyen veri ile diğer verileri arasındaki mesafeyi hesaplar ve en yakın k adet komşuyu seçer ancak atama işlemi mesafeye göre değil, sınıfa ait üyelik derecesine göre yapılır. Algoritma içerisinde elde edilen üyelik değerleri, sonuçtaki sınıflandırmaya eşlik edecek bir güvence düzeyi sağlar. Bu sayede algoritma içerisinde keyfi atamalar yapılmaz [4].

KNN algoritması yukarıda da bahsedilen verilere eşit önem verme durumu nedeniyle bazen istenilen sonuçlara ulaşmada zorluklara neden olmaktadır. Örneğin, etiketli tüm verilere eşit önem verilmesi, mesafe temelli bir sınıflandırma yapılmasına neden olur. Protein dizisi o proteine özgüdür ve proteinin yapısını belirler. Mesafeye göre yapılan bir sınıflandırma, protein dizisinin yapısını göz ardı eder. Bulanık yöntem, protein dizisinin yapısı nedeniyle sahip olduğu sınıfın da işleme dâhil edilmesini sağlayarak sınıflandırmanın mesafe ile birlikte proteinin yapısının da göz önünde bulundurularak yapılmasını sağlar. KNN algoritmasında bulanık yaklaşımın kullanıldığı çalışmalar incelendiğinde; proteinin yapısal sınıf tahmini [5], protein çözücü erişebilirliğinin tahmini [6], hücre altı konumlarının tahmin edilmesi [7], proteinlerin ikincil yapısının tahmin edilmesi [8], DNA mikro dizi sınıflandırması [9], gen fonksiyon sınıflandırılması [10], gibi konularda bu yaklaşımın kullanıldığı görülmektedir. Farklı çalışmalarda, KNN'nin biyolojik ve tıbbi verilerin sınıflandırılmasında yaygın olarak kullanılmasına rağmen, henüz uygulanmamış başka araştırma alanlarının olduğunu ve bu alanlarda bulanık KNN ile yapılan deneysel sonuçlarda yüksek tahmin doğrulukları elde edildiği de görülmektedir [11]. İncelenen birçok çalışmada bulanık k-en yakın komşu algoritmasının çoğunlukla proteinlerde tahmin amacıyla kullanıldığı görülmektedir. Kendi çalışmamızda bulanık KNN algoritması, protein dizilerinin sınıflandırılması amacıyla kullanılmaktadır.

KNN, eğitim verilerine olan mesafenin hesaplanmasına dayanan bir sınıflandırma yöntemidir. Dolayısıyla KNN algoritmasının performansı önemli ölçüde kullanılan mesafeye bağlıdır [12]. Öklid uzaklığı KNN'de kullanılan en yaygın uzaklık metriğidir. Ayrıca farklı çalışmalarda, KNN'de, Manhattan, Minkowski, Kosinüs, Hamming, Jaccard,

Mahalanobis, City Block, Chebyshev uzaklık modellerinin [13]; bulanık KNN’de, Manhattan, Kosinüs, Hamming, City Block uzaklık modellerinin [14] kullanıldığı görülmektedir. Mesafe ölçümleri, bulanıklık derecesini hesaplamak için önemlidir [15]. Lempel-Ziv, kayıpsız bir veri sıkıştırma algoritmasıdır. Ek olarak Lempel-Ziv karmaşıklığı bir dizideki farklı yapıların sayısını vermektedir. Lempel-Ziv, DNA dizilerinin karmaşıklığını incelemek için kullanılmıştır [16]. Çalışmamızda, bulanık KNN algoritmasında test verisi ile eğitim verileri arasındaki mesafeyi ölçmek ve bilgi kaybını önlemek için protein sekanslarının Lempel-Ziv karmaşıklık değerlerinin bir tür mesafe ölçümü olarak kullanılması önerilmektedir.

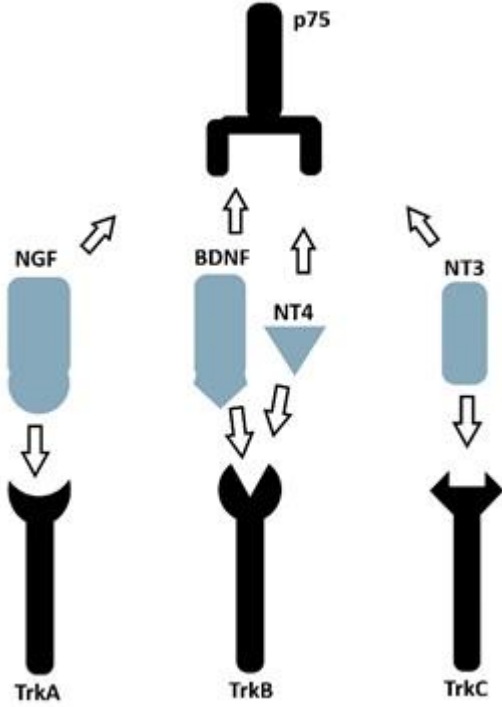
Şekil 1’de gösterildiği gibi, büyüme faktörleri, hücreler üzerinde çoğalma, farklılaşma, onarım ve bakım gibi birçok süreçte yer alan, hücre yüzeyindeki reseptörlere bağlanan proteinlerdir. Büyüme faktörleri, yapısal ve evrimsel olarak kendi içinde ilişkili olan protein ailelerinden oluşur. Her bir büyüme faktörü ailesi, farklı fonksiyonel özelliklere sahiptir ve farklı hücresel faktörleri yalnızca süreçlerde rol alırlar. Büyüme faktörleri, yalnızca onarım gibi süreçlerde değil ayrıca programlı hücre ölümü gibi süreçlerde de yer alabilir. Aktiviteleri, hücre tipine ve organizmanın gelişim aşamasına göre değişir [17]. Büyüme faktörlerinin in vivo çalışmaları kısa yarı ömre, zayıf bir dayanıklılığa yol açar [18]. Etkili sonuç alabilmek için yüksek dozlar gereklidir ve bu da yüksek maliyete neden olmaktadır [19]. Büyüme faktörlerinin biyoformatik alanında incelenmesi düşük maliyetle, daha hızlı sonuçlara ulaşılmasını sağlayabilir.



Şekil. 1. Büyüme faktörü (Growth factor)

Nörotrofinler (NGF), sinir hücrelerinin büyümesi, çoğalması, farklılaşması, fonksiyonları üzerinden etkisi olan ve sinaptik plastisitenin sağlanmasında etkili olan büyüme faktörü ailelerinden biridir. NGF’ler, biyolojik ve yapısal olarak birbirlerine benzemektedirler [20]. İlk olarak tükürük bezleri üzerinde yapılan deneyde molekül saflaştırılması sonucu NGF adı verilen bir protein keşfedilmiştir [21]. Daha sonraki deneyler NGF’nin, nöronların hayatta kalması ve farklılaşmasını destekleyen bir protein olduğunu göstermiştir [22]. NGF, sinir hücrelerinin ulaştığında hayatta kaldığı, ulaşmadığında öldüğü sınırlı miktarda üretilen bir proteindir [23]. NGF, sempatik ve duyuşal nöronların hayatta kalması ve bakımı için önemlidir; beyinde türetilmiş sinir hücresi büyüme faktörü (BDNF), merkezi ve çevresel sinir sistemindeki nöronların gelişimi için önemlidir. Şekil 2’de gösterildiği üzere, NGF’ler, tirozin kirazlar (Trk) reseptörlerine ve ayrıca p75 reseptörüne de bağlanabilmektedirler. Örneğin, BDNF, düşük afinitede p75 reseptörüne bağlanarak hücre ölümüne neden olurken yüksek afinitede TrkB reseptörüne bağlanarak hücrenin yaşamasını sağlar, Uzun Süreli Güçlendirme’ye (Long Term Potentiation) neden olur. NGF’ler farklı reseptör bağlantılarında farklı işlevlere sahiptirler. Bu nedenle yapılarının, bağlantılarının incelenmesi önemlidir. Literatürdeki çalışmalar NGF ve BDNF’nin çok benzer bir yüksek dereceli protein yapısına sahip olduklarını göstermektedir [24]. “Her iki protein arasında maksimum hizalama için amino asit dizilerinde yalnızca birkaç boşluk eklenmesi gerekir” [25]. “Amino asit düzeyinde NGF ve BDNF’nin olgun formları arasında yaklaşık %50 amino asit özdeşliği mevcuttur” [24]. Çalışmalar her ne kadar bu proteinlere dair bilgiler sunsa da hücresel ve moleküler işlevlerinin hala iyi derecede anlaşılmadığını da göstermektedir [24] [26]. Ayrıca çalışmalar, bu iki nörotrofik faktörün farklı görevlerini ortaya koymasıyla beraber paralel ve karşılıklı rollere sahip olduklarını da göstermektedir [24] [27]. NGF ve BDNF ile ilgili çalışmaların moleküler biyoloji teknikleri kapsamında gerçekleştirildiği görülmektedir [24]. Biyoformatik alanı temelinde literatürde NGF ve BDNF’nin sınıflandırılmasıyla ilgili herhangi bir çalışma bulunmamaktadır. Çalışmada, Lempel-Ziv karmaşıklığının

bulanık kNN algoritmasında uzaklık metriği olarak kullanılarak, ortak bir atadan gelen ve yapısal olarak birbirine benzeyen NGF ve BDNF'nin bulanık sınıflandırılması yapılmaktadır. Böylelikle bu çalışma, makine öğrenmesi tekniklerinin nörotrofinlerin sınıflandırılmasında ilk kez uygulanması açısından bir yenilik sunmaktadır.

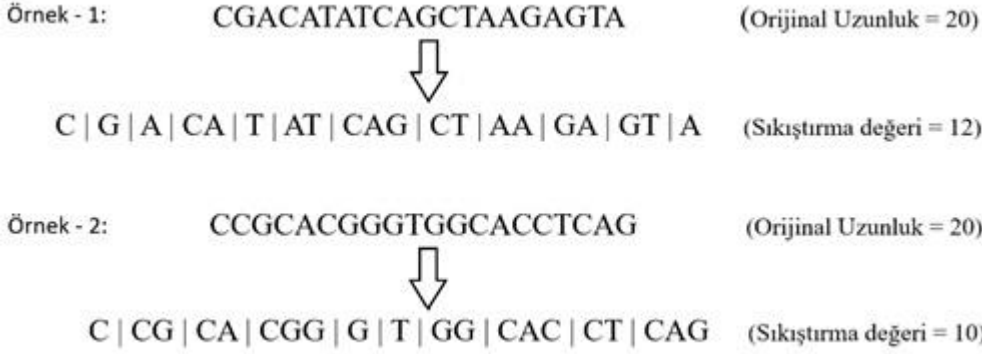


Şekil 2. Nörotrofinler (NGF)

II. MALZEME VE YÖNTEMLER [MATERIALS AND METHODS]

A. Lempel-Ziv karmaşıklığı (Lempel-ziv complexity)

Veri sıkıştırma, kayıplı ve kayıpsız olarak iki türdür. Kayıpsız sıkıştırma, istatistiksel fazlalığı ortadan kaldırarak bitleri azaltır. Kayıpsız sıkıştırma, sıkıştırılmış verilerin yeniden yapılandırılarak orijinal verilerin elde edilmesini sağlayan bir tekniktir. Bu işlem sırasında hiçbir veri kaybolmaz. Kayıplı sıkıştırma, daha az önemli veya gereksiz bilgileri ortadan kaldırarak bitleri azaltır. Farklı sıkıştırma yöntemleri bulunmaktadır. Tek geçiş sıkıştırma veya uyarlamalı sıkıştırma, verileri yalnızca tek geçişte sıkıştırır. İki geçişli sıkıştırma veya yarı uyarlanabilir sıkıştırma, verileri bir geçişte analiz eder ve daha sonra başka bir geçişte sıkıştırır [28]. İki geçişli sıkıştırma algoritmalarından biri olan Huffman Kodlaması, veri içerisindeki en çok kullanılan karakterler üzerine odaklanan bir algoritmadır. Ne kadar çok tekrar eden karakter varsa o kadar iyi sıkıştırma gerçekleşir. Ancak Huffman Kodlaması'nın başarısı, kaynak dizinin dağılımına bağlıdır [29]. Her zaman kaynak dizinin dağılımı sık tekrar eden karakterlerden oluşmayabilir. Bu durumda, veri içerisindeki en çok tekrar eden karakterlerden ziyade tekrar eden yapılarla odaklanan sözlük tabanlı ve kayıpsız veri sıkıştırma algoritmalarından biri olan Lempel-Ziv (LZ78) kullanılabilir. Huffman gibi teknikler, bir kerede tek bir sembolü kodlarken sözlük tabanlı sıkıştırıcı olan Lempel-Ziv, bir verideki belirli bir sembol grubunu kodlar [30]. Bu teknik, Huffman Kodlaması gibi statik tekniklerin aksine daha verimlidir [31].



Şekil 3. Lempel-Ziv Örnek Gösterimi

Lempel-Ziv algoritması, tek geçişte verileri sıkıştırır ve sıkıştırılacak veri hakkında önceden herhangi bir bilgiye ihtiyaç duymaz [32]. Temel olarak, bir dizi soldan sağa doğru incelendiğinde karşılaşılan farklı alt dizilerin sayısı olarak tanımlanabilir. Lempel-Ziv algoritması şu şekilde işler: İlgili verinin içerisindeki farklı karakterlerin olduğu bir sözlük mevcuttur. Algoritma veriyi karakter karakter okur ve sözlükte olup olmadığını kontrol eder. Eğer sözlükte yoksa sözlüğe ekler. Eğer sözlükte varsa, sözlükte olmayan karakterle karşılaşılan kadar karakter karakter okumaya devam eder ve bu elde edilenleri bir desen yapıları olarak gruplandırmaya başlar. Bu sayede farklı yapı veya desenler aranır. Son olarak Lempel-Ziv sıkıştırma değeri, bulunan farklı yapıların veya desenlerin sayısına göre belirlenir. Lempel-Ziv, bir veri sıkıştırma algoritması olduğu kadar aynı zamanda veride bulunan kapıların ne kadar çeşitli olduğunu ölçmesi bakımından bir karmaşıklık ölçüsüdür.

Algoritma 1 – Lempel-Ziv

P = ilk girdi karakteri

WHILE okunacak karakter olduğu sürece

C = bir sonraki girdi karakter

IF P+C sözlükte varsa

P = P + C

ELSE

P'nin indeksini yazdır

P + C'yi sözlüğe ekle

P = C

END WHILE

P'nin indeksini yazdır

Sınıflandırma için kullanılan algoritmalar, sayısal girdiler almak zorundadır. Elde edilen DNA, protein veya enzim gibi veriler sayısal veriler olmadığı için bu verilerin algoritmalarda kullanılması için sayısal dönüştürülmesi gerekir. Kimi zaman bu dönüştürme işlemleri verilerde kayıplara neden olabilmektedir. Kayıpsız veri sıkıştırma algoritmaları, biyolojik çalışmalardan elde edilen sekansların algoritmalarda verimli bir şekilde kullanılmasına olanak sağlar. Bu açıdan Lempel-Ziv algoritması, sayısal olmayan verileri kayıpsız şekilde sıkıştırarak sayısal bir şekilde algoritmada kullanılmasını sağlar. Ayrıca, özellikle çalışmamızdaki bulanık sınıflandırma işleminde protein dizisinin yapısı nedeniyle sahip olduğu sınıfın da işleme dahil edilmesini istemediğimiz için Lempel-Ziv sıkıştırma değeri veya Lempel-Ziv karmaşıklığı, protein verilerinin yapısını da yansıtmış olacaktır.

B. Lempel-Ziv karmaşıklığına dayalı mesafe ölçümü (Lempel-Ziv complexity based distance measure)

S = ACGAGCTATT ve R = TCCTCTTT şeklinde iki dizi verildiğinde her iki dizinin LZ karmaşıklığı $c(S) = 7$ ve $c(R) = 5$ olarak bulunur.

$c(S)$: A | C | G | AG | CT | AT | T

$c(R)$: T | C | CT | CTT | T

S ve R dizileri iki farklı sırayla birleştirilir:

S.R = ACGAGCTATTTTCCTCTTT
R.S = TCCTCTTTACGAGCTATT

Daha sonra birleştirme sonucu elde edilen iki dizinin Lempel-Ziv karmaşıklıkları $c(S.R) = 11$ ve $c(R.S) = 10$ olarak bulunur.

$c(S.R) = A | C | G | AG | CT | AT | T | TC | CTC | TT | T$
 $c(R.S) = T | C | CT | CTT | TA | CG | A | G | CTA | TT$

Lempel-Ziv karmaşıklıklarının farkına dayalı olarak iki dizi arasındaki benzerlik derecesini hesaplamak için aşağıdaki formül (1) kullanılır.

$$d(S, R) = \frac{\max[c(S.R) - c(S), c(R.S) - c(R)]}{\max[c(S), c(R)]} \quad (1)$$

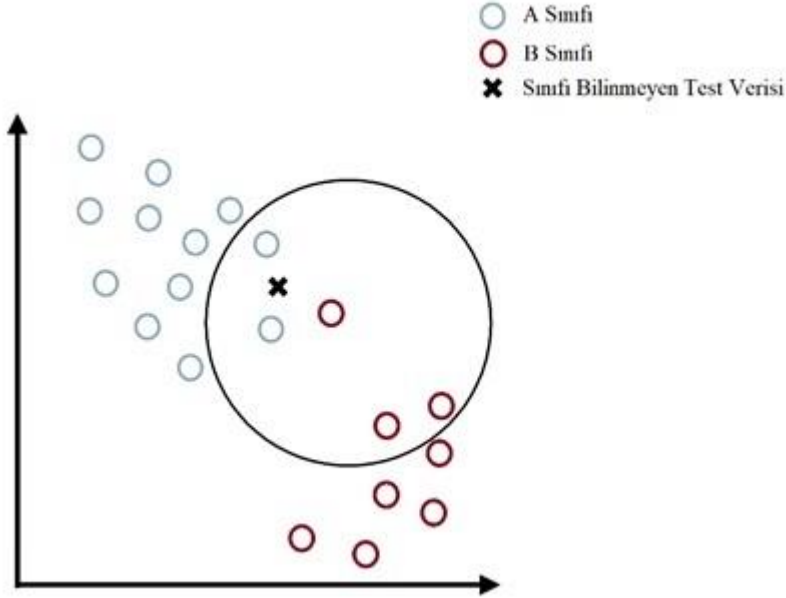
Bu formül (1), dizi uzunluğunun mesafe ölçümlerinin hesaplanması üzerindeki etkisini ortadan kaldırabilen normalleştirilmiş bir mesafe ölçümüdür [33].

Formüle dayanarak S ve R dizilerinin arasındaki Lempel-Ziv mesafesi şu şekilde hesaplanır:

$$d(S, R) = \frac{\max[11 - 7, 10 - 5]}{\max[7, 5]} = \frac{5}{7} = 0.71428 \quad (2)$$

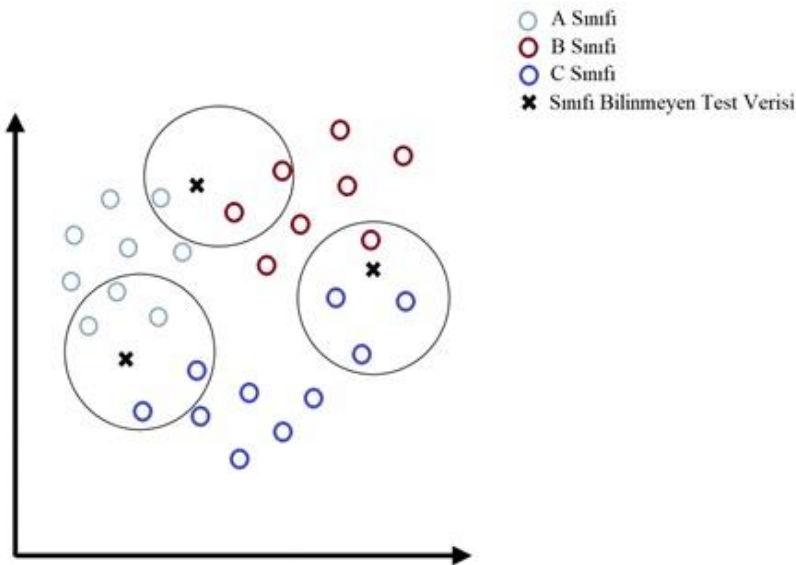
C. Bulanık k-en yakın komşu algoritması (Fuzzy k-nearest neighbor algorithm)

Makine öğrenimi teknikleri denetimli öğrenme ve denetimsiz öğrenme şeklinde iki alt kategoriye ayrılır. Denetimsiz öğrenmede tüm veriler etiketli değildir ve algoritmalar, veriler hakkında daha çok bilgi sahibi olmak için verilerdeki temel yapıyı modeller. Denetimli öğrenmede, etiketli veri kümesi kullanılarak algoritmalar, girdi verilerinden çıktıyı tahmin etmeyi öğrenir. K-en yakın komşu algoritması (KNN), etiketli olmayan veriyi, mesafe ölçümleri kullanarak kendisine en yakın k adet etiketli verilerin sınıflarına göre sınıflandıran denetimli makine öğrenmesi algoritmalarından biridir. K, en yakın komşu sayısını belirleyen önemli bir parametredir. Sabit bir değeri yoktur ve en etkili sonuç için algoritma farklı k değerleri için çalıştırılmalıdır. KNN'de, k adet en yakın komşudan çoğunluk hangi sınıf ise yeni değer o sınıfa atanır. Bu duruma çoğunluk oylaması veya oylama KNN kuralı [34] adı verilir. Komşu veriler, mesafeye göre belirlenir ve genellikle Öklid mesafesi kullanılır. Bayes sınıflandırıcı, sinir ağları gibi birçok sınıflandırma yöntemi, eğitim ve test veri kümelerinin aynı dağılıma sahip olduğu durumlarda çok iyi performans gösterirler. Ancak benzer ama farklı dağılımlarda performansları iyi değildir. KNN, verilerin dağılımlarının aynı olmasını gerektirmeyen bir yöntemdir [35]. Klasik KNN, seçilen tüm komşulara aynı önemi verir. Bu durum, algoritmanın en yakın k komşunun sınıflarından çoğunluk oylamasıyla sınıflandırmaya karar verirken her komşuya oy için aynı ağırlığı verdiği anlamına gelir. Sonuçta bu özellik, KNN'nin k değerine oldukça fazla duyarlı olduğunu gösterir [10].



Şekil 4. Bulanık k-en yakın komşu algoritması: belirsizlik, örnek 1 (Fuzzy k-nearest neighbor algorithm: uncertainty, example 1)

Klasik KNN’de, bir veri bir sınıfa atandığında, o sınıfa üyeliğin gücünün hiçbir etkisi yoktur. Sınıf üyelikleri olmaması nedeniyle belirsizliklerle baş edemez. KNN’nin performansını artırmak için bulanık mantığa [36] dayalı bulanık k-en yakın komşu algoritması (FKNN) geliştirilmiştir. FKNN, sınıf üyeliklerini dâhil eder ve rastgele atama yapılmamasını sağlayarak sınıflandırmada bir güvence düzeyi sağlar [4]. Algoritmanın temelinde, veriyi belirli bir sınıfa atamak yerine veriye sınıf üyeliği atamak vardır. Şekil 4, k değeri 5 olması karşılığında bir test verisinin en yakın 5 komşusu alındığını ve bu 5 komşudan 3 tanesi B sınıfına ait olduğu için test verisinin de B sınıfına ait olduğunu gösterir. Şekil 4’te test verisi mesafe olarak A sınıfındaki verilere daha yakın olsa da çoğunluk oylaması nedeniyle B sınıfına atanır. Bu durum da bir belirsizlik oluşturur [10]. Şekil 5, üç test örneğinin ve komşularının belirsiz alan oluşturduğu bir örnektir. Klasik KNN, belirsizlikle baş edemeyeceği için FKNN’nin kullanılması gerekmektedir. Klasik KNN’de olduğu gibi FKNN’de de k değeri önemlidir. K değerinin sabit bir değer olması, belirsizlikler içeren eğitim örneklerinde FKNN’nin performansını olumsuz bir şekilde etkiler [35].



Şekil 5. Bulanık k-en yakın komşu algoritması: belirsizlik, örnek 2 (Fuzzy k-nearest neighbor algorithm: uncertainty, example 2)

Bulanık k-en yakın komşu algoritmasında belirsizlikle baş edebilmek için her test verisi, en yakın eğitim verileri kullanılarak yeniden temsil edilir. Örneğin şekil 5'teki test noktalarından biri k değeri 3 olduğunda, diğeri k değeri 4 olduğunda ve bir diğeri k değeri 5 olduğundaki komşulukları ile yeniden temsil edilirler. Daha sonra algoritma içerisinde bu komşulukların, sınıflara ait üyelik dereceleri hesaplanır.

Algoritma 2 – Bulanık k en yakın komşu algoritması

Algoritma öncesinde; tüm sekansların Lempel-Ziv karmaşıklıkları hesaplanır. Bu karmaşıklık değerleri, formül (1)'de kullanılarak Lempel-Ziv uzaklık değerleri hesaplanır. Lempel-Ziv uzaklıklarından simetrik matris oluşturulur ve algoritma bu matris üzerinden işlemleri gerçekleştirir.

Adım 1: Her bir test verisi ile diğer tüm eğitim verileri arasındaki k adet en yakın komşuyu klasik KNN kullanarak bul.

Seçilen k adet komşunun kaç tanesinin hangi sınıfa ait olduğunu bul.

Sınıf adedi frekans değerlerini k değerine böl.

Elde edilen değeri k değerine tekrar böl. Son değer $\left(\frac{V_i}{kInit}\right)$ 'tir.

Adım 2: Adım 1'de elde edilen $\left(\frac{V_i}{kInit}\right)$ değerini formül (3)'te kullanarak ilgili sınıfın kendi ve diğer sınıflara ait üyelik derecelerini hesapla.

Adım 3: Elde edilen k adet komşuların birbirleri arasındaki Lempel-Ziv uzaklıklarını matriste ara.

Adım 4: Adım 2'de elde edilen üyelik dereceleri ve Adım 3'te elde edilen Lempel-Ziv uzaklıklarını formül (4) içerisinde kullanarak test verisinin sınıflara ait üyelik derecelerini hesapla.

Adım 5: Hangi sınıf üyeliği daha yüksekse test verisini o sınıfa ata.

$$u_{ji} = \begin{cases} 0.51 + \left(\frac{V_i}{kInit}\right) * 0.49 & \text{eğer } i = j \\ \left(\frac{V_i}{kInit}\right) * 0.49 & \text{aksi halde} \end{cases} \quad (3)$$

i , en yakın komşunun gerçek sınıflarıdır. j , eğitim veri setinden alınan test verilerinin gerçek sınıf değerleridir. V_i , ilgili i sınıfının en yakın k komşu içerisindeki sayısıdır. $kInit$, toplam komşu değeri olan k 'dır. $\left(\frac{V_i}{kInit}\right)$, k adet komşudaki sınıf frekans bilgisinin k değerine oranının tekrar k değerine oranı ile elde edilir. Her sınıfa üyelik bu formüle göre atanır.

$$\mu^j(x) = \frac{\sum_{i=1}^k u_{ji} \left(\frac{1}{\|x-y_i\|^{2/(m-1)}}\right)}{\sum_{i=1}^k \left(\frac{1}{\|x-y_i\|^{2/(m-1)}}\right)} \quad (4)$$

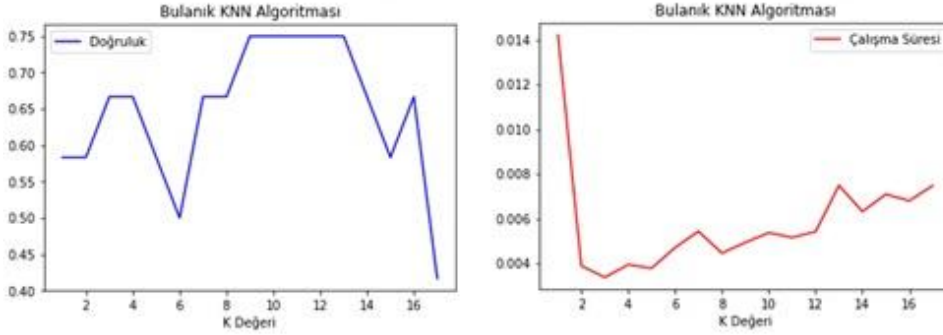
$\|x - y_i\|$, ilgili test verisinin j . komşudaki Lempel-Ziv uzaklık değeridir. m , ağırlıklandırma parametresidir. Bu parametre, bulanık üyelik değerinin hesaplanmasında her bir en yakın komşunun ağırlığını belirler. m , 2 olarak seçildiğinde her komşunun etkisi, uzaklığın tersi ile ağırlıklandırılır. Ters uzaklık, bir verinin incelenen veriden yakınsa daha fazla, uzaksa daha az üyeliğini ağırlıklandırmaya yarar. m , bire yaklaştıkça, yakın komşular uzaktakilerden çok daha fazla ağırlıklandırılır; m arttıkça, komşular daha eşit ağırlıkta olur ve göreceli mesafeleri daha az etkiye sahip olur [4].

III. SONUÇ VE DEĞERLENDİRME [CONCLUSION]

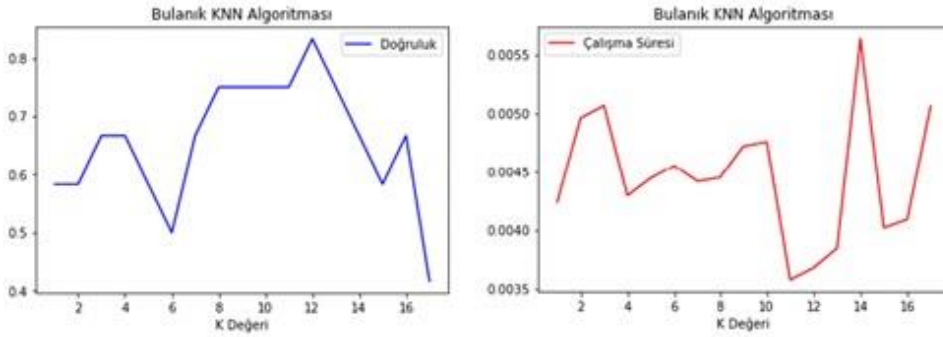
Geliştirilen algoritmaların gerçek dünya verilerindeki performansını yansıtması açısından doğru değerlendirme yöntemlerinin kullanılması kritik öneme sahiptir. İstatistiksel tahmin yöntemlerinde, bağımsız bir veri seti, jackknife testi birçok araştırmacı tarafından modelin başarısını test etme amacıyla kullanılmaktadır. Jackknife testi, bu değerlendirmelerde yaygın olarak tercih edilen bir tekniktir çünkü her bir veri örneğini sırasıyla test verisi olarak kullanarak, modelin her bir veri noktasındaki başarısını objektif bir şekilde ölçmeye olanak tanır. Jackknife testi, matematiksel olarak kanıtlanmış olan daha anlamlı sonuçlar vermektedir [37-38]. Bu yaklaşım, özellikle biyoinformatik alanında, her protein veya gen dizisinin doğru bir şekilde sınıflandırılmasını sağlamak ve modelin genel doğruluğunu güvenilir bir şekilde belirlemek için kullanılır. Bu sayede, algoritmanın overfitting (aşırı uyum) veya underfitting (yetersiz uyum) gibi problemlere karşı daha dayanıklı olması sağlanabilir. Çalışmamızda, Jackknife testi, her bir sekans için algoritma performansını değerlendirmek için kullanılmaktadır; burada her bir sekans, test verisi olarak davranırken

geriye kalanlar eğitim verisi olarak kullanılır. Veri tabanlarından alınan nörotrofin sekansları listesinde baştan sona kadar, her protein sırayla test verisi olarak görev yapmaktadır. Çalışmada, Uniprot veri tabanından Homo Sapiens için NGF ile ilişkili 15 tane ve BDNF ile ilişkili 15 tane sekans alındı. Lempel-Ziv uzaklığı ve Öklid uzaklığı kullanıldığında bulanık k-en yakın komşu algoritmasının sonucu Şekil 6'da gösterilmektedir.

Öklid Uzaklığı Kullanıldığında Elde Edilen Sonuçlar

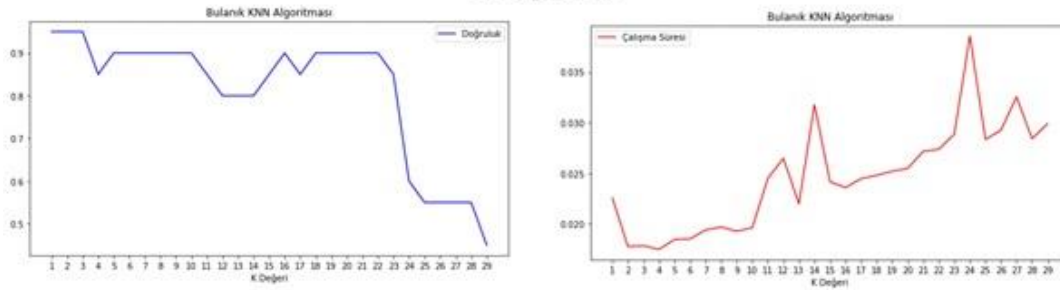


Lempel-Ziv Uzaklığı Kullanıldığında Elde Edilen Sonuçlar

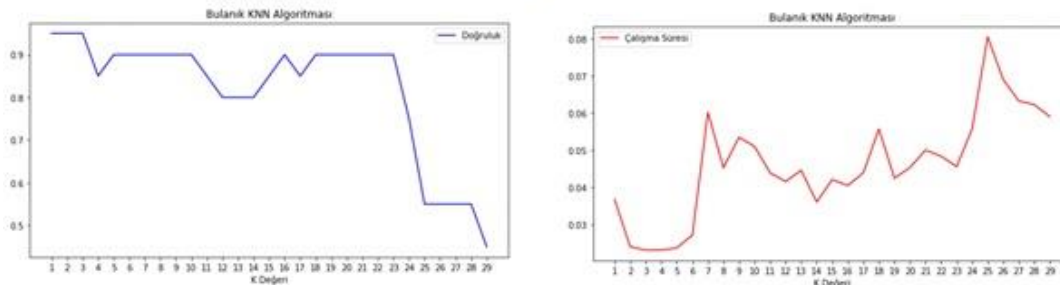


Şekil 6. Lempel-Ziv ile Öklid uzaklığı arasındaki fark 1 (Difference between Lempel-Ziv and Euclidean distance 1)

Lempel-Ziv

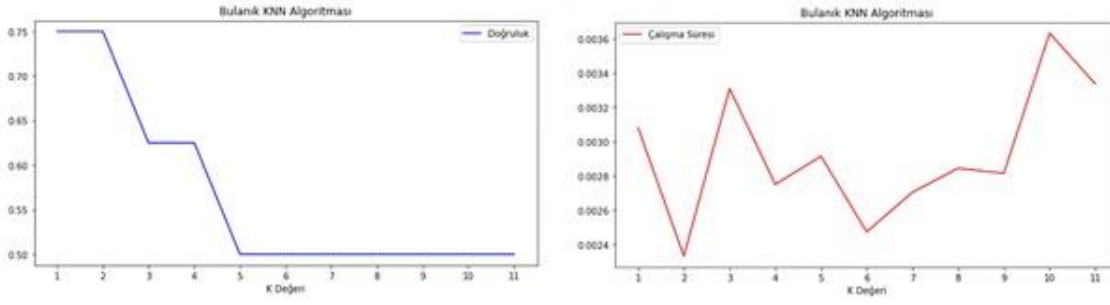


Öklid

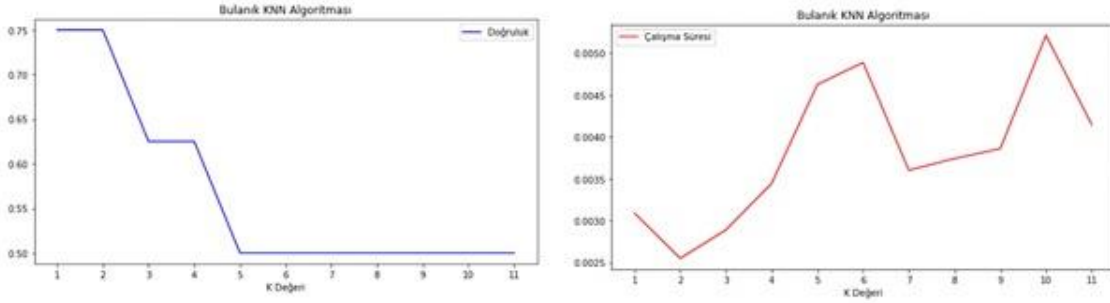


Şekil 7. Lempel-Ziv ile Öklid uzaklığı arasındaki fark 2 (Difference between Lempel-Ziv and Euclidean distance 2)

Lempel-Ziv

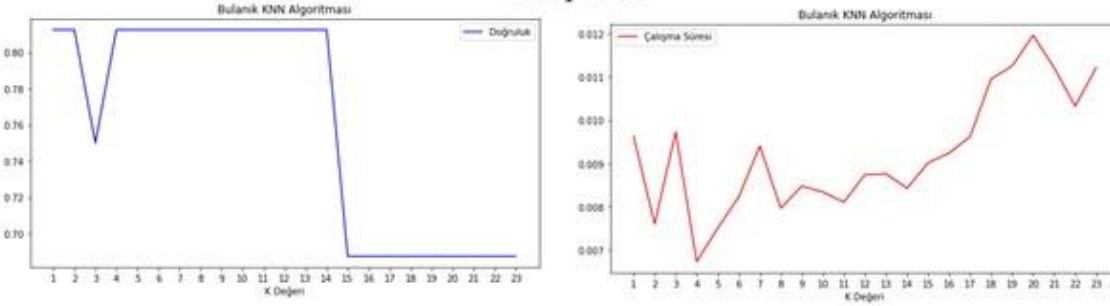


Öklid

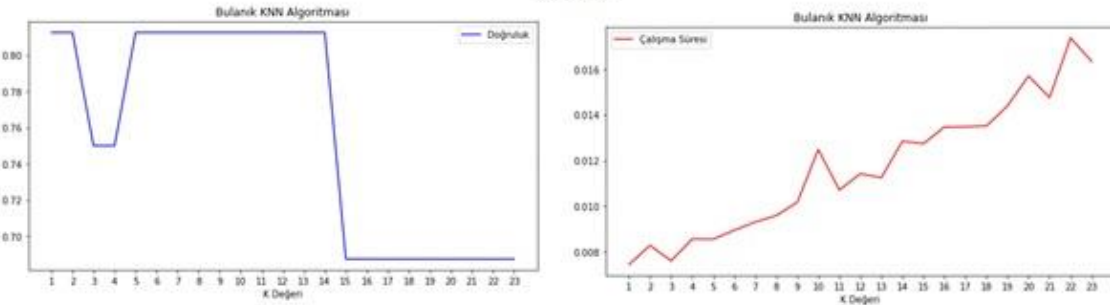


Şekil 8. Lempel-Ziv ile Öklid uzaklığı arasındaki fark 3 (Difference between Lempel-Ziv and Euclidean distance 3)

Lempel-Ziv



Öklid



Şekil 9. Lempel-Ziv ile Öklid uzaklığı arasındaki fark 3 (Difference between Lempel-Ziv and Euclidean distance 3)

National Library of Medicine'den Homo Sapiens için 30 adet NGF, 30 adet BDNF ve 7 adet NT-3 sekansları FASTA formatında alındı. Çalışmamızda izoform olanları elenerek o sınıfa ait farklı veriler kullanıldı ancak veri sayısını yüksek tutmak açısından birkaç adet izoform da kullanıldı. 23 adet NGF, 21 adet BDNF ve 6 adet NT-3 şeklinde 3 farklı sınıf olarak toplamda 50 sekans algoritmamızda kullanıldı. Sonuçları Şekil 7'dedir. 28 adet NGF ve 12 adet BDNF şeklinde

2 farklı sınıf olarak toplamda 40 sekans algoritmamızda kullanıldı. Sonuçları Şekil 8’dedir. 13 adet NGF ve 7 adet NT-3 şeklinde 2 farklı sınıf olarak toplamda 20 veri algoritmamızda kullanıldı. Sonuçları Şekil 9’dadır.

Çalışmamızda ilk olarak yapısal olarak birbirine benzeyen iki nörotrofin olan NGF ve BDNF sekanslarının Lempel-Ziv karmaşıklıkları hesaplanmıştır. Lempel-Ziv karmaşıklığı, protein verilerinin orijinal yapısını korumaktadır. Bu karmaşıklıklara dayalı Lempel-Ziv uzaklık değerleri hesaplanmıştır. Çalışmamızda protein sekanslarının, bulunduğu konumdaki halini değiştirmeden ve herhangi bir bilgi kaybı olmadan kullanabilmek için Lempel-Ziv karmaşıklığına dayalı uzaklık değerleri kullanıldı. Uniprot veri tabanından alınan verilerle birlikte Bulanık K-En Yakın Komşu algoritmasında Lempel-Ziv uzaklığı kullanıldığında K komşu sayısının 12 olması karşılığında, sınıflandırma performansı %83 olarak elde edilmiştir. Öklid Uzaklığı kullanıldığında elde edilen en yüksek sınıflandırma performansı ise %75’tir. Maksimum doğruluk oranını elde ettiğimiz noktada Öklid uzaklığını kullandığımızda algoritmamızın çalışma süresi 0.0054 ms iken Lempel-Ziv uzaklığı kullandığımızda 0.0038 ms’dir.

National Library of Medicine’den alınan verilerde ise şu sonuçlar elde edilmiştir: 50 adet ve 3 farklı sınıf olarak (NGF, BDNF ve NT-3) verilerin, FKNN algoritmamızda kullanılması sonucunda Lempel-Ziv uzaklığı kullanıldığında çalışma süresinin 0.020 ms ile 0.035 ms arasında iken Öklid uzaklığı kullanıldığında çalışma süresinin 0.04 ms ile 0.08 ms arasında olduğu görülmektedir. 40 adet ve 2 farklı sınıf olarak (NGF ve BDNF) verilerin, FKNN algoritmamızda kullanılması sonucunda Lempel-Ziv uzaklığı kullanıldığında çalışma süresinin 0.007 ms ile 0.012 ms arasında iken Öklid uzaklığı kullanıldığında çalışma süresinin 0.008 ms ile 0.016 ms arasında olduğu görülmektedir. 20 adet ve 2 farklı sınıf olarak (NGF ve NT-3) verilerin, FKNN algoritmamızda kullanılması sonucunda Lempel-Ziv uzaklığı kullanıldığında çalışma süresinin 0.0024 ms ile 0.0036 ms arasında iken Öklid uzaklığı kullanıldığında çalışma süresinin 0.0024 ms ile 0.0050 ms arasında olduğu görülmektedir.

Bulanık K-En Yakın Komşu (FKNN) algoritması, makine öğrenmesi ve veri madenciliği alanlarında sıklıkla kullanılan güçlü bir sınıflandırma yöntemidir. Protein sınıflandırmasında FKNN, özellikle amino asit dizilerinin ikincil yapılarını tahmin etmek amacıyla etkili bir şekilde uygulanmaktadır. Bu yöntem, verilerdeki belirsizlikleri ve düzensizlikleri daha iyi modelleyebilme kapasitesi sayesinde, geleneksel K-En Yakın Komşu (KNN) algoritmalarına kıyasla üstün performans sergileyebilir. FKNN algoritması, proteinlerin ikincil yapılarını sınıflandırırken, verinin bulanık doğasını dikkate alarak daha doğru ve güvenilir sonuçlar elde edilmesine olanak tanır. Literatürdeki birçok çalışma, FKNN'nin protein sınıflandırma problemlerinde başarıyla kullanıldığını ve sınıflandırma doğruluğunu artırdığını göstermektedir. Proteinlerin ikincil yapısının tahmin edilmesi için profiller ve Bulanık K-En Yakın Komşu algoritmasının kullanıldığı yeni bir yöntem, Bondugula ve arkadaşları tarafından önerilmiş ve pozisyon-ağırlıklı mutlak mesafe ölçüsü kullanılarak sınıflandırma doğruluğu %75.75 olarak elde edilmiştir [39]. Mirceva ve arkadaşları [40] tarafından yapılan çalışmada ise Bulanık K-En Yakın Komşuluk algoritmasında standart olarak Öklid mesafe ölçüsü kullanıldığında, protein sınıflandırma performansı en yüksek %79.97 olarak elde edilmiştir. Bu çalışmalar ışığında, çalışmamızda önerilen yaklaşımda ise, FKNN algoritmasının sınıflandırma performansını daha da yükseltecek yeni bir mesafe metriği olarak Lempel-Ziv Karmaşıklığı kullanılmıştır. Çalışmamızda önerilen algoritmadan elde edilen sonuçlara göre, Bulanık K-En Yakın Komşuluk Algoritması'nda mesafe metriği olarak Lempel-Ziv mesafesi kullanıldığında, Öklid mesafesine kıyasla daha hızlı bir çalışma süresi sağlandığı ve aynı zamanda sınıflama performansı olarak daha yüksek sonuçlar elde edildiği gözlemlenmiştir. Bu bağlamda, literatürde yapılan bu çalışmalara referans olabilecek şekilde, önerilen yaklaşımımızın yeni bir bakış açısı sunduğu ve daha yüksek sınıflama performansı sağladığı ortaya konmuştur.

Biyoenformatik, biyolojik verilerin analiz edilmesi ve yorumlanmasında kullanılan önemli bir alandır. Özellikle, büyük veri setlerinin işlenmesi gerektiğinde, veri işleme sürelerinin kısaltılması ve doğru sınıflandırma yapılabilmesi önemli bir zorluk oluşturur. Bu nedenle, verilerin büyük olmasından kaynaklanan zorlukları aşmak için geliştirilen çeşitli algoritmalar ve metrikler, bu alanda büyük önem taşımaktadır. Lempel-Ziv uzaklığı gibi yeni mesafe ölçütlerinin kullanılması, biyoenformatik çalışmalarda algoritma verimliliğini artırırken, aynı zamanda işlem sürelerini de optimize etmeye olanak tanımaktadır. Bu tür yöntemler, özellikle büyük ve karmaşık veri setlerinde, daha hızlı ve daha doğru analizler yapılmasını sağlayabilir. Önerilen yaklaşımımızın biyoenformatik çalışmalarına katkı sağlayacak potansiyeli bulunmaktadır. Çalışmamızın üç temel katkısı, önerilen yöntemin biyoenformatikteki mevcut tekniklerle nasıl uyumlu bir şekilde çalıştığını ve alanı nasıl ileriye taşıyabileceğini ortaya koymaktadır. Biyoenformatikte verilerin çok büyük olduğunu düşünecek olursak büyük verilerle çalıştığımızda süre daha önemli bir hale gelir. Sonuç olarak Lempel-Ziv

uzaklığının, biyoenformatik çalışmalarında ve uzaklık tabanlı sınıflandırma algoritmalarında kullanılması önerilmektedir.

Çalışmamızın üç ana katkısı bulunmaktadır. İlk olarak, biyoenformatik alanında yaygın olarak kullanılan makine öğrenimi tekniklerinden biri olan KNN algoritmasının bulanık versiyonu için Lempel-Ziv Karmaşıklığı'nın bir uzaklık metriği olarak kullanılması önerilmektedir. Bu yöntem, kayıpsız sıkıştırma ve farklı kalıpların çeşitliliğini ölçme açısından algoritmalarda önemli iyileştirmeler sağlamaktadır. İkinci olarak, algoritmamızda kullanılan veriler, yüksek yapısal benzerliklere sahip olmasının yanı sıra, farklı hücresel işlevlerde etkili ve paralel rolleri olan proteinlere ait olduğu için, bu verilerin sınıflandırılması, proteinlerin daha kolay analiz edilmesini ve anlamlı sonuçların elde edilmesini sağlayacaktır. Son olarak, bu çalışma, makine öğrenmesi yöntemlerinin nörotrofinlerin sınıflandırılmasında ilk kez uygulanmasıyla alana yenilikçi bir yaklaşım sunmaktadır.

KATKI ORANI BEYANI [STATEMENT OF CONTRIBUTION RATE]

Yazarların çalışmadaki katkı oranları eşittir.

ÇIKAR ÇATIŞMASI [CONFLICTS OF INTEREST]

Yazarlar arasında ve ilgili kurumları arasında herhangi çıkar çatışması olmadığını bildirmişlerdir.

ETİK KURALLARA UYGUNLUK [COMPLIANCE WITH ETHICAL RULES]

Yazarlar bu makalenin etik kurul onayı veya herhangi bir özel izin gerektirmediğini beyan ederler.

KAYNAKLAR [REFERENCES]

- [1] "Protein structure", nature.com, 2014. [Online]. Available: <https://www.nature.com/scitable/topicpage/protein-structure-14122136/>. [Accessed: 6 June 2022].
- [2] K. Ahern, I. Rahagopal, T. Tan, "2.3: Structure & fuction- proteins I", bio.libretext.org, Mar. 7, 2022. [Online]. Available: [https://bio.libretexts.org/Bookshelves/Biochemistry/Book%3A_Biochemistry_Free_For_All_\(Ahern_Rajagopal_and_Tan\)/02%3A_Structure_and_Function/203%3A_Structure__Function-_Proteins_I](https://bio.libretexts.org/Bookshelves/Biochemistry/Book%3A_Biochemistry_Free_For_All_(Ahern_Rajagopal_and_Tan)/02%3A_Structure_and_Function/203%3A_Structure__Function-_Proteins_I) [Accessed: June. 6, 2022]
- [3] J. Maillou, J. Luengo, S. Garcia, F. Herrera, I. Triguero, "Exact fuzzy k-nearest neighbor classification for big datasets", 2017 IEEE International Conference on Fuzzy Systems (FUZ-IEEE), July 09-12, 2017, Naples, Italy [Online]. Available: IEEE Xplore, <https://ieeexplore.ieee.org/document/8015686/authors#authors>, [Accessed: 12 June 2022]
- [4] James M. Keller, Michael R. Gray, James A. Givens, "A fuzzy k-nearest neighbor algorithm", IEEE Transactions on Systems, Man, and Cybernetics, vol: SMC-15, issue:4, pp. 580-585, July-Aug 1985, Doi: 10.1109/TSMC.1985.6313426. [Accessed: 15 June 2022]
- [5] X. Zheng, C. Li, J. Wang, "An information-theoretic approach to the prediction of protein structural class", Journal of Computational Chemistry, vol. 31, issue 6, pp. 1201-1206, September 2009, Doi: 10.1002/jcc.21406. [Accessed: 28 June 2022]
- [6] JY. Chang, JJ. Shyu, YX. Shi (2008). "Fuzzy k-nearest neighbor classifier to predict protein solvent accessibility" Ishikawa, M., Doya, K. Miyamoto, H., Yamakawa, T., Neural Information Processing. ICONIP 2007, vol 4985, pp. 837-845, Springer, Berlin, Heidelberg. [Online]. Doi: https://doi.org/10.1007/978-3-540-69162-4_87. [Accessed: 28 June 2022]
- [7] Y. Huang, Y. Li, "Prediction of protein subcellular locations using fuzzy k-NN method", Bioinformatics, vol. 20, no. 1, pages. 21-8, 2004 Jan. [Online]. Doi: 10.1093/bioinformatics/btg366. [Accessed: 25 June 2022]
- [8] R. Bondugula, O. Duzlevski, D. XU, "Profiles and fuzzy k-nearest neighbor algorithm for protein secondary structure prediction", Proceedings of the 3rd Asia-Pacific Bioinformatics Conference, pp. 85-94, January 2005, Singapore, [Online]. Doi: 10.1142/9781860947322_0009. [Accessed: 1 July 2022]
- [9] M. Kumar, SK. Rath, "Microarray data classification using fuzzy k-nearest neighbor", International Conference on Contemporary Computing and Informatics (IC3I), Mysore, India, IEEE, pp. 1032-1038, November 2014, Doi: 10.1109/IC3I.2014.7019618 [Accessed: 1 July 2022]

- [10] D. Li, JS, Deogun, K. Wang, "Gene function classification using fuzzy k-nearest neighbor approach", 2007 IEEE International Conference on Granular Computing (GRC 2007), Fremont, CA, USA, IEEE Xplore, pp. 644-644, November 2007, Doi: 10.1109/GrC.2007.99. [Accessed: 28 June 2022]
- [11] J. Sim, SY. Kim, J. Lee, "Prediction of protein solvent accessibility using fuzzy k-nearest neighbor method", *Bioinformatics*, vol. 21, issue 12, pages 2844-2849, April 2002 [Online] Doi: <http://doi.org/10.1093/bioinformatics/bti423>. [Accessed: 25 June 2022]
- [12] HA. Abu Alfeilat, ABA. Hassanat, O. Lasassmed, AS. Tarawneh, MB. Alhasanah, HS. Eyal Salman, VBS. Prasath, "Effects of distance measure choice on k-nearest neighbor classifier performance: a review", *Big Data*, 7(4): 221-248, Dec 2019, Doi: 10.1089/big.2018.0175. Epub 2019 Aug 14. [Accessed: 8 July 2022]
- [13] K. Chomboon, P. Chujai, P. Teerarassamee, K. Kerdprasop, N. Kerdprasop, "An empirical study of distance metrics for k-nearest neighbor algorithm", *Proceedings of the 3rd International Conference on Industrial Application Engineering 2015, Japan*, pp. 280-285, Doi: 10.12792/iciae2015.051. [Accessed: 5 July 2022]
- [14] P. Melin, E. Ramirez, G. Prado- Arechiga, "A new variant of fuzzy k-nearest neighbor using interval type-2 fuzzy logic", 2018 IEEE International Conference on Fuzzy Systems (FUZZ-IEEE), 2018, pp. 1-7, Doi: 10.1109/FUZZ-IEEE.2018.8491472. [Accessed: 5 July 2022]
- [15] PK. Jena, S. Chattopadhyay, "Comparative study of fuzzy k-nearest neighbor and fuzzy c-means algorithms", *International Journal of Computer Applications*, vol. 57, no. 7, pp. 22-32, November 2012, Doi: 10.1007/978-3-642-30157-5_45. [8 July 2022]
- [16] F. Rosas, P. Mediano, "When and how to use Lempel-Ziv complexity", *Information Dynamics*, 26 June 2019, [Online]. Available: <https://information-dynamics.github.io/complexity/information/2019/06/26/lempel-ziv.html>. [Accessed: 10 July 2022]
- [17] AW. Norman, HL. Henry, *Hormones: Growth factors*, Third Edition, Academic Press, 2015, pp. 363-379, Doi: 10.1016/B978-0-08-091906-5.000-3. [Accessed: 15 July 2022]
- [18] AC. Mitchell, PS. Briquez, JA. Hubbell, JR. Cochran, "Engineering growth factors for regenerative medicine applications", *Acta Biomater*, Jan 2016, 1-12, Doi: 10.1016/j.actbio.2015.11.007. [Accessed: 16 July 2022]
- [19] X. Ren, M. Zhao, B. Lash, MM. Martino, Z. Julier, "Growth factor engineering strategies for regenerative medicine applications", *Frontiers in Bioengineering and Biotechnology journal*, vol. 7, January 2020, Doi: 10.3389/fbioe.2019.00469. [Accessed: 16 July 2022]
- [20] İB. Çitçi, DA. Jafari, B. Kosova, *Sağlık Bilimleri Alanında Akademik Çalışmalar-II: Nörotrofin ailesi*, Gece Kitaplığı, vol. 2, pp. 333-349, June 2020. [Accessed: 31 July 2022]
- [21] S.Cohen, R. Levi-Montalcini, V. Hamburger, "A nerve growth-stimulating factor isolated from sarcom as 37 and 180", *Proc Natl Acad Sci USA*, 40 (10): 1014-1018, Oct 1954; Doi: 10.1073/pnas.40.10.1014. [Accessed: 10 August 2022]
- [22] L. Aloe, "Rita Levi-Montalcini: the discovery of nerve growth factor and modern neurobiology", *Trends in Cell Biology*, vol. 14(7), pp. 395-9, Jul 2004, Doi: 10.1016/j.tcb.2004.05.011. [Accessed: 10 August 2022]
- [23] M. Costandi, *Nöroplastisite: Büyüme faktörleri ve hücre intiharı*, Pan Yayıncılık, January 2019, pp. 49-51. [Accessed: 10 August 2022]
- [24] U. Suter, C. Angst, CL. Tien, CC. Drinkwater, RM. Lindsay, EM. Shooter, "NGF/BDNF chimeric proteins: analysis of neurotrophin specificity by homolog-scanning mutagenesis", *The Journal of Neuroscience: the official journal of the Society for Neuroscience*, vol. 12, 1, pp. 306-318, Jan 1992, Doi: 10.1523/JNEUROSCI.12-01-00306.1992. [Accessed: 16 July 2022]
- [25] J. Leibrock, F. Lottspeich, A. Hohn, M. Hofer, B. Hengerer, P. Masiakowski, H. Thoenen, YA. Barde, "Molecular cloning and expression of brain-derived neurotrophic factor", *Nature*, vol. 341, 6238, pp 149-152, Sep 1989, Doi: 10.1038/341149a0. [Accessed: 25 July 2022]
- [26] J. Langhnoja, L. Buch, P. Pillai, "Potential role of NGF, BDNF, and their receptors in oligodendrocytes differentiation from neural stem cell: an in vitro study", *Cell Biology International*, vol. 45, issue 2, pp. 432-446, February 2021, Doi: 10.1002/cbin.11500. [Accessed: 25 July 2022]
- [27] PC. Maisonpierre, L. Belluscio, B. Friedman, RF. Alderson, SJ. Wiegand, ME. Furth, RM. Lindsay, GD. Yancopoulos, "NT-3, BDNF, and NGF in the developing rat nervous system: Parallel as well as reciprocal patterns of expression", *Neuron*, vol. 5, issue 4, pp. 501-509, October 1990, Doi: 10.1016/0896-6273(90)90089-X. [Accessed: 25 July 2022]

-
- [28] C. Zeeh, "The Lempel Ziv algorithm", uwaterloo.ca, January 16, 2003. [Online]. Available: <https://ece.uwaterloo.ca/~ece611/LempelZiv.pdf>. [Accessed: 10 July 2022]
- [29] T. Weissman, "Chapter 1. Lempel-Ziv compression", web.stanford.edu, [Online]. Available: https://web.stanford.edu/class/ee376a/files/EE376C_lecture_LZ.pdf. [Accessed: 10 July 2022]
- [30] E. Roberts, "Dictionary-based compressors", cs.stanford.edu, [Online]. Available: <https://cs.stanford.edu/people/eroberts/courses/soco/projects/data-compression/lossless/lz78/index.htm>. [Accessed: 10 July 2022]
- [31] ST. Brink, "Lempel-Ziv compression", webdemo.inue.uni-stuttgart.de, [Online]. Available: https://webdemo.inue.uni-stuttgart.de/webdemos/03_theses/Lempel-Ziv-Compression/index.php?id=1. [Accessed: 10 July 2022]
- [32] G. Sharma, "Analysis of Huffman Coding and Lempel-Ziv-Welch (LZW) coding as data compression techniques", International Journal of Scientific Research in Computer Science and Engineering, vol. 8, issue 1, pp. 37-44, Feb 2020. [Accessed: 12 July 2022]
- [33] YT. Tan, BA. Rosdi, "FPGA-based hardware accelerator for the prediction of protein secondary class via fuzzy K-nearest neighbors with Lempel-Ziv complexity-based distance measure", Neurocomputing, vol. 148, pp. 409-419, January 2015, Doi: 10.1016/j.neucom.2014.06.001. [Accessed: 5 July 2022]
- [34] HB. Shen, J. Yang, KC. Chou, "Fuzzy KNN for predicting membrane protein types from pseudo-amino acid composition", Journal of Theoretical Biology, 240, 9-13, June 2006, Doi: 10.1016/j.jtbi.2005.08.016. [Accessed: 20 July 2022]
- [35] Z. Bian, CM. Vong, PK. Wong, S. Wang, "Fuzzy KNN method with adaptive nearest neighbors", IEEE Transactions on Cybernetics, vol. 52, no. 6, pp. 5380-5393, June 2022, Doi:10.1109/TCYB.2020.3031610. [Accessed: 20 July 2022]
- [36] LA. Zadeh, "Fuzzy sets", Information and Control, vol. 8, issue 3, pp. 338-353, 1965, Doi: 10.1016/S0019-9958(65)90241-X. [Accessed 20 July 2022]
- [37] KC. Chou, CT. Zhang, "Review: prediction of protein structural classes", Critical Reviews in Biochemistry and Molecular Biolog, 30, 275-349, 1995. [Accessed 25 November 2024]
- [38] S. Sinharay, "Jackknife Methods", International Encyclopedia of Education (Third Edition), 229-231, 2010. [Accessed 25 November 2024]
- [39] R. Bondugula, O. Duzlevski, D. Xu, "Profiles and fuzzy k-nearest neighbor algorithm for protein secondary structure prediction", In Proceedings of the 3rd Asia-Pacific Bioinformatics Conference pp. 85-94, 2005.
- [40] G. Mirceva, A. Naumoski, A. Kulakov, "Classification of protein structures by using fuzzy KNN classifier and protein voxel-based descriptor", Mathematical Modeling, 2(3), 116-118, 2018.



RESEARCH ARTICLE

Investigation of the effects of laser power and gas pressure on the top and bottom HAZ widths in AISI 1040 steels

* Mehmet Şükrü Adin

*Batman University, Besiri OSB Vocational School, Batman, 72060, Türkiye
mehmetsukru.adin@batman.edu.tr, Orcid:0000-0002-2307-9669

Citation:

Adin, M.Ş. (2024). *Investigation of the effects of laser power and gas pressure on the top and bottom HAZ widths in AISI 1040 steels*, Journal of Science Technology and Engineering Research, 5(2): 163-175. DOI: 10.53525/jster.1583593

HIGHLIGHTS

- Fiber laser technology was utilized.
- A different cutting method was applied for the HAZ.
- Especially top and bottom HAZ widths were investigated.

Article Info

Received : 12 Novem. 2024

Accepted : 02 Decem. 2024

DOI:

10.53525/jster.1583593

***Corresponding Author:**

Mehmet Şükrü Adin

mehmetsukru.adin@batman.edu.tr

Phone: +90 488 217 3929

ABSTRACT

In this research, AISI 1040 steels, which are extensively used in different manufacturing industries, were used as workpieces to better comprehend the influences of laser beam cutting parameters on workpieces. In this context, such parameters as laser power, gas pressure and cutting speed were established as variable parameters. In present research, unlike the investigations available in the literature, the workpieces that started to be cut in a straight line were stopped 3 mm before the end of the cutting process. Thus, it could be possible to both see and investigate the top and bottom HAZ (Heat Affected Zone) widths occurring just outside the workpieces. Within the scope of the research, especially the top and bottom HAZ widths occurring in workpieces cut with a different method were investigated. At the gas pressure of 0.7 Bar, considering the largest and smallest bottom HAZ width values, it was studied out that the largest bottom HAZ width value (9.23 mm) was 32.83% larger than the smallest bottom HAZ width value (6.95 mm). On the other side, considering the largest and smallest top HAZ width values, it was studied out that the largest top HAZ width value (5.33 mm) was 71.39% larger than the smallest top HAZ width value (3.11 mm). At 1.4 Bar gas pressure, considering the largest and smallest bottom HAZ width values, it was found that the largest bottom HAZ width value (11.47 mm) was 28.19% larger than the smallest bottom HAZ width value (8.95 mm). On the other side, considering the largest and smallest top HAZ width values, it was studied out that the largest top HAZ width value (6.79 mm) was 42.95% larger than the smallest top HAZ width value (4.75 mm). Additionally, considering the largest and smallest average HAZ width values based on gas pressure of 0.7 Bar and 1.4 Bar, it was found that the largest the average HAZ width values were 33.29% and 44.75% larger than the smallest the average HAZ width values, respectively.

Keywords: AISI 1040 steel, Fiber laser cutting, laser machining, Top and bottom HAZ widths, Kerf width

I. INTRODUCTION

Contemporary manufacturing industries are conducting intensive research to provide better quality, more cost-effective and shorter delivery times in line with consumer demands. One of the research areas carried out in this context is the processing of materials with very different properties using laser beam technology (Guo & Singh, 2021; Salem, Mansour, Badr, & Abbas, 2008; Sargar, Jadhav, & Gautam, 2023; Steen & Mazumder, 2010). Laser beam technology is rapidly becoming widespread in contemporary manufacturing industries with its many advantages such as high production speed, cost-effectiveness and high processing quality. Laser beam is generally used for needs such as cutting, drilling, welding and surface treatment of materials with different properties (Batishcheva, Kuznetsov, Orlova, & Vympina, 2021; Kannatey-Asibu, 2023; Khdaif & Melaibari, 2023; Wu et al., 2024; Wu, Wang, Zhang, Liu, et al., 2023). In recent years, the employment of laser beams in cutting chemically and physically very different materials such as metals and composites has become increasingly important. Laser beam cutting technology is used extensively in many different manufacturing industries, from the aerospace industry where high technology is used, to the electrical household appliance production industry where simple technologies are used (Guo & Singh, 2021; Steen & Mazumder, 2010; Wu et al., 2024). Research on this technology, which is used in such different fields intensively, has gained both importance and attention. However, when the usage rates of laser beam cutting technologies used in the contemporary manufacturing industries were compared, it was noticed that fiber and CO₂ lasers had the highest rates (Hilton, Lloyd, & Tyrer, 2016; Kannatey-Asibu, 2023). In particular, in recent years, indicators have been pointing entirely to fiber laser technologies.

The main reasons for this situation are that it has highly demanded features such as having a more advanced technology and lower maintenance costs (Amaral, Silva, Pinto, Campilho, & Gouveia, 2019; Guo & Singh, 2021; Kannatey-Asibu, 2023; Kardan, Levichev, Castagne, & Duflou, 2023; Steen & Mazumder, 2010). Despite all these superior features of fiber laser beam technology, as in other laser technologies, each processing parameter and its effects need to be intensively investigated in order to process each material with different properties in high quality. For this purpose, firstly, the influences of laser beam cutting parameters, for instances, cutting speed, laser power, assist gas pressure and cutting geometry on the workpiece should be investigated and optimized separately. Afterwards, the influences of other important agents such as laser technology, physical and chemical properties of the workpiece, and thickness of the workpiece should be examined. As a consequence, laser beam machining parameters will be optimized for each material individually, allowing manufacturing industries and therefore consumers to obtain high-quality and minimum-cost products (Amaral et al., 2019; Kannatey-Asibu, 2023; Steen & Mazumder, 2010).

In this research, AISI 1040 steels, which are extensively used in different manufacturing industries, were used as workpieces to better comprehend the influences of cutting parameters of laser beam on workpieces. In this context, laser power, gas pressure and cutting speed parameters were established as variable parameters. In the research, especially the top and bottom HAZ widths occurring in workpieces cut with a different method were investigated.

II. MATERIALS AND METHODS

A. Workpiece material

In this research, AISI 1040 steel materials were preferred (in order to guide manufacturing industries where these materials are used) as work pieces. AISI 1040 steel materials preferred as workpieces within the scope of this research are widely used in many different manufacturing industries from aerospace to automotive (Callister & Rethwisch, 2020; Gupta, Singh, & Sood, 2015). Pictures of the workpieces (four pieces) used in this research and their mechanical and melting temperature properties are presented in Fig. 1.

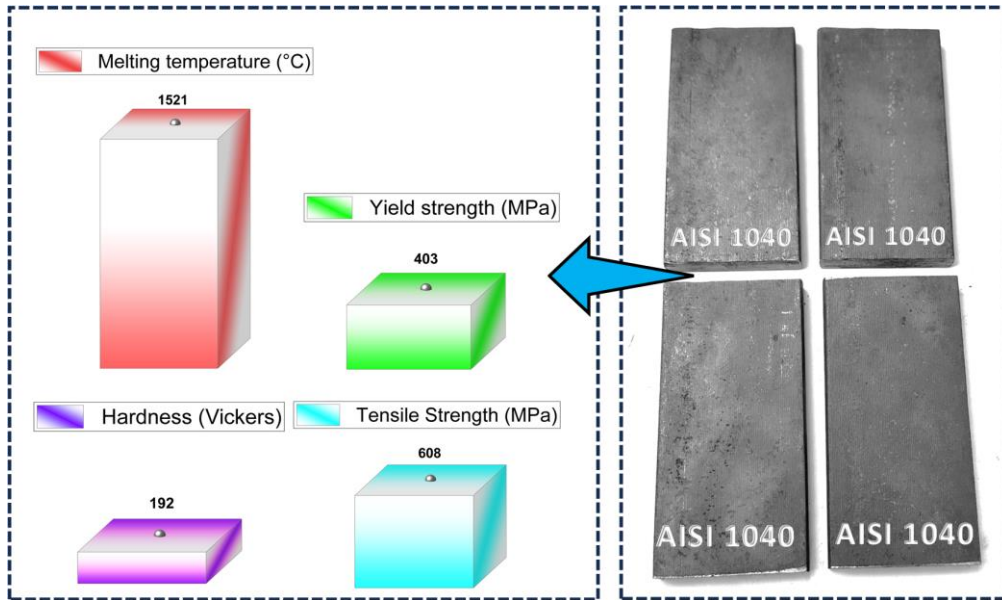


Figure 1. Pictures and properties of workpieces

The chemical compositions (as wt. %) of the AISI 1040 steel workpieces used in the research, which was carried out experimentally, are given in Fig. 2. As described in Fig. 2, the weight percentages of the elements found in AISI 1040 steel materials are within the lower and upper limits specified in the literature (Callister & Rethwisch, 2020; Dieter, 1997). The dimensions (length x width x thickness) of the workpieces used in this research are 100 mm, 50 mm and 10 mm (in the research, minimum dimensions were determined to achieve the goals of the experimental study in a cost-effective way), respectively.

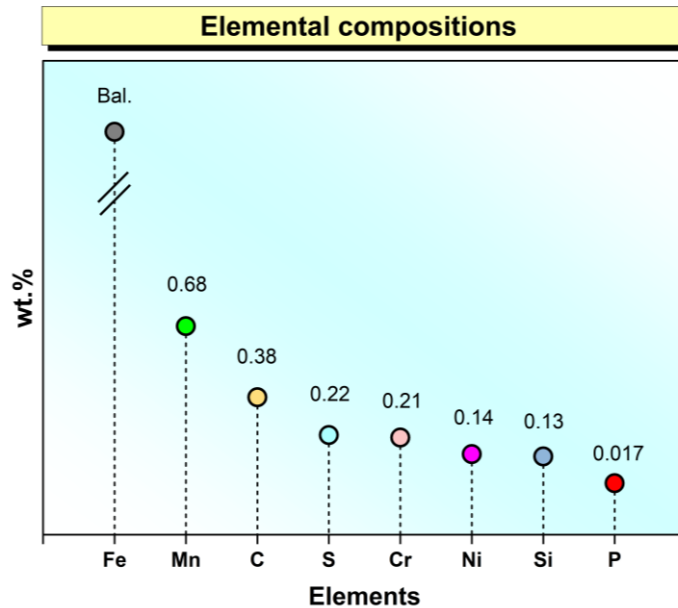


Figure 2. Chemical compositions of the workpiece

B. Laser cutting experiments

In this research, the cutting parameters and their levels determined (different values were determined, taking into account the upper and lower values.) for laser cutting experiments were selected as a result of intensive literature review (Guo & Singh, 2021; Kardan et al., 2023; Liu & Zhang, 2024a, 2024b; Steen & Mazumder, 2010), but the originality of the investigation was preserved by applying different values. In Table 1, the cutting parameters and levels applied to cut the workpieces with laser beam within the scope of this experimental research are given.

Table 1. Laser cutting parameters and levels

Parameter	Unit	Level 1	Level 2	Level 3
Gas pressure	Bar	0.7	1.4	-
Laser power	W	2400	2600	2800
Cutting speed	mm/min	380	480	580

In Table 2, the machining parameters of 18 laser cutting experiments performed according to the determined parameters and their levels (based on Table 1) are given. As displayed in Table 2, laser power, gas pressure and cutting speed were established as variable parameters. Also, as observed in Table 2, the increases in laser power, gas pressure and cutting speed were applied as 0.7 bar, 200 W and 100 mm/min, respectively. With these constant value increases in each parameter, the effects of each parameter and level have been provided with a clearer understanding. On the other side, parameters such as nozzle diameter and assist gas type were determined (since the workpieces are metal) as 2 mm and Oxygen gas, respectively, in line with literature investigations (Guo & Singh, 2021; Powell, Al-Mashikhi, Kaplan, & Voisey, 2011; Shin et al., 2018). The CNC fiber laser machine used in this research is HGStar 3015 (trademarked) with a wavelength and a power of 1064 nm and 6000 W, respectively.

Table 2. Laser machining parameters

Exp. no	Gas pressure (Bar)	Laser power (W)	Cutting speed (mm/min)
H1	0.7	2400	380
H2	0.7	2400	480
H3	0.7	2400	580
H4	0.7	2600	380
H5	0.7	2600	480
H6	0.7	2600	580
H7	0.7	2800	380
H8	0.7	2800	480
H9	0.7	2800	580
H10	1.4	2400	380
H11	1.4	2400	480
H12	1.4	2400	580
H13	1.4	2600	380
H14	1.4	2600	480
H15	1.4	2600	580
H16	1.4	2800	380
H17	1.4	2800	480
H18	1.4	2800	580

At the beginning, middle and end of the research (i.e., measured three times), the relative humidity and ambient temperatures in the experimental environment (considering the experimental results are known to be significantly impacted by it (Guo & Singh, 2021; Kannatey-Asibu, 2023; Steen & Mazumder, 2010) were measured with the HTC-1 brand device, then the arithmetic averages of them were computed. The measurements' results showed that the average relative humidity was 53% and the ambient temperature was 26°C. Within the scope of this research, a picture taken during the cutting process, the dimensions of the workpieces (Three-Dimensional, 3D) and the picture of the laser cutting method are presented in Fig. 3. In the research carried out experimentally, as displayed in Fig. 3, unlike the investigations found in the literature, the workpieces that started to be cut in a straight line were stopped 3 mm before the end of the cutting process. Thus, it became possible to both see and investigate the top and bottom HAZ widths occurring just outside (3 mm) the workpieces.

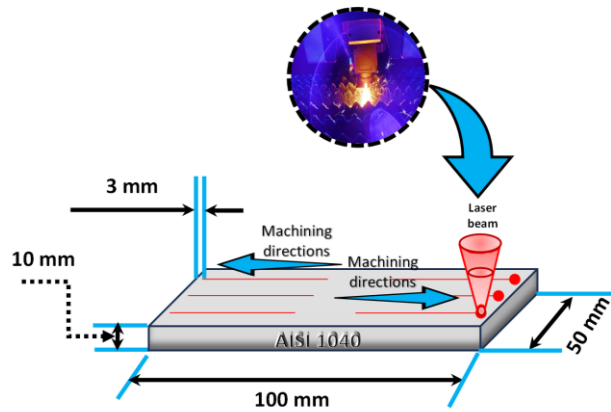


Figure 3. Dimensions of the workpieces and laser cutting method (also, an image taken during the cutting)

C. HAZ (top and bottom) and Kerf width measurements

In this research, although research was conducted especially on the top and bottom HAZ widths, the kerf widths that occurred during laser cutting processes were also measured. In Fig. 4, the locations of HAZ (top and bottom) and Kerf width measurements are shown.

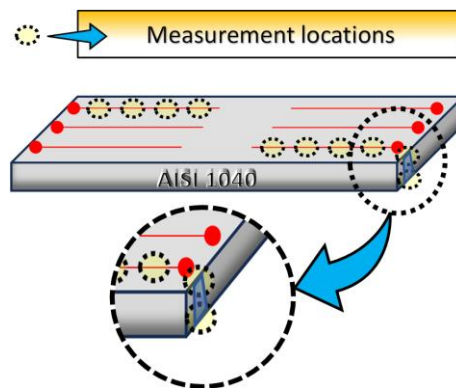


Figure 4. HAZ (top and bottom) and kerf width measurements

As displayed in Fig. 4, the kerf widths were measured at 4 (four) different locations and then their arithmetic means were calculated. On the other hand, HAZ widths were measured in the top and bottom regions where the HAZ occurred (Fig. 4). In order to precisely measure the HAZ and kerf widths, images were first taken with a Leica DM 750P microscope (for each laser cutting experiment separately. i.e., eighteen (18) experiments) and then measurements were made digitally on these images employing ImageJ software.

III. RESULTS AND DISCUSSION

A. HAZ (top and bottom) and Kerf widths

In this experimental research, as displayed in Fig. 5, unlike the investigations found in the literature, the specimens that started to be cut in a straight line were stopped 3 mm before the end of the cutting process. Thus, it is possible to both see and investigate the top and bottom HAZ widths occurring just outside (3 mm) the specimens.

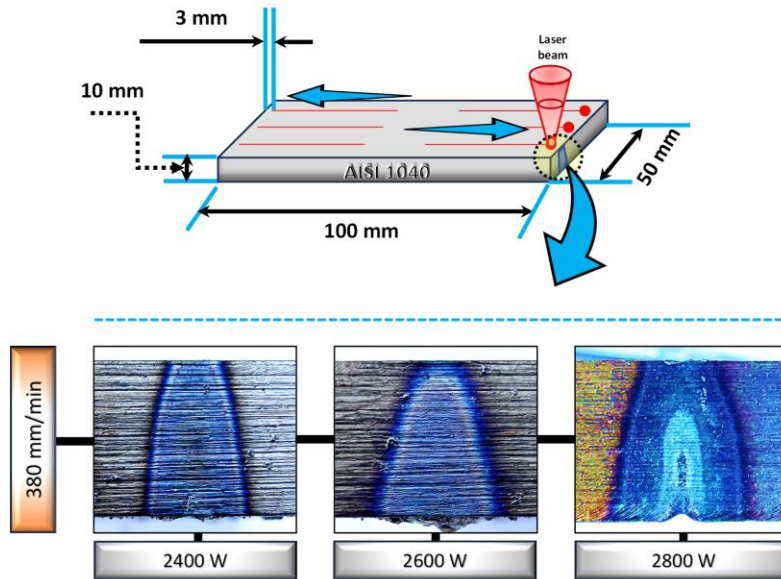


Figure 5. Change of top and bottom HAZ widths

The change of top and bottom HAZ widths depending on the increase in laser power at constant cutting speed is shown in Fig. 5. As displayed in Fig. 5, it is clearly observed that both top and bottom HAZ widths increase as the laser power increases. On the other side, as seen in Fig. 6, graphs of top and bottom HAZ width values obtained based on different gas pressure and laser power are given. As depicted in Fig. 6 a, at 0.7 Bar gas pressure, the largest bottom HAZ width value was studied out to be 9.23 mm and the smallest bottom HAZ width value was studied out to be 6.95 mm. This largest bottom HAZ width value was obtained at 2800 W laser power and 380 mm/min cutting speed parameters, while the smallest bottom HAZ width value was achieved at 2400 W laser power and 380 mm/min parameters. Considering these largest and smallest bottom HAZ width values, it was studied out that the largest bottom HAZ width value (9.23 mm) was 32.83% larger than the smallest bottom HAZ width value (6.95 mm). On the other side, as displayed in Fig. 6 b, at 0.7 Bar gas pressure, the largest top HAZ width value was studied out to be 5.33 mm and the smallest top HAZ width value was studied out to be 3.11 mm. This largest top HAZ width value was achieved at 2800 W laser power and 380 mm/min cutting speed parameters, while the smallest top HAZ width value was obtained at 2400 W laser power and 380 mm/min parameters. Considering these largest and smallest top HAZ width values, it was studied out that the largest top HAZ width value (5.33 mm) was 71.39% larger than the smallest top HAZ width value (3.11 mm).

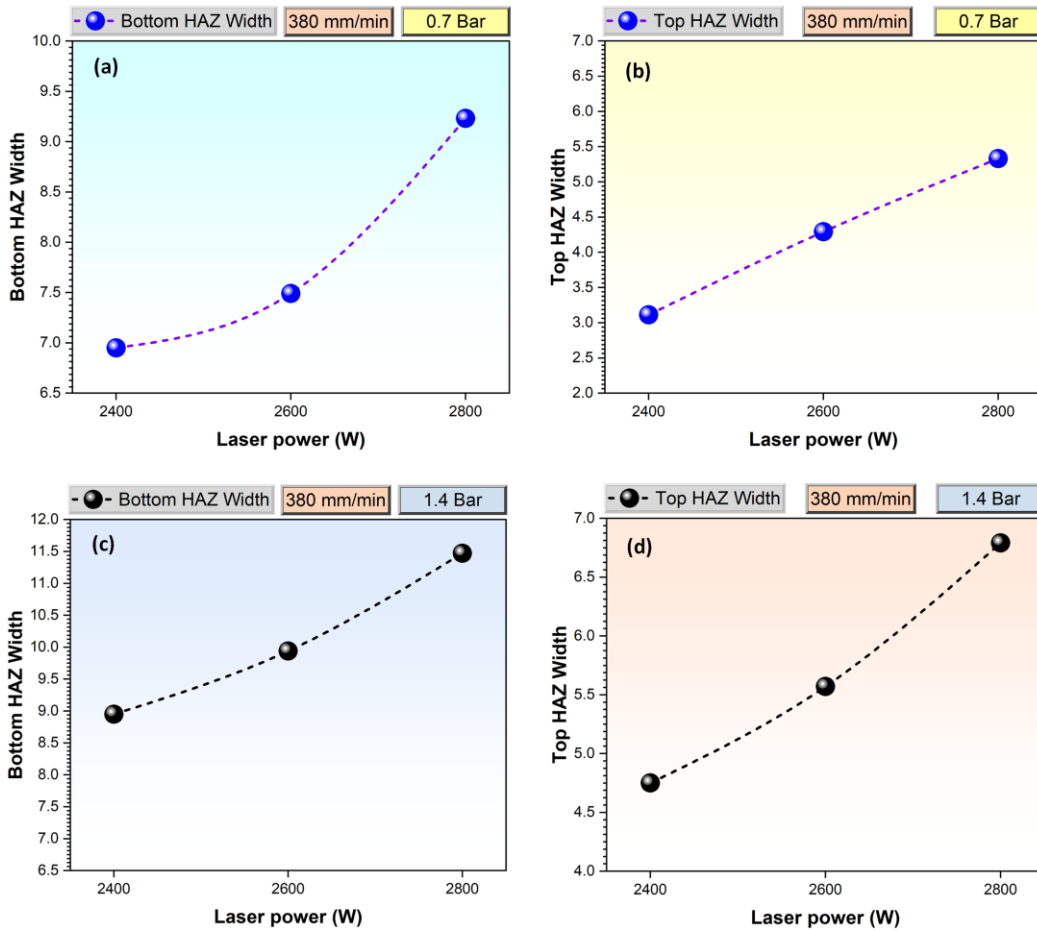


Figure 6. Top and bottom HAZ width values according to laser cutting parameters

As presented in Fig. 6 c, at gas pressure of 1.4 Bar, the largest bottom HAZ width value was studied out to be 11.47 mm and the smallest bottom HAZ width value was studied out to be 8.95 mm. This largest bottom HAZ width value was obtained at laser power of 2800 W and cutting speed of 380 mm/min, while the smallest bottom HAZ width value was achieved at the parameters of laser power of 2400 W and cutting speed of 380 mm/min. Considering these largest and smallest bottom HAZ width values, it was studied out that the largest bottom HAZ width value (11.47 mm) was 28.19% larger than the smallest bottom HAZ width value (8.95 mm). On the other side, as displayed in Fig. 6 d, at gas pressure of 1.4 Bar, the largest top HAZ width value was studied out to be 6.79 mm and the smallest top HAZ width value was studied out to be 4.75 mm. This largest top HAZ width value was obtained at parameters of laser power 2800 W and cutting speed of 380 mm/min, while the smallest top HAZ width value was achieved at parameters of laser power of 2400 W and cutting speed of 380 mm/min. Considering these largest and smallest top HAZ width values, it was studied out that the largest top HAZ width value (6.79 mm) was 42.95% larger than the smallest top HAZ width value (4.75 mm). Consequently, considering these largest and smallest top and bottom HAZ width values based on gas pressures of 0.7 Bar and 1.4 Bar, it was studied out that the largest bottom HAZ width values (i.e., 11.47 mm and 9.23 mm) were 141.47% and 196.78% larger than the smallest top HAZ width values (i.e., 4.75 m and 3.11 mm), respectively. In this experimental research, to better comprehend the HAZ widths, the arithmetic averages of the top and bottom HAZ widths obtained based on gas pressure and laser power were calculated and depicted in Fig. 7.

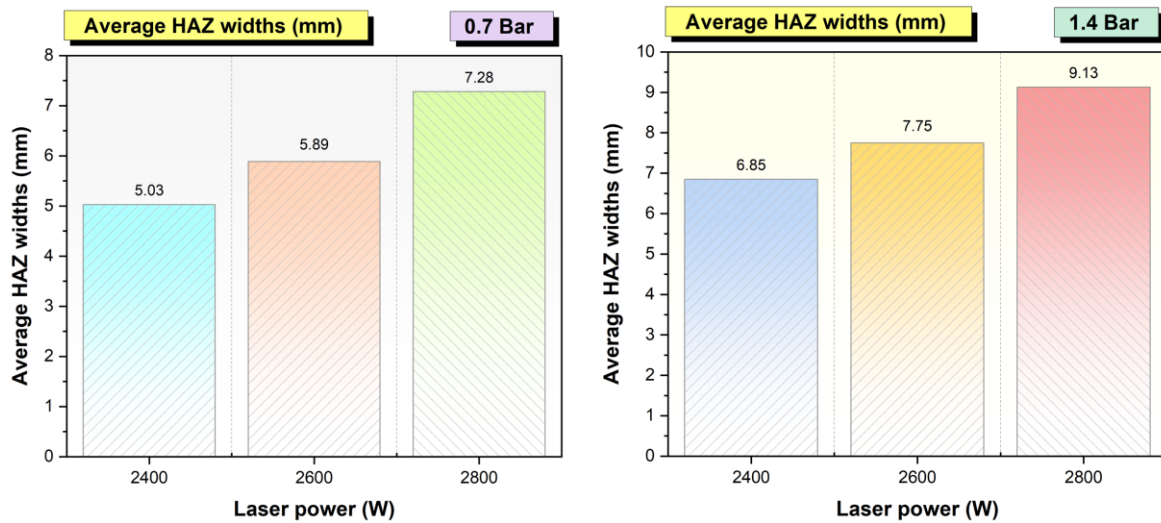


Figure 7. Average HAZ widths based on gas pressures

As displayed in Fig. 7, when the average HAZ width values obtained at gas pressure of 0.7 Bar were checked, it was understood that the largest average HAZ width value was obtained as 7.28 mm at 2800 W laser power. Additionally, it was inspected that at gas pressure of 0.7 Bar, the smallest average HAZ width of 5.03 mm was obtained at 2400 W laser power. On the other side, as depicted in Fig. 7, when the average HAZ width values obtained at gas pressure of 1.4 Bar were visually inspected, it was understood that the largest average HAZ width value was obtained as 9.13 mm at 2800 W laser power. Moreover, it was found that at gas pressure of 1.4 Bar, the smallest average HAZ width of 6.85 mm was obtained at 2400 W laser power. Consequently, considering these largest and smallest the average HAZ width values based on gas pressures of 0.7 Bar and 1.4 Bar, it was found that the largest the average HAZ width values (i.e., 9.13 mm and 7.28 mm) were 33.29% and 44.75% larger than the smallest the average HAZ width values (i.e., 6.85 m and 5.03 mm), respectively. Additionally, as a consequence of the experiments, it was revealed that the average HAZ widths were negatively affected by high gas pressure (based on the results obtained at 0.7 Bar and 1.4 Bar gas pressures). As depicted in Figs. 5, 6 and 7, it was understood that the HAZ widths were negatively affected by both high laser power and high gas pressure.

This can be explained by the fact that the laser beam concentrated on the metal material penetrates more into the metal material owing to the influence of high laser power, resulting in an increase in both the molten metal volume and the width of the HAZ. Moreover, because of high pressured oxygen penetrating into the same location for a longer period of time and reacting with the metal material, extra energy is generated and with the impact of this additional energy, both the HAZ width and the molten metal volume increase (Adin, 2024; Guo & Singh, 2021; Kannatey-Asibu, 2023; Karatas, Keles, Uslan, & Usta, 2006; Rao, Raju, Suresh, Ranganayakulu, & Krishna, 2024; Scintilla & Tricarico, 2012). As a matter of fact, when the results of the investigations in the literature on metal materials were examined, it was noticed that increases in gas pressure and laser power caused similar effects (Guo & Singh, 2021; Kannatey-Asibu, 2023; Steen & Mazumder, 2010; Wu et al., 2024; Wu, Wang, Zhang, Liu, et al., 2023; Wu, Wang, Zhang, Xue, et al., 2023).

In this research, although research was conducted especially on the top and bottom HAZ widths, the kerf widths that occurred during laser cutting processes were also measured. In Fig. 8, the kerf widths occurring at different cutting speeds at a constant laser power of 2800 W are displayed. As depicted in Fig. 8, it is understood that at constant laser power, kerf widths tend to decrease as the cutting speed increases. On the other part, it is observed that kerf widths are negatively affected due to the increase in molten metal volume at a cutting speed of 380 mm/min and its inability to be sufficiently removed (due to high laser power) (Steen & Mazumder, 2010; Wu, Wang, Zhang, Liu, et al., 2023) from the cutting area.

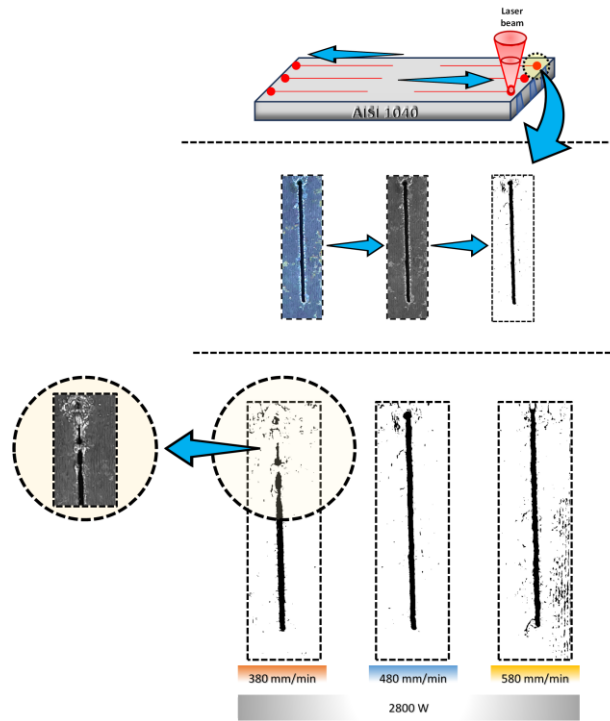


Figure 8. Kerf widths occurring at different cutting speeds at constant laser power

Fig. 9 shows the effects of laser power, gas pressure and cutting speed on the kerf width. When the graphs given in Figure 9 are visually examined, it is clearly understood that high laser power and gas pressures negatively affect the kerf widths.

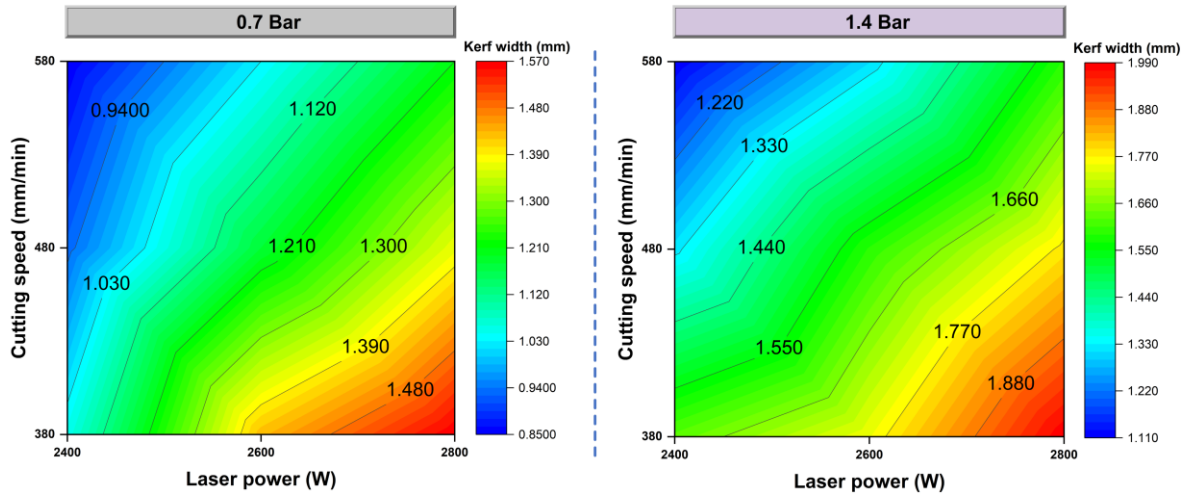


Figure 9. Influences of laser power, cutting speed, and gas pressure on the kerf widths

Moreover, it is inspected that the smallest kerf width values are concentrated (blue colored area) in the range of laser power of 2400 W and cutting speed of 580 mm/min, whereas the largest kerf widths are concentrated (red colored area) in the range of laser power of 2800 W and cutting speed of 380 mm/min. Additionally, it was understood that the largest kerf width values occurred at high gas pressure (i.e., 1.4 Bar). In order to better see the effects of high

gas pressure (i.e., gas pressure 1.4 Bar) on kerf widths, a comparison graph was drawn and presented in Fig. 10.

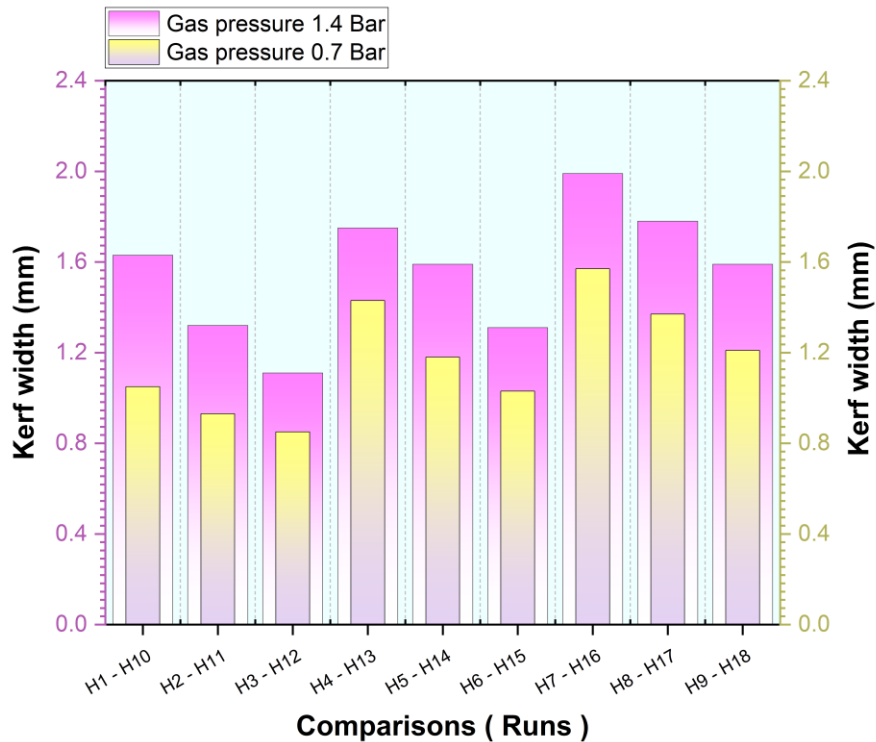


Figure 10. Comparison graph of gas pressures according to kerf width results

As displayed in Fig. 10, although the specimens were cut with the same processing parameters, it is evidently observed that the kerf width values are higher owing to the influence of high gas pressure, which may be explained by the fact that the laser beam concentrated on the metal material penetrates more into the metal material because of the influence of high laser power, resulting in an increase in the molten metal volume. Moreover, as a result of the high pressured oxygen gas penetrating into the same location for a longer period of time and reacting with the metal material, extra energy is generated and with the impact of extra energy obtained, not only HAZ width but also the molten metal volume increases. As a consequence of these situations, kerf widths are negatively affected, resulting in wider kerf widths compared to specimens cut with low gas pressure (i.e., 0.7 Bar). (Guo & Singh, 2021; Kannatey-Asibu, 2023; Steen & Mazumder, 2010; Yu, 1997). On the other hand, when the results given above are evaluated together, it is understood that the most optimum machining parameters for AISI 1040 steels used as workpieces within the scope of this article are gas pressure of 0.7 Bar, laser power of 2400 W and cutting speed of 580 mm/min, respectively.

IV. CONCLUSIONS

In present research article, the influences of laser cutting parameters applied during the machining of AISI 1040 steel workpieces, which are used extensively in contemporary manufacturing industries, were investigated. The results from the experimental research are summarized below:

- ❖ At 0.7 Bar gas pressure, the largest bottom HAZ width value was studied out to be 9.23 mm and the smallest bottom HAZ width value was studied out to be 6.95 mm. This largest bottom HAZ width value was obtained at the parameters of laser power of 2800 W and cutting speed of 380 mm/min, while the smallest bottom HAZ width value was achieved at the parameters of laser power of 2400 W and cutting speed of 380 mm/min.

Considering these largest and smallest bottom HAZ width values, it was studied out that the largest bottom HAZ width value (9.23 mm) was 32.83% larger than the smallest bottom HAZ width value (6.95 mm). The largest top HAZ width value was studied out to be 5.33 mm and the smallest top HAZ width value was found to be 3.11 mm. This largest top HAZ width value was obtained at the parameters of laser power of 2800 W and cutting speed of 380 mm/min, while the smallest top HAZ width value was achieved at the parameters of laser power of 2400 W and cutting speed of 380 mm/min. Considering these largest and smallest top HAZ width values, it was studied out that the largest top HAZ width value (5.33 mm) was 71.39% larger than the smallest top HAZ width value (3.11 mm).

- ❖ At gas pressure of 1.4 Bar, the largest bottom HAZ width value was studied out to be 11.47 mm and the smallest bottom HAZ width value was studied out to be 8.95 mm. This largest bottom HAZ width value was obtained at the parameters of laser power of 2800 W and cutting speed of 380 mm/min, while the smallest bottom HAZ width value was achieved at the parameters of laser power of 2400 W and cutting speed of 380 mm/min. Considering these largest and smallest bottom HAZ width values, it was studied out that the largest bottom HAZ width value (11.47 mm) was 28.19% larger than the smallest bottom HAZ width value (8.95 mm). The largest top HAZ width value was studied out to be 6.79 mm and the smallest top HAZ width value was studied out to be 4.75 mm. This largest top HAZ width value was obtained at the parameters of laser power of 2800 W and the cutting speed of 380 mm/min, while the smallest top HAZ width value was achieved at the parameters of laser power 2400 W and the cutting speed of 380 mm/min. Considering these largest and smallest top HAZ width values, it was studied out that the largest top HAZ width value (6.79 mm) was 42.95% larger than the smallest top HAZ width value (4.75 mm).
- ❖ Considering the largest and smallest top and bottom HAZ width values based on the gas pressures of 0.7 Bar and 1.4 Bar, it was studied out that the largest bottom HAZ width values (i.e., 11.47 mm and 9.23 mm) were 141.47% and 196.78% larger than the smallest top HAZ width values (i.e., 4.75 m and 3.11 mm), respectively.
- ❖ When the average HAZ width values obtained at the gas pressure of 0.7 Bar were checked, it was understood that the largest average HAZ width value was obtained as 7.28 mm at 2800 W laser power. Additionally, it was inspected that at the gas pressure of 0.7 Bar, the smallest average HAZ width of 5.03 mm was obtained at 2400 W laser power. On the other side, when the average HAZ width values obtained at the gas pressure of 1.4 Bar were visually inspected, it was understood that the largest average HAZ width value was obtained as 9.13 mm at 2800 W laser power. Moreover, it was found that at the gas pressure of 1.4 Bar, the smallest average HAZ width of 6.85 mm was obtained at 2400 W laser power.
- ❖ Considering the largest and smallest the average HAZ width values based on 0.7 Bar and the gas pressure of 1.4 Bar, it was found that the largest the average HAZ width values (i.e., 9.13 mm and 7.28 mm) were 33.29% and 44.75% larger than the smallest the average HAZ width values (i.e., 6.85 m and 5.03 mm), respectively. Additionally, as a consequence of the experiments, it was revealed that the average HAZ widths were negatively affected by high gas pressure.
- ❖ Although the specimens were cut with the same processing parameters, it is evidently observed that the kerf width values are higher owing to high gas pressure effect.
- ❖ When the results obtained are evaluated together, it is understood that the most optimum machining parameters for AISI 1040 steels used as workpieces within the scope of the present study are the gas pressure of 0.7 Bar, the laser power of 2400 W and the cutting speed of 580 mm/min, respectively.

STATEMENT OF CONTRIBUTION RATE

Conceptualization, Data curation, Investigation, Methodology, Software, Validation, Visualization, Writing-Original Draft, Writing-review & editing, etc. were performed by Mehmet Şükrü Adin.

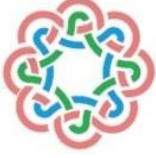
CONFLICTS OF INTEREST

The author declares that I have no known competing financial interests or personal relationships that could have appeared to influence the work reported in this paper.

REFERENCES


- [1] Adin, M. Ş. (2024). Effects of cutting geometries and cutting parameters on the surface roughness and kerf width of X60 steel machined by laser beam. *Journal of Materials Engineering and Performance*, 1-20.
- [2] Amaral, I., Silva, F., Pinto, G., Campilho, R., & Gouveia, R. (2019). Improving the cut surface quality by optimizing parameters in the fibre laser cutting process. *Procedia Manufacturing*, 38, 1111-1120.
- [3] Batishcheva, K., Kuznetsov, G., Orlova, E., & Vympina, Y. N. (2021). Evaporation of colloidal droplets from aluminum–magnesium alloy surfaces after laser-texturing and mechanical processing. *Colloids and Surfaces A: Physicochemical and Engineering Aspects*, 628, 127301.
- [4] Callister, W. D., & Rethwisch, D. G. (2020). *Materials science and engineering: an introduction*: John Wiley & Sons.
- [5] Dieter, G. (1997). *Materials Selection and Design ASM Handbook. ASM International Handbook Committee*, 20.
- [6] Guo, C., & Singh, S. C. (2021). *Handbook of Laser Technology and Applications: Lasers Applications: Materials Processing and Spectroscopy (Volume Three): CRC Press*.
- [7] Gupta, M. K., Singh, G., & Sood, P. K. (2015). Experimental investigation of machining AISI 1040 medium carbon steel under cryogenic machining: a comparison with dry machining. *Journal of the Institution of Engineers (India): Series C*, 96, 373-379.
- [8] Hilton, P. A., Lloyd, D., & Tyrer, J. R. (2016). Use of a diffractive optic for high power laser cutting. *Journal of Laser Applications*, 28(1).
- [9] Kannatey-Asibu, E. (2023). *Principles of Laser Materials Processing: Developments and Applications. John Wiley & Sons, Inc.*, 1-611.
- [10] Karatas, C., Keles, O., Uslan, I., & Usta, Y. (2006). Laser cutting of steel sheets: Influence of workpiece thickness and beam waist position on kerf size and stria formation. *Journal of materials processing technology*, 172(1), 22-29.
- [11] Kardan, M., Levichev, N., Castagne, S., & Dufflou, J. R. (2023). Dynamic beam shaping requirements for fiber laser cutting of thick plates. *Journal of Manufacturing Processes*, 103, 287-297.
- [12] Khdaif, A. I., & Melaibari, A. A. (2023). Experimental evaluation of cut quality and temperature field in fiber laser cutting of AZ31B magnesium alloy using response surface methodology. *Optical Fiber Technology*, 77, 103290.
- [13] Liu, Y., & Zhang, S. (2024a). Improving the cutting process and quality of thick plates with high-power fiber laser. *Optical Fiber Technology*, 83, 103684.
- [14] Liu, Y., & Zhang, S. (2024b). Modeling of separation speed in thick plate cutting with a high-power fiber laser. *Optics & Laser Technology*, 177, 111130.
- [15] Powell, J., Al-Mashikhi, S., Kaplan, A., & Voisey, K. (2011). Fibre laser cutting of thin section mild steel: An explanation of the ‘striation free’ effect. *Optics and Lasers in Engineering*, 49(8), 1069-1075.
- [16] Rao, K. V., Raju, L. S., Suresh, G., Ranganayakulu, J., & Krishna, J. (2024). Modelling of kerf width and surface roughness using vibration signals in laser beam machining of stainless steel using design of experiments. *Optics & Laser Technology*, 169, 110146.
- [17] Salem, H. G., Mansour, M. S., Badr, Y., & Abbas, W. A. (2008). CW Nd: YAG laser cutting of ultra low carbon steel thin sheets using O2 assist gas. *Journal of materials processing technology*, 196(1-3), 64-72.
- [18] Sargar, T., Jadhav, A., & Gautam, N. K. (2023). Experimental study of heat affected zone for CO2 and fiber laser machining of SS 316L material. *Materials Today: Proceedings*.
- [19] Scintilla, L., & Tricarico, L. (2012). Estimating cutting front temperature difference in disk and CO2 laser beam fusion cutting. *Optics & Laser Technology*, 44(5), 1468-1479.
- [20] Shin, J. S., Oh, S. Y., Park, H., Chung, C.-M., Seon, S., Kim, T.-S., . . . Lee, J. (2018). Laser cutting of steel plates up to 100 mm in thickness with a 6-kW fiber laser for application to dismantling of nuclear facilities. *Optics and Lasers in Engineering*, 100, 98-104.
- [21] Steen, W. M., & Mazumder, J. (2010). *Laser material processing. Springer science & business media, Fourth Edition*, 1-577.

- [22] Wu, Z., Liu, Y., Wang, S., Zhang, Y., Li, C., & Zhang, Z. (2024). Research on the influence of laser process parameters on the quality of magnesium alloy laser cutting. *The International Journal of Advanced Manufacturing Technology*, 1-15.
- [23] Wu, Z., Wang, S. J., Zhang, Y., Liu, Y. L., Huang, L. J., & Wu, R. Z. (2023). Effect of Laser Power on Processing Quality of AZ31B Magnesium Alloy. *Journal of Materials Engineering and Performance*, 32(24), 11457-11465.
- [24] Wu, Z., Wang, S. J., Zhang, Y., Xue, B., Yang, C. M., Wan, J. Q., & Song, J. Y. (2023). Effect of Laser Cutting Process Parameters on the Cutting Quality of AZ31B Magnesium Alloy. *Journal of Materials Engineering and Performance*, 32(11), 5201-5210.
- [25] Yu, L. (1997). Three-dimensional finite element modelling of laser cutting. *Journal of materials processing technology*, 63(1-3), 637-639.



RESEARCH ARTICLE

Evaluation of the usability of biodiesel fuels obtained from oils with different free fatty acid ratios in diesel engines in terms of chemical properties

*  Mahmut Uyar

* Siirt University, Technical Sciences Vocational School, Siirt 56100, Türkiye
mahmutuyar@siirt.edu.tr, Orcid: 0000-0002-4981-393X

Citation:

Uyar, M.(2024). *Farklı Serbest Yağ Asidi Oranlarına Sahip Yağlardan Elde Edilen Biyodizel Yakıtlarının, Dizel Motorlardaki Kullanılabilirliğinin Kimyasal Özellikler Açısından Değerlendirilmesi*, Journal of Science Technology and Engineering Research, 5(2): 176-185. DOI: 10.53525/jster.1590794

HIGHLIGHTS

- Biodiesel was produced from two different oils with low and high free fatty acid (FFA) contents.
- The physical and chemical properties of the produced fuels were examined.
- The effects of oil exposure to acid reaction and differences in production processes on engine performance were investigated.

Article Info

Received : 25 Novem. 2024

Accepted : 02 Decem. 2024

DOI:

10.53525/jster.1590794

***Corresponding Author:**

Mahmut Uyar

mahmutuyar@siirt.edu.tr

Phone: +90 484 224 1080

ABSTRACT

In this experimental study, biodiesel production was carried out from two different oils with low and high free fatty acid (FFA) content. The physical and chemical properties of the produced fuels were examined and the aim was to interpret their usability in a diesel engine within the scope of chemical laboratory results. It was determined that the FFA rates of canola and waste vegetable oil were 3.8% and 15.05%, respectively. Acidic pre-neutralization process was performed on the oil with high FFA rate. It was observed that there was a partial decrease in the values such as Density, Viscosity, Heating value and Cetane number of the fuel sample produced with acidic reaction compared to the sample produced with transesterification reaction. It was concluded that the long-chain chemical bond structures of the fuel produced with acid-catalyzed pre-treatment were broken down during the reaction phase. It was determined that this change in the fuel sample did not prevent its usability as fuel in a diesel engine.

Keywords: Vegetable oil, Biodiesel, Diesel engine, Canola oil, Fatty acid



ARAŞTIRMA MAKALESİ

Farklı Serbest Yağ Asidi Oranlarına Sahip Yağlardan Elde Edilen Biyodizel Yakıtlarının, Dizel Motorlardaki Kullanılabilirliğinin Kimyasal Özellikler Açısından Değerlendirilmesi

* Mahmut Uyar

* Siirt Üniversitesi, Teknik Bilimler Meslek Yüksekokulu, Siirt, 56100, Türkiye
mahmutuyar@siirt.edu.tr, Orcid: 0000-0002-4981-393X

Alıntı / Citation :

Uyar, M. (2024). *Farklı Serbest Yağ Asidi Oranlarına Sahip Yağlardan Elde Edilen Biyodizel Yakıtlarının, Dizel Motorlardaki Kullanılabilirliğinin Kimyasal Özellikler Açısından Değerlendirilmesi*, Journal of Science Technology and Engineering Research, 5(2): 176-185. DOI: 10.53525/jster.1590794

ÖNE ÇIKANLAR / HIGHLIGHTS

- Düşük ve yüksek serbest yağ asit (SYA) içeriğine sahip iki farklı yağdan biyodizel üretilmiştir.
- Üretilen yakıtların fiziksel ve kimyasal özellikleri incelenmiştir.
- Yağın asit reaksiyonuna maruz kalmasının ve üretim prosesindeki farklılığın motor performansına etkisi incelenmiştir.

Makale Bilgileri / Article Info

Geliş Tarihi : 25 Kasım 2024

Kabul Tarihi : 02 Aralık 2024

DOI: 10.53525/jster.1590794

***Sorumlu Yazar:**

Mahmut Uyar

mahmutuyar@siirt.edu.tr

Tel: +90 484 224 1080

ÖZET / ABSTRACT

Bu deneysel çalışmada, düşük ve yüksek serbest yağ asit (SYA) içeriğine sahip iki farklı yağdan biyodizel üretimi gerçekleştirilmiştir. Üretilen yakıtların fiziksel ve kimyasal özellikleri incelenerek, dizel bir motorda kullanılabilirliğinin kimyasal laboratuvar sonuçları kapsamındaki yorumlanması amaçlanmıştır. Kanola ve atık bitkisel yağın SYA oranlarının sırasıyla %3,8 ve %15,05 oranlarında olduğu tespit edilmiştir. SYA oranı yüksek olan yağda asidik ön nötrleştirme işlemi yapılmıştır. Asidik reaksiyon ile üretilen yakıt numunesinin, transesterifikasyon reaksiyonu ile üretilen numuneye kıyasla; Yoğunluk, Viskozite, Isıl değer ve Setan sayısı gibi değerlerinde kısmi bir azalma olduğu gözlemlenmiştir. Asit katalizörlü ön işlem ile üretilen yakıtın, reaksiyon aşamasında uzun zincirli kimyasal bağ yapılarının parçalanmış olduğu sonucuna varılmıştır. Yakıt numunesindeki bu değişimin, dizel bir motorda yakıt olarak kullanılabilirliğine engel teşkil etmediği tespit edilmiştir.

Anahtar Kelimeler: Bitkisel yağ, Biyodizel, Dizel motor, Kanola yağı, Yağ asidi

I. GİRİŞ [INTRODUCTION]

Kamu kurum ve kuruluşlarında kullanılan dizel jeneratörler ve ağır tonajlı iş makineleri başta olmak üzere dizel motorlara birçok sektörde etkin bir şekilde ihtiyaç duyulmaktadır. Otomotiv firmaları her ne kadar, içten yanmalı motorlara alternatif olarak hibrid veya tam elektrikli araçları üretme çabası içerisinde olsalar da uzunca bir süre daha dizel motorların sektörde kullanılmaya devam edeceği düşünülmektedir. Çünkü birçok gelişmekte olan ülkenin, elektrik ana şebeke altyapısının yetersiz olduğu bilinmektedir. Kısa süreli araç şarj işlemleri yüksek amper gerektirmektedir. Bu durum, besleme trafolarının ve kablo kesitlerinin yetersiz kalmasına ortam hazırlayarak, ancak kısıtlı sayıda aracın şarj edilebilmesine imkân tanıyacaktır. Bu hususa ek olarak, dizel yakıtlar, mobil güç santrallerinde ve zorlu arazi şartlarında çalışmak zorunda kalan ağır iş makinalarında kullanılmaktadır. Elektrikli motorların belirtilen bu talebe kısa vadede çözüm üretmesi teknik olarak mümkün görünmemektedir. Belirtilen bu açıklamalar doğrultusunda, binek araçlarda kullanılan benzinli motorlar sektör dışı kalacak olsa bile, dizel motorların hayatımızda uzunca bir süre daha yer alacağı düşünülmektedir. Dizel motorların sunduğu yüksek performans ve muhtelif sektörlerdeki vazgeçilmezliği dikkate alındığında, tükenmekte olan dizel yakıtı alternatif oluşturmaktan başka bir çare görülmemektedir. Gerek çevreci olması ve gerek se kolay elde edilebilir nitelikte olması sebebiyle hususları dikkate alındığında biyodizel'in dizel yakıtın alternatifi olacağı değerlendirilmektedir. Dizel motorun tasarımcısının da ilk olarak bitkisel yağları dizel motorda denemiş olduğu gözden kaçırılmamalıdır.

Fosil kaynaklı yakıt rezervlerinin gün geçtikçe azalmaya yüz tutması neticesinde dünya genelinde dizel yakıtı alternatif oluşturabilecek yakıt numuneleri üzerine çalışmalar yapılmaktadır. Bu kapsamda muhtelif bitkisel yağlar [1–3,7], muhtelif hayvansal yağlar [4-6], ve muhtelif atık yağlardan [8-9] biyodizel üretimi yapılabilmektedir. Motor performansının artırılması ve zararlı emisyonlarının minimize edilmesi amacıyla sadece dizel motorlarda değil, aynı zamanda benzinli motorlar üzerinde de araştırmaların sürdürüldüğü anlaşılmaktadır. Benzin yakıtı ile ilgili çalışmalarda çeşitli katkı maddelerinin belirli oranlarda katkı olarak kullanılmasıyla motor performans değerlerinin iyileştiği ve zararlı emisyon değerlerinin minimize edildiği şeklindeki çalışmaların da bulunduğu gözlemlenebilmektedir [10-13]. Hidrojen ve karbon içeriğine sahip olan tüm yağlardan biyodizel üretimi yapılabilmektedir. Ancak üretim prosesinin tespitinde en önemli parametre Serbest Yağ Asit (SYA) oranıdır. SYA oranı %5'in üzerinde olan yağlardan biyosizel üretimi mümkün olmakla beraber proses ve üretimdeki yol haritası değişkenlik göstermektedir. SYA oranı %5'in üzerinde olan yağlarda faz ayrışmasının sağlanabilmesi için asit katalizörlü bir ön reaksiyona ihtiyaç duyulmaktadır. Aksi takdirde yakıt yerine sabun üretilmektedir. Hal böyle olunca biyodizel üretimi öncesinde ilk olarak yapılması gereken işlem SYA tespiti olmalıdır. [14-19].

Bu çalışmanın temel amacı, yüksek SYA oranlarına sahip olan yağların en ekonomik şartlarda nötralleştirilmesi ve nötralleştirme işlemi sonunda üretilen biyodizel yakıtlarının, fiziksel ve kimyasal özelliklerinin geleneksel üretim yöntemleri ile karşılaştırılmasıdır. Elde edilen yakıtların fiziksel ve kimyasal özellikleri laboratuvarında test işlemine tabi tutularak, asit kullanımı ile elde edilen yakıt ile asit kullanılmadan elde edilen yakıtların içerik itibarıyla farklılığı analiz edilmiştir. Bu çalışmanın, özellikle hayvansal ürün kızartması yapan (balık, köfte vb) işletmelerden atık olarak temin edilen yüksek SYA içerikli yağların en etkili ve en ekonomik şekilde nötralleştirmesine hizmet edebileceği değerlendirilmektedir. Diğer taraftan uzunca bir süre rafta beklemiş, acılaşmış ve gıda olarak kullanılabilirliğini yitirmiş olan yağlardaki SYA oranının oldukça yüksek olduğu bilinmektedir. Bu tip yağlarında, bu çalışmada kullanılan asidik nötralleştirme yöntemi ile biyodizel yakıtına dönüştürülebileceği değerlendirilmiştir.

A. Yağ Asit Kompozisyonu

Biyodizel üretiminde kullanılacak olan yağların, yağ asit kompozisyonu farklılık gösterebilmektedir. Bu farklılık motor performansını ve emisyon değerlerini etkilememekle beraber yağın reaksiyona tabi tutulması durumunda ortaya çıkacak olan biyodizel yakıt numunesinin yakıt olarak kullanılabilirliği hususunda ip uçları vermektedir. Üretimde kullanılacak olan yağın, doymuş yağ asit kompozisyonu setan sayısı ile yakından ilişkilidir [20]. Deneysel çalışmada kullanılan yağların oleik ve linoleik asit içeriğinin benzerlik gösterdiği Tablo 1'deki analizler neticesinde anlaşılmaktadır.

Tablo 1. Yağ asit kompozisyonu

Yağ asiti türü	Karbon Bağı	Kanola yağı (%)	Atık Bitkisel yağ (%)
Oleik asit	C18:1	67,39	18,60
Linoleik asit	C18:2	24,61	57,61
Palmitik asit	C16:0	5,59	6,67
Stearik asit	C18:0	1,30	2,90
Palmitoleik asit	C16:1	0,77	0,15
Margarik asit	-	-	-
Linolenik asit	C18:3	0,06	13,77
Miristik asit	C14:0	-	-
Ekosenoik asit	-	0,09	0,17
Araşidik asit	C20:0	0,12	0,13
Heptadesenenoik asit	-	0,09	-
Toplam (%)	-	100	100

II. METARYAL VE METOD [METARIAL AND METHOD]

A. Kullanılan yağların Serbest Yağ Asiti Tayini

DeneySEL çalışma kullanılan yağların SYA tayini yapılırken; yağdan 30 gr ölçüğünde numune alınarak, bu yağın 3'de biri oranında fenol ftaleinin alkoldeki çözeltisi ile karışımı sağlanır, sonrasında ise 0,2 mol ölçüğünde NaOH eşliğinde titrasyon işlemine tabi tutulmaktadır. Kademeli olarak devam ettirilen titrasyon işleminde, yağ numunesi pembeleşme noktasına gelene kadar NaOH dozlaması yapılmaktadır. Şekil 1'deki gibi yağ kendi rengini kaybedip pembe renge bürünene kadar işleme devam edilmektedir. Pembeleşme anındaki dozlama miktarı tespit edilerek, bu miktar asidin mol kütlesi ile çarpılır. Elde edilen sonuç reaksiyonda kullanılan yağın yoğunluğuna bölünerek SYA oranı tespiti yapılmaktadır.



Şekil 1. Yağın SYA değerinin tespitindeki titrasyon işlemi

İki farklı yağ asidi cinsinden deneylerde kullanılacak yağların SYA oranlarının yüzdesel oranları tespit edilmiştir. Bu tespitlere ilişkin sayısal veriler Tablo 2’de sunulmuştur.

Tablo 2. Reaksiyonda kullanılan yağların içeriğindeki SYA oranları

Yağ Numunesi	Stearik asit (%)	Oleik asit (%)
Kanola Yağı	3,80	3,86
Atık Bitkisel Yağ	15,05	14,95

Serbest yağ asidi tayini analizi işlemlerinin sonunda, kanola yağının serbest yağ asit oranının %5’in altında, atık bitkisel yağın ise %15’in üzerinde olduğu tespit edilmiştir. Yapılan analiz neticesinde kanola yağının asidik reaksiyona ihtiyaç duyulmadan sadece baz katalizörlü transesterifikasyon reaksiyonu ile biyodizele dönüştürülebileceği tespit edilmiştir. Ancak atık bitkisel yağın SYA oranının yüksek olması sebebiyle asidik reaksiyona tabi tutulması gerektiği anlaşılmıştır.

Yapılan bilimsel ve akademik çalışmalarda SYA oranı %5’in üzerinde olan yağ numuneleri için iki aşamalı reaksiyona ihtiyaç duyulduğu belirtilmektedir [21-23]. Birinci aşama, asit katalizörlü nötrleştirme işlemi iken ikinci aşamanın standart baz katalizörlü transesterifikasyon reaksiyonu olduğu belirtilmektedir.

B. Kullanılacak yağ numunesinde bulunan nemin sistemden uzaklaştırılması

Asit ve baz katalizörlü reaksiyonlar öncesinde yağın nemden ayrıştırılması reaksiyonun hatasız sürdürülebilmesi için oldukça önem arz etmektedir. Yağ numunesi içerisindeki nemin sabun oluşumuna ve gliserinin ayrıştırılması engel teşkil etmesinin yanı sıra yeni SYA oluşumuna zemin hazırladığı bilinmektedir. Şekil 2’deki görselde sunulan evaporasyon cihazı yardımıyla yağın kimyasal içeriğine zarar vermeden nemin yağdan uzaklaştırılması sağlanmıştır. Bu işlem, çalışmada kullanılacak olan her bir yağ numunesi için gerçekleştirilerek, reaksiyonların ve prosesin standart sapması önlenmiştir.



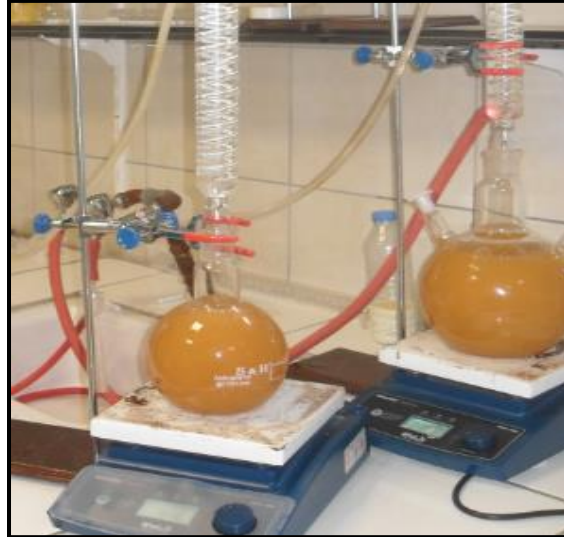
Şekil 2. Kullanılan yağ ve üretilen biyodizelin nemden arındırılması

C. Etil Ester (Biyodizel) üretimindeki ön hazırlıklar

Reaksiyon öncesi yapılan bu çalışmalarda, proses şartlarının eşitliğinin sağlanması amacıyla yapılmış olup reaksiyondaki sıcaklık ve katalizör oranlarının eşdeğerliği sağlanmıştır.

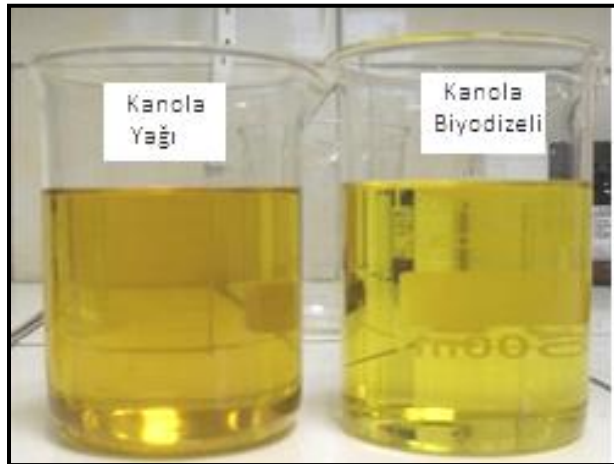
D. Kanola Yağı Biyodizelinin hazırlık aşamaları

500 ml ölçөгindeki kanola yağı, 65 °C ve 600 devir şartlarında reaksiyona tabi tutulmuştur. Katalizör olarak etanol ve NaOH tuzu kullanılmıştır. Şekil 3'te gösterilen deneysel şartlarda reaksiyon işlemi 2 saat süre ile sürdürülmüştür.



Şekil 3. Transesterifikasyon reaksiyonu

Bu araştırma kapsamında, işlemin sonunda elde edilen etil ester (biyodizel) ile ham yağın görsel kıyaslaması Şekil 4'te gösterilmiştir.



Şekil 4. Kanola yağı ve etil esterini

E. Atık Bitkisel Yağı Etil Esterinin (biyodizelin) üretim süreci

Tablo 2.1’de sunulan SYA oranları dikkate alındığında, atık bitkisel yağ içerisindeki %15,05 oranındaki SYA'nın nötrleştirilmesi gerektiği anlaşılmaktadır [24-26]. Yağın kimyasal özelliğinin bozulmaması adına reaksiyonda kullanılacak olan asit miktarının gram cinsinden tespiti ve hesaplamasının yapılması gerektiği tespit edilmiştir. Bu kapsamda, hesaplamalar kütleli olarak tespit edilmiştir.

Atık bitkisel yağın yoğunluk değeri = 0,890 gr/cm³ , diğer bir deyişle 1000ml = 890gr'a karşılık gelmektedir. $890 \times \frac{15,05}{100} = 133,94$ gr SYA olduğu tespit edilmiştir. 133,94 gram SYA'nın nötrleştirilmesi için ihtiyaç duyulan asit miktarının $133,94 \text{ gr} \times 0,01 = 1,339$ gr olduğu tespit edilmiştir. Tespiti yapılan gram cinsinden değer ml cinsine çevrilmesi gerekmektedir. $1,3394 \text{ gr} / 1,841 \text{ gr / ml} = 0,727$ ml olup, 500ml yağ numunesi için ise 0,363 ml asite ihtiyaç duyulmaktadır [14-19].

500 ml ölçөгindeki atık bitkisel yağ, 83 °C ve 400 devir şartlarında asidik reaksiyona tabi tutulmuştur. 100 ml etanol ve 0. 363 ml sülfürik asit eşliğindeki reaksiyon, 5 saat sürdürülmüştür. Reaksiyon bitiminde SYA' içeriğinin ve diğer atıkların alt fazda kaldığı görülmüş olup, ayırma hunisi marifetiyle sistemden uzaklaştırılmıştır. Yapılan son analiz neticesinde %15,05 oranındaki SYA oranının %1.8'e kadar düştüğü tespit edilmiştir. Bu işlemin ardından ikinci reaksiyon olan baz katalizörlü transesterifikasyon reaksiyonu uygulanmıştır. 500 ml ölçөгindeki atık bitkisel yağ, 65 °C ve 600 devir şartlarında ikinci reaksiyona tabi tutulmuştur. Katalizör olarak etanol ve NaOH tuzu kullanılmıştır. Şekil 5.(a)'deki faz ayrıştırması ve Şekil 5 (b)'deki yıkama işleminin ardından buharlaştırma ve filtrasyon işlemi yapılarak Şekil 6'daki şekilde yakıt numunesi depolanmıştır.



Şekil 5. Atık bitkisel yağın; (a) Gliserin ayrışması, (b) Saf su ile yıkama işlemi



Şekil 6. Atık bitkisel yağ ve üretilen (biyodizel) Etil esteri

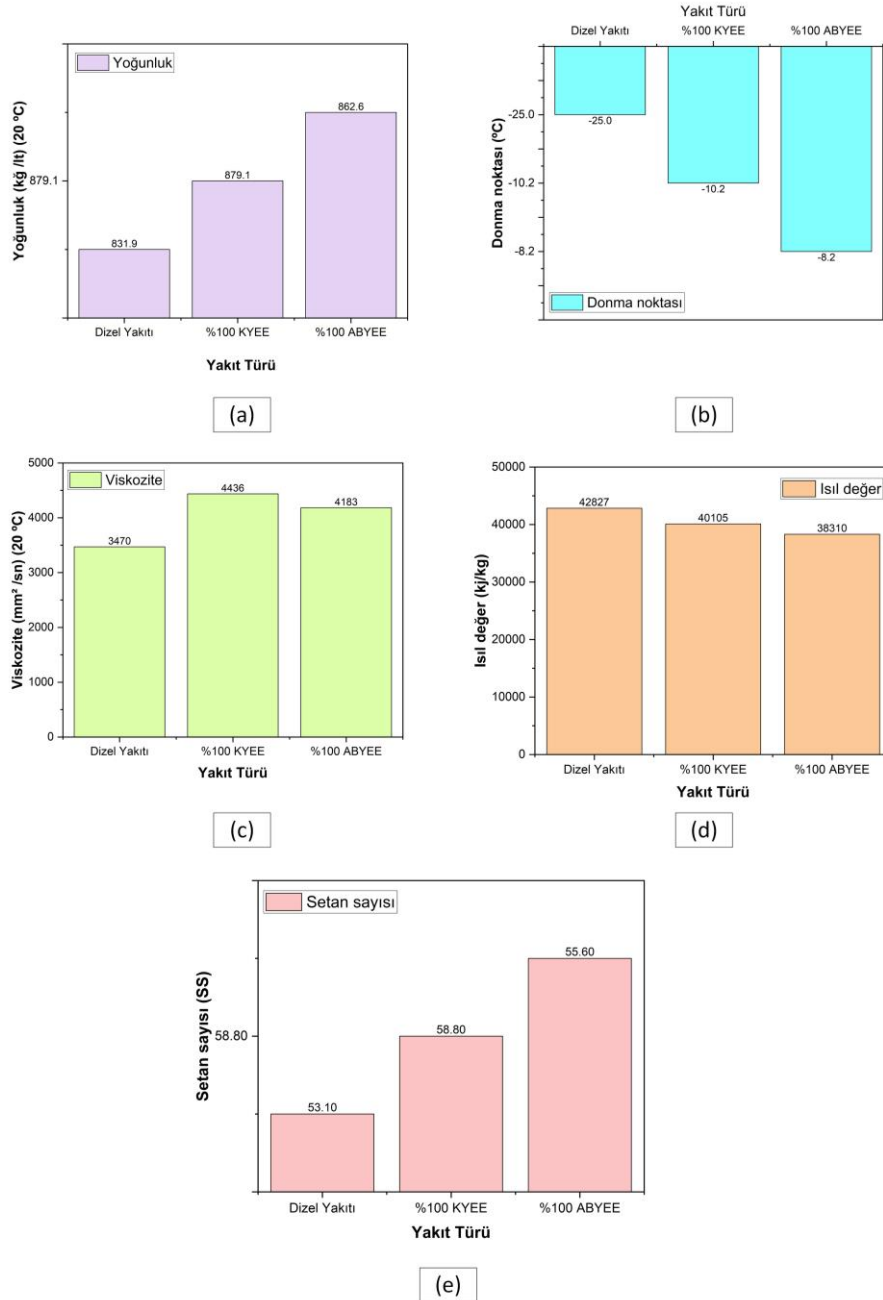
Elde edilen yakıt numuneleri, LİMAK Kurtalan Çimento Fabrikasının Kimya Laboratuvarında ek ücret karşılığında hizmet alınarak ölçülmüştür. Her bir numunenin test işlemi 3 defa tekrarlanmış olup kararlı sonuçların alınmasının ardından tespit edilen değerlerin ortalaması alınarak Tablo 3'teki sonuçlara ulaşılmıştır. Elde edilen analiz sonuçları

sonuç kısmında mütalaa edilmiştir.

Tablo 3. Dizel ve biyodizel yakıtlarının fiziksel ve kimyasal özellikleri analiz sonuçları

Yakıt türü	Yoğunluk (kg /lt) (20 °C)	Viskozite (mm ² /sn) (20 °C)	Isıl değer (kJ/kg)	Donma noktası (°C)	Setan sayısı (SS)
Dizel Yakıtı	831,9	3,470	42,827	-25,0	53,10
% 100 KYEE	879,1	4,436	40,105	-10,2	58,80
% 100 ABYEE	862,6	4,183	38,310	-8,2	55,60

Bu araştırma kapsamında elde edilen Dizel ve biyodizel yakıtlarının fiziksel ve kimyasal özellikleri analiz sonuçları ayrıca Şekil 7’de grafikler olarak sunulmuştur.



Şekil 7. Elde edilen sonuçların grafikleri; (a) yoğunluk, (b) donma noktası, (c) viskozite, (d) ısı değer, (e) setan sayısı

III. SONUÇ VE DEĞERLENDİRME [CONCLUSION]

Bu deneysel çalışmanın sonunda düşük ve yüksek serbest yağ asit içeriğine sahip iki farklı yağdan biyodizel üretimi gerçekleştirilmiştir. Üretilen yakıtların fiziksel ve kimyasal özellikleri incelenerek, dizel bir motorda kullanılabilirliğinin kimyasal laboratuvar sonuçları kapsamındaki yorumlaması amaçlanmıştır.

Deneysel çalışmada; rafine kanola yağı ve Atık bitkisel yağ kullanılmıştır. Kullanılan yağların asit kompozisyonu (oleik ve linoleik içeriği bakımından) benzer özellikler taşıırken, serbest yağ asit içeriği bakımından belirgin farklılıklar olduğu tespit edilmiştir. Gıda mühendisliği ve yağ rafineri tesislerinde SYA ölçümü, Spektroskopi, Gaz kromatografisi, Spektrofotometrik ve Titrasyon yöntemi ile gerçekleştirilmektedir. En ekonomik ve en yaygın olarak kullanılan yöntem titrasyon olarak karşımıza çıkmaktadır. Diğer yöntemlerde maliyetli analiz cihazları kullanılırken titrasyon yönteminde, herhangi bir cihaza ihtiyaç duyulmaksızın en maliyetsiz iki kimyasal olan NaOH tuzu ve etil alkol ile ölçüm ve analizler yapılabilmektedir. Deneysel çalışmalarımızda SYA ölçümlerinde titrasyon yöntemi kullanılmıştır. Fenol ftaleinin alkoldeki çözeltisi ile SYA analizi yapıldığında, Kanola yağında %3,8, atık bitkisel yağda ise %15,05 oranında SYA olduğu tespit edilmiştir. Bu durumda %5'in üzerinde SYA oranına sahip olduğu tespiti yapılan atık bitkisel yağa transesterifikasyon reaksiyonu öncesinde asidik ön nötrleştirme işlemi yapılması gerektiği anlaşılmıştır. SYA varlığında biyodizel üretimi teknik olarak mümkün değildir. Bu sebeple, SYA oranı %5'in altında olan kanola yağı ile biyodizel üretiminde tek aşamalı baz katalizörlü transesterifikasyon yöntemi kullanılırken, SYA oranı %5'in üzerinde olan atık bitkisel yağı ile biyodizel üretiminde önce asit katalizörlü nötrleştirme işlemi ardından ise baz katalizörlü transesterifikasyon yöntemi ile üretim tamamlanmıştır. İki farklı yöntem ile elde edilen biyodizel yakıtlarının, üretim prosesi farklılığından kaynaklı olarak fiziksel ve kimyasal özelliklerindeki değişimin karşılaştırmasının yapılabilmesi için elde edilen biyodizel yakıtları 5 farklı analize tabi tutulmuştur. Bu çalışmada elde edilen yakıt numunelerinin içerik itibarıyla dizel motorlarda kullanılan standart yakıtın fiziksel ve kimyasal özelliklerini taşıyıp taşımadığı araştırılmıştır.

Bu çalışma kapsamında elde edilen yakıtların ASTM standartlarının alt ve üst sınır değer aralığında olduğu yönünde tespit yapılmıştır. Bir sonraki akademik çalışmada, bu çalışmada üretimi yapılan yakıt numunelerinin dizel bir motordaki güç karakteristiğine ve emisyon değerlerine etkisinin araştırılması planlanmaktadır. Asit nötrleştirmesine tabi tutularak 2 aşamalı olarak üretilen biyodizel yakıtının diğer yakıta kıyasla; Yoğunluk değerinde % 2.4, Viskozite değerinde %6.3, Isıl değerinde %4.5 ve Setan sayısında %5.55 oranlarında kısmi bir azalma olduğu gözlemlenmiştir. Bu azalmanın gerekçeleri ise; SYA oranı yüksek olan atık bitkisel yağa, asit katalizörlü ön işlem uygulanmış olması sebebiyle reaksiyon aşamasında uzun zincirli kimyasal bağ yapısına sahip hidrokarbonların kırılma (kraking) olarak tabir edilen parçalanma reaksiyonuna maruz kalmış olması olarak yorumlanmıştır.

KATKI ORANI BEYANI [STATEMENT OF CONTRIBUTION RATE]

Yazarın çalışmadaki katkı oranı %100'dür.

ÇIKAR ÇATIŞMASI [CONFLICTS OF INTEREST]

Yazar ve ilgili kurumlar arasında herhangi çıkar çatışması olmadığını bildirmiştir.

ETİK KURALLARA UYGUNLUK [Compliance With Ethical Rules]

Yazar bu makalenin etik kurul onayı veya herhangi bir özel izin gerektirmediğini beyan eder.

KAYNAKLAR [REFERENCES]

- [1]- Hazar, H., 2009.Effect of biodiesel on a low heat loss diesel engine, Renewable Energy, 34, 1533-1537.
- [2]- Hazar, H., 2008. Kanola metil esterinin dizel motorunun performansına ve emisyon karakteristiklerine etkilerinin belirlenmesi, Doğu Anadolu Bölgesi Araştırmaları, 60-65.
- [3]- Mazed, M.A., 1984. Test of vegetable oil as fuel in direct and indirect injection diesel engine, Ph.D. Thesis, Oklahoma State University, ABD.

- [4]- Behçet, R. ve Çakmak, A.V., 2011. Bir dizel motorda yakıt olarak kullanılan balık yağı metil esteri karışımlarının motor performans ve emisyonlarına etkisi, 6th International Advanced Technologies Symposium (LATS'11), 16-18 Mayıs, Elazığ, Turkey, 161-165.
- [5]- Gürü, M., Koca, A., Can, Ö., Cakir, C. and Şahin, F., 2010. Biodiesel production from waste chicken fat based sources and evaluation with Mg based additive in a diesel engine, *Renewable Energy*, 35, 637-643.
- [6]- Altun, Ş., 2009. Hayvansal yağlardan biyo-yakıt üretimi ve bir dizel motorunda kullanılabilirliğinin deneysel araştırılması, Doktora Tezi, Fırat Üniversitesi Fen Bilimleri Enstitüsü, Elazığ.
- [7]- Budak, N., Bayındır, H., ve Yücel, H.L., 2009. Dizel motorlarda biyodizel kullanımının performans ve egzoz emisyonlar açısından değerlendirilmesi, V. Yenilenebilir enerji kaynakları sempozyumu Diyarbakır 123-130.
- [8]- Hazar, H., 2010. Cotton methyl ester usage in a diesel engine equipped with insulated combustion chamber, *Appl. Energy*, 87, 134-140.
- [9]- Arpa, O., Yumrutaş, R. ve Kaşka, O., 2008. Atık motor yağından elde edilen dizel benzeri yakıtın motor performans ve eksoz emisyonu üzerindeki etkisinin incelenmesi, VII. Ulusal temiz Enerji Sempozyumu, 17-19 Aralık İstanbul, 293-304.
- [10]- Uçkan, İ., Yakın, A., & Behçet, R. (2024). Second law analysis of an internal combustion engine for different fuels consisting of NaBH₄, ethanol and methanol mixtures. *International Journal of Hydrogen Energy*, 49, 1257-1267
- [11]- Yakın, A., & Behçet, R. (2021). Effect of different types of fuels tested in a gasoline engine on engine performance and emissions. *International Journal of Hydrogen Energy*, 46(66), 33325-33338.
- [12]- Uçkan, İ., Yakın, A., Cabir, B. (2024). Investigation the performance of a new fuel produced from the phthalocyanine-gasoline mixture in an internal combustion engine. *International Journal of Hydrogen Energy*, 71, 884-893.
- [13]- Yakın, A., Behcet, R., Solmaz, H., & Halis, S. (2022). Testing sodium borohydride as a fuel additive in internal combustion gasoline engine. *Energy*, 254, 124300.
- [14]- Keskin, A., 2005. Tall yağı esaslı biyodizel ve yakıt katkı maddesi üretimi ve bunların dizel motor performansı üzerindeki etkileri, Doktora Tezi, Gazi Üniversitesi Fen Bilimleri Enstitüsü, Ankara.
- [15]- Gürü, M., Karakaya, U., Altıparmak, D. ve Alıcılar, A., 2002. Improvement of diesel fuel properties by using additives, *Energy Conversion & Management*, 43, 1021-1025.
- [16]- Haas, M. J., Scott, K. M., Marmer, W. N., Foglia, T. A., "In situ Alkaline Transesterification: An Effective Method for the Production of Fatty Acid Esters from Vegetable Oils" *Journal of American Oil Chemists Society*, 81:1, 83-89, 2004.
- [17]- J.M. Marchetti, A.F. Errazu, Esterification of free fatty acids using sulfuric acid as catalyst in the presence of triglycerides, *Biomass and Bioenergy* 32, (2008), 892- 895.
- [18]- Altıparmak D., Keskin A., Koca A. And Gürü M., 2007. Alternative fuel properties of tall oil fatty acid methyl ester-diesel fuel blends, *Bioresource Technology*, 98, 241-246.
- [19]- Naik, M., Meher, L.C., Naik, S.N. and Das, L.M., 2008. production of biodiesel from high free fatty acid karanja (pongamia pinnata) oil, *Biomass and Bioenergy*, 32, 354-357.
- [20]- Alptekin, E. and Çanakçı, M., 2010. Optimization of pretreatment reaction for methyl ester production from chicken fat, *Fuel*, 89, 4035-4039.
- [21]- Reyes, J.F. and Sepulveda, M.A., 2006. PM-10 emissions and power of a diesel engine fueled with crude and refined biodiesel from salmon oil, *Fuel*, 85, 1714-1719.
- [22]- Naik, M., Meher, L.C., Naik, S.N. and Das, L.M., 2008. production of biodiesel from high free fatty acid karanja (pongamia pinnata) oil, *Biomass and Bioenergy*, 32, 354-357.
- [23]- Sharma, Y.C. and Singh, B., 2008. Development of biodiesel from karanja, a tree found in rural India, *Fuel*, 87, 1740-1742.
- [24]- Graboski, M.S. and McCormick, R.L., 1998. Combustion of fat and vegetable oil derived fuels in diesel engines, *Prog. Energy Combust. Sci.*, 24, 125-164.
- [25]- Fukuda, H., Kondo A. and Noda H., 2001. Review biodiesel fuel production by transesterification of oils, *Journal of Biosci. and Bioeng.*, 92, 405-416.
- [26]- Sims, Ralph E.H., 1985, Tallow esters as an alternative diesel fuel, *transactions of ASAE*, 28, 716-721.



RESEARCH ARTICLE

Evaluating the Educational Effectiveness of Radar Systems Laboratory Sessions in the Undergraduate Curriculum

*¹ Bengisu Yalcinkaya, ¹ Mohamed Benzaghta, ² Remziye Busra Coruk, and ³ Ali Kara

*Atılım University, Faculty of Engineering, Electrical and Electronics Engineering Department, Ankara, Turkey
bengisu.yalcinkaya@atilim.edu.tr, [Orcid.0000-0003-3644-0692](https://orcid.org/0000-0003-3644-0692)

¹University Pompeu Fabra, Faculty of Engineering, Department of Information and Communication Technologies, Ankara, Turkey
mohamed.benzaghta@upf.edu, [Orcid.0000-0002-9927-1649](https://orcid.org/0000-0002-9927-1649)

²Atılım University, Faculty of Engineering, Electrical and Electronics Engineering Department, Ankara, Turkey
rbusratezel@gmail.com, [Orcid.0000-0002-9466-3862](https://orcid.org/0000-0002-9466-3862)

³Gazi University, Faculty of Engineering, Electrical and Electronics Engineering Department, Ankara, Turkey
akara@gazi.edu.tr, [Orcid.0000-0002-9739-7619](https://orcid.org/0000-0002-9739-7619)

Citation:

Yalcinkaya, B., Benzaghta, M., Coruk, R.B., Kara, A. (2024) *Evaluating the Educational Effectiveness of Radar Systems Laboratory Sessions in the Undergraduate Curriculum*, Journal of Science, Technology and Engineering Research, (5) 2:186-198. DOI: 10.53525/jster.1571904

HIGHLIGHTS

- A full laboratory module for undergraduate radar systems courses.
- Iterative design of modular radar system as well as fully operational commercial radar platform.
- Educational effectiveness measurement: both quantitative and qualitative assessments of the proposed teaching method.

Article Info

Received: October 22, 2024

Accepted: December 3, 2024

DOI:

10.53525/jster.1571904

***Corresponding Author:**

Bengisu Yalcinkaya
bengisu.yalcinkaya@atilim.edu.tr

Phone: +90 312 586 83 74

ABSTRACT

Introductory courses regarding radar technologies are very popular in the undergraduate curriculum of many electrical and electronics engineering programs. Hands-on experience is crucial for understanding the theoretical concepts covered in lectures. However, acquiring experimental radar systems is often unaffordable, especially for universities in developing countries. This paper presents a detailed description of a cost-effective, easy-to-deploy radar system laboratory sessions and measures the educational effectiveness of the proposed material. The provided radar models allow undergraduate students to grasp the working principles of frequency modulated continuous wave (FMCW) radar systems, as well as assist graduate-level research activities. The educational effectiveness of the laboratory sessions was assessed through both qualitative and quantitative methods, focusing on the proposed learning process and students' performance. The results indicate that the proposed lab sessions have increased the students' understanding of the course topics, and the students' general perception is positive.

Keywords: Educational Technology, Engineering Education, Frequency Modulated Continuous Wave, Radar Systems

I. INTRODUCTION

Research in engineering education has progressed significantly over the years, with rapid technological advancements introducing new teaching and learning methods [1,2]. In faculty of engineering, improving the effectiveness of education is a critical concern, given the complexity of self-learning and the requirement of advanced computational skills [3]. Numerous applications, such as project-based learning, computer-based simulation tools, and hands-on laboratory sessions, have been implemented to enhance traditional teaching approaches [4-6].

Introductory radar technology courses are essential for deepening students' knowledge and equipping them to apply concepts to practical engineering challenges, such as advanced driver assistance systems, autonomous driving, industrial applications, and defense technologies [7]. However, years of teaching experience have revealed a common challenge: students often struggle to apply theoretical radar concepts to real-world scenarios. To illustrate, interpreting the radar baseband signals and reasoning the use of Fourier transform to transfer the echoed signal into range calculations are examples of such concepts that undergraduate students have difficulties understanding. Thus, laboratory sessions designed to complement in-class lectures are essential.

A laboratory model of five training sessions was proposed in [8]. The sessions demonstrate the use of monopulse tracking systems and their use cases in engineering applications. An experimental setup based on the use of commodity WiFi hardware, two commercial panel antennas, and MATLAB signal processing package was presented in [9] to teach amplitude monopulse radar models. In [10], hands-on learning modules were proposed for teaching weather radar applications. The learning modules provide theoretical and practical understanding by allowing students to visualize and analyze weather data. A frequency modulated continuous wave (FMCW) based Synthetic Aperture Radar (SAR) lab model was developed in [11]. Two simple SAR methods were applied on the data obtained from a 24 GHz FMCW radar implemented on a linear drive for educational purposes in [12], and a similar model based on the use of a Vector Network Analyzer was proposed in [13]. In [14], the material described the development and testing of low-cost Inverse Synthetic Aperture Radar (ISAR) turn table system having a machine learning back end. These radar lab models were found to be very useful for both undergraduate and graduate students in their research activities. Also, an X-band lab model of SAR was given in [15]. However, many of these approaches rely on components that are either expensive or not readily available.

A firmware program was given in [16] regarding interactive control of an FMCW ground-penetrating radar (GPR). Students were able to realize control functionalities; for example, selecting the signal period, frequency range, and waveform type of the transmitted signal. Similar methods were proposed in [17,18], in which students built their own radar systems from provided kits of off-the-shelf components and made use of simulation environments to understand the operational concepts of FMCW radars. In [19], the authors presented a phased array, multiple-input, multiple-output radar system built for educational uses. Students were able to build and test those radar systems. A set of RF and Microwave modules that may be accumulated into a short-range modulated scattered radar system was given in [20]. The module blocks were used by students in the senior and graduate level curriculum.

An approach to substitute laboratory experiments with virtual sessions utilizing advancements in computer technology and electromagnetic modeling software was presented in [21]. An Android-based electronic module application having an intuitive graphical user interface was proposed in [22] for science, technology, engineering, and mathematics (STEM) education. The application was used to teach advanced signal processing systems such as Radar, Lidar, and Sonar. The application provided students the ability to determine distances to objects by allowing them to virtually manipulate several signal shapes, signal envelopes, and frequency constraints. In [23], employing a systematic literature review methodology, the necessity of a virtual electronics laboratory to enhance students' learning process is investigated. Along with several research questions, the need for an aeronautical radar simulator to increase the efficiency of learning in education is pointed out. Simulation based experiments are very useful, as they can provide understanding of the physics phenomena's that could be difficult to understand when using a lab-bench approach.

Although simulation-based experiments are attractive due to the advantages mentioned, they cannot replace the hands-on experience of building real radar systems and performing real-time advanced measurements to fully understand the operation concepts of those systems [21]. Different from many examples of hands-on radar laboratory sessions that can be found in literature [8,9,24-26], which rely on extensive and expensive projects, this study presents a laboratory module for undergraduate radar courses that emphasizes cost-effectiveness, ease of deployment, and alignment with lecture topics. The module includes ten laboratory sessions that incorporate both modular radar system design and fully operational commercial radar platforms.

The contributions of this study are as follows: it presents a full laboratory module for undergraduate radar systems courses, consisting of ten laboratory sessions which are structured based on the lecture topics. The proposed laboratory structure includes iterative design of modular radar system as well as fully operational commercial radar platform. Importantly, unlike previous studies, this paper evaluates the educational impact of the proposed materials on students' success using both qualitative and quantitative assessments. The findings offer new insights into the effectiveness of radar laboratory sessions.

The rest of the paper is organized as follows: In section 2, the proposed laboratory sessions are described along with the quantitative and qualitative measurement methods regarding the effectiveness of the developed materials. In section 3, we provide the results of the assessments. Finally, section 4 draws conclusions and points out potential future work.

II. MATERIALS AND METHODS

In this section, we provide a detailed description of the two different radar system setups that have been used in the laboratory sessions, followed by an explanation of the objectives and the methods used for each session.

A. Experimental Setups

Laboratory sessions based on FMCW radar systems are examples of real-world applications, invested in extensive physical and mathematical contents. The laboratory sessions focus on FMCW radar systems, which emphasize frequency-domain operations over conventional time-domain methods. Therefore, spectral and phase analyses are needed to determine the range and velocity of a variety of targets. Thus, to proceed with the laboratory sessions, students are introduced to signal processing topics such as Fourier transform, sampling as well as amplifiers and filters. In the proposed laboratory structure, two different types of FMCW radars were used;

- Radar-I: A fully modular system operating in 4.4-4.9 GHz band.
- Radar-II: A commercial radar platform operating at 77-81 GHz band.

The former is intended to develop module/component level RF design of a radar system while the latter aims to develop signal analysis, functionality as well as operational aspects of a radar system.

1) Radar-I

A low-cost modular FMCW radar system has been developed at our university's Radio Research Laboratory (RRL) for research and educational purposes [27]. It consists of key components such as a voltage-controlled oscillator (VCO) for signal generation, a DC power supply for offset voltage adjustment, a splitter, a mixer, a low-pass filter (LPF), a low-noise amplifier (LNA), and a power amplifier. Operational testing has been done in the university laboratory, using metal plates as targets. The received signals are analyzed by using a spectrum analyzer (SA). Radar-I operates with a bandwidth of 525 MHz, offering a 30 cm range resolution. In Figure 1, the prototype of the radar is shown along with the manufacturer code numbers.

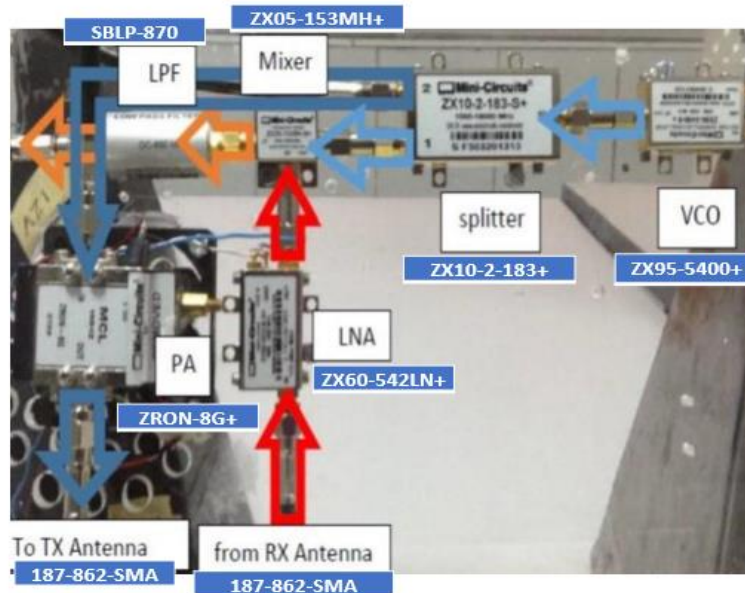


Figure. 1. Radar-I Modular FMCW radar system.

2) *Radar-II*

A commercial-of-the-shelf (COTS) millimeter wave (mmWave) FMCW radar system, has been used as the second type of radar in the proposed laboratory sessions. The radar platform consists of an AWR1642BOOST evaluation module which has two transmit and four receive PCB antennas, also a DCA1000EVM data capture card that is connected to the PC for post-processing using the mmWave Studio program. The radar system operates with 4 GHz available bandwidth, allowing users to employ different applications, i.e., radar cross section (RCS) measurements, range determination, and velocity and angle estimations [28]. In Figure 2, the functional block diagram of AWR1642 is shown. As shown in the figure, the individual modules used in Radar-I are compactly integrated in Radar-II, providing students with insights into diverse radar configurations.

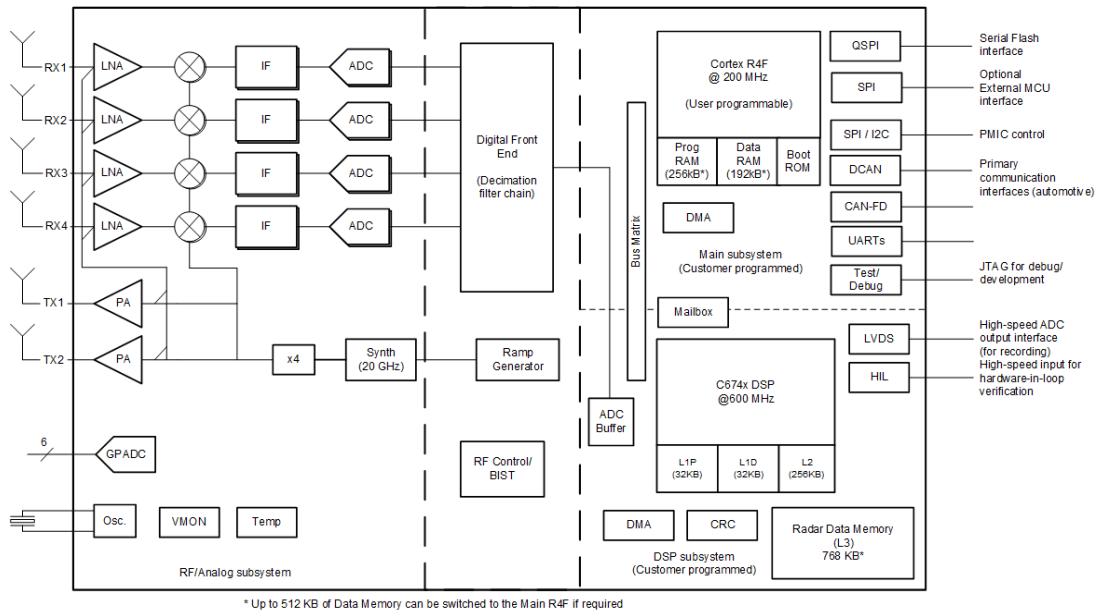


Figure. 2. Functional Block Diagram of Radar-II [29].

B. Laboratory Sessions

In the laboratory sessions, two types of radar systems described previously, and their modular components are used for teaching fundamental and advanced concepts. While Radar-I is used in sessions from 1 to 8, Radar-II is featured in sessions 9 and 10. Students are first introduced to each of the modular components which were used to build the FMCW radar, as described in sessions from 1 to 5. Later, understanding the use of the complete radar system and performing experimental measurements are done in sessions from 6 to 8. The last two experiments (9-10) introduce the compact commercial off-the-shelf radar version of the previous experiments. Laboratory experiments and course videos are shared online to enhance accessibility [30]. The details of the lab session are as follows:

1) *FMCW radar waveform generation*: Understanding the operation of Voltage Control Oscillator (VCO), FMCW signal generation using VCO, and experimental analysis of FMCW signals in the frequency domain are performed in this lab session. VCO is connected to the DC voltage supply and an analog wave generator. These are adjusted to tune with the frequency in the range of 4200 MHz to 4600 MHz. The output is connected to a SA to see the generated FMCW signal in the frequency domain.

2) *Up/Down conversion*: Understanding frequency mixing in FMCW Radar systems, and experimental analysis of the use of the mixer for down conversion are given in this lab session. The original signal to be down converted is at 4272-4600 MHz band. The aim is to obtain a down-converted signal at a frequency over 272-600 MHz. The original signal is transmitted using the VCO and applied to the RF input port of the Mixer. A signal generator is used to transmit a signal of frequency 4000 MHz to the LO input port of the Mixer. The output (IF port of the Mixer) is connected to an SA in order to observe the down converted signal spectrum.

3) *Amplification and attenuation*: Experimental analysis of Power Amplifiers (PA) and Low Noise Amplifiers (LNA) for use in FMCW radar systems and understanding of amplification and attenuation of RF signals are implemented in this lab session. The experimental setups are given in Figure 3. The experiment is conducted in two parts using PA and LNA, separately. Experimental setups are set up to observe the power of the signal. This process is repeated for different bandwidths and for different attenuator values (e.g., 3 dB, 10 dB, and 15 dB).

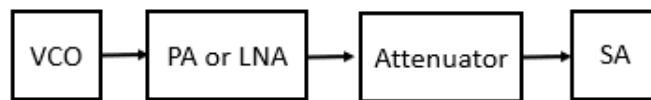


Figure 3. Amplification and attenuation experimental setup for PA and LNA.

4) *Signal mixing and filtering*: Analysis of the use of the combination of a mixer and an LPF in FMCW radar systems is performed in this lab session. By repeating the procedures in Experiment 2, an IF signal is obtained at the mixer output. The presence of harmonics beyond the desired wideband down-converted signal (270-783 MHz) is interpreted. On the other hand, the output of the mixer is connected to LPF. Results are compared using SA to understand the effect of the LPF.

5) *Antennas, connectors, and cabling*: Basic concepts regarding antenna gain and connectors/cabling loss are covered in this lab session, as well as analysis of the radio link in terms of link budget. The experimental setup of this experiment is given in Figure 4. In this experiment, the received signal power is going to be recorded from the SA for different separation distances between the two antennas, as well as for different frequency bands. Finally, the theoretical values of the received signal power are compared with the experimental values. The difference margins between the theoretical and experimental results are discussed and analyzed.

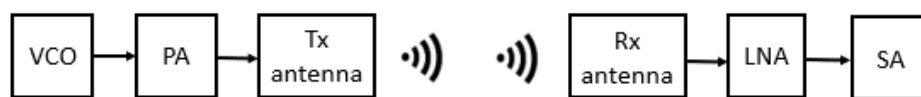


Figure 4. Experimental setup for radio link.

6) *Modular transmitter design:* The modular transmitter design used for the FMCW radar system is explained in this lab session. Furthermore, the experimental analysis regarding determining the radar range is performed. Using the recorded received signal on the SA at different distances, the link budget equation is written and all the losses (cable, connectors, channel, etc.) are estimated. The bandwidth of the FMCW signal is determined such that the range resolution is 30 cm. The range resolution formula is given as $d_{res} = c/2B$ where B is the bandwidth of the signal and c is the speed of the light. The maximum distance between the Tx and Rx has been estimated such that the peak power to noise power level is higher than 25 dB.

7) *Modular receiver design:* The modular receiver design used for the FMCW radar system is given in this lab session. Additionally, determining the RCS of a reflector plate is measured by performing an experimental demonstration to the students. The experimental setup is given in Figure 5. The FMCW radar used in this experiment is a monostatic radar system. In this experiment, the received signal power is recorded from the SA for different separation distances between the radar and the target. Using the radar range equation formula given in (1), the RCS (σ) of the target at every distance of observation is estimated.

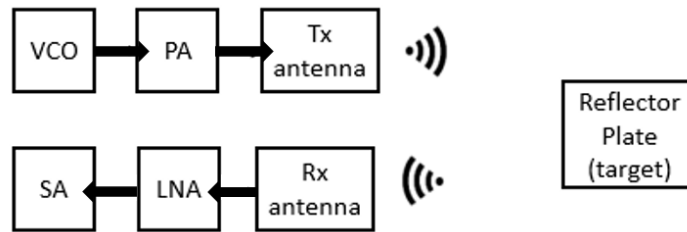


Figure 5. Experimental setup for radio link with reflector.

$$R_{max} = \left(\frac{P_t G^2 \lambda^2 \sigma}{(4\pi^3) S_{min}} \right)^{\frac{1}{4}} \quad (1)$$

where R_{max} refers to the distance that the received power is measured at, S_{min} is the recorded received power from the SA, P_t is the transmitted power, G is the gain of each antenna, and λ is the wavelength at the desired frequency.

8) *Modular radar design:* This lab session focuses on explaining the complete modular FMCW radar design given in Figure 1, as well as performing several experimental analyses for determining the range of targets. The target used in the monostatic radar system is a metallic plate (reflector plate) to be placed at four different ranges. The measurement of the beat frequency, $f_b = 4BR/cT_m$ which gives the range information is recorded from the SA and is compared with the theoretical value. Also, the presence of frequency offset due to the cables and connectors is discussed. In the later equation, B is the modulation bandwidth and T_m is the period of triangular signal (modulation period) [31].

9) *Introduction to TI mmWave Radar Platform:* Understanding of the TI mmWave radar platform [32], its hardware components, and the radar parameters that affect the practical RCS measurement of a target are discussed in this lab session. The combination of the AWR1642 radar module and the DCA1000 data capture is used. The platform transmits an FMCW signal via two transmitters and it receives back the echoed signal via four separate receiving channels. The received signal is presented in the form of complex I/Q at Intermediate Frequency (IF) band. The signal is transferred to a computer and the processed data is acquired using the mmWave studio program. The settings and calculations of the radar parameters and their association with each other are discussed [33], and the measurement of the target RCS is performed.

10) *TI mmWave radar platform:* Understanding the configuration parameters of an FMCW radar according to the maximum range, best range resolution scenarios, and RCS measurements of different objects are demonstrated in this session. With the calculation of the chirp signal parameters, several experiments based on different scenarios are conducted. Measurements of targets at different distances are conducted considering the maximum range equation

given in (3) and the measurement of the range resolution is also performed to see the ability of distinguishing two objects close to each other.

$$d_{max} = \frac{c * f_{ADC_{sampling}}}{2 * S} \tag{2}$$

where $f_{ADC_{sampling}}$ is the Analog Digital Converter (ADC) sampling frequency and S is the slope of the transmitted chirp. Finally, the relationship between the maximum range and the range resolution is considered based on the theoretical formulas.

At each of the lab sessions, a detailed repetition of the theoretical foundations which were given in the course lectures is given to the students. These are followed by practical exercises and in-lab quizzes which the students must work on. Finally, a short oral quiz is given toward the end of the lab sessions to determine the students' understanding of the topic. Additionally, students' perceptions of the contribution of the experiments are evaluated based on interviews and anonymous surveys.

C. Assessment Methods

The effectiveness measurement of the proposed laboratory activities is conducted using several qualitative and quantitative assessments, including face-to-face interviews, anonymous surveys, quizzes, along with the course exam results. Figure 6 represents the flowchart of the material preparation and assessment process. After the feedback from the assessments is collected and analyzed, deficiencies in the proposed laboratory activities are corrected and the material is improved. When the material is completed, the results are presented, and the process is finalized.

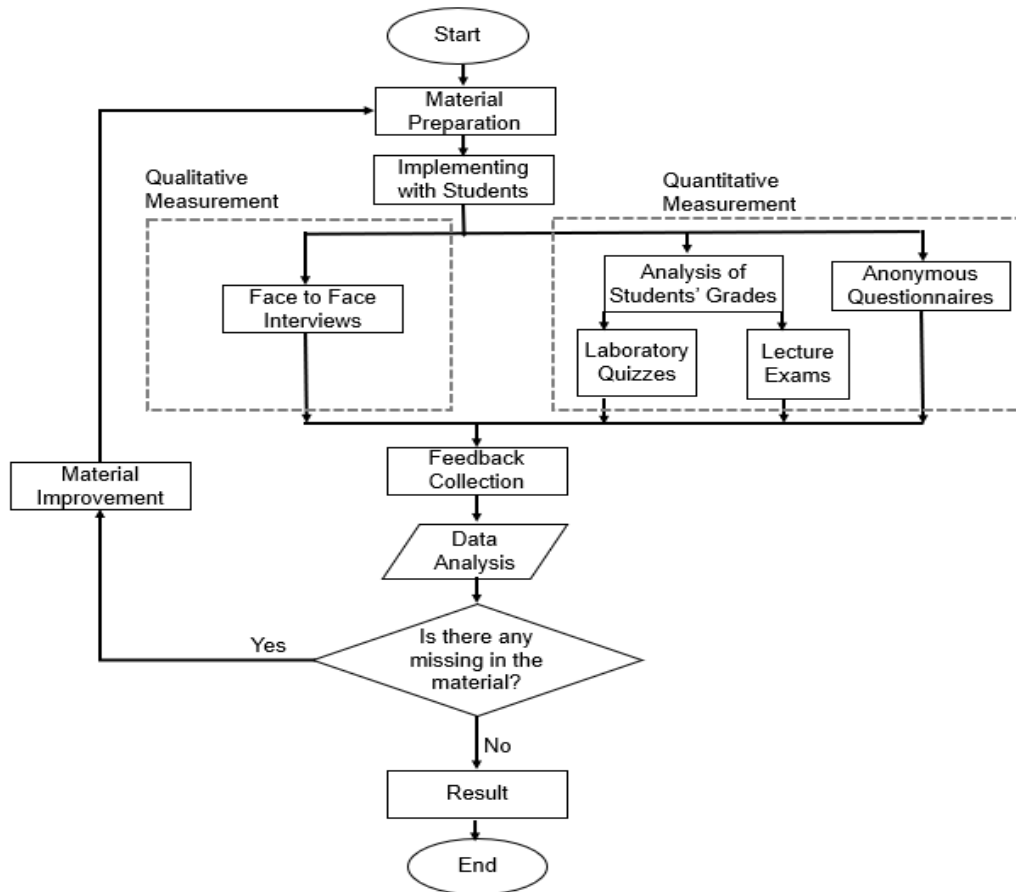


Figure. 6. Flow chart of the educational method.

The key assessment methods are as follows:

1) *Interviews*

At the beginning and middle of the semester, two different face-to-face interviews were done with the students. Interviews were conducted based on the contribution of the laboratory sessions to the students' learning process and how their perceptions changed during the course.

2) *Anonymous Surveys*

A total of three anonymous surveys containing both a five-point Likert scale and open-ended questions were conducted at the beginning, middle, and end of the semester (Survey-1, Survey-2, and Survey-3, respectively). Survey-1 was an introductory survey aiming to analyze the educational background and general skills of the students. It included questions about gender, age, cumulative GPA, knowledge/background about probability and random processes, communication systems, and signals and systems courses. Additionally, the evaluation of the ability to use laboratory equipment such as a SA, waveform generator, and oscilloscope was asked. Finally, opinions about the contribution of the laboratory sessions to their learning process and the purpose/expectation of taking the radar systems course were noted. Survey-2 and 3 aimed at obtaining information regarding the students' progress during the semester. Questions were asked aiming to observe the quality of the proposed educational method and its contribution to the learning process.

3) *Laboratory Quizzes*

An online pre-quiz was given to encourage students to study for the experiment before coming to the laboratory sessions. In the lab, two quizzes were done, one of them being before the experiment (pre-test) and the other after (post-test). This is done to continuously measure the contribution of the laboratory activities to the student's learning process. In addition, during the experiments, it was ensured that the students participated in the experiments and reinforced the subject with short oral questions.

III. RESULTS AND DISCUSSION

A comprehensive analysis of the qualitative and quantitative assessments including face-to-face interviews, anonymous surveys, and achievements on both the quizzes and exams are conducted.

A. Interviews

The first interview was applied after the second experiment. In the first interview, students were asked to evaluate the workload of the course, the provided course materials, and resources, as well as their perceptions regarding the first two experiments. Additionally, it was asked what the pros and cons of the proposed applied course material were, and how they related the experiments with the theory covered in the lectures. While students noted that the workload was heavier compared to other technical electives, they acknowledged improved comprehension of the course topics. Most of the students found that the course materials provided were sufficient and helpful enough. The common expectation from the laboratory activities is to learn the working principles of radars and to have knowledge of designing and operating radars in a simple way. As a matter of fact, it was the black spot of the lecture and the motivation of the authors. Also, they stated that the lab manuals were instructive and helped them in their learning process. They praised the lab manuals as instructive and the lab quizzes as effective in encouraging consistent study habits. They agreed that the first two experiments formed the basis of the first lectures and the laboratories helped them to visualize their theoretical background. Moreover, they added that the relation between mathematical equations and the practical applications had become clearer. They stated that they have obtained hands-on experience on how to use an oscilloscope, signal generator, waveform generator, and SA. After the second laboratory session, they stated that they completely understand the concept of up/down conversion which they had been taught in several different courses before.

The second interview was conducted after the sixth experiment. In the second interview, the workload was asked again. It was found that the students do not think that the workload is heavy for them anymore. They emphasized

once again that they found the course resources provided sufficient. They stated again that the logic of the lessons was understood together with the experiments. They confirmed that the experiments are understandable, and the content is adequate and supplementary. Also, they highlighted that the laboratory activities are strongly related to the lectures and had a great impact on the learning process. Observing each component individually, and then combining them to obtain a fully operating radar system is what the students found to be the best about the laboratory activities.

B. Anonymous Surveys

In the first survey, the average CGPA of the class was found as 3,15. The average letter grade of the probability and random processes course, and communication systems course was BB. Students are asked to score the course materials on a five-point Likert scale (1: absolute insufficient, 5: absolute sufficient), the average result was found as 4,1. The ability to use the hardware laboratory equipment was asked again as in interviews, all of the students indicated that they know how to use them. The general contribution of other courses' laboratories in the past 4 years to the students' learning process is asked and 66% of the class graded this question as 5. It can be said that students' opinion about the general laboratory activities is quite positive. Students' expectations from the radar systems course are asked. The following comments were reported by some of the students:

- "I enjoyed the signals and systems and the communication systems courses. So, I believe I will be successful in the radar systems course."
- "I want to gain knowledge about radar systems and perform a simple radar design."
- "I am currently interested in the RCS applications. I think this course will be helpful for this."
- "I want a career in which I can advance in the defense industry in the future."

In the second survey, the content of the course and the laboratory were investigated individually. The list of the items asked for in the survey and the mean values of each item are presented in Table 1. All the students attended the lectures and the experiments regularly. From Table 1, we can say that they were quite satisfied with the content and the materials of the course. Similar questions were asked in both the course and experiment assessments to observe the consistency of the scores. Students gave the lowest score on the face-to-face quizzes for both the course and the laboratory, which is understandable since they are more challenging than online quizzes. Also, students found that the contribution of the experiments to their learning process was notably sufficient. The ability to relate the theory to the experiments was asked both in the course and the experiment assessments. A large majority of the students graded that item as 5 with reasonable consistency. Their overall comments were also asked in the survey. While some of them criticized taking pre and post-quizzes every week, a large majority of them found that the quizzes were helpful, and they stated that they came prepared for the lectures and experiments and it made the topic more understandable for them.

The questions asked in the final survey and the mean values of each question (out of 5) are given in Table 2. After the low grading of face-to-face post-tests in Survey-2, the students were asked regarding it, and it has been observed that the score given to this item has increased both for the course and the laboratory activities.

The score of the contribution of the laboratory activities to the students' learning process showed consistency with Survey-2. However, when the difficulty of the course and the experiments were asked, the average score showed up as equal. From these results, we can say that the hands-on experiments were quite effective in terms of the contribution to the students learning of the radar systems course, especially in the introductory levels. When their perception about whether they have obtained enough knowledge about the radar systems was asked, a decrease is observed in the average score compared to Survey-2. The final answers can be considered more realistic as they learn more, they realize there is more to learn.

Table I. Survey-2

Item Asked	Avg. score	
About the course	1. Content of the course:	4,4
	a. Information about theory.	4,2
	b. The relationship between theory and experiments.	4,5
	c. Contribution of the course to the learning process.	4,5
	2. Visuals of course videos.	4,7
	3. Audio of course videos.	4,7
	4. Do you consider yourself having enough knowledge about radar system course?	4,3
About the experiments	5. Contribution of online quiz for theory (pre-test) to your learning process.	4,5
	6. Contribution of face-to-face quiz for theory (post-test) to your learning process.	3,3
	7. How many courses did you attend? (L1-L5)	4,7
	1. Content of the experiments:	4,5
	a. Information about theory.	4,3
	b. The relationship between theory and experiments.	4,7
	c. Contribution of experiments to your learning process.	4,5
2. Visuals of experiment videos.	4,5	
3. Audio of experiment videos.	4,3	
4. Do you consider yourself having enough knowledge about experiments?	4,7	
5. Contribution of online quiz for experiment (pre-test) to your learning process.	3,5	
6. Contribution of face-to-face quiz for experiment (post-test) to your learning process.	4,8	
7. How many experiments did you attend? (Exp1-Exp10)	4,5	

Table II. Survey-3

Item Asked	Avg.	
General Questions	1. What is the contribution of the course videos, pre-test and post-tests to your learning process?	3,7
	2. What is the contribution of the lab experiments, laboratory pre-tests and post-tests to your learning process?	4,0
	3. Evaluate the difficulty of the course.	3,4
	4. Evaluate the difficulty of the experiments.	3,4
	5. Evaluate whether you were able to spend enough time to learn the course.	4,3
	6. Evaluate whether you were able to spend enough time to learn the experiments.	4,4
	7. Considering the scope and topics of the course, do you think you have learned radar systems?	3,6
	8. How useful did you find the experiments?	4,1

C. Laboratory Quizzes

It is aimed to evaluate the performance of the new educational method by comparing the GPA of the students in the last three terms. When the average of the students' grades is observed in the 3rd term, during which the proposed laboratory activities were applied, a significant increase is observed as can be seen from Table 3. It should be noted

that the difficulty level, content, and types of questions on the exams of the course were the same for all 3 terms. In the 1st and 2nd terms, only Radar-I was used in the experiments, while in the 3rd term, by adding Radar-II, students had the chance to work on different radar modules. In the first term's laboratory, 5 experiments which are a combination of the first 8 experiments mentioned earlier were conducted. In the last term, the full 10 laboratory activities were carried out. For each experiment, both the online and in-class pre-tests along with in-class post-tests were given to the students. The average grade for the laboratory online pre-tests is 85,8 and for the in-class pre-tests was 71,9. Although the control of the students is a challenging issue in online exams, no significant difference is observed between the online and in-class quizzes. The average grade of the post-tests applied after each laboratory activity was 79,9. We observed that most of the class came to the laboratories prepared, and they followed the experiments during the session. Also, a question-based assessment was conducted for the laboratory quizzes. It was seen that the average score of the class regarding the questions that evaluate the ability to relate theory to practice was 81,1. In the first 5 experiments, the main components of a radar system such as VCO, mixer, LPF, antennas, connectors, and cables were introduced, and their operation principles were discussed. At each laboratory session, a new component was added to the system and its output was observed. The total average of the exam results regarding these experiments is 84,4. In the following three experiments, all the individual components are combined, and a modular structure of the transmitter and the receiver is obtained. Various radar ranges, RCS, and link budget experiments are conducted. The total average exam result regarding these experiments is 74,06. A decrease is observed according to the first five experiments since the students are expected to use their theoretical knowledge more as the content of the course develops further. The last two experiments cover a COTS ready-to-use radar in a compact form. This radar platform was quite different from what they have worked on so far in terms of principle and platform. However, the total average of the exam results regarding these experiments was 73,93 not so different than the previous average. Thus, it was observed that students were able to adapt very easily and learn the working logic faster when they encountered different radar types.

Table III. Grades

Exams	1st Term	2nd Term	3rd Term
Laboratory Average	53,3	81,3	77,0
Course Quiz Average	56,5	55,7	74,2
Midterm Average	51,5	67,0	60,1
Final Average	46,7	40,7	67,7
Grade Average	52,7	58,6	71,4

IV. CONCLUSION

In this paper, a laboratory for the radar systems course and a methodology for measuring its effectiveness are presented. Ten radar lab sessions are designed to give a comprehensive understanding of the theoretical topics covered in the course. By understanding the radar components one by one in each session, the theoretical knowledge of the students based on radar systems is examined experimentally. Students gain experience in radar design and operation when the final system is shown. Then, with a different radar structure, students showed their ability to adapt by using their previous hands-on experience. To measure the effectiveness of these laboratory activities in the students' learning, both qualitative and quantitative assessments are employed. Considering the assessments, the proposed applied course material has affected the students' success level positively. In addition, the perception of the students regarding the lab structure and material was found satisfactory.

STATEMENT OF CONTRIBUTION RATE

Authors' contribution rates to the study are equal.

CONFLICTS OF INTEREST

They reported that there was no conflict of interest between the authors and their respective institutions.

RESEARCH AND PUBLICATION ETHICS

In the studies carried out within the scope of this article, the rules of research and publication ethics were followed.

REFERENCES

- [1] Sianez, D. M., Fugère, M. A., & Lennon, C. A. (2010). Technology and engineering education students' perceptions of hands-on and hands-off activities. *Research in Science & Technological Education*, 28(3), 291-299.
- [2] Vásquez-Carbonell, M. (2022). A systematic literature review of augmented reality in engineering education: Hardware, software, student motivation & development recommendations. *Digital Education Review*, 41, 249-267.
- [3] Wankat, P. C., & Oreovicz, F. S. (2005). Teaching prospective engineering faculty how to teach. *International Journal of Engineering Education*, 21(5), 925.
- [4] Gokdogan, B. Y., Coruk, R. B., Benzaghta, M., & Kara, A. (2023). A hybrid-flipped classroom approach: Students' perception and performance assessment. *Ingeniería e Investigación*, 43(3), 16.
- [5] Singh, J., Perera, V., Magana, A. J., Newell, B., Wei-Kocsis, J., Seah, Y. Y., & Xie, C. (2022). Using machine learning to predict engineering technology students' success with computer-aided design. *Computer Applications in Engineering Education*, 30(3), 852-862.
- [6] Coruk, R. B., Yalcinkaya, B., & Kara, A. (2020). On the design and effectiveness of simulink-based educational material for a communication systems course. *Computer Applications in Engineering Education*, 28(6), 1641-1651.
- [7] Coruk, R. B., Gokdogan, B. Y., Benzaghta, M., & Kara, A. (2022). On the classification of modulation schemes using higher order statistics and support vector machines. *Wireless Personal Communications*, 126(2), 1363-1381.
- [8] Diewald, A. R., Wallrath, P., & Müller, S. (2018, September). Five radar sessions for university education. In *2018 48th European Microwave Conference (EuMC)* (pp. 456-459). IEEE.
- [9] Poveda-García, M., López-Pastor, J. A., Gómez-Alcaraz, A., Martínez-Tamargo, L. M., Pérez-Buitrago, M., Martínez-Sala, A., & Gómez-Tornero, J. L. (2018, September). Amplitude-monopulse radar lab using WiFi cards. In *2018 48th European Microwave Conference (EuMC)* (pp. 464-467). IEEE.
- [10] Chilson, P. B., & Yearly, M. B. (2011). Hands-on learning modules for interdisciplinary environments: An example with a focus on weather radar applications. *IEEE Transactions on Education*, 55(2), 238-247.
- [11] Ali, T., & Burki, J. (2016, December). Design and development of X-band FMCW based lab model of Synthetic Aperture Radar (SAR) for applications in engineering education. In *2016 19th International Multi-Topic Conference (INMIC)* (pp. 1-6). IEEE.
- [12] Berg, J., Müller, S., & Diewald, A. R. (2022). Far-and near-range measurements with a synthetic aperture radar for educational purposes and comparison of two different signal processing algorithms. *Advances in Radio Science*, 19, 221-232.
- [13] Burki, J., Ali, T., & Arshad, S. (2013, December). Vector network analyzer (VNA) based synthetic aperture radar (SAR) imaging. In *INMIC* (pp. 207-212). IEEE.
- [14] Blomerus, N. D., Cilliers, J. E., & de Villiers, J. P. (2020, April). Development and testing of a low-cost audio-based ISAR imaging and machine learning system for radar education. In *2020 IEEE International Radar Conference (RADAR)* (pp. 766-771). IEEE.
- [15] Charvat, G. L., & Kempel, L. C. (2006). Synthetic aperture radar imaging using a unique approach to frequency-modulated continuous-wave radar design. *IEEE Antennas and Propagation Magazine*, 48(1), 171-177.
- [16] Chizh, M., Pietrelli, A., Ferrara, V., & Zhuravlev, A. (2017, November). Development of embedded and user-side software for interactive setup of a frequency-modulated continuous wave ground penetrating radar dedicated to educational purposes. In *2017 IEEE International Conference on Microwaves, Antennas, Communications and Electronic Systems (COMCAS)* (pp. 1-5). IEEE.
- [17] Charvat, G. L., Fenn, A. J., & Perry, B. T. (2012, May). The MIT IAP radar course: Build a small radar system capable of sensing range, Doppler, and synthetic aperture (SAR) imaging. In *2012 IEEE Radar Conference* (pp. 0138-0144). IEEE.
- [18] Luttamaguzi, J., Eslami, A., Brooks, D. M., Sheybani, E., Javidi, G., & Gabriel, P. M. (2017). Using simulations and computational analyses to study a frequency-modulated continuous-wave radar. *International Journal of Interdisciplinary Telecommunications and Networking (IJITN)*, 9(1), 38-51.
- [19] Perry, B. T., Levy, T., Bell, P., Davis, S., Kolodziej, K., O'Donoghue, N., & Herd, J. S. (2013, October). Low-cost phased array radar for applications in engineering education. In *2013 IEEE International Symposium on Phased Array Systems and Technology* (pp. 416-420). IEEE.
- [20] Campbell, R. L., & Pejcinovic, B. (2015, September). Project-based RF/microwave education. In *2015 10th European Microwave Integrated Circuits Conference (EuMIC)* (pp. 456-459). IEEE.
- [21] Hum, S. V., & Okoniewski, M. (2007). A low-cost hands-on laboratory for an undergraduate microwave course. *IEEE Antennas and Propagation Magazine*, 49(3), 175-184.
- [22] Robistow, B., Newman, R., DePue, T. H., Banavar, M. K., Barry, D., Curtis, P., & Spanias, A. (2017, March). Reflections: An eModule for echolocation education. In *2017 IEEE International Conference on Acoustics, Speech and Signal Processing (ICASSP)* (pp. 1562-1566). IEEE.

-
- [23] Pereira Júnior, E. L., Moreira, M. Â. L., Portella, A. G., de Azevedo Junior, C. M., de Araújo Costa, I. P., Fávero, L. P., & dos Santos, M. (2023). Systematic literature review on virtual electronics laboratories in education: Identifying the need for an aeronautical radar simulator. *Electronics*, 12(12), 2573.
- [24] Bonefacic, D., & Jancula, J. (2006, June). Laboratory model of a monopulse radar tracking system. In *Proceedings ELMAR 2006* (pp. 227-230). IEEE.
- [25] Bonefačić, D., Jančula, J., & Majurec, N. (2007). Model of a monopulse radar tracking system for student laboratory. *Radioengineering*, 16(3), 63.
- [26] Saratayon, P., Pirom, V., & Saelim, T. (2013). RSSI monopulse azimuth tracking demonstration using wideband personal area network device. *International Journal of Engineering Research and Technology*, 2(9), 663-670.
- [27] Abdulrazigh, M. Y., Uzundurukan, E., & Kara, A. (2018, May). Analysis of measurement instrumentation delay in modular experimental radar at C band. In *2018 26th Signal Processing and Communications Applications Conference (SIU)* (pp. 1-4). IEEE.
- [28] Doğanay, B., Arslan, M., Demir, E. C., Çoruk, R. B., Gökdoğan, B. Y., & Aydın, E. (2022, May). UAV Detection and Ranging with 77-81 GHz FMCW Radar. In *2022 30th Signal Processing and Communications Applications Conference (SIU)* (pp. 1-4). IEEE.
- [29] Texas Instruments. (2017). AWR1642 single-chip 77-and 79-GHz FMCW radar sensor. *Datasheet AWR1642*, Rev. 60.
- [30] Atılım. (2020). Radar systems [Video list]. YouTube. <https://youtu.be/ImRsq5WwrhM?si=sA4b2Oq86yuGdSNs> (accessed on 27 February 2024).
- [31] Mahafza, B. R. (2017). *Introduction to radar analysis*. CRC Press.
- [32] Dham, V. (2017). Programming chirp parameters in TI radar devices. *Application Report SWRA553*, Texas Instruments, 1457.
- [33] Gökdoğan, B. Y., Çoruk, R. B., Aydın, E., & Kara, A. 2D Millimeter-Wave SAR Imaging with Automotive Radar. *Journal of Science, Technology and Engineering Research*, 5(1), 68-77.



REVIEW ARTICLE

Hydrogen generation from sodium borohydride solutions using different catalysts for the survival of living beings in the long-time space flights

*  Erk Inger,* Atılım University, School of Civil Aviation, Ankara, Türkiye
erk.inger@atilim.edu.tr, <https://orcid.org/0000-0002-5794-5385>**Citation:**

Inger, E. (2024). Hydrogen generation from sodium borohydride solutions using different catalysts for the survival of living beings in the long-time space flights, *Journal of Science Technology and Engineering Research*, 5(2):199-222. DOI:10.53525/jster.9886xx

HIGHLIGHTS

- This article is an exchange of chemistry knowledge concerning catalysts, state of the art of technology useable in space requirements, such examples include energy, waterproof for long duration space flights.
- It provided a review for wide range of catalysts available for this purpose.
- Introduction of sodium borohydride as a safe alternative for long duration space flights.
- For fuel cells applicable catalyst hydrogen generation rate optimization and also generation rate reduction in critically space flights such as re-entry.

Article Info

Received: November 29, 2024

Accepted: December 16, 2024

DOI:

10.53525/jster.1593599

***Corresponding Author:**

Erk Inger

erk.inger@atilim.edu.tr

Phone: +90 532 2606333

ABSTRACT

Hydrogen (H₂), an environmentally friendly effective energy carrier with the most advantageous combustion by-products, readily attained from borohydride (NaBH₄) with higher hydrogen (H₂) generation rates (HGRs) as safer than other hydrates necessitating the use of various catalysts. The catalysts' performances are major factors in high HGR from NaBH₄ regardless of hydrolysis or methanolysis reactions. The HGR is influenced by NaBH₄ concentrations, reaction temperature, and the catalyst amounts. Nobel metals e.g., ruthenium (Ru), platinum (Pt), Rhodium (Rh) etc reported as highly effective catalysts for fast H₂ production from NaBH₄ solutions including ethanol, methanol, and ethylene glycol. Due to shortage and cost considerations of noble metals, transition metal-based catalysts e.g., cobalt (Co), nickel (Ni), and manganese (Mn) have gained great interest for H₂ production from NaBH₄ hydrolysis/alcoholysis. Metal nanoparticle-based catalysts, and their synthetic and natural polymer composites along with non-metallic catalyst including micro/nanogels, bulk hydrogels, cryogels, and polymeric ionic liquids (PILs) have been employed as catalysts in methanolysis/hydrolysis of NaBH₄ to attain lower E_a and high HGR values. Therefore, in this review catalysts whether metal or non-metal used in H₂ generation reactions will be surveyed. Moreover, space application of H₂ energy systems with their commercial application for future use will be assessed.

Keywords: Hydrogel; supporting material; Metal Organic Frame (MOF); energy; hydrogen generation

I. INTRODUCTION

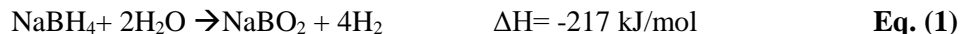
The space vehicle should have a similar environment to Earth for the crew living on board. Air, food, water, and a comfortable temperature are survival requirements of space life including taking away the waste that humans and plants produce such as carbon dioxide, urine, feces. The space vehicle should have an atmosphere similar to Earth and should remove carbon dioxide and contaminated gases and finally should provide to crew and plants a normal humid environment such that;

- Oxygen and nitrogen systems are used to pressurize the space vehicle cabin during the entire flight including launching and landing.
- The circulated air is picking up carbon dioxide and removing carbon dioxide by reacting it with lithium hydroxide. Lithium hydroxide is an attractive choice for space flight because of its high absorption capacity for carbon dioxide and the small amount of heat produced by the reaction.
- Filters and charcoal containers accumulated with odors, dust, and volatile chemicals from leakage, spilling and gas formations must be changed every required period.
- Out of space vehicle is an extremely cold environment and temperatures will vary drastically in different parts of the vehicle. The heating system of the vehicle would be a problem. However, the electronic equipment generates more than enough heat for the ship. The problem is getting rid of the excess heat.
- Cabin heat exchanger cools the air and condenses the moisture which collects in a liquid mixture. The air is recirculated, and the water goes to a wastewater tank using centrifugal force of fan separator to keep apart water from air. Air and water are the most important quantity aboard the space vehicle. Water is made from liquid oxygen and hydrogen in the space shuttle's fuel cells, nearly 11 kg of water per hour. The water tanks are pressurized by nitrogen for the circulation of water that can be used by the crew. Drinkable water is then filtered to remove microbes and can be warmed or cooled through various heat exchangers depending upon the use of food preparation, consumption, and personal hygiene.
- The space vehicle has internal fluorescent floodlights that illuminate the crew compartment. The vehicle has external projectors to illuminate the load compartment. Finally, the control panels are lit internally for easy viewing.
- Necessary electrical interspace shuttle navigation, for the changing direction of the space shuttle and the space communications should be produced during the flight.

The author is highly interested in the space life scenario requirements listed above and the hydrogen and electrical energy production from sodium borohydride solution which will be one of the major sources for space vehicle energy. So that presented article “new catalysts review” would create very important and beneficial alternatives for the rational design alternatives of space fuel cell technology using NaBH_4 hydrolysis.

Hydrogen (H_2) is the most abundant compound in the universe. It is present in compounds and 80% by mass of the sun. The most H_2 in the world is present as compounds and the most common compound is water which composes 11.1% H_2 in its mass. H_2 forms compounds in its compositions more than any other element such as of all natural gases, mineral acids, ammonia, hydrocarbons and organic compounds, alcohols and even in proteins containing hydrogen (Grochala, 2015[40]). Environmentally friendly H_2 should be used as alternative secondary energy and more, as primary energy source required to produce for separating hydrogen from water, since 33% more energy is consumed than what will be gained from H_2 which is traditionally produced from hydrocarbons and water (Retnamma et al., 2011[77]). Limited oil, coal fossil-derived energies and their negative impact of green house, air pollution on the environment, increased use of hydraulic energy and insufficient energy coming from water were strengthened by alternative energy such as solar, wind, biofuel and H_2 sources. Unfortunately, H_2 is secondary energy. The most probable candidates of the energy sources are listed above but nuclear energy can be used as primary energy to produce H_2 and NaBH_4 . Use of H_2 in any vehicle by using NaBH_4 requires less volume, but more energy is highly expensive than the energy of the fossil-derived fuels should we exclude air pollution and human health considerations. The energy content of liquid hydrogen has as 120 MJ/kg whereas 44 MJ/kg for gasoline on mass basis; however, on the volume basis the situation is reversed, the energy content of liquid hydrogen is 8 MJ/L, which is less than gasoline with 32 MJ/L (Giappa et al., 2021[39]; Osman et al., 2022[71]).

Among the H₂ storage systems, the most important high hydrogen containing materials are metal hydrides, and sodium borohydride (NaBH₄) is the most remarkable source because it is considered as stable, non-toxic and contains high amounts of hydrogen and easy to process. Turkey has the richest resources in the world in the high-rate capacity of boric acid production which is used for the storage of H₂ in NaBH₄. The hydrolysis reaction of NaBH₄ forwarded from the well-known Eq. (1);



Water handling Eq. (1) is an exothermic and spontaneous reaction, and this kind of reaction can be accelerated by adding different types of catalysts in the reactor system (Santos and Sequeira, 2011[94]). A major issue is the required water volume, but the second major issue is determination of types of catalytic material to be used (Demirci et al., 2010[30]).

In Table 1, the solubility of NaBH₄ in different solvents is presented. The stoichiometric chemical reaction of Eq. (1) regarded as at least 2 molar equivalents of water are required for each mole of sodium borohydride in the reaction. The solubility of NaBH₄ in water is 550 mg/g (Brack et al., 2015[16]). The gravimetric hydrogen storage capacity of NaBH₄ is stated to be quite lower than the theoretical value of 10.8 weight % (wt%), and it is recommended not to be used in automotive engine sector due to its cost as well (Demirci et al., 2009[31]). NaBH₄ is cost-effective for small portable equipment such as chargers for mobile phones, tablets, and laptops (Bartkus et al., 2013[13]) where pH can be used as an "on-off" control to reduce E_a and increase HGR in contact with a heterogeneous catalyst.

Table 1. Solubility of NaBH₄ in various solvents.

Solvents	Boiling Point (°C)	Reaction Temperature (°C)	Solubility (g/100g solvent)
Water	100	25	55
Methanol	67	20	16.4
Ethanol	78.5	20	4.0
Isopropyl amine	34	28	6.0
Ammoniac	-33.3	25	104.0

H₂ production reactor, lines, and fuel cell with H₂ production unit is shown in Figure 1, and the catalyst made up of fine noble metal powder will be highly explanatory for figuring out the role of catalysts in full aspects of H₂ generation and fuel cell technology. In a NaBH₄ used type of fuel cell, H₂ is produced at the anode, and the catalyst platinum powder breaks down electrons, similarly water or carbon dioxide are eluted, and metal ions are accumulated at the cathode catalyst is zinc, Zn. Typical voltage produced with a loss of energy drops due to voltage drops are caused by component resistance of the fuel cell, ohmic loss of interconnections, and consumption of reactants at catalyst sites in fuel cells.

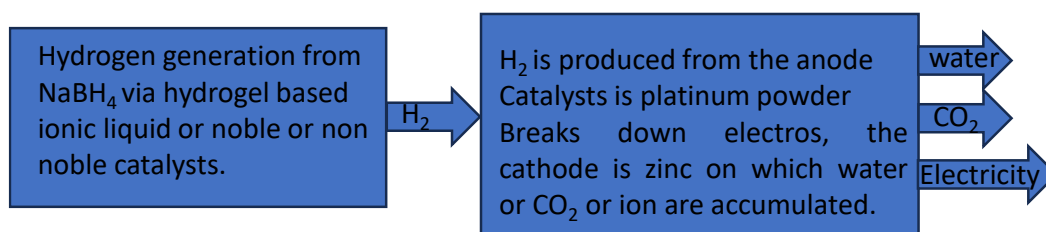


Figure 1. Schematic presentation of fuel cell energy using NaBH₄ (Bartkus et al., 2013[13]).

The reaction will progress at the anode with hydrogen reaction energy transfer till the temperatures become very high. In the use of catalysts, catalyst itself, temperature and increase of electrode area are the three main factors of the slowing down of the reaction rates, so that the electrodes are made highly porous. This has the effect of greatly increasing the

effective surface area. In fuel cell design the reaction rate is proportional with the area of electrode and the cooperation of catalyst regarding temperature conditions. The fuel is oxidized by the catalyst, and H_2 turns the fuel into a positively charged ion at the anode and it produces negatively charged electrons. The electrolyte is a substance specifically designed so that the ions can pass through it, the ions are reunited with the electrons and the two reacts with a third chemical, usually oxygen, to create water or carbon dioxide. But the electrons cannot pass through it, the freed electron can travel through a wire creating the electric current. In Eq. (1), in the electrolyte, E_a is required for the generation of fuel gas H_2 , and (OH^-) ions which should be placed on the surface of the electrode must be removed as the electrons produced. Electrons flow from anode to cathode, but conventional positive current flows from cathode to anode.

II. CATALYSTS USED in H_2 PRODUCTION FROM $NaBH_4$

The developed catalysts used for renewable and environmentally friendly secondary energy source, H_2 , obtained $NaBH_4$ hydrolysis are categorized and presented in Figure 2 due to their specific advantages (Abdelhamid, 2021[1]) such as, -rendering faster reactions kinetics and lowering the activation energy by accurately selecting the catalysts. -Hydrogen generation rate (HGR) values of $NaBH_4$ hydrolysis reaction generally increases with use of rough and porous catalysts that afford maximum surface area.

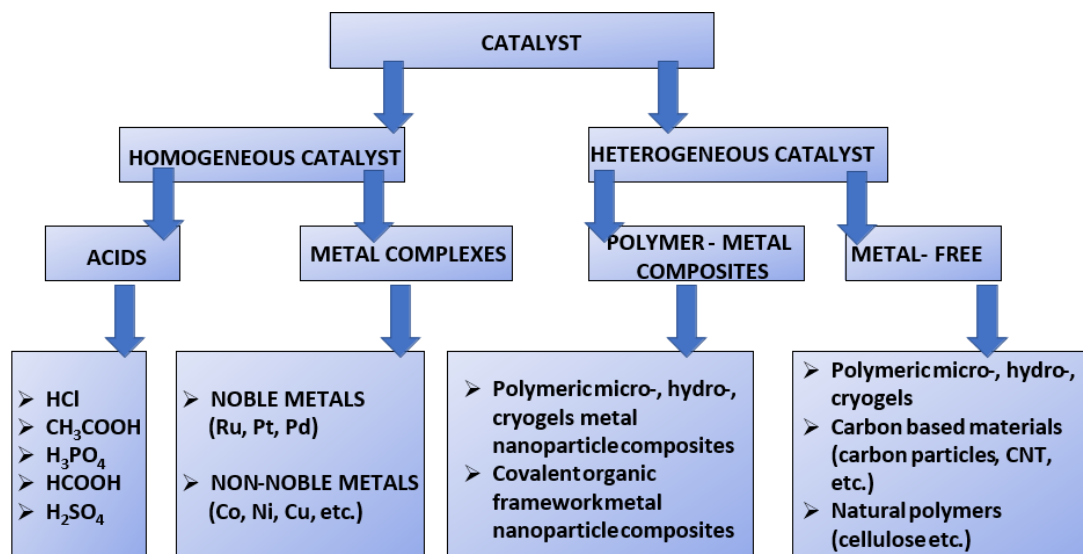


Figure 2. Classification of the catalyst used to obtain hydrogen using $NaBH_4$ (Abdelhamid, 2021[1]).

2.1 Homogeneous Catalysts

As the catalysts and reactants are in the same phase e.g., gas, liquid, and solid, those catalysts are called homogeneous catalysts.

2.1.1 Acids

The mineral acids, hydrochloric acid (HCl), nitric acid (HNO_3), phosphoric acid (H_3PO_4), sulfuric acid (H_2SO_4), acetic acid (CH_3COOH), or the carboxylic acids ($R-COOH$) are used as homogenous catalysts in production of H_2 from the hydrolysis or even alcoholysis of $NaBH_4$ reactions.

Homogeneous catalysts made from acids are highly reactive at the optimum conditions; however, these catalysts have no recovery and recycling or minimum side reactions (Abdelhamid, 2021[1]). The most important advantage of these catalysts is their derivation from acids which are considered cheap, easy attainability and usability, and highly controllable nature. As seen in Table 2, the low activation energy of H_2SO_4 and the higher HGR compared to CH_3COOH played an important role in the use of H_2SO_4 in the fuel cell production of the unmanned aerial vehicles (Kwon et al., 2019[57]). Activation energy (E_a) and HGR values of sulfuric acid and acetic acid regarding to ratios at $60^\circ C$ and $80^\circ C$ temperature degrees are investigated (Akdim et al., 2009[5]) and summarized in Table 2.

Table 2. Comparison of E_a and HGR values of H_2SO_4 and CH_3COOH used in $NaBH_4$ hydrolysis used at $60^\circ C$ and $80^\circ C$ (Akdim et al., 2009[5]).

[$H_2SO_4/NaBH_4$] Ratio	E_a /HGR of (H_2SO_4) [(kJ/mol)/(ml/min.g)]		E_a /HGR of (CH_3COOH) [(kJ/mol)/(ml/min.g)]	
	Temperatures		Temperatures	
	60 °C	80 °C	60 °C	80 °C
0.5	6.2/1800	6.2/1970	7.5/1240	7.5/1240
1.0	5.5/1800	5.5/2040	8.3/1330	8.3/1360
2.0	4.9/2000	4.9/2100	8.8/1350	8.8/1410

CH_3COOH compared to H_2SO_4 is less hazardous, as reactive as H_2SO_4 with similar hydrogen production rates (HGR) and similar total $NaBH_4$ conversions when the experimental conditions are optimized with similar kinetics for hydrolysis, methanolysis or ethanolysis. Also, some E_a and HGR values of different acids are compared in respect to concentration, reaction, condition and illustrated in Table 3 from the catalytic H_2 production from $NaBH_4$.

Table 3. HGR and E_a values for various acids used as catalytic for H_2 generation reaction from $NaBH_4$ (Akdim et al., 2009[5]).

Acid	Acid Concentration (M)	Reaction types	HGR (ml/min.g)	E_a (kJ/mol)	References
CH_3COOH	0.32	Hydrolysis	920	7.5	(Akdim et al., 2009[5])
HCl	0.32	Hydrolysis	1530	6.2	
CH_3COOH	1	Methanolysis	3960	2.81	(Balbay and Saka, 2018a[11])
HCl	1	Methanolysis	4875	5.84	
H_3PO_4	0.5	Semi-Methanolysis	11684	9.08	(Saka and Balbay, 2019[92])
H_3PO_4	0.5	Semi-Ethanolysis	9981	32.47	
H_3PO_4	1	Semi-Methanolysis	5779	1.45	(Balbay and Saka, 2018b[12])
H_3PO_4	1	Ethanolysis	6423	2.98	(Wang et al., 2017[101])
H_3PO_4	1	Hydrolysis	4296	2.60	(Balbay and Şahin, 2014[10])
H_3BO_3	50	Hydrolysis	-	18.01	

It was also reported that cryogenically cooled liquid hydrogen can be used in a conventional submarine under the sea (Choudhury et al., n.d.[26]). High density, controllable source of H_2 for fuel cells for the oxygen requirement and power generation must rise to the atmospheric surface which makes submarine undefended to adversaries. For that reason, H_2 is produced whenever H_2 demanded in the submarine with an air-independent propulsion (AIP) system. The AIP supply H_2 and fuel cell provides quieter energy for submarines with very high endurance for tactical behaviors. Production designed in the mid-1960s and field-tested since the 1970s, is based on a phosphoric acid (PAFC) fuel cell technology

with an onboard sodium borohydride hydrolysis (Choudhury et al., n.d.[26]). Since then, this system has been used successfully with its stable and cost effective performance.

2.1.2 Metal-based homogenous catalysts

Various metal-based catalyst from transition metals or noble metals are commonly used in H₂ production from NaBH₄ or other H₂ sources. Some of the reported E_a and HGR values for metal-based homogeneous catalysts such as zinc chloride (ZnCl₂), iron (III) chloride (FeCl₃), and aluminum oxide (Al₂O₃) catalyzed NaBH₄ hydrolysis reactions are summarized in Table 4. Due to very fast dissolution of ZnCl₂, the reaction is proceeds very fast with high extent value of heat transfer and very rapid proton production in a short time (Wang et al., 2017[101]). In the FeCl₃ catalyzed reaction, the HGR values calculated as 2600 mL/(min.g) with an efficiency of 76% were reported (Boran et al., 2019[15]).

Table 4. Some of the HGR and E_a values of metal halides catalysts used in NaBH₄ hydrolysis.

Metal halides	HGR (ml/min.g) (5, 10, 120 min)	E _a (kJ/mol) (0/5/10/15/20 Wt%)	Reference
ZnCl ₂ (298K)	844, 1039, 1933	79.5/64.3/59.8/54.8/47.7	(Wang et al., 2017[101])
FeCl ₃	2600	-	(Boran et al., 2019[15])
γ-Al ₂ O ₃ nanoparticles	(0.09 moles/l)	29	(Kaur et al., 2015[52])

Metal complex catalysts have been categorized into two based on metal sources such as noble and non-noble metals. Noble metal is regarded as a metallic chemical element resistant to corrosion. Amongst these mobile metals are gold, platinum, ruthenium, rhodium, palladium, osmium, and iridium are the most common ones whereas silver, copper and mercury are also sometimes included or considered as noble metals. Noble metals because of their catalytic capabilities are also called as active components of three-way catalysts (TWC) as they also play curial role in the mechanism of oxidation of carbon monoxides (CO), hydrocarbons (HC), and in the decomposition of nitrogen oxides (NO_x).

Noble metal-based catalysts are presented in Table 5, with the best catalytic active characteristics towards the hydrolysis of NaBH₄ with high HGR. By Ozkar et al.in (Özkar and Zahmakıran, 2005[72]) reports that ruthenium-based catalysts have high HGR of 96,800 ml/(min.g) with water dispersible ruthenium nanoclusters at environmental temperatures. Reaction rate constants at different temperatures are determined from the experimental data and the E_a is found as 66.9 kJ/mol from an Arrhenius plot in (Zhang et al., 2007[108]). The highest HGR of 18,600 ml/(min.g) performance exhibited with ruthenium-based catalyst in powder form generated from a ruthenium salt by reduction with sodium borohydride in (Walter et al., 2008[100]).

Table 5. Some of the E_a and HGR values of noble metal catalyst used in NaBH₄ hydrolysis.

Catalyst	HGR (ml/min.g)	NaBH ₄ (wt%)	NaOH (wt%)	Reference
Ni ₃ B	1300	5	5	(Walter et al., 2008[100])
Co ₃ B	6000	5	5	
Ru	18600	5	5	
Pt/Ru-LiCoO ₂	3000	10	5	

Ru-Pt	15200	10	3	(Demirci and Garin, 2008[32])
Polymer-Ru composite	132	5	1	(Hsueh et al., 2008[42])
Ru Polymer supported	216	1	1	(Chen et al., 2009[20])
Ru on graphite	32300	10	5	(Liang et al., 2010[61])
Ru-RuO ₂ /C	16800	5	1	(Li et al., 2013[59])
Ultrasmall Ru chitin Nanofibers	55290	-	-	(Zhang et al., 2020[107])

In the recent studies of H₂ production, the range of highest HGR values of 15200 mL/(min. g) was reported (Demirci and Garin, 2008[32]). The used Ru₂Pt₁-TiO₂ catalyst was re-evaluated and almost the same catalytic activities as fresh catalyst was obtained during several cycles, after separation and rinsing with deionized water (Demirci and Garin, 2008[32]). Also, ultrasmall Ru chitin Nanofibers with a HGR value of 55290 mL/(min.g) and Ru particles on graphite with HGR value of 32300 mL/min.g (Li et al., 2013[59]) are very impressive statistics to be considered (Zhang et al., 2020[107]).

Important concentration dependent performance with supported catalysts, LiCoO₂ was investigated such that the borohydride concentration was increased beyond 10% in weight, and it is reported that the HGR was decreased. The efficiency of PtRu-LiCoO₂ was almost two times higher than the efficiency of Ru-LiCoO₂ or Pt-LiCoO₂ for NaBH₄ concentrations up to 10% in weight in hydrolysis reactions (Liu et al., 2008[63]).

New homogeneous catalysts based on transition metals such as Mn, Fe, Co, Ni, and Cu are desirable due to their economics and environmental advantages compared to noble metals and some of them are summarized in Table 6 for HGR values at certain reaction conditions. As can be seen from the table, Co and Ni have been found to be the most common transition metals with their low cost and similar catalytic performances compared to noble metals.

Table 6. Non-noble metal based, or transition metal-based catalysts used in hydrolysis of NaBH₄ for H₂ generation with their HGR and reaction conditions.

Catalyst	HGR (ml/min.g)	NaBH ₄ (wt%)	NaOH (wt%)	Reference
CoMnPt/Al ₂ O ₃	5600	2	3.75	(Çakanyildirim and Guru, 2021[18])
CoMnPt/TiO ₂	6250			
CoB/TiO ₂	12503	1	3.75	(Lu et al., 2012[65])
CoB/Al ₂ O ₃	11649			
CoB/CeO ₂	10389			
Co-Mo-B	4200/19000	5	5	(Zhuang et al., 2013[112])
CoB/SiO ₂	10586	0.5 g	1.875 g	(Yang et al., 2011[105])
Ni/Fe/B	2910	5	4	(Nie et al., 2012[69])

2.2 Heterogeneous catalysts

In general, solid materials added into liquid or gas reaction environments for effective catalytic performance that can reduce E_a and/or increase HGR, called heterogeneous catalysts (Kaur et al., 2015[52]). The heterogeneous catalysts can improve hydrolysis of NaBH₄ are cost efficient for hydrogen storage material in portable applications. The pH of water in hydrolysis of NaBH₄ can also be influenced based on the nature of catalysts as the catalyst can also be acidic or basic in nature. Recently different heterogeneous noble metals catalyst such as ruthenium, palladium, platinum and rhodium have been used for H₂ production reaction in the hydrolysis of NaBH₄ (Chen et al., 2009[20]; Demirci and Garin, 2008[32]; Hsueh et al., 2008[42]; Kaur et al., 2015[52]; Li et al., 2013[59]; Liang et al., 2010[61]; Özkar and Zahmakıran, 2005[72]; Walter et al., 2007[100]; Zhang et al., 2020[107], 2007[108]).

2.2.1. Polymer Metal Based Composites

Transition metals are the most common elements with electron rich clouds in the outermost shells that take part in the formation of chemical bonds with other elements including metallic bounds. Their compounds as heterogeneous and homogeneous catalysts including metals e.g., Yttrium (Y), Zirconium (Zr), Niobium (Nb), Molybdenum (Mo), Technetium (Tc), Ruthenium (Ru), Rhodium (Rh), Palladium (Pd), Silver (Ag), and Cadmium (Cd), with their sulfides and metallic salts, and other formulations with other materials can be used as heterogenous catalysts. Also, hydroperoxides and ion exchangers are also heterogeneous catalysts in a different phase from the reactants. For the catalysts various supporting materials including polymer, silicate and alumina are widely used. Since the surface area of the catalyst plays a significant role in the catalytic performance, to prepare catalysts with high surface area is of significant importance. One of the well-known methods to increase the surface area the catalyst covers is their distribution over the support material. Support material may or may participate in the catalytic reactions. Some of the inert or active supports material are presented in Table 7.

Table 7. Most commonly used support materials with some of their specifications employed in the preparation of catalysts.

Supporting Material	Symbol	M _w (g/mol)	Surface area (m ² /g)
Active Carbon Vulcan XC72	C	12.01	240
Active Carbon,5303	C	12.01	253
Active Carbon Ensaco	C	12.01	65
Zirconia Oxide	ZrO ₂	123.22	<10
Aluminum Oxide	Al ₂ O ₃	101.945	255
Carbon Nanotube (multiwall)	C	12.01	>>100
Silicon Carbur Powder, 30 nm	SiC, β	40.10	109

Some of the values of HGR and E_a Co based catalyst prepared in different support materials are given in Table 8. In the references (Baydaroglu et al., 2014[14]) and (Zhu et al., 2012[111]), a quite high HGR values are obtained as 8034 ml/min.g and 10400 ml/min.g, respectively. In the alumina supported amorphous alloy Ni–Co–P/γ-Al₂O₃ catalysts were prepared by using electroless plating for H₂ production from catalytic hydrolysis of NaBH₄ (Li et al., 2014[60]). Various parameters such as deposition time, pH, NaBH₄ concentration and the Co/Ni atomic ratio are the parameters that are affective on the HGR, and the optimum values of HGR of 6600 mL/min.g and E_a = 52.05 kJ/mol were reported (Li et al., 2014[60]).

Table 8. HGR and E_a values of some Co based catalyst prepared on some C and on γ-Al₂O₃ supports used in NaBH₄ hydrolysis.

Catalysts	HGR (ml/min.g)	E _a (kJ/mol)	Reference
Co-B, supported C	8034	56.7	(Baydaroglu et al., 2014[14])
Coll. Carbon Supported CCS Cobalt	10400	24.04	(Zhu et al., 2012[111])
Alumina supported catalysts (Ni–Co–P/γ-Al ₂ O ₃)	6600	52.05	(Li et al., 2014[60])

2.2.2 Electrocatalysts

An electrocatalyst is a catalyst that participates in electrochemical reactions. Electrocatalysts are the catalyst that contain functional groups on the electrode surface itself. An electrocatalyst can be heterogeneous such as a platinized electrode or homogeneous electrocatalysts, which are soluble assist in transferring electrons between the electrode and reactants and facilitate an intermediate chemical transformation for an overall half reaction. The rate of chemical reactions of the materials in the process of functioning at electrode where the surfaces are modified and increased

without being consumed is also named as electrocatalyst. Electrochemical sensing applications of 3D porous nanomaterials which are derived from noble metal-based alloys can be prepared readily using different reaction tools for different electrocatalytic applications (Demir et al., 2018[27]; Dursun and Solmaz, 2024[35]; Kutyla et al., 2020[56]; Lu, 2019[64]; Solmaz and Yüksel, 2019[97]). Fuel cells with electrocatalysts can also afford advantages for electrochemical sensors, and the by implementing nanoporous noble metal-based alloys in electrocatalysis in fuel cells using methanol, ethanol, formic acid and oxygen can also be used as electrochemical sensors for small biomolecules such as glucose, hydrogen peroxide, dopamine, ascorbic acid, uric acid, nitrite, drugs, etc.

2.2.3 Carbon based materials

Various forms of carbon materials have been utilized including sheets made of a single layered carbon atoms, graphene, and carbon nanotubes (CNT), carbon particles and carbon black and so on. CNTs are long, hollow tubes made of carbon atoms in a lattice just thickness of one atom. Dimensional and structural advantages of various forms CNTs are leading to intriguing applications including nanotechnology, electronics, water treatment because of their attractive physicochemical properties e.g., electrical conductivity, mechanical strength, chemical resistant, optical properties, and thermal stability, large surface areas and so on. Some of the carbon-based macromolecules, used for different purposes including catalytic application is demonstrated in Figure 3.

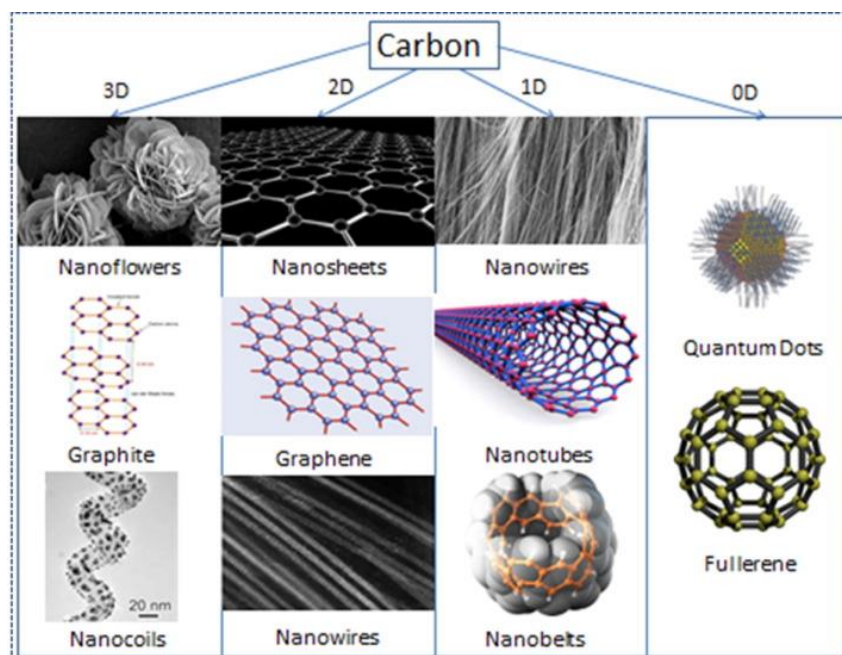


Figure 3. Some examples of carbon-based materials (Karamveer Sheoran et al., 2022[51]).

Multi wall carbon nanotubes (MWCNTs), carbon fibers, mica and most types of carbon black, are widely used as additives to improve the material properties of the starting even with 0.01% by total weight. As shown in Figure 4, MWCNT differs from single walled carbon nanotubes (SWCNT) based on their multi-walled telescopic tube structure and rigidity, and from carbon nanofibers based on their different wall structure such as smaller outer diameter, and hollow interior.

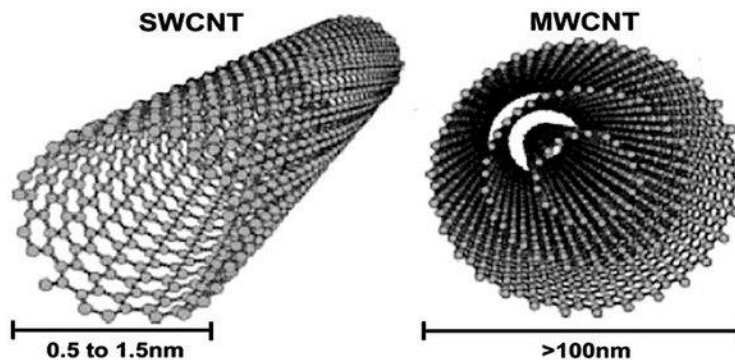


Figure 4. Comparison of the lumen size of single walled (SWCNT) and multi walled (MWCNT) nanotubes (Meyyappan and Srivastava, 2002[68]).

Catalysts that are used in H_2 production from $NaBH_4$ hydrolysis utilizing various formulation of CNT are presented in Table 9 with relevant HGR and E_a values.

Table 9. Various forms of CNT coating catalyst used in $NaBH_4$ hydrolysis and/or methanolysis with relevant HGR and E_a values.

Carbon nano tubes	Temperature (°C)	E_a (kJ/mol)	HGR (ml/min.g)	Reference
CoPt nanoparticle PEDOT:PSS/MWCNT	25	47.3	6900	(Wang et al., 2015[102])
(Co-B/MWCNT)	25	40.40	3100	(Huang et al., 2008[43])
(Pt/MWCNT) - (Pt/C)	27–67	27-36	-	(Uzundurukan and Devrim, 2019[99])

It was reported that CoPt-PEDOT:PSS/MWCNT catalyst performs excellent catalytic performances in $NaBH_4$ hydrolysis reaction with an E_a value of 47.3 kJ/mol and HGR value of 6900 mL/(min.g) at 298 K (Wang et al., 2015[102]). The mesoporous catalyst, Co-B/MWCNT was found to have a lower E_a , 40.40 kJ/mol, and HGR value of 3100 mL/(min.g) which is lower than the average HGR of 5100 mL/(min. g) of Co-B/C catalyst and quite stable for the continuous hydrolysis under the same conditions for the hydrolysis of $NaBH_4$ (Huang et al., 2008[43]).

On the other hand, a natural clay, halloysite nanotubes (HNTs) which similar to CNT in shapes were reacted with (3-aminopropyl)triethoxysilane (APTES) and then protonated upon HCl treatment to obtain modified HNT, mod-HNTs (HNTs-NH₂.HCl) and used as catalyst in H_2 generation from methanolysis $NaBH_4$ (Sahiner and Sengel, 2017[84]) also demonstrated comparable catalytic performances with CNT base materials used for the same purposes..

The activation energies values for Pt/MWCNT and Pt/C catalysts were found to be 27 kJ/mol and 36 kJ/mol, respectively however, it was reported that Pt/MWCNT is more efficient than Pt/C catalyst, and the efficiency% were approximately 98% and 95%, respectively (Uzundurukan and Devrim, 2019[99]). The hydrolysis system based on $NaBH_4$ in the presence of Pt/MWCNT catalyst was suggested to be an alternative source as HGR are concerned in mobile proton exchange membrane fuel cell (PEMFC) applications. On the other hand, MWCNT-COOHs are found to be very efficient catalysts compared to the metal-based nanoparticle catalyzed for H_2 production reactions from the methanolysis of $NaBH_4$ (Sahiner, 2017[78]). HGR of H_2 is found as 8766 ml/(min. g) and the activation energy E_a is calculated as 20.1 kJ/mol, for the methanolysis of $NaBH_4$ with MWCNT-COOHs and assumed highly preferable among the metal based nanoparticle catalyst in the literature.

2.2.4 Three Dimensional (3D) Structures

For larger catalyst e.g., 3D structured catalysts, the distribution of specific atoms on the surface of catalyst particles are generally investigated by atomic resolution atom probe tomography, electron microscopy and spectroscopy equipment. For example, 3D structures of 10 nm sized Co_2FeO_4 and $CoFe_2O_4$ nanoparticles during Oxygen Evolution Reaction, OER, are investigated by using atom probe tomography and the performance of electrocatalysts has been optimized

(Xiang et al., 2022[103]) for effective catalytic performances. In Ni-Co@3DG nanostructure, simply 3D graphene with nickel and cobalt, Ni-Co@3DG used as the catalyst in the NaBH₄ hydrolysis reaction for H₂ production (Karaman, 2022[50]) using the artificial neural network, ANN, and the structure, and performance were evaluated. The active surface area such as 885 m²/g was established by the physicochemical characterizations with homogeneous Ni-Co bimetallic alloy distributions. The results were shown as an excellent catalytic performance for Ni-Co@ 3DG with HGR of 82650 mmol/min.g. Also, it was found that Ni-Co@ 3DG catalyst can maintain 95.96% reusability of its initial performance after five successive uses in the same catalytic H₂ production reaction of NaBH₄ hydrolysis.

2.2.5 Metallic Nanoparticles within Polymeric Hydrogel Network

Hydrogels are chemically stable material with high amounts of water imbibing ability within their polymeric network. The hydrogel matrices can embed various metal particles are found to be cost efficient and superior usable catalyst for various aquatic and non-aquatic catalytic reactions. As the metal particles are protected from the outside environments within hydrogel matrices, they have shield from the oxidation and interact with the functional groups of hydrogel network e.g., these functional groups act as chelating and capping agents for metal nanoparticles. Additionally, the metal ions such as Fe(II/III), Co(II), Ni(II), Cu(II), Ru(II), Au(III) metal ions can be precipitated to their corresponding metallic particle forms with the different size within hydrogels network using preferably green chemicals or non-toxic reduction agents such as NaBH₄, or H₂ (Sahiner, 2013[79]). Metal composites of hydrogels have been reported using natural and synthetic hydrogels for the in-situ preparation various metal nanoparticles or nanoclusters as flexible and tunable systems (Sahiner, 2013[79]). Various techniques in the use of hydrogel-metal composite with excellent size, composition, and topography and interfaces can be readily designed and used in not just in H₂ production reactions but also in the catalytic degradation of toxic chemicals such as dyes and nitro compounds. Therefore, the use of soft and flexible hydrogel reactors of polymeric network at various dimensions provides many advantages over bare or other support materials for a continuously and environmentally benign workable capabilities. In addition to categorizing hydrogels based on sources such as natural and synthetic in origin, they can also be categorized depending on the nature of functional groups such as neutral or charged (anionic or cationic) (Sahiner, 2013[79]).

Some of the hydrogel templated metal nanoparticles used as catalyst in NaBH₄ hydrolysis and hydrolysis reaction along with reaction temperature and Ea values are given in Table 10.

Table 10. Comparison Ea values of hydrogel-metal nanoparticle composite catalyst used in NaBH₄ hydrolysis and/or methanolysis.

Hydrogels	Temperature (°C)	E _a (kJ/mol)	Reference
p(EP-g-AA) Cu & Ni	30	42.61&39.10	(Zhao et al., 2017[109])
P(AMPS)-Ag	25	29.95	(Ghorbanloo and Nazari, 2020[38])
GH-CoCu	30	63.16	(Zaier and Metin, 2021[106])
P(AAm)-Pd-NiB	30	31.10	(Liu et al., 2013[62])
WSC based hydrogel-Ni	30	32.66	(Ding et al., 2018[33])
Starch hydrogel-Co	30	52.18	(Chairam et al., 2019[19])

In the preparation of hydrogel from diverse sources such as monomer and polymer different polymerization and crosslinking techniques were utilized (Elsayed, 2019[36]). An efficient hydrogen generator for portable fuel cell applications was designed using nickel–cobalt–boride (Ni–Co–B) catalysts and their catalytic hydrolysis reaction with alkaline NaBH₄ solution elaborated (Ingersoll et al., 2007[47]). The activation energy for hydrogen generation is found to be 62 kJ mol⁻¹ which may be considered as very close and reasonable result with that of hydrogen generation catalyst such as ruthenium. These kinds of catalyst systems can also be prepared within a super porous hydrogel network called cryogels. Cryogels present better catalytic performance than conventional hydrogels due to their highly porous network and some of the cryogels used as template for metal nanoparticle preparation and as catalyst in the hydrolysis NaBH₄ reaction are given in Table 11.

Table 11. Metal nanoparticle embedded super porous cryogels composites used as catalyst in H₂ production from NaBH₄ hydrolysis.

Cryogels	Temperature (°C)	E _a (kJ/mol)	HGR (ml/min.g)	Reference
p(HEMA)M:Co	18	-	26641	(Seven and Sahiner, 2014[95])
Q-P(VI)-M cryogel	70	-	14566.9	(Sahiner et al., 2015[86])
P(4-VP)-M (M:Co, Ni, Cu)	25	28.78		(Sahiner and Yildiz, 2014[87])

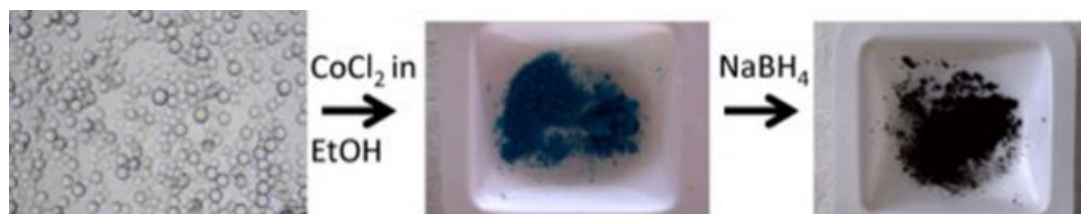
The micro/nano structures are an artificial structure with special functionality, dimensions, , and physical properties at micro-nano scale such as nanoparticles, graphene, CNT, nanocomposites, titanium dioxide, core-shell, etc. Recent advances in nanoparticle–hydrogel composites have been focused on the specific material design, synthesis, potential applications, and their inherent accompanying feature utilization (Thoniyot et al., 2015[98]). For example, polymeric particles can also be directly used as catalyst in H₂ production reactions with or without containing metal nanoparticles for hydrolysis or methanolysis reactions of NaBH₄, respectively.

Some of the values of E_a and HGR for the polymeric microparticle hydrogel catalyzed NaBH₄ reactions are presented in Table 12. Various cross-linking techniques using different monomer/comonomer ratios, and some structures materials such as graphene can be used to prepare hydrogels with suitable pore and functional groups.

Table 12. Microgels, microgels-metal nanoparticle composites used as catalyst in H₂ generation reactions in NaBH₄.

Microgels	Temperature (°C)	E _a (kJ/mol)	HGR (ml/min.g)	Reference
(p(AMPS-TDA-1)	25	14.3	854	(Demirci et al., 2019[29])
p(MTMA)	(-15)-(45)	24.1	-	(Ozturk et al., 2018[73])
Poly(styrene)-Ru	25	-	215.9	(Sahiner and Sengel, 2016[85])
P(NIPAM)-Ni	40-60	48.28	-	(Cai et al., 2016[17])
PVDF-NiB capsules	30-50	-	-	(Chen et al., 2011[22])
Co@AHs	30-60	55.6	-	(Ai et al., 2014[2])

Upon synthesizing the cationic microgel from (3-Acrylamidopropyl)-trimethyl ammonium chloride (p(APTMACl)) by inverse suspension polymerization technique, these polymeric microparticles were mixed with CoCl₂, NiCl₂, CuCl₂, FeCl₂ and FeCl₃ metal salts solutions in ethanol (Sahiner et al., 2014[80]). As shown in Figure 5, the digital camera images of bare metal salts are loaded, and *in situ* metal nanoparticle prepared microgel composite have different colors. Using this Co metal nanoparticle containing microgels composite as catalyst, H₂ is produced by as magnetic ionic liquid colloid catalyst (Sahiner et al., 2014[80]).

**Figure 5.** The digital camera images of bare microgels, CoCl₂ loaded microgels, and microgel-metal nanoparticle composites (Sahiner et al., 2014[80]).

The microgel system based on p(APTMACI)-M composite IL are used as catalyst systems in H₂ generation from the hydrolysis of NaBH₄ or ammonia borane. The activation energy values for the hydrolysis reaction were calculated for two of the catalyst systems and were found to be 53.43 and 26.74 kJ/mol for p(APTMACI)-[CoCl₄] and p(APTMACI)-[NiCl₄], respectively (Sahiner et al., 2014[80]). Some of the HGR and E_a values of PIL catalysts used in H₂ production reaction from NaBH₄ are given in Table 13.

Table 13. The HGR and E_a values of polymeric ionic liquid as catalyst used in H₂ production from NaBH₄.

Catalyst	Reaction	Temperature (°C)	E _a (kJ/mol)	HGR (ml/min.g)	Reference
Hypercross-linked microporous polystyrene (PS) ionic liquid (IL) membranes	Hydrolysis	30-50	52.50	3621	(Chinnappa n et al., 2015a[23])
graphene oxide-ionic liquid grafted chitosan composites	Hydrolysis	20-50	38.0	-	(Jia et al., 2018[48])
PVDF/PEG/EGDMA/IL chemically cross-linked nanofibers	Hydrolysis	25-55	37.86	-	(Chinnappa n et al., 2015b[24])
Co-doped Co _x O _y nanofilms water/ionic liquid	Hydrolysis	30-45	43.19	8055	(Guan et al., 2022[41])
MWCNTs/IL/Mn nanohybrids	Hydrolysis	30-50	40.80	350	(Chinnappa n et al., 2015c[25])
RuNP@NH ₂ -PIILS	Hydrolysis	21-40	38.9	-	(Paterson et al., 2022[76])

Polymeric ionic liquids (PILs) have been stated as a rising class of ion-conducting polymers based on the familiar chemistries of ionic liquids and these PILs have afford many advantageous such as high conductivities, strong thermal and chemical stability (Lebedeva et al., 2024[58]). The preparation of magnetic (Fe₃O₄) nanoparticles (NPs) by coating them with amino-functionalized silica (SiO₂@NH₂) as Fe₃O₄@SiO₂@NH₂ particles were turned into ionic liquid (IL) colloids with the treatment of hydrochloric acid (HCl), nitric acid (HNO₃) and sulfuric acid (H₂SO₄), respectively. The maximum HGR value of 13188 mL/(min.g) was attained at 500mM NaBH₄ by Fe₃O₄@SiO₂@NH₃⁺Cl⁻ as catalyst at 25 °C. Moreover, the activation energy E_a values for the methanolysis of NaBH₄ was found as 32.5 kJ/mol.

Protonation is the addition of a proton to a chemical species such as an atom, molecule, or ion making the structure more acidic and ionic (Martínez et al., 2023[67]). Protonation is different from hydrogenation, as during protonation, a change in charge of the protonated species occurs, while the charge is unaffected during hydrogenation. Examples can be given as the formation of the ammonium group where NH₄⁺ is formed by protonation of ammonia NH₃ or water may be protonated by sulfuric acid:



As protonation occurs in many catalytic reactions, both protonation and deprotonation occur in most acid-base reactions. As a species is either protonated or deprotonated, its mass and charge change, as well as its chemical properties are altered. For example, protonation may change the optical properties, hydrophobicity/hydrophilicity, or reactivity of a substance. Protonation can be described as a fundamental chemical reaction, and it is an important step in many stoichiometric and catalytic processes. For example, polyethyleneimine (PEI) is a cationic polyelectrolyte and investigated for various purposes including as catalysts. PEI modification and protonation, the reuse and regeneration as catalysts in NaBH₄ dehydrogenation in methanol was reported (Sahiner and Demirci, 2016[82]).

Nonmetal green catalysts attracted many researchers greatly because a green nonmetal catalyst has many advantages such as high activity, low cost, and environmental friendliness. A nonmetal catalyst for NaBH₄ hydrolysis produced through the covalent modification of sand samples with PEI and then protonated (Inger et al., 2020[46]). The successful formation of the catalyst was verified by transmission electron microscopy, thermogravimetric analysis, and Fourier transform infrared spectroscopy. The hydrolysis of 15 mg NaBH₄ catalyzed by 50 mg catalyst could provide a hydrogen generation rate as high as 117.53 mL min⁻¹ at 20 °C (Inger et al., 2020[46]). Although the catalytic activity decreased after several uses, it could be restored easily by regenerating in hydrochloric acid treatment of used catalysts (Inger et al., 2020[46]).

The HGR and turnover frequency (TOF) values were calculated and compared for PEI hydrogels with different sizes and morphologies (Sahiner and Demirci, 2016[82]). The specific HGR and TOF are formulated by Eq. 3&4 below.

$$HGR = \frac{V_{H_2O}(mL)}{t(\min).m(g)} \quad \text{Eq. (3)}$$

Turnover frequency (TOF), which quantifies how many catalytic reaction cycles proceed per site and per unit of time can be formulated as:

$$TOF = \frac{n_{H_2}(mol)}{t(\min).n_{cat}(mol)} \quad \text{Eq. (4)}$$

The natural minerals such as sulfide rich ore of pyrite was modified with PEI used as a catalyst in H₂ generation from NaBH₄ methanolysis (Inger, 2019[45]). The effect of solvent at various ratios of methanol/water, and the amount of catalyst, concentrations of NaBH₄, and temperature on H₂ production from NaBH₄ in methanol in the presence of PEI modified pyrite as catalyst were investigated. The catalytic performances of pyrite, pyrite-PEI, and protonated pyrite-PEI (pyrite-PEI⁺) were determined as HGR values of 795, 2883, and 4320 mL H₂/(g of catalyst.min), respectively for H₂ production from NaBH₄ methanolysis. The E_a values were calculated for pyrite-PEI, and pyrite-PEI⁺ catalyzed in H₂ production as 47.2 and 36.8 kJ/mol, respectively. It is important that the amount for the pyrite-PEI⁺ catalyst is decreased to 76.2% after five consecutive uses with 100% conversion for each re-use study. Therefore, pyrite was reported to be to be a useful re-generable and economic green catalyst for H₂ production in many important applications (Inger, 2019[45]).

2.2.6 Metal Organic Frameworks (MOF)

Metal-organic frameworks (MOFs) as depicted in Figure 6 is an organic-inorganic hybrid crystalline porous materials consisting of an array of positively charged metal ions or clusters surrounded by organic linkers together to form a repeating cage-like structure of organic linkers.

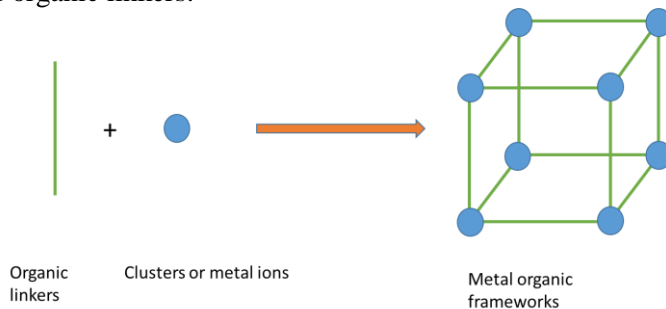


Figure 6. Schematic demonstration of Metal-organic frameworks (MOFs) prepared from a organic linker and metal ions (Singh et al., 2021[96]).

MOFs are constructed from organic linkers and metal ion nodal points coordinated in 1D, 2D and 3D forms of frameworks. 3D MOF structures are porous and can be filled with guest molecules like sponges absorbing water. The pore sizes of most reported MOFs have pore diameter smaller than 2 nm, which makes them suitable for the adsorption

and separation of small guest molecules, such as gas, small organic molecules and coordination complexes where an ion or molecule attached to a metal atom by coordinated bonding. Due to this hollow structure, in some cases an extraordinary amount of large internal surface area, 7800 m²/g for certain MOFs have been synthesized reported (Xu et al., 2021[104]). Uniform pore structures, atomic-level structural uniformity, tunable porosity, extensive varieties, and flexibility in network topology, geometry, dimension, and chemical functionality are the options of various metal ions containing porous MOF structure. Moreover, MOFs are capable of storing hydrogen even at high gravimetric and volumetric density requirements, as a clean alternative to hydrocarbon fuels in cars and other mobile applications. With exceptionally high surface areas and chemically-tunable structures, microporous metal-organic frameworks have recently emerged as some of the most promising candidate in many energy-related applications.

Moreover, magnetic MOFs, containing cobalt ion with two identical monomers linked by strong and/or weak covalent or intermolecular bonds, various magnetic exchange interactions which can also be strong or weak, covalent or intermolecular interaction has been studied (Kurmo, 2009[55]). The different forms of short-range magnetic ordering, rising to single-molecule-magnets and single-chain-magnets, to long-range ordering of two- and three-dimensional networks were constantly investigated for certain applications. The H₂ production reaction from NaBH₄ hydrolysis in the presence of MOF structures as catalyst were also studied (Jung et al., 2018[49]; Luo et al., 2019[66]; Onat et al., 2021[70]) Some of these MOF based catalysts used in H₂ generation from NaBH₄ are given in Table 14. As can be seen because of the high specific surface area and metal content, the determined HGR values are higher in comparison to the common metal nanoparticles.

Table 14. Some of the E_a and HGR values of metal-organic frameworks (MOF) used as catalyst in H₂ production from NaBH₄.

Catalyst	Temperature (°C)	E _a (kJ/mol)	HGR (ml/mol.g)	Reference
CoNPs@ZIF-8	30	-	14000	(Luo et al., 2019[66])
Co-Ru@ MOF	30	41.41	15144	(Onat et al., 2021[70])

Various platforms of MOF have been successively investigated and significantly low E_a and high HGR are reported (Jung et al., 2018[49]). For unmanned aerial vehicles (UAVs) hydrogen is produced by a NaBH₄ hydrogen generation system and electrical energy was produced 95.96 W maximum power and 185.2 Wh energy density by using a PEMFC system (Jung et al., 2018[49]).

2.2.7 Thin Film Coating

The deactivation of Co catalyst prepared as thin film by magnetron sputtering technique was reported (Paladini et al., 2017[75]). Magnetron sputtering is a high-rate vacuum coating technique and can be utilized for various materials e.g., for metals and ceramics are deposited onto as many types of substrate materials by the use of a magnetic field applied to a diode sputtering target. Study of the catalyst surface and solid reaction precipitations were investigated by using X-ray photoelectron spectroscopy (XPS), transmission electron microscope (TEM) and scanning transmission electron microscope (STEM). Similarly, magnetron sputtering thin film coating method was reported form different support for diverse application (Arzac et al., 2018[9]; Arzac and Fernández, 2020[8]; Kutyla et al., 2020[56]; Paladini et al., 2014[74]). For example, electrodeposition of cobalt supported catalyst supported on nickel foam was reported as catalyst in hydrolysis of NaBH₄ (Akdin et al., 2011b[4]). Similarly, for cobalt electrodeposition over nickel polycarbonate membrane (PCM) foam is used as stable supported catalyst thin films for H₂ production (Akdin et al., 2011a[3]). Furthermore, thin-film CoB alloy catalysts were prepared on Ni-foam substrates using electroless as well as electroplating techniques (Krishnan et al., 2009[54]).

Many catalyst systems are developed for the recycling of byproducts obtained from aqueous NaBH₄ hydrolysis, NaBO₂·4H₂O. For example, this by product can be reacted with Mg₂Si to regenerate NaBH₄ via ball milling at room temperature under an argon atmosphere (Zhong et al., 2018[110]). The regenerated NaBH₄, with a maximum yield of 74%, has the same physicochemical properties as a commercial sample. Also, the regeneration of NaBH₄ by ball milling

for the by-product, $\text{NaBO}_2 \cdot 2\text{H}_2\text{O}$ or $\text{NaBO}_2 \cdot 4\text{H}_2\text{O}$, with MgH_2 at room temperature and atmospheric pressure has been reported (Chen et al., 2017[21]). Results show that NaBH_4 at 90.0% for $\text{NaBO}_2 \cdot 2\text{H}_2\text{O}$ and 88.3% for $\text{NaBO}_2 \cdot 4\text{H}_2\text{O}$ are achievable.

It was reported that NaBH_4 reacted slowly with water to liberate H_2 at room temperature and was accelerated by applying metal-metal oxide catalysts such as Pt-TiO_2 , Pt-CoO and Pt-LiCoO_2 (Kojima, 2005[53]). The gravimetric Hydrogen densities of some of the H_2 storage material are given in Table 15.

Table 15. Gravimetric hydrogen densities of several H_2 storage materials (Kojima, 2005[53]).

Materials	Temperature (K)	Density (wt%) of Grav. H_2
$\text{NaBH}_4 + 2\text{H}_2\text{O} + \text{PtLiCoO}_2$, high pressure	296	9.2
$\text{LiH} + \text{H}_2\text{O}$ (H_2 yield:34%)	ordinary	2.6
$\text{NaH} + 1.5 \text{H}_2\text{O}$	ordinary	4.0
MgH_2	573	7.6
NaAlH_4	373	3.4
$\text{Ti-xV-Cr-MnX=45-55}$, Ti-Cr-Mn=24-31-10 , H_2 , 7-0.01MPa	313	2.5
Super activated carbon, (AX21,5MPa)	298	0.9
Super activated carbon, (AX21,3MPa)	77	5.1

The chemical hydrides such as NaBH_4 , LiH , and NaH are high amounts of H_2 containing materials (Dragan, 2022[34]; “Hydrogen Storage and Transport by Organic Hydrides and Application of Ammonia,” 2019[44]). Pt-LiCoO_2 is a favorable catalyst for the production of H_2 by the hydrolysis of NaBH_4 solution where water to NaBH_4 mole to mole ratio is 2 at high pressure (0.6 MPa) ratio of H_2 . In the 10kW capacity hydrogen generator is equipped with NaBH_4 storage solution pump vessel, storage tank of NaBO_2 solution separator, hydride reactor, is monolith coated with the Pt-LiCoO_2 catalysis. NaBH_4 is synthesized by annealing NaBO_2 with MgH_2 at high pressure as shown in Figure 7.

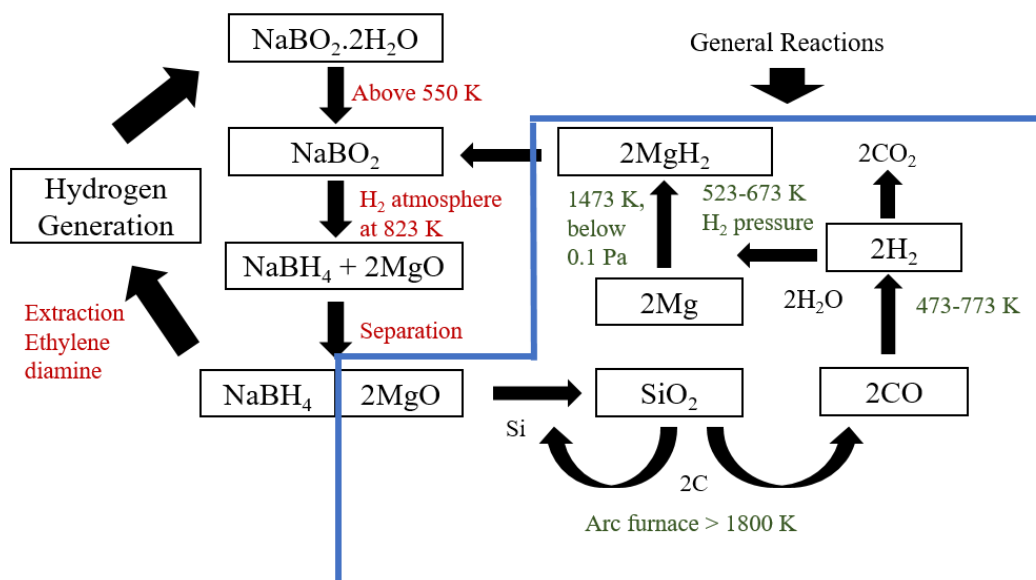


Figure 7. Recycling process of the NaBH_4 (Kojima, 2005[53]).

The authors stated that “energy efficiency of the recycling process is low with very high gravimetric densities in the chemical hydride systems, the system can be highly effective for a fuel cell uninterrupted power supply (FCUPS) for the use of emergency power supply” (Kojima, 2005[53]).

2.2.8 Non-Metal Based Complex as catalyst for H₂ production

Non-metal catalysts have been utilized as an alternative to metal-based catalysts in H₂ production from NaBH₄ or other hydrides due to their non-metallic nature. They are considered effective but environmentally friendly and economical. In this section, non-metal-based materials such that carbon-based nanomaterials, cellulose based nanomaterials, silica-based nanomaterials as well as their PIL forms are considered as metal-free catalysts.

2.2.8.1 Carbon Based Catalyst

Catalysts based on carbonaceous material with adjustable porosity, uniform geometry, surface functionality, controllable particle size distribution, and chemical inertness and thermally stable are the important fabrication specifications of carbon particles or carbon spheres (CSs). Natural and synthetic forms of carbon, metals, metal oxides others such as clays are used as catalyst with nano sized or high surface area are of catalyst afford high catalytic activity, with absorptive characteristics in H₂ production. Carbon, carbon blacks, carbon nano tubes, inorganic tungsten and boron nitride nanotubes, graphite, diamonds, buckyballs (which is 1 nanometer in diameter, a hollow spherical molecule composed of many carbon atoms in active layer of materials), fullerene and finally graphene are considered as nano size catalysts (Saka, 2021a[90], 2021b[91]; Samatya Ölmez et al., 2022[93]). For example, porous carbon (PC) particles were modified with PEI to obtain amine functionalized PC-PEI particles (Demirci et al., 2020[28]). PC-PEI was treated with HCl, PC-PEI⁺ and used as catalyst for H₂ production studies in the methanolysis of NaBH₄. In the methanolysis reaction of NaBH₄ catalyzed by PC-PEI⁺ catalyst, high HGR value, 4040 mL/(min.g) and low E_a value of 23.9kJ/mol were obtained.

As a carbon source, carbon black (CB) obtained from car tires rubber was used as catalys (Ari et al., 2019[7]). Firstly, CB was oxidized by treatment with H₂SO₄ and HNO₃ and then the oxidized CB was modified with PEI and treated with HCl for protonation. Protonated CB-PEI as CB-PEI-HCl was used as a catalyst in the methanolysis of NaBH₄. The E_a was calculated as 34.7 kJ/mol in the temperature range of -20 °C to +30 °C. The HGR value was calculated as 3089 mL/min.g for the conditions reactions conditions of 50 mg catalyst, 125 mM NaBH₄, 20 mL methanol, at 25 °C under 1000 rpm mixing rate).

Another biobased waste as green catalyst used is apricot kernel shell utilized as a free-metal catalyst with 15% H₃PO₄ for NaBH₄ hydrolysis reaction and a HGR value of 20,199 mL min⁻¹ gcat⁻¹ and the activation energy was equal to 30.23 kJ mol⁻¹ was reported.

2.2.8.2 Natural materials as catalysts

A natural clay, halloysite nanotubes (HNTs) shown in Figure 8 have been experimented as catalyst in H₂ production from methanolysis of NaBH₄ and the natural HNTs upon modification with (3-aminopropyl) triethoxysilane (APTES) and then treated with HCl to obtain mod-HNTs (HNTs-NH₂·HCl) (Sahiner and Sengel, 2017[85]). The activation energy was calculated as 30.41 kJ/mol, the catalytic activity of mod-HNTs. The mod-HNT catalysts showed greater reusability with catalytic activity (91%) after 10th use having 100% conversion at each time with comparable HGR of about 220.5 ml/(min.g) as well. There is also montmorillonite-based catalyst were also reported in literature (Saka, 2024[88], 2023[89]).

The schematic presentation of amine modified Halloysite Nanotubes as catalyst for H₂ production from NaBH₄ methanolysis reaction is shown in Figure 8.

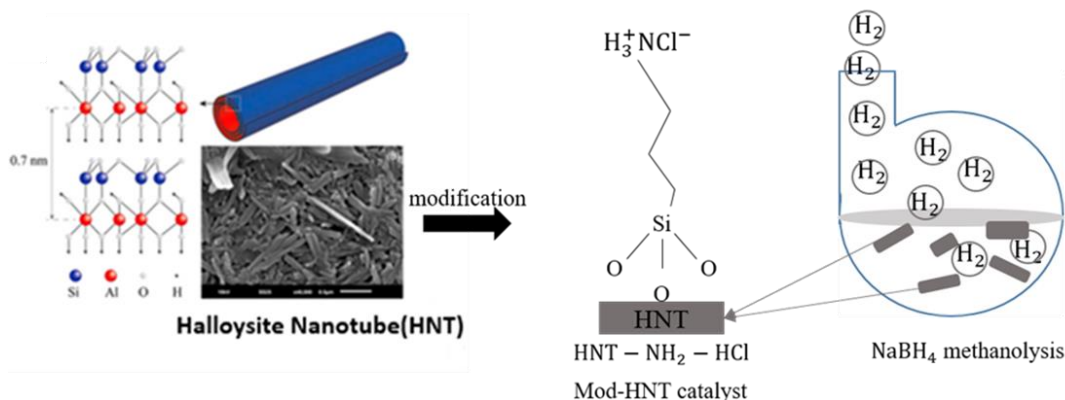


Figure 8. The schematic demonstration of amine modified Halloysite Nanotubes (HNT) as their use catalyst for H₂ production from NaBH₄ methanolysis (Sahiner and Sengel, 2017[84]).

Microgranular cellulose were modified with epichlorohydrin and followed by the modification with diethylenetriamine (Cell-EPC-DETA) and then protonation by hydrochloric acid as Cell-EPC-DETA-HCl and was used as metal free catalyst directly in methanolysis reaction of NaBH₄ for hydrogen (H₂) production (Sahiner and Demirci, 2017[84]). The (HGR) values for bare Cell catalyzed NaBH₄ methanolysis reaction were calculated as 408 mL H₂/(g of catalyst.min), and increased to 2015 mL H₂/g of catalyst.min for Cell-EPC-DETA. Remarkably, HGR value has almost increased 160% to 3215 mL H₂/(g of catalyst.min) for Cell-EPC-DETA-HCl catalyzed NaBH₄ methanolysis reaction. Likewise, the activation energies of Cell-EPC-DETA and Cell-EPC-DETA-HCl were determined as 38.2 and 34.4 kJ/mol.

A low activation energy (E_a), almost 14.41 ± 0.46 kJ mol⁻¹ is calculated for NaBH₄ methanolysis reaction using Cellulose cotton fibers (CF) coated chitosan (CH), CF-A-CH as catalyst at temperature range 0 °C - 45 °C (Ali et al., 2019[6]). Moreover, the catalyst reusability is also analyzed and no decline in conversion % is reported, whereas a little reduction in performance % is detected after every cycle and only 18% lost is observed in its percent activity after completion of five successive cycles.

2.2.8.3 Silica Based catalysts

Silica (SiO₂) particles are classified as an alternative catalyst for the production of green energy carriers such as H₂. Nanosilica shells, nano structured silica, silica-carbon composites, silica hybrid, organic, inorganic, and mesoporous silicas are the silica-based material which can be used as natural minerals as catalysts. For example, the hydrolysis of NaBH₄ offers substantial applications in the production of H₂ but requires an inexpensive catalyst. Consequently, phosphorylated silica (SP-PA) was reported to be used as catalyst in NaBH₄ hydrolysis to generate H₂ as shown in Figure 9. The HGR values of 762.4 mL min⁻¹ g⁻¹ for SP-PA particles is higher than that of bare silica particles, 133 mL min⁻¹ g⁻¹ of catalyst. The calculated activation energy for NaBH₄ hydrolysis for SP-PA catalyst is 29.92 kJ.mol⁻¹ indicating the high catalytic activity of SP-PA particles.



Figure 9. Catalytic hydrolysis of NaBH₄ for H₂ production catalyzed by phosphorylated silica particles (SP-PA) (Ganesan et al., 2022[37]).

The H₂ production from dehydrogenation of NaBH₄ in methanol was carried out in the presence of PEI modified two different sand samples (T and P) as catalysts (Inger et al., 2020[46]). Similar HGR values of these PEI modified sand samples have been found, 1344 and 1190 mL H₂/(g of catalyst.min). It was also reported that the activation energy of sand catalyst was found to be lower than the several metal catalysts which were 24.6 and 25.9 kJ/mol and increased higher values upon, protonation e.g., 36.1, and 36.6 kJ/mol for T-PEI⁺ and P-PEI⁺ samples, respectively.

III. CONCLUSION AND OUTLOOK

In this review article, homogenous and heterogeneous catalysts are examined for H₂ production from NaBH₄ hydrolysis reactions. As H₂ is the most important energy carrier, energy production system using H₂ is of paramount significance for the future of humanity. For example, during the long trip of the spacecraft flight in space, long term accommodation in space stations, stays in the planets and habitats, H₂, O₂, water, electric energy profoundly be needed by the travelling crew members, plants and animals for their survival. The weight and volume data for sodium borohydride (NaBH₄) hydrolysis or methanolysis and the catalyst requirements for the production of H₂, O₂, water, and electric energy including space agriculture will be important input data for designing spacecraft. Here, all types of catalyst including homogeneous to heterogenous catalysts that can be used in H₂ production from hydrides hydrolysis or methanolysis were evaluated. HGR and E_a are two important performance parameters that depend on the choice of catalyst. Although high HGR would be preferable, it is desirable to control HGR as desired for specific applications.

On January 28, 1986, the Space Shuttle Challenger crashed 73 seconds just after takeoff. Several hundred-ton liquid cryogenic fuel elements stored in external tank units stored liquid hydrogen at -253 °C and liquid oxygen at -183 °C. The storage and handling of these cryogenic liquids requires high performance insulation technology. The seven astronauts of the Colombian vehicle were lost during the takeoff, because of the very small damage occurred in the insulation of the external fuel storage system, caused few degrees °C increase of the fuel temperature. The function of catalysts that provide sodium borohydride and H₂ production rate plays crucial role in the return of spacecraft to the atmosphere (REENTRY), especially when the vehicle reaches about 23 times the speed of sound and turns the space shuttle into a fireball at a temperature of about 2000°C-2500°C, the system should be able to slow down or even to stop the H₂ production if necessary. H₂ should only be produced supply for on demand basis without being stored can reduce the risk of explosion.

A manned spacecraft is a clustered volume that flies in a vacuum, close to external environments. In addition to the CO₂ emission of the living beings in the spacecraft, if there is a CO₂ release from the catalyst used from the sodium borohydride hydrolysis, this is an undesirable result. It is preferred that the catalyst be environmentally friendly and green in nature. Otherwise, CO₂ emissions accumulated in the spacecraft must be cleared by converting to energy.

Although, even HCl can be used as a homogeneous catalyst in NaBH₄ hydrolysis in Unmanned Aerial Vehicle. Then, phosphoric acid (PAFC) was used as a catalyst in NaBH₄ hydrolysis for Submarines. Finally, H₂, O₂, H₂O and electricity were produced by three sets of fuel cells located in the vehicle's Service Module and transmitted to the Apollo Command Module, using sodium borohydride hydrolysis and catalysts ranging from 300 W to 5 kW in the Apollo spacecraft. Apollo 11, the first to land on the Moon, had three hydrogen fuel cells in its modules. Apollo 11's hydrogen fuel cell, capable of producing up to 2,300 W per unit, produced electricity to power countless devices on spaceships, and the electricity generation met most of the astronauts' needs. Finally, it is concluded that discussions for current perspectives and future outlook of NaBH₄ as an efficient energy/hydrogen carrier of space vehicle requirements.

Catalytic decomposition of hydrogen peroxide was used to generate O₂, and H₂O. Pure O₂, was provided to a fuel cell and the H₂O was stored separately. NaBH₄ in the solid state was used as a H₂ source in the present study. Pure H₂ can be generated by a catalytic hydrolysis reaction in which the H₂O source can be obtained from the H₂O₂ decomposition. Two catalytic reactors were prepared; one is for decomposition reaction of H₂O₂ and the other is for hydrolysis reaction of NaBH₄. For that reason, acids, metal hydrides, noble metals and then non-noble metals and their powders as homogeneous/heterogenous catalysts have been examined. In the further research of hydrolysis and fuel cell concepts hydrogel, Polymeric Ionic Liquid (PIL), polyethyleneimine (PEI), magnetic hydrogel-M composites, Metal Organic Frames (MOF) and Thin Film Coating type of catalysts will play important roles in space technology requirements.

ACKNOWLEDGMENTS

The author is thankful to Dr Sahin Demirci and Betül Ari for their great support, suggestions and editing of the first draft of the manuscript.

CRedit authorship contribution statement

Erk Inger: Conceptualization, Funding acquisition, Formal analysis, Investigation, Methodology, Project administration, Resources, Supervision, Validation, Visualization, Writing – original draft, Writing – review & editing.

Conflict of Interest: None

Declaration of funding: No funding was received.

REFERENCES

- [1]. Abdelhamid, H.N., 2021. A review on hydrogen generation from the hydrolysis of sodium borohydride. *Int. J. Hydrogen Energy* 46, 726–765. <https://doi.org/10.1016/j.ijhydene.2020.09.186>
- [2]. Ai, L., Gao, X., Jiang, J., 2014. In situ synthesis of cobalt stabilized on macroscopic biopolymer hydrogel as economical and recyclable catalyst for hydrogen generation from sodium borohydride hydrolysis. *J. Power Sources* 257, 213–220. <https://doi.org/10.1016/j.jpowsour.2014.01.119>
- [3]. Akdim, O., Chamoun, R., Demirci, U.B., Zaatari, Y., Khoury, A., Miele, P., 2011a. Anchored cobalt film as stable supported catalyst for hydrolysis of sodium borohydride for chemical hydrogen storage. *Int. J. Hydrogen Energy* 36, 14527–14533. <https://doi.org/10.1016/j.ijhydene.2011.07.051>
- [4]. Akdim, O., Demirci, U.B., Miele, P., 2011b. Deactivation and reactivation of cobalt in hydrolysis of sodium borohydride. *Int. J. Hydrogen Energy* 36, 13669–13675. <https://doi.org/10.1016/j.ijhydene.2011.07.125>
- [5]. Akdim, O., Demirci, U.B., Miele, P., 2009. Acetic acid, a relatively green single-use catalyst for hydrogen generation from sodium borohydride. *Int. J. Hydrogen Energy* 34, 7231–7238. <https://doi.org/10.1016/j.ijhydene.2009.06.068>
- [6]. Ali, F., Khan, S.B., Asiri, A.M., 2019. Chitosan coated cellulose cotton fibers as catalyst for the H₂ production from NaBH₄ methanolysis. *Int. J. Hydrogen Energy* 44, 4143–4155. <https://doi.org/10.1016/j.ijhydene.2018.12.158>
- [7]. Ari, B., Ay, M., Sunol, A.K., Sahiner, N., 2019. Surface-modified carbon black derived from used car tires as alternative, reusable, and regenerable catalysts for H₂ release studies from sodium borohydride methanolysis. *Int. J. Energy Res.* 43, 7159–7172. <https://doi.org/10.1002/er.4742>
- [8]. Arzac, G.M., Fernández, A., 2020. Advances in the implementation of PVD-based techniques for the preparation of metal catalysts for the hydrolysis of sodium borohydride. *Int. J. Hydrogen Energy* 45, 33288–33309. <https://doi.org/10.1016/j.ijhydene.2020.09.041>
- [9]. Arzac, G.M., Paladini, M., Godinho, V., Beltrán, A.M., Jiménez de Haro, M.C., Fernández, A., 2018. Strong activation effect on a Ru-Co-C thin film catalyst for the hydrolysis of sodium borohydride. *Sci. Rep.* 8, 9755. <https://doi.org/10.1038/s41598-018-28032-6>
- [10]. Balbay, A., Şahin, Ö., 2014. Hydrogen Production from Sodium Borohydride in Boric Acid-water Mixtures. *Energy Sources, Part A Recover. Util. Environ. Eff.* 36, 1166–1174. <https://doi.org/10.1080/15567036.2011.618818>
- [11]. Balbay, A., Saka, C., 2018a. The effect of the concentration of hydrochloric acid and acetic acid aqueous solution for fast hydrogen production from methanol solution of NaBH₄. *Int. J. Hydrogen Energy* 43, 14265–14272. <https://doi.org/10.1016/j.ijhydene.2018.05.131>
- [12]. Balbay, A., Saka, C., 2018b. Semi-methanolysis reaction of potassium borohydride with phosphoric acid for effective hydrogen production. *Int. J. Hydrogen Energy* 43, 21299–21306. <https://doi.org/10.1016/j.ijhydene.2018.09.167>
- [13]. Bartkus, T.P., T'ien, J.S., Sung, C.-J., 2013. A semi-global reaction rate model based on experimental data for the self-hydrolysis kinetics of aqueous sodium borohydride. *Int. J. Hydrogen Energy* 38, 4024–4033. <https://doi.org/10.1016/j.ijhydene.2013.01.041>
- [14]. Baydaroglu, F., Özdemir, E., Hasimoglu, A., 2014. An effective synthesis route for improving the catalytic activity of carbon-supported Co-B catalyst for hydrogen generation through hydrolysis of NaBH₄. *Int. J. Hydrogen Energy* 39, 1516–1522. <https://doi.org/10.1016/j.ijhydene.2013.04.111>
- [15]. Boran, A., Erkan, S., Eroglu, I., 2019. Hydrogen generation from solid state NaBH₄ by using FeCl₃ catalyst for portable proton exchange membrane fuel cell applications. *Int. J. Hydrogen Energy* 44, 18915–18926. <https://doi.org/10.1016/j.ijhydene.2018.11.033>
- [16]. Brack, P., Dann, S.E., Wijayantha, K.G.U., 2015. Heterogeneous and homogenous catalysts for hydrogen generation by hydrolysis of aqueous sodium borohydride (NaBH₄) solutions. *Energy Sci. Eng.* 3, 174–188. <https://doi.org/10.1002/ese3.67>
- [17]. Cai, H., Liu, L., Chen, Q., Lu, P., Dong, J., 2016. Ni-polymer nanogel hybrid particles: A new strategy for hydrogen production from the hydrolysis of dimethylamine-borane and sodium borohydride. *Energy* 99, 129–135. <https://doi.org/10.1016/j.energy.2016.01.046>
- [18]. Çakanyıldırım, Ç., Guru, M., 2021. Farklı destekler ile hazırlanan sentetik Co-Mn-Pt katalizörünün NaBH₄ hidroliz performansı ve kinetik değerlendirmesi. *Gazi Üniversitesi Mühendislik Mimar. Fakültesi Derg.* 37, 423–438. <https://doi.org/10.17341/gazimmfd.877826>

- [19]. Chairam, S., Jarujamrus, P., Amatatongchai, M., 2019. Starch hydrogel-loaded cobalt nanoparticles for hydrogen production from hydrolysis of sodium borohydride. *Adv. Nat. Sci. Nanosci. Nanotechnol.* 10, 025013. <https://doi.org/10.1088/2043-6254/ab23fb>
- [20]. Chen, C.-W., Chen, C.-Y., Huang, Y.-H., 2009. Method of preparing Ru-immobilized polymer-supported catalyst for hydrogen generation from NaBH₄ solution. *Int. J. Hydrogen Energy* 34, 2164–2173. <https://doi.org/10.1016/j.ijhydene.2008.12.077>
- [21]. Chen, W., Ouyang, L.Z., Liu, J.W., Yao, X.D., Wang, H., Liu, Z.W., Zhu, M., 2017. Hydrolysis and regeneration of sodium borohydride (NaBH₄) – A combination of hydrogen production and storage. *J. Power Sources* 359, 400–407. <https://doi.org/10.1016/j.jpowsour.2017.05.075>
- [22]. Chen, Y., Liu, L., Wang, Y., Kim, H., 2011. Preparation of porous PVDF-NiB capsules as catalytic adsorbents for hydrogen generation from sodium borohydride. *Fuel Process. Technol.* 92, 1368–1373. <https://doi.org/10.1016/j.fuproc.2011.02.019>
- [23]. Chinnappan, A., Chung, W.-J., Kim, H., 2015a. Hypercross-linked microporous polymeric ionic liquid membranes: synthesis, properties and their application in H₂ generation. *J. Mater. Chem. A* 3, 22960–22968. <https://doi.org/10.1039/C5TA06142C>
- [24]. Chinnappan, A., Jadhav, A.H., Puguan, J.M.C., Appiah-Ntiamoah, R., Kim, H., 2015b. Fabrication of ionic liquid/polymer nanoscale networks by electrospinning and chemical cross-linking and their application in hydrogen generation from the hydrolysis of NaBH₄. *Energy* 79, 482–488. <https://doi.org/10.1016/j.energy.2014.11.041>
- [25]. Chinnappan, A., Puguan, J.M.C., Chung, W.-J., Kim, H., 2015c. Hydrogen generation from the hydrolysis of sodium borohydride using chemically modified multiwalled carbon nanotubes with pyridinium based ionic liquid and decorated with highly dispersed Mn nanoparticles. *J. Power Sources* 293, 429–436. <https://doi.org/10.1016/j.jpowsour.2015.05.096>
- [26]. Choudhury, Suman Roy, Pillai, J.N., Somaiah, B., Pareta, M., Satvilkar, P., Kumar, A., Negi, P.K., Mahtre, N.N., Choudhury, Suhasini Roy, Verma, V., Dalvi, V., Singh, P.K., Suryawanshi, S.E., Mandal, S.K., n.d. Atmospheric-independent propulsion system for phosphoric acid fuel cell-based submarines with on-board hydrogen generator.
- [27]. Demir, D.D., Salci, A., Solmaz, R., 2018. Preparation, characterization and hydrogen production performance of MoPd deposited carbon felt/Mo electrodes. *Int. J. Hydrogen Energy* 43, 10530–10539. <https://doi.org/10.1016/j.ijhydene.2018.01.030>
- [28]. Demirci, S., Yildiz, M., Inger, E., Sahiner, N., 2020. Porous carbon particles as metal-free superior catalyst for hydrogen release from methanolysis of sodium borohydride. *Renew. Energy* 147, 69–76. <https://doi.org/10.1016/j.renene.2019.08.131>
- [29]. Demirci, S., Zekoski, T., Sahiner, N., 2019. The preparation and use of p(2-acrylamido-2-methyl-1-propanesulfonic acid)-tris(dioxa-3,6-heptyl)amine (p(AMPS)-TDA-1) ionic liquid microgel in hydrogen production. *Polym. Bull.* 76, 1717–1735. <https://doi.org/10.1007/s00289-018-2465-0>
- [30]. Demirci, U.B., Akdim, O., Andrieux, J., Hannauer, J., Chamoun, R., Miele, P., 2010. Sodium Borohydride Hydrolysis as Hydrogen Generator: Issues, State of the Art and Applicability Upstream from a Fuel Cell. *Fuel Cells* 10, 335–350. <https://doi.org/10.1002/face.200800171>
- [31]. Demirci, U.B., Akdim, O., Miele, P., 2009. Ten-year efforts and a no-go recommendation for sodium borohydride for on-board automotive hydrogen storage. *Int. J. Hydrogen Energy* 34, 2638–2645. <https://doi.org/10.1016/j.ijhydene.2009.01.038>
- [32]. Demirci, U.B., Garin, F., 2008. Ru-based bimetallic alloys for hydrogen generation by hydrolysis of sodium tetrahydroborate. *J. Alloys Compd.* 463, 107–111. <https://doi.org/10.1016/j.jallcom.2007.08.077>
- [33]. Ding, J., Li, Q., Su, Y., Yue, Q., Gao, B., Zhou, W., 2018. Preparation and catalytic activity of wheat straw cellulose based hydrogel-nanometal composites for hydrogen generation from NaBH₄ hydrolysis. *Int. J. Hydrogen Energy* 43, 9978–9987. <https://doi.org/10.1016/j.ijhydene.2018.04.077>
- [34]. Dragan, M., 2022. Hydrogen Storage in Complex Metal Hydrides NaBH₄: Hydrolysis Reaction and Experimental Strategies. *Catalysts* 12, 356. <https://doi.org/10.3390/catal12040356>
- [35]. Dursun, Y.A., Solmaz, R., 2024. Fabrication of Bingöl pollen self-assembled monolayer films on copper as a novel cathode for electrochemical hydrogen production. *Int. J. Hydrogen Energy* 52, 1280–1290. <https://doi.org/10.1016/j.ijhydene.2023.11.218>
- [36]. Elsayed, M.M., 2019. Hydrogel Preparation Technologies: Relevance Kinetics, Thermodynamics and Scaling up Aspects. *J. Polym. Environ.* 27, 871–891. <https://doi.org/10.1007/s10924-019-01376-4>
- [37]. Ganesan, K., Hayagreevan, C., Rahul, R., Jeevagan, A.J., Adinaveen, T., Bhuvaneshwari, D.S., Muthukumar, P., Amalraj, M., 2022. Catalytic hydrolysis of sodium borohydride for hydrogen production using phosphorylated silica particles. *Environ. Sci. Pollut. Res.* 30, 21199–21212. <https://doi.org/10.1007/s11356-022-23672-8>
- [38]. Ghorbanloo, M., Nazari, P., 2020. A soft anionic hydrogel reactor for silver nanoparticle preparation and use in H₂ production, 4-nitrophenol reduction and alcohol oxidation. *J. Porous Mater.* 27, 37–47. <https://doi.org/10.1007/s10934-019-00794-y>
- [39]. Giappa, R.M., Tylanakis, E., Di Gennaro, M., Gkagkas, K., Froudakis, G.E., 2021. A combination of multi-scale calculations with machine learning for investigating hydrogen storage in metal organic frameworks. *Int. J. Hydrogen Energy* 46, 27612–27621. <https://doi.org/10.1016/j.ijhydene.2021.06.021>
- [40]. Grochala, W., 2015. First there was hydrogen. *Nat. Chem.* 7, 264–264. <https://doi.org/10.1038/nchem.2186>
- [41]. Guan, S., An, L., Chen, Y., Li, M., Shi, J., Liu, X., Fan, Y., Li, B., Liu, B., 2022. Stabilized cobalt-based nanofilm catalyst prepared using an ionic liquid/water interfacial process for hydrogen generation from sodium borohydride. *J. Colloid Interface Sci.* 608, 3111–3120. <https://doi.org/10.1016/j.jcis.2021.11.041>
- [42]. Hsueh, C.-L., Chen, C.-Y., Ku, J.-R., Tsai, S.-F., Hsu, Y.-Y., Tsau, F., Jeng, M.-S., 2008. Simple and fast fabrication of polymer template-Ru composite as a catalyst for hydrogen generation from alkaline NaBH₄ solution. *J. Power Sources* 177, 485–

492. <https://doi.org/10.1016/j.jpowsour.2007.11.096>
- [43]. Huang, Y., Wang, Y., Zhao, R., Shen, P.K., Wei, Z., 2008. Accurately measuring the hydrogen generation rate for hydrolysis of sodium borohydride on multiwalled carbon nanotubes/Co–B catalysts. *Int. J. Hydrogen Energy* 33, 7110–7115. <https://doi.org/10.1016/j.ijhydene.2008.09.046>
- [44]. Hydrogen Storage and Transport by Organic Hydrides and Application of Ammonia, 2019. , in: *Science and Engineering of Hydrogen-Based Energy Technologies*. Elsevier, pp. 229–236. <https://doi.org/10.1016/B978-0-12-814251-6.00011-3>
- [45]. Inger, E., 2019. Can fool's gold “pyrite” become real gold as a catalyst for clean-energy H₂ production? *Int. J. Hydrogen Energy* 44, 32124–32135. <https://doi.org/10.1016/j.ijhydene.2019.10.106>
- [46]. Inger, E., Demirci, S., Can, M., Sunol, A.K., Philippidis, G., Sahiner, N., 2020. PEI modified natural sands of Florida as catalysts for hydrogen production from sodium borohydride dehydrogenation in methanol. *Int. J. Energy Res.* <https://doi.org/10.1002/er.6060>
- [47]. Ingersoll, J.C., Mani, N., Thenmozhiyal, J.C., Muthaiah, A., 2007. Catalytic hydrolysis of sodium borohydride by a novel nickel–cobalt–boride catalyst. *J. Power Sources* 173, 450–457. <https://doi.org/10.1016/j.jpowsour.2007.04.040>
- [48]. Jia, H., Chen, X., Liu, C.-Y., Liu, X.-J., Zheng, X.-C., Guan, X.-X., Liu, P., 2018. Ultrafine palladium nanoparticles anchoring graphene oxide-ionic liquid grafted chitosan self-assembled materials: The novel organic-inorganic hybrid catalysts for hydrogen generation in hydrolysis of ammonia borane. *Int. J. Hydrogen Energy* 43, 12081–12090. <https://doi.org/10.1016/j.ijhydene.2018.04.156>
- [49]. Jung, E.S., Kim, H., Kwon, S., Oh, T.H., 2018. Fuel cell system with sodium borohydride hydrogen generator for small unmanned aerial vehicles. *Int. J. Green Energy* 15, 385–392. <https://doi.org/10.1080/15435075.2018.1464924>
- [50]. Karaman, O., 2022. Three-dimensional graphene network supported nickel-cobalt bimetallic alloy nanocatalyst for hydrogen production by hydrolysis of sodium borohydride and developing of an artificial neural network modeling to forecast hydrogen production rate. *Chem. Eng. Res. Des.* 181, 321–330. <https://doi.org/10.1016/j.cherd.2022.03.028>
- [51]. Karamveer Sheoran, Thakur, V.K., Siwal, S.S., 2022. Synthesis and overview of carbon-based materials for high performance energy storage application: A review. *Mater. Today Proc.* 56, 9–17. <https://doi.org/10.1016/j.matpr.2021.11.369>
- [52]. Kaur, A., Gangacharyulu, D., Bajpai, P.K., 2015. Kinetic studies on the NaBH₄/H₂O hydrogen storage system with CoCl₂ as a catalyst. *Bulg. Chem. Commun.* 48, 757–761.
- [53]. Kojima, Y., 2005. Hydrogen storage and generation using sodium borohydride. *R&D Rev. Toyota CRDL* 40, 31–36.
- [54]. Krishnan, P., Advani, S.G., Prasad, A.K., 2009. Thin-film CoB catalyst templates for the hydrolysis of NaBH₄ solution for hydrogen generation. *Appl. Catal. B Environ.* 86, 137–144. <https://doi.org/10.1016/j.apcatb.2008.08.005>
- [55]. Kurmoo, M., 2009. Magnetic metal–organic frameworks. *Chem. Soc. Rev.* 38, 1353. <https://doi.org/10.1039/b804757j>
- [56]. Kutyla, D., Salci, A., Kwiecińska, A., Kołczyk-Siedlecka, K., Kowalik, R., Żabiński, P., Solmaz, R., 2020. Catalytic activity of electrodeposited ternary Co–Ni–Rh thin films for water splitting process. *Int. J. Hydrogen Energy* 45, 34805–34817. <https://doi.org/10.1016/j.ijhydene.2020.05.196>
- [57]. Kwon, S., Kim, M.J., Kang, S., Kim, T., 2019. Development of a high-storage-density hydrogen generator using solid-state NaBH₄ as a hydrogen source for unmanned aerial vehicles. *Appl. Energy* 251, 113331. <https://doi.org/10.1016/j.apenergy.2019.113331>
- [58]. Lebedeva, O., Kultin, D., Kustov, L., 2024. Polymeric ionic liquids: Here, there and everywhere. *Eur. Polym. J.* 203, 112657. <https://doi.org/10.1016/j.eurpolymj.2023.112657>
- [59]. Li, Y., Zhang, Q., Zhang, N., Zhu, L., Zheng, J., Chen, B.H., 2013. Ru–RuO₂/C as an efficient catalyst for the sodium borohydride hydrolysis to hydrogen. *Int. J. Hydrogen Energy* 38, 13360–13367. <https://doi.org/10.1016/j.ijhydene.2013.07.071>
- [60]. Li, Z., Li, H., Wang, L., Liu, T., Zhang, T., Wang, G., Xie, G., 2014. Hydrogen generation from catalytic hydrolysis of sodium borohydride solution using supported amorphous alloy catalysts (Ni–Co–P/γ-Al₂O₃). *Int. J. Hydrogen Energy* 39, 14935–14941. <https://doi.org/10.1016/j.ijhydene.2014.07.063>
- [61]. Liang, Y., Dai, H.-B., Ma, L.-P., Wang, P., Cheng, H.-M., 2010. Hydrogen generation from sodium borohydride solution using a ruthenium supported on graphite catalyst. *Int. J. Hydrogen Energy* 35, 3023–3028. <https://doi.org/10.1016/j.ijhydene.2009.07.008>
- [62]. Liu, W., Cai, H., Lu, P., Xu, Q., Zhongfu, Y., Dong, J., 2013. Polymer hydrogel supported Pd–Ni–B nanoclusters as robust catalysts for hydrogen production from hydrolysis of sodium borohydride. *Int. J. Hydrogen Energy* 38, 9206–9216. <https://doi.org/10.1016/j.ijhydene.2013.05.109>
- [63]. Liu, Z., Guo, B., Chan, S.H., Tang, E.H., Hong, L., 2008. Pt and Ru dispersed on LiCoO₂ for hydrogen generation from sodium borohydride solutions. *J. Power Sources* 176, 306–311. <https://doi.org/10.1016/j.jpowsour.2007.09.114>
- [64]. Lu, L., 2019. Nanoporous noble metal-based alloys: a review on synthesis and applications to electrocatalysis and electrochemical sensing. *Microchim. Acta* 186, 664. <https://doi.org/10.1007/s00604-019-3772-3>
- [65]. Lu, Y.-C., Chen, M.-S., Chen, Y.-W., 2012. Hydrogen generation by sodium borohydride hydrolysis on nanosized CoB catalysts supported on TiO₂, Al₂O₃ and CeO₂. *Int. J. Hydrogen Energy* 37, 4254–4258. <https://doi.org/10.1016/j.ijhydene.2011.11.105>
- [66]. Luo, C., Fu, F., Yang, X., Wei, J., Wang, C., Zhu, J., Huang, D., Astruc, D., Zhao, P., 2019. Highly Efficient and Selective Co@ZIF-8 Nanocatalyst for Hydrogen Release from Sodium Borohydride Hydrolysis. *ChemCatChem* 11, 1643–1649. <https://doi.org/10.1002/cctc.201900051>

- [67]. Martínez, R.J., Godínez, L.A., Robles, I., 2023. Waste resources utilization for biosorbent preparation, sorption studies, and electrocatalytic applications, in: Valorization of Wastes for Sustainable Development. Elsevier, pp. 395–418. <https://doi.org/10.1016/B978-0-323-95417-4.00015-9>
- [68]. Meyyappan, M., Srivastava, D., 2002. Carbon nanotubes. *Handb. Nanosci. Eng. Technol.* 18-1-18–26. <https://doi.org/10.1177/0022034513490957>
- [69]. Nie, M., Zou, Y.C., Huang, Y.M., Wang, J.Q., 2012. Ni–Fe–B catalysts for NaBH₄ hydrolysis. *Int. J. Hydrogen Energy* 37, 1568–1576. <https://doi.org/10.1016/j.ijhydene.2011.10.006>
- [70]. Onat, E., Çevik, S., Şahin, Ö., Horoz, S., İzgi, M.S., 2021. Investigation of high catalytic activity catalyst for high hydrogen production rate: Co-Ru@MOF. *J. Aust. Ceram. Soc.* 57, 1389–1395. <https://doi.org/10.1007/s41779-021-00643-9>
- [71]. Osman, A.I., Mehta, N., Elgarahy, A.M., Hefny, M., Al-Hinai, A., Al-Muhtaseb, A.H., Rooney, D.W., 2022. Hydrogen production, storage, utilisation and environmental impacts: a review. *Environ. Chem. Lett.* 20, 153–188. <https://doi.org/10.1007/s10311-021-01322-8>
- [72]. Özkar, S., Zahmakıran, M., 2005. Hydrogen generation from hydrolysis of sodium borohydride using Ru(0) nanoclusters as catalyst. *J. Alloys Compd.* 404–406, 728–731. <https://doi.org/10.1016/j.jallcom.2004.10.084>
- [73]. Ozturk, O.F., Demirci, S., Sengel, S.B., Sahiner, N., 2018. Highly regenerable ionic liquid microgels as inherently metal-free green catalyst for H₂ generation. *Polym. Adv. Technol.* 29, 1426–1434. <https://doi.org/10.1002/pat.4254>
- [74]. Paladini, M., Arzac, G.M., Godinho, V., Haro, M.C.J. De, Fernández, A., 2014. Supported Co catalysts prepared as thin films by magnetron sputtering for sodium borohydride and ammonia borane hydrolysis. *Appl. Catal. B Environ.* 158–159, 400–409. <https://doi.org/10.1016/j.apcatb.2014.04.047>
- [75]. Paladini, M., Arzac, G.M., Godinho, V., Hufschmidt, D., de Haro, M.C.J., Beltrán, A.M., Fernández, A., 2017. The role of cobalt hydroxide in deactivation of thin film Co-based catalysts for sodium borohydride hydrolysis. *Appl. Catal. B Environ.* 210, 342–351. <https://doi.org/10.1016/j.apcatb.2017.04.005>
- [76]. Paterson, R., Alharbi, A.A., Wills, C., Dixon, C., Šiller, L., Chamberlain, T.W., Griffiths, A., Collins, S.M., Wu, K., Simmons, M.D., Bourne, R.A., Lovelock, K.R.J., Seymour, J., Knight, J.G., Doherty, S., 2022. Heteroatom modified polymer immobilized ionic liquid stabilized ruthenium nanoparticles: Efficient catalysts for the hydrolytic evolution of hydrogen from sodium borohydride. *Mol. Catal.* 528, 112476. <https://doi.org/10.1016/j.mcat.2022.112476>
- [77]. Retnamma, R., Novais, A.Q., Rangel, C.M., 2011. Kinetics of hydrolysis of sodium borohydride for hydrogen production in fuel cell applications: A review. *Int. J. Hydrogen Energy* 36, 9772–9790. <https://doi.org/10.1016/j.ijhydene.2011.04.223>
- [78]. Sahiner, N., 2017. Modified multi-wall carbon nanotubes as metal free catalyst for application in H₂ production from methanolysis of NaBH₄. *J. Power Sources* 366, 178–184. <https://doi.org/10.1016/j.jpowsour.2017.09.041>
- [79]. Sahiner, N., 2013. Soft and flexible hydrogel templates of different sizes and various functionalities for metal nanoparticle preparation and their use in catalysis. *Prog. Polym. Sci.* 38, 1329–1356. <https://doi.org/10.1016/j.progpolymsci.2013.06.004>
- [80]. Sahiner, N., Demir, S., Yildiz, S., 2014. Magnetic colloidal polymeric ionic liquid synthesis and use in hydrogen production. *Colloids Surfaces A Physicochem. Eng. Asp.* 449, 87–95. <https://doi.org/10.1016/j.colsurfa.2014.02.046>
- [81]. Sahiner, N., Demirci, S., 2017. Natural microgranular cellulose as alternative catalyst to metal nanoparticles for H₂ production from NaBH₄ methanolysis. *Appl. Catal. B Environ.* 202, 199–206. <https://doi.org/10.1016/j.apcatb.2016.09.028>
- [82]. Sahiner, N., Demirci, S., 2016. Very fast H₂ production from the methanolysis of NaBH₄ by metal-free poly(ethylene imine) microgel catalysts. *Int. J. Energy Res.* <https://doi.org/10.1002/er.3679>
- [83]. Sahiner, Nurettin, Demirci, S., 2016. PEI-based hydrogels with different morphology and sizes: Bulk gel, microgel, and cryogel for catalytic energy and environmental catalytic applications. *Eur. Polym. J.* 76, 156–169. <https://doi.org/10.1016/j.eurpolymj.2016.01.046>
- [84]. Sahiner, N., Sengel, S.B., 2017. Environmentally benign halloysite clay nanotubes as alternative catalyst to metal nanoparticles in H₂ production from methanolysis of sodium borohydride. *Fuel Process. Technol.* 158, 1–8. <https://doi.org/10.1016/j.fuproc.2016.12.009>
- [85]. Sahiner, N., Sengel, S.B., 2016. Quaternized polymeric microgels as metal free catalyst for H₂ production from the methanolysis of sodium borohydride. *J. Power Sources* 336, 27–34. <https://doi.org/10.1016/j.jpowsour.2016.10.054>
- [86]. Sahiner, N., Seven, F., Al-Lohedan, H., 2015. Super-fast hydrogen generation via super porous Q-P(VI)-M cryogel catalyst systems from hydrolysis of NaBH₄. *Int. J. Hydrogen Energy* 40, 4605–4616. <https://doi.org/10.1016/j.ijhydene.2015.02.049>
- [87]. Sahiner, N., Yildiz, S., 2014. Preparation of superporous poly(4-vinyl pyridine) cryogel and their templated metal nanoparticle composites for H₂ production via hydrolysis reactions. *Fuel Process. Technol.* 126, 324–331. <https://doi.org/10.1016/j.fuproc.2014.05.025>
- [88]. Saka, C., 2024. Fabrication of protonated chitosan/montmorillonite catalyst for hydrogen production via sodium borohydride in the optimum methanol/propylene glycol mixture. *Int. J. Hydrogen Energy* 65, 410–420. <https://doi.org/10.1016/j.ijhydene.2024.03.371>
- [89]. Saka, C., 2023. Highly active hydrogen generation from sodium borohydride methanolysis and ethylene glycolysis reactions using protonated chitosan-zeolite hybrid metal-free particles. *Appl. Catal. B Environ.* 325, 122335. <https://doi.org/10.1016/j.apcatb.2022.122335>
- [90]. Saka, C., 2021a. Highly active and durable hydrogen release in NaBH₄ methanolysis reaction with sulphur and phosphorus-doped metal-free microalgal carbon nanoparticles. *Appl. Catal. B Environ.* 292, 120165.

<https://doi.org/10.1016/j.apcatb.2021.120165>

- [91]. Saka, C., 2021b. Very efficient dehydrogenation of methanolysis reaction with nitrogen doped *Chlorella Vulgaris* microalgae carbon as metal-free catalysts. *Int. J. Hydrogen Energy* 46, 20961–20971. <https://doi.org/10.1016/j.ijhydene.2021.03.220>
- [92]. Saka, C., Balbay, A., 2019. Influence of process parameters on enhanced hydrogen generation via semi-methanolysis and semi-ethanolysis reactions of sodium borohydride using phosphoric acid. *Int. J. Hydrogen Energy* 44, 30119–30126. <https://doi.org/10.1016/j.ijhydene.2019.09.172>
- [93]. Samatya Ölmez, S., Balbay, A., Saka, C., 2022. Phosphorus doped carbon nanodots particles based on pomegranate peels for highly active dehydrogenation of sodium borohydride in methanol. *Int. J. Hydrogen Energy* 47, 31647–31655. <https://doi.org/10.1016/j.ijhydene.2022.07.091>
- [94]. Santos, D.M.F., Sequeira, C.A.C., 2011. Sodium borohydride as a fuel for the future. *Renew. Sustain. Energy Rev.* 15, 3980–4001. <https://doi.org/10.1016/j.rser.2011.07.018>
- [95]. Seven, F., Sahiner, N., 2014. Modified macroporous P(2-hydroxyethyl methacrylate) P(HEMA) cryogel composites for H₂ production from hydrolysis of NaBH₄. *Fuel Process. Technol.* 128, 394–401. <https://doi.org/10.1016/j.fuproc.2014.08.008>
- [96]. Singh, C., Mukhopadhyay, S., Hod, I., 2021. Metal–organic framework derived nanomaterials for electrocatalysis: recent developments for CO₂ and N₂ reduction. *Nano Converg.* 8, 1. <https://doi.org/10.1186/s40580-020-00251-6>
- [97]. Solmaz, R., Yüksel, H., 2019. Fabrication, characterization and application of three-dimensional copper nanodomes as efficient cathodes for hydrogen production. *Int. J. Hydrogen Energy* 44, 14108–14116. <https://doi.org/10.1016/j.ijhydene.2019.02.112>
- [98]. Thoniyot, P., Tan, M.J., Karim, A.A., Young, D.J., Loh, X.J., 2015. Nanoparticle–Hydrogel Composites: Concept, Design, and Applications of These Promising, Multi-Functional Materials. *Adv. Sci.* 2. <https://doi.org/10.1002/advs.201400010>
- [99]. Uzundurukan, A., Devrim, Y., 2019. Hydrogen generation from sodium borohydride hydrolysis by multi-walled carbon nanotube supported platinum catalyst: A kinetic study. *Int. J. Hydrogen Energy* 44, 17586–17594. <https://doi.org/10.1016/j.ijhydene.2019.04.188>
- [100]. Walter, J.C., Zurawski, A., Montgomery, D., Thornburg, M., Revankar, S., 2008. Sodium borohydride hydrolysis kinetics comparison for nickel, cobalt, and ruthenium boride catalysts. *J. Power Sources* 179, 335–339. <https://doi.org/10.1016/j.jpowsour.2007.12.006>
- [101]. Wang, M.C., Ouyang, L.Z., Liu, J.W., Wang, H., Zhu, M., 2017. Hydrogen generation from sodium borohydride hydrolysis accelerated by zinc chloride without catalyst: A kinetic study. *J. Alloys Compd.* 717, 48–54. <https://doi.org/10.1016/j.jallcom.2017.04.274>
- [102]. Wang, X., Zhao, Y., Peng, X., Wang, J., Jing, C., Tian, J., 2015. Synthesis and characterizations of CoPt nanoparticles supported on poly(3,4-ethylenedioxythiophene)/poly(styrenesulfonate) functionalized multi-walled carbon nanotubes with superior activity for NaBH₄ hydrolysis. *Mater. Sci. Eng. B* 200, 99–106. <https://doi.org/10.1016/j.mseb.2015.07.002>
- [103]. Xiang, W., Yang, N., Li, X., Linnemann, J., Hagemann, U., Ruediger, O., Heidelmann, M., Falk, T., Aramini, M., DeBeer, S., Muhler, M., Tschulik, K., Li, T., 2022. 3D atomic-scale imaging of mixed Co-Fe spinel oxide nanoparticles during oxygen evolution reaction. *Nat. Commun.* 13, 179. <https://doi.org/10.1038/s41467-021-27788-2>
- [104]. Xu, G.-R., An, Z.-H., Xu, K., Liu, Q., Das, R., Zhao, H.-L., 2021. Metal organic framework (MOF)-based micro/nanoscaled materials for heavy metal ions removal: The cutting-edge study on designs, synthesis, and applications. *Coord. Chem. Rev.* 427, 213554. <https://doi.org/10.1016/j.ccr.2020.213554>
- [105]. Yang, C.-C., Chen, M.-S., Chen, Y.-W., 2011. Hydrogen generation by hydrolysis of sodium borohydride on CoB/SiO₂ catalyst. *Int. J. Hydrogen Energy* 36, 1418–1423. <https://doi.org/10.1016/j.ijhydene.2010.11.006>
- [106]. Zaier, I., Metin, O., 2021. One-pot synthesis of graphene hydrogel-anchored cobalt-copper nanoparticles and their catalysis in hydrogen generation from ammonia borane. *Turkish J. Chem.* 45. <https://doi.org/10.3906/kim-2107-32>
- [107]. Zhang, J., Lin, F., Yang, L., He, Z., Huang, X., Zhang, D., Dong, H., 2020. Ultrasmall Ru nanoparticles supported on chitin nanofibers for hydrogen production from NaBH₄ hydrolysis. *Chinese Chem. Lett.* 31, 2019–2022. <https://doi.org/10.1016/j.ccllet.2019.11.042>
- [108]. Zhang, J.S., Delgass, W.N., Fisher, T.S., Gore, J.P., 2007. Kinetics of Ru-catalyzed sodium borohydride hydrolysis. *J. Power Sources* 164, 772–781. <https://doi.org/10.1016/j.jpowsour.2006.11.002>
- [109]. Zhao, L., Li, Q., Su, Y., Yue, Q., Gao, B., 2017. A novel Enteromorpha based hydrogel for copper and nickel nanoparticle preparation and their use in hydrogen production as catalysts. *Int. J. Hydrogen Energy* 42, 6746–6756. <https://doi.org/10.1016/j.ijhydene.2017.02.092>
- [110]. Zhong, H., Ouyang, L., Liu, J., Peng, C., Zhu, X., Zhu, W., Fang, F., Zhu, M., 2018. Sodium borohydride regeneration via direct hydrogen transformation of sodium metaborate tetrahydrate. *J. Power Sources* 390, 71–77. <https://doi.org/10.1016/j.jpowsour.2018.04.037>
- [111]. Zhu, J., Li, R., Niu, W., Wu, Y., Gou, X., 2012. Facile hydrogen generation using colloidal carbon supported cobalt to catalyze hydrolysis of sodium borohydride. *J. Power Sources* 211, 33–39. <https://doi.org/10.1016/j.jpowsour.2012.03.051>
- [112]. Zhuang, D.-W., Kang, Q., Muir, S.S., Yao, X., Dai, H.-B., Ma, G.-L., Wang, P., 2013. Evaluation of a cobalt–molybdenum–boron catalyst for hydrogen generation of alkaline sodium borohydride solution–aluminum powder system. *J. Power Sources* 224, 304–311. <https://doi.org/10.1016/j.jpowsour.2012.09.106>



RESEARCH ARTICLE

The Analysis of Water Losses and Leakages in Drinking Water Networks Using Scada System: A Case Study from Yozgat

^{1,*} Yunus GÖRKEM, and ² Muhammet Furkan KARAMAN, and ³ Şekip Esat HAYBER

^{1,*}Kırşehir Ahi Evran University, Kaman Vocational School, Department of Electricity and Energy, Kırşehir, Türkiye
yunus.gorkem@ahievran.edu.tr, [Orcid.0000-0002-8776-6951](https://orcid.org/0000-0002-8776-6951)

²Kırşehir Ahi Evran University, Institute of Natural and Applied Sciences, Department of Advanced Technologies, Kırşehir, Türkiye
m.furkan-karaman@hotmail.com, [Orcid.0000-0002-5500-8240](https://orcid.org/0000-0002-5500-8240)

³Bursa Uludağ University, Faculty of Engineering, Electrical-Electronics Engineering Department, Bursa, Türkiye
sehayber@uludag.edu.tr, [Orcid.0000-0003-0062-3817](https://orcid.org/0000-0003-0062-3817)

Citation:

Görkem, Y., Karaman, M.F., Hayber, Ş.E. (2024). *The Analysis of Water Losses and Leakages in Drinking Water Networks Using Scada System: A Case Study from Yozgat*, Journal of Science Technology and Engineering Research, 5(2):223-243. DOI:10.53525/jster.1575916

HIGHLIGHTS

- This study contributes significantly to the existing literature on remote water quality monitoring using SCADA systems.
- The implementation of SCADA-based management strategies to reduce water losses offers an effective solution for the management and optimization of resources in related domains.
- The study presents a compelling case for the significant impact of SCADA systems in water distribution, demonstrating their potential to reduce physical water losses markedly.
- The findings are crucial for ensuring clean water through real-time monitoring of sediment formation, aiding in the prevention of infectious diseases.

Article Info

Received: October 30, 2024

Accepted: December 4, 2024

DOI:

10.53525/jster.1575916

***Corresponding Author:**

Yunus GÖRKEM
yunus.gorkem@ahievran.edu.tr
Phone: +90 535 4908265

ABSTRACT

For water to be delivered to people cleanly and healthily, the tanks in which it is stored before being made available must also be reliable and clean. Preventing the transmission of infectious diseases through water necessitates rigorous purification and disinfection of water stored in tanks. For this reason, monitoring the sediments in the storage tank and their properties, such as pH, pressure, and temperature, are necessary in real-time. With SCADA systems, water flow is monitored remotely by providing central control and monitoring in drinking water distribution. The data collected allows for the automatic detection of tank issues, intervention in the system, and effective leak management, thereby ensuring the effective delivery of water to users. In this study, data from four pumping stations and 13 reservoirs in Yozgat were subjected to analysis, and all processes from the water source to public use were remotely controlled via the SCADA system. Prior to the implementation of SCADA, the total water losses in Yozgat Province were recorded at 64.35%, with physical losses accounting for 27.59%. From 2019 to 2023, the implementation of SCADA resulted in a 51% reduction in physical losses, thereby demonstrating the effectiveness of the system in water management and its scalability for addressing global water scarcity. Furthermore, the system guarantees the prompt prevention of sediment formation, thereby ensuring the delivery of clean and safe water to users.

Keywords: Water Tank, pH, Pressure, Sediment

I. INTRODUCTION

Türkiye is not considered a water-rich country, and it is anticipated that with the growing population, the country may face a significant water crisis in the coming years (Aslan, 2016). For this reason, institutions responsible for water management in the country must establish complete control over all processes leading to water delivery to the end user. However, managing water distribution systems is challenging because they consist of complex networks of interconnected pipes, pumps, valves, and controls. Many of these components are buried, making maintenance and repair operations particularly difficult. Despite these challenges and complexities, distribution systems are expected to supply households and other areas with safe drinking water under pressure (Grigg, 2024). Water management oversees groundwater, drinking water, and wastewater systems. The rapid depletion of water resources, particularly in cities with increasing population density, has shortly heightened the risk of water scarcity. Due to the rising urbanization rate, smart systems must manage water consumption (Uçar, 2022). To address this issue, institutions responsible for water management are undertaking intensive efforts.

In contemporary times, supervisory control and data acquisition (SCADA) systems are employed across various fields, particularly in communication, transportation, and imaging technologies. SCADA is a data-based control and monitoring system. Widely used across various fields, SCADA has played a direct role in developing new methods and engineering products. Predictive solutions to future water scarcity depend on establishing an effective control mechanism in water management systems (WMS). In this regard, it is evident that the SCADA system will provide significant advantages. By enabling centralized monitoring of the entire system, SCADA will expedite the resolution process of disruptions. In addition to tracking illegal water usage and water losses due to malfunctions, SCADA will also facilitate comprehensive water management by detecting potential malfunctions in water storage tanks above and below ground. SCADA systems collect information from sensors installed on network lines, valves, reservoirs, and pumping stations used in distribution, execute control operations requested by operators through remote terminals, and generate statistical data from measurements taken at stations (SUEN, 2017). Implementing integrated systems like SCADA can potentially reduce recorded water losses (Klosok-Bazan et al., 2021).

A. *Regional Studies in Turkey*

This section will present regional studies related to WMS, leak detection methods, and the use of smart systems in water management in Turkey. An investigation of the amounts of water produced and consumed in Konya province revealed the water loss caused by unknown leaks and illegal connections in the network (Demir, 2001). Although the balance between the flow from wells and the flow at the pump output was maintained using electronic flow meters, the volume of water loss could not be determined due to erroneous readings from old meters. To overcome this issue and identify losses and leaks, meters were installed at meterless usage sites at regular intervals to conduct readings. The data was converted into annual consumption to calculate the unknown water quantity at usage sites. By subtracting the billed water amount from the produced water quantity and the amount used at other locations, the water loss from unknown leaks and illegal connections in the network was determined to be 22.78% of the total water produced. Another study conducted in Konya examined the water loss in the drinking water network of Konya Province by analyzing data obtained from the Konya Water and Sewerage Administration (KOSKİ) for the years 2015-2017 (Körpe, 2018). Water losses from malfunctions in the drinking water network were identified, and the financial cost of these losses to KOSKİ was calculated (Görgülü, 2022). In Kayseri province, the causes and degrees of water loss in three drinking water network pilot areas were investigated using statistical methods. Variables that could directly or indirectly affect the formation of water losses were determined for each pilot area from statistical records, urban planning documents, and network measurements (Pala, 2002). Between 2006 and 2022, data from 8,224 residential water meters, subscribers, and consumption in Kayseri province were analyzed using machine learning methods to identify abnormal drinking water consumption (Güney and Selvi, 2023). In Istanbul, a GIS-based decision support system was applied for water management in drinking water distribution systems (Aydın, 2007). In another study in Istanbul, a case study was conducted in the Sultanahmet and Fatih pilot areas to identify water loss components and determine necessary actions (Karaca, 2009). In Sakarya province, applications were made to reduce water losses through pressure management in the city center of Adapazarı (Cinal, 2009). The software was developed to integrate the database of the SCADA system established for remote monitoring and control of drinking

water and sewage systems in Sakarya Water and Sewerage Administration (SASKİ) with the GIS database (Çelik et al., 2016). An assessment of existing water resources in Sivas province was carried out considering future population changes and water needs (Yıldız and Değirmenci, 2010). The levels of water loss and leakage in the drinking water network in the Esentepe and Yunus Emre neighborhoods of Sivas city center were identified (Karakuş et al., 2013). In a study conducted in Diyarbakır city center, information technologies were utilized to detect losses and leaks in an isolated urban water distribution network, and it was reported that physical losses were minimized using these methods (Songur, 2016). In Diyarbakır's central districts (Sur, Bağlar, Yenişehir, and Kayapınar), studies were conducted on water losses in the distribution network using SCADA systems (Yüksel et al., 2018). In the Gölbaşı district of Ankara, improvements to prevent physical water losses in the customer area managed by the Ankara Water and Sewerage Administration (ASKİ) were reported to have repeated failures without a SCADA system, emphasizing the importance of continuous monitoring with a SCADA-like system (Songur et al., 2021). In Kilis, studies were conducted to determine residential water consumption through measurements from the network (Öztürk and Abama, 2023). Antalya determined the water loss ratio by examining the Kaleiçi drinking water distribution network data for 2015 and 2016, using subscriber consumption values, SCADA data, and a water balance table (Gülaydın, 2017). In Tekirdağ, SCADA applications implemented by Tekirdağ Water and Sewerage Administration (TESKİ) within the framework of smart water management were examined (Başa and Kurt, 2017). Results of water balance studies conducted by the Şanlıurfa Water and Sewerage Administration (ŞUSKİ) between 2015 and 2016 to detect drinking water losses and leaks were shared (Gerger and Aslan, 2019). The study reported that the volume of water loss was significantly above desired levels and identified that the high-water loss was due to operating the network at pressures far exceeding regulatory values. Research on urban water management in the Merzifon district of Amasya province addressed groundwater, drinking water, and wastewater management from a holistic perspective (Tuna and Armut, 2021). A water balance was established to determine the level of water loss and leakage in the drinking water network in Merzifon, and the importance of protecting water resources from physical losses in the water network was emphasized (Tuna et al., 2023). In a study for Erzincan province, drinking water network data from 2014-2020 were examined, and comparisons were made between data recorded before and after the installation of the SCADA system in 2018 (Bulut and Ertugay, 2022). The study found that the total physical and administrative water loss rate was 64.46% before SCADA implementation and decreased to 36.53% with SCADA use; physical water loss decreased from 27.89% to 13.64% with SCADA use. In a study conducted for Muş province, water network and drinking water data from 2017-2023 were analyzed, and comparisons were made between data before and after the integration of the SCADA system with the new drinking water network line completed in 2022 (Güçlü, 2024).

B. Studies Across Turkey

This section presents broader and more generalizable studies on WMS, leak detection methods, and the use of smart systems in water management in Turkey. An assessment of water losses in distribution systems was conducted by examining the water resource potential in Turkey (Toprak et al., 2007a). Information on the PROWAT project, in which Turkey is a partner, was provided regarding water losses and potential solutions (Toprak et al., 2007b). Another study emphasized the importance of digitization activities in preventing water losses. It provided insights into the measures taken by municipalities due to recent actions by the Ministry of Forestry and Water Affairs (Alicı and Özaslan, 2016). It was reported that SCADA systems could not be effectively utilized due to the lack of digitization of all infrastructure facilities. Thus, the lost water could not be reduced to the desired level. By examining the water loss rates in metropolitan municipalities, the benefits and issues arising from using SCADA systems, one of the smart water technologies preferred by municipalities in combating water losses, were identified (Akıllı and Özaslan, 2017). The documents of the water and sewerage administrations (SUKİ) of 30 metropolitan municipalities in Turkey were reviewed to analyze differences in performance indicators and their causes despite the SUKİs being subject to the same regulations (Özaslan and Alicı, 2018). To examine the sustainable management of water resources in the context of the European Union (EU) Water Framework Directive (WFD), a general framework was provided on the fundamental principles and institutional requirements introduced by the WFD for water management and leakage data from some cities in Turkey and other countries were analyzed (Dilcan et al., 2018). Water losses in drinking water networks in Turkey were classified (Karakaya and Toprak, 2018). Efforts to minimize leakage in

water distribution systems through pressure optimization were studied (Köker Gökçöl, 2018). The contributions of software developed for efficiently managing isolated sub-regions by determining the physical leakage amounts in the network to operational efficiency and water management were demonstrated (Kılıç, 2021). To enable systematic, planned, and sustainable water management, calculation tools for water loss analyses were developed and tested on five different pilot datasets (Firat et al., 2021). The impact of real-time control of pressure-reducing valves on water losses in drinking water networks was studied through model analysis (Olmuştur, 2021). Information on the components of water supply and distribution systems, problems encountered in their construction, solutions, and the current and potential uses of Industry 4.0, Internet of Things, cloud computing, machine learning, and optimization techniques in improving system efficiency was provided. The characteristics introduced to WMS by SCADA systems were also discussed (Kurban, 2022). Leaks were calculated using the Fixed and Variable Area Discharges (FAVAD) equation, which establishes a relationship between leakage and pressure in isolated measurement areas where pressure regulation was applied and compared with field data (Akdemir and Yılmaz, 2023). The study found that the FAVAD equation, which theoretically relates pressure and leakage, provided accurate results only for constant discharge pressure control and was insufficient for other methods. Thus, a new method was developed for calculating the benefits derived from leaks for all pressure regulation methods. Based on the analysis results of the standard water balance (SWB) tables of some metropolitan municipalities in Turkey, it was revealed that errors in detecting administrative water losses led to mistakes in calculating physical water losses and suggestions for solving this problem were provided (Akdeniz and Muhammetoğlu, 2023). To identify the causes of pipe failures, which are a significant factor in physical water losses, factors such as pipe material, age, diameter, burst pressure, and average water pressure were examined using a logistic regression model, and a success rate of 70.1% was reported (Karadirek et al., 2024).

C. Global Studies

This section presents some studies conducted worldwide on WMS, leak detection methods, and the use of smart systems in water management. In a pressure test applied to detect water leaks in the water network of Mecca, it was found that the water loss due to leaks was relatively high, and recommendations were provided on the measures to be taken to reduce the leaks to acceptable levels (Al-Ghamdi and Gutub, 2002). In 2022, Ma et al. employed SCADA systems to identify leakage in urban water distribution networks in real time. An algorithm applicable to SCADA systems in water distribution networks (SDNs) was developed, proposing a new model for leak detection (Radaković and Šenk, 2020). Decision support systems were used to detect and control leaks in water distribution systems (Shabangu et al., 2020). Considering that monitoring and remote-control devices could increase the likelihood of system failures and cyber-attacks, an automatic early warning system for detecting cyber-attacks in water distribution systems was proposed (Brentan et al., 2021). Machine learning models were developed to detect leaks in SDNs, and it was reported that leak detection could be achieved quickly and with high accuracy using machine learning methods (Fan et al., 2021). To objectively compare the performance of methods for detecting leaks and leak areas based on SCADA systems, the results of the 2020 "Leak Detection and Isolation Methods Battle" (BattLeDIM) competition and the analysis of methods used to solve problems in the competition were presented (Vrachimis et al., 2022). A PLC-controlled system was developed to automate water distribution, detect theft, prevent waste, and determine water's pH and dissolved solid content (Babu et al., 2023). An advanced metering infrastructure (AMI) system was proposed for leak detection in water distribution networks, and AMI and SCADA systems were compared (Jun and Lansley, 2023). The combined use of SCADA and GIS for delivering produced water to consumers without loss and reducing non-revenue water (NRW) was reported to achieve successful results in controlling and monitoring water management, early problem detection, increased efficiency, and reduced water loss (Ahmed, 2024). SCADA systems were used to improve pressure monitoring and control to reduce water loss in urban water systems (Stătescu et al., 2024). In a water distribution system serving 200,000 people, the risk of water loss from pipes with potential leak sources was analyzed, and information on appropriate pipe selection was provided (Tchórzewska-Cieślak et al., 2024). A systematic method for the optimal placement of pressure sensors for leak detection in SDNs was proposed (Tornyeviadzi et al., 2024).

This study examined the use of SCADA in the WMS of Yozgat Province and reported that using SCADA system data in field teams' work planning significantly reduced the water loss rate. A comprehensive water management mechanism was created by monitoring water levels, turbidity, temperature, pressure, pH, and chlorine values in water storage tanks in real time from a single center using the SCADA system. While the study is specific to Yozgat, the generalizable data presented is considered a valuable contribution to the literature regarding widespread use and is expected to illuminate future research in similar fields.

This research presents a comprehensive review of the technical and economic impact of SCADA applications in reducing citywide water losses, with a particular focus on the case study of Yozgat. In contrast to previous research, this study examines the issue in greater detail and depth.

II. MATERIAL AND METHODS

A. System Equipment

The automation system installation for Yozgat Municipality's pumping stations, water collection, and distribution reservoirs, as well as the transfer of data to the cloud-based WMS via a wireless communication network, and the subsequent data interpretation processes, are examined under this heading. The study covers the procurement, installation, and commissioning of control panels planned for the water collection reservoirs, pumping stations, and primary distribution reservoirs within Yozgat Municipality's service area. The scope includes supplying and installing 13 reservoir control panels, updating existing panels at four pumping stations, six pumping SCADA panels, three master panels, and 2 data point SCADA panels. All panels and mechanical components were transported to the designated locations by the institution, and the necessary electrical, physical, and mechanical installations were completed. The study also encompasses the planned refurbishment of the Main Branch, 13 water reservoirs, and four pumping stations, including mechanical installations, remote control and monitoring systems, and water production and distribution network integration into the WMS. The technical design of the WMS control panels was completed, and the panels were manufactured accordingly. Connections between WMS panels and field equipment at specified locations were established, and regional communication infrastructure was set up within the panels. At pressure control locations, WMS panels and pressure, residual chlorine, turbidity sensors, and PT100 temperature sensors were installed. Existing equipment (sensors, flow meters, liquid chlorine pumps, electric actuators, etc.) at all installation sites will be integrated into the new system, enabling monitoring and control via the WMS. The PLC and its modules include at least nine digital inputs, six digital outputs, five analog inputs (4-20mA), two analog outputs (4-20mA), and 4 PT100/thermocouple inputs. Additionally, slim-type relays with 24V DC coils were installed to provide isolation for PLC digital outputs. The panel also includes a UPS with a minimum capacity of 600 VA, a 220V AC power supply, a panel socket, an automatic fuse, a Class C automatic switch, and terminal blocks for input and output connections. All signal cables within the panel were labeled at both ends. NYAF cables, suitable for the current of drivers and other devices, were used for connections, and cables were concealed with perforated cable channels to avoid exposure. The installation of control panels and leading panel equipment, sensors used in drinking water and pumping stations, and other system components was completed, finalizing the hardware operations.

The web-based and HTML5-compatible software interface can perform monitoring, management, graphing, and analysis tasks without additional plugins. The interface software does not utilize plugins that require installation, such as Shockwave, Flash, Java Applet, ActiveX, or Silverlight. It is compatible with all modern browsers, including Internet Explorer, Chrome, Firefox, and Safari. Since the interface software is web-based, it is independent of any operating system and works seamlessly on Linux, Windows, and macOS. The interface design is optimized for mobile device sizes and functions effectively on mobile operating systems (Android, iOS) and devices. The monitoring screens feature dynamic interface updates. Data updates are handled through asynchronous JavaScript scripts, with update intervals ranging from 2 to 10 seconds, depending on the internet speed of the PLC, WMS server, and the user. Parameters on the monitoring screens, such as healthy levels, water cones, reservoir levels, and water flow, are displayed with easily distinguishable animations. For parameters with maximum values, such as reservoir levels, the interface will scale them appropriately to ensure clarity and ease of understanding.

SCADA systems provide centralized control and monitoring for drinking water distribution. These systems manage water distribution by monitoring water flow from remote locations, collecting and transmitting this information, controlling storage tanks, and automatically intervening in emergencies. They are generally controlled systems that observe and record processes within the SCADA environment. A series of functions, including data collection, transfer, computer-based storage, automatic notification, and remote activity control, can describe SCADA. The capability of SCADA systems to use various communication methods for information exchange is crucial. This capability allows SCADA systems to receive and send data from and to remote or other digital systems. SCADA systems can communicate through various protocols, including telephone lines, UHF/VHF bands, microwave systems, satellite systems, and fiber optic cables.

Building on this, particularly in drinking water remote monitoring systems, the integration of SCADA-connected measurements has made these systems more accessible and widespread today. As a result, it has become possible to monitor and control water quality remotely.



Figure 1. Plan of water storage tanks in Yozgat city center.

Figure 1 shows the locations of the water storage tanks in Yozgat city center. Sediment formation in the tanks is monitored using level sensors, the water supplied to the system is measured with flow meters, and losses and leaks are assessed by comparing the volume of water exiting the tank with the metered volume of water. These parameters are controlled remotely through the SCADA system. The equipment used at the specified work points in Figure 1 is detailed in Table I.

B. Data Monitoring from the SCADA Interface

Figure 2 illustrates the real-time data monitoring from tanks located in various regions via the SCADA interface. These screens show the tank's water volume, chlorine level, turbidity, pH value, and outgoing water in m^3/h . Additionally, the panel temperature and indoor temperature are displayed in $^{\circ}\text{C}$. Blue pipes represent inlets, red pipes represent outlets, and green pipes are overflow discharge pipes. Using the white-colored on/off valves shown on the pipes, blue pipes fill the tanks from the top, while red pipes discharge near the zero-level point.

Figure 3 shows the main monitoring screen of the SCADA system. The screen displays data from the pumping stations of various cities. Additionally, the alarm status for units with a lost communication connection is monitored

on this screen.

Table I. Equipment at the work points

Equipment	Bahçeşehir water tank 500 m ³	Muslubelen DSI 4000 m ³	Muslubelen DSI 2000 m ³	Muslubelen pumping station	Sanayi water tank 900 m ³	Treatment pumping station	Prison water tank 500 m ³	Nohutlu water tank 500 m ³	Ahmet Efendi water tank 500 m ³	Bağlar İçi pumping station	Main water tank 15.000 m ³	Fatih pumping station	Fatih water tank 1	Fatih water tank 2	Toki water tank 1000 m ³	Toki water tank 500 m ³	Main branch water tank	Total	
Level sensor	2	2	2	2	2	4	2	2	2	2	2	2	2	2	2	2	2	2	36
Pressure sensor				2		6				2		6							16
Differential pressure sensor				2		4				2		4							12
PT 100 temperature sensor	2	2	2	9	2	16	2	2	2	9	2	16	2	2	2	2	2	2	76
Master SCADA panel						2						1							3
Water tank SCADA panel	1	1	1		1		1	1	1		1		1	1	1	1	1	1	13
Pumping SCADA panel				1		2				1		2							6
Data point SCADA panel						1						1							2
DN 80 electromagnetic flow meter												1							1
DN 100 electromagnetic flow meter						2													2
DN 150 electromagnetic flow meter					1	1		1					1						4
DN 200 electromagnetic flow meter	2				1			1						1	1				6
DN 250 electromagnetic flow meter								1											1
DN 300 electromagnetic flow meter							1												1
Ultrasonic flow meter											1								1
Solar energy production system	1				1	1							1	1	1	1			7
Residual chlorine and turbidity			1								1								2
Electrical and mechanical renovation	2				2	3		3	2		2	2	2	2	2				20

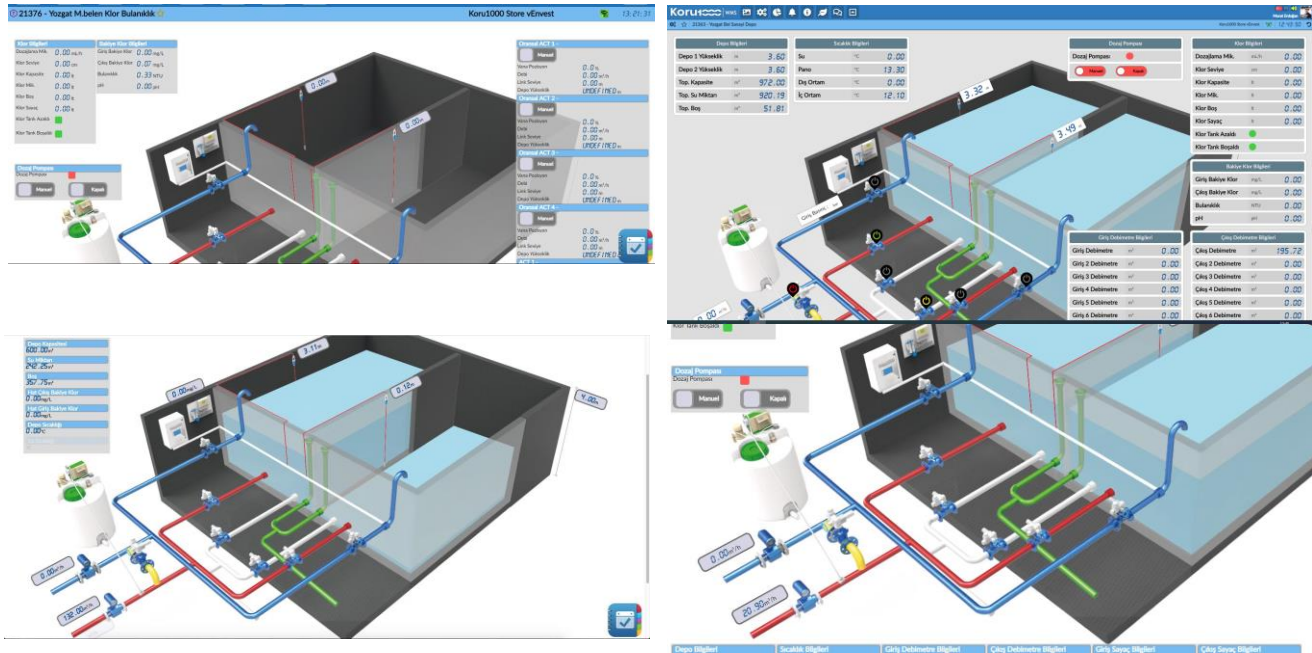
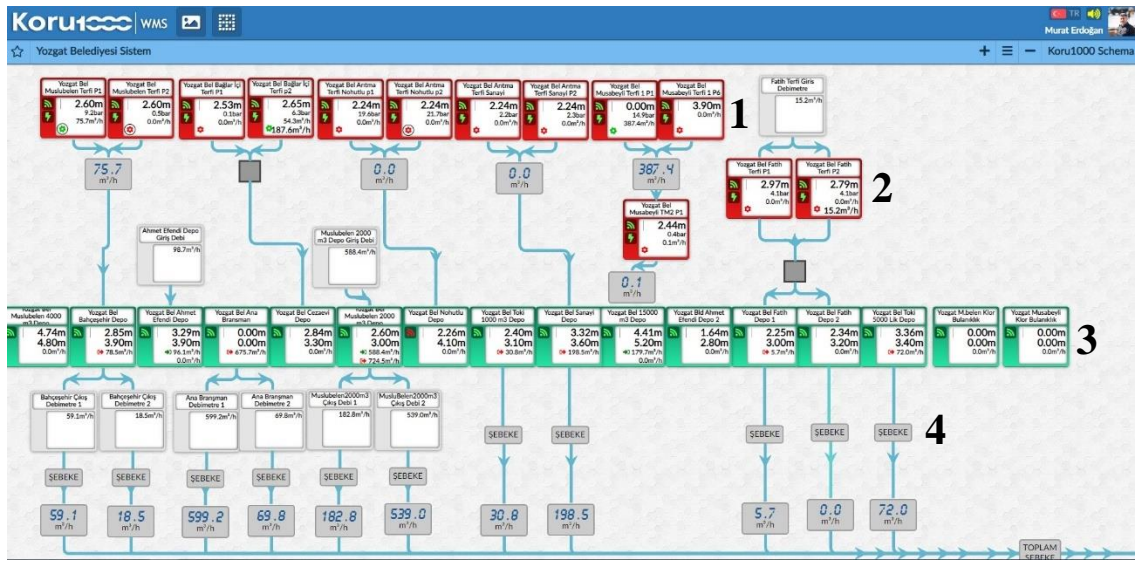


Figure 2. Data monitoring from the SCADA interface



Figure 3. Central control of the pumping stations

Figure 4 is the screen that displays the Wi-Fi connections, electrical connections, pressure values, and water levels in the pumping stations and storage tanks, as well as the amount of water pumped from the pumping stations to the storage tanks. The red section labeled “1” represents the pumping stations. Section “2” shows how water is transferred from which pump to which storage tank, along with the pressure information of the sent water. The green section labeled “3” represents the water tanks. Finally, section "4" indicates the flow rates of the water sent to the network.



In Figure 5, the left section of the information screen contains data from the recently monitored areas and the favorite storage and pumping stations. The right section of the screen lists the alarm statuses of the storage and pumping stations that have data outside of normal conditions.

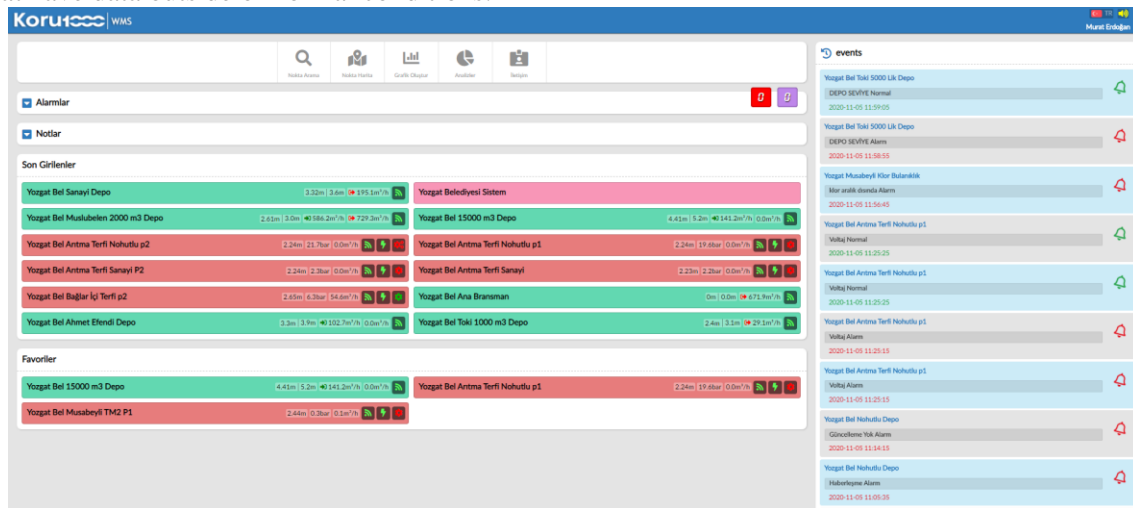


Figure 5. Real-time notifications from storage tanks at different locations

Figure 6 demonstrates the real-time monitoring of water levels, pressure values, and other critical data from different centers. The platform’s capability for simultaneous tracking enables a comprehensive analysis of water levels and pressure values across all centers, facilitating prompt intervention when necessary. Continuous monitoring and real-time data presentation accelerate decision-making processes, aiding in the early detection of potential issues, thus providing a significant advantage in data management and monitoring.

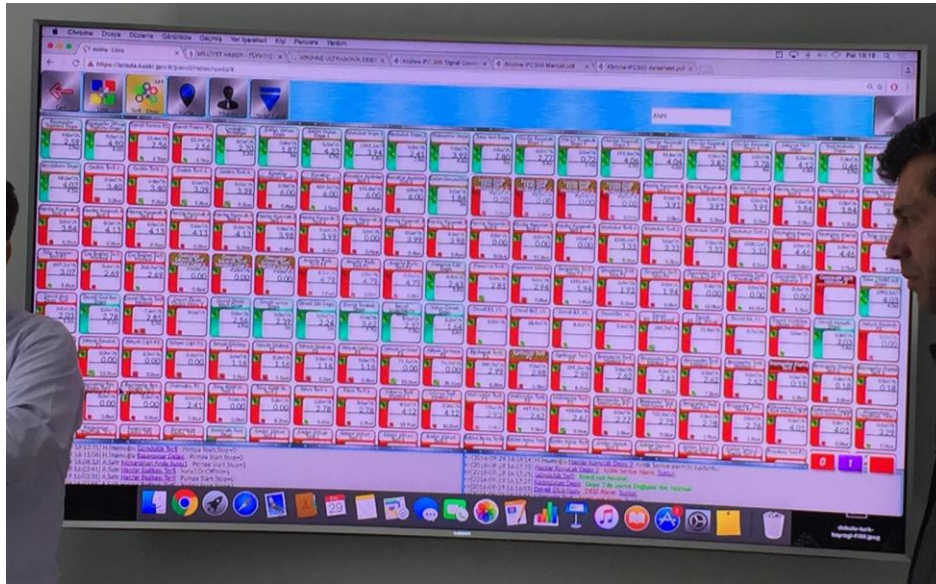


Figure 6. Monitoring the entire network from the central office

The schematic diagram of the system is presented in Figure 7, with an explanation based on data obtained from the Bağlar İçi pump station. In this figure: Section 1 features a water level sensor placed inside the storage tank, measuring the current water height to detect the amount of sediment accumulated in the tank. Sections 2, 3, and 4 display flow meters that regulate the water pressure increasing it from 0.14 bar to 6 bar, thereby pumping the water to the reservoir that supplies the distribution network. Section 5 represents the valve control buttons for opening and closing. Section 6 contains the SCADA panel.

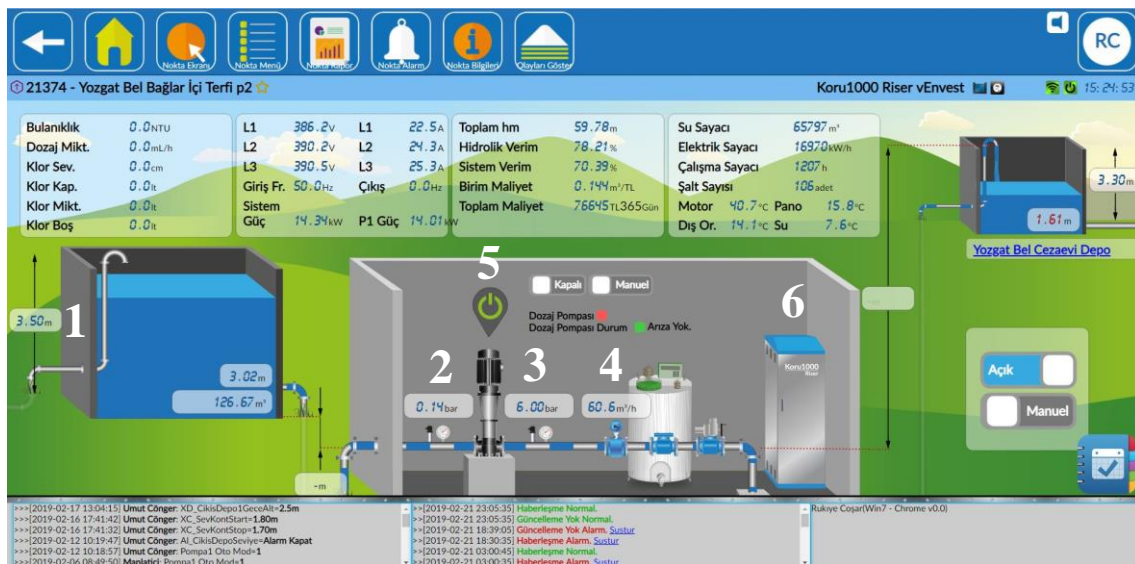


Figure 7. Data from Bağlar İçi pumping station

Additionally, the screen provides data from voltmeters and ammeters, such as voltage and current readings, maximum water level, hydraulic efficiency, system efficiency, unit cost, total cost, total water supplied since system installation, electricity consumption, the number of opening and closing operations performed, and the temperatures of the motor, control panel, external environment, and water.

In Figure 8, the data from Kayabaşı Pumping Station is presented.

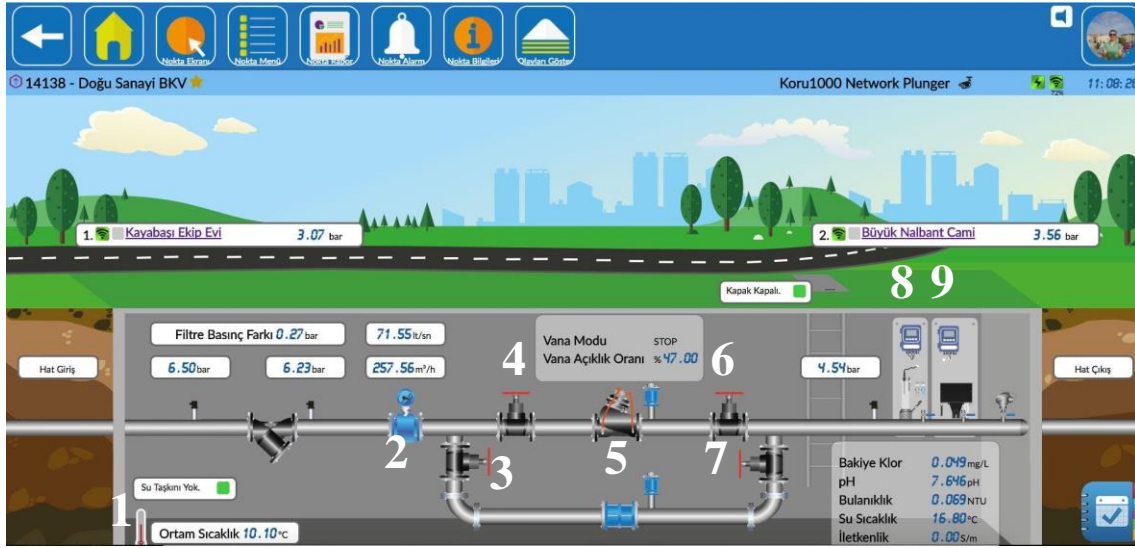


Figure 8. Data from Kayabaşı pumping station

In this figure: Section 1 represents the thermometer used to measure ambient temperature, providing data on the water temperature. Section 2 corresponds to the flow meter, which measures water pressure. The SCADA system remotely regulates the water pressure to maintain stable flow, preventing pipe damage. Sections 3 to 7 represent the valves controlling the inflow and outflow of water to and from the reservoir. The SCADA system remotely manages the opening and closing of these valves based on reservoir fill levels. Section 8 displays the pH level of the water. Section 9 includes sensors that measure the turbidity level of the water.

Figure 9 presents the graph generated from the Sanayi water tank flow meter data.



Figure 9. Sanayi water tank flow meter data graph

In this analysis, the hourly monitoring of water levels in the tanks was conducted, and water losses were identified by tracking the hours of least and most intensive water usage. Based on the hourly flow data from Yozgat Municipality's Sanayi Water Tank between February 19-20, 2019, the average hourly flow was recorded at 200 m³,

while between 01:00-06:00 (indicated by the orange zone), an average of 125 m³/h of water was used. Since water consumption is expected to be near zero during these hours, observing such a high usage suggests a potential loss of approximately 125 m³/h, attributed to leakage or unauthorized water use.

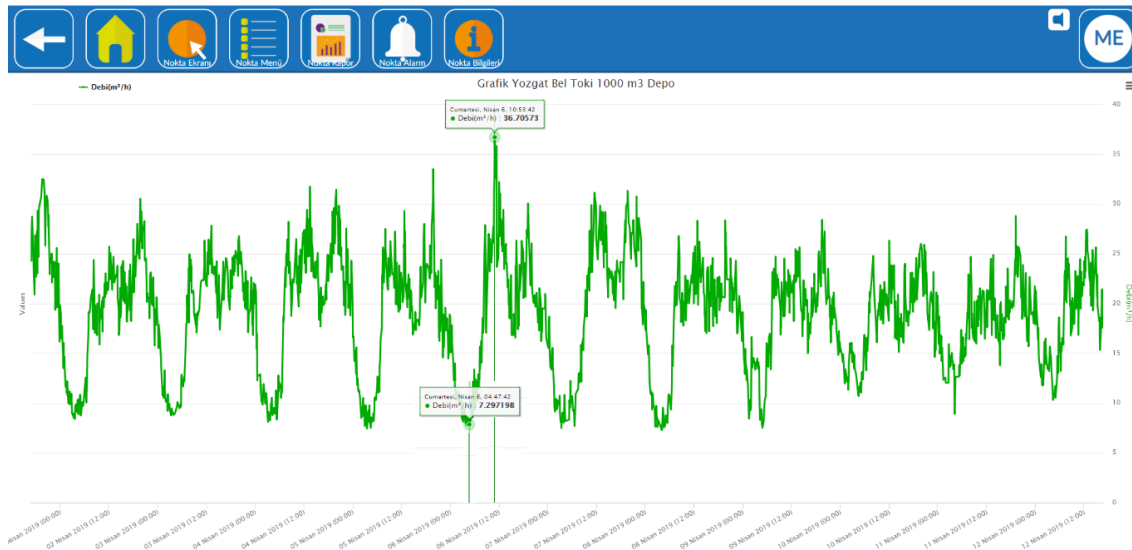


Figure 10. Flow data for the Toki 1000 m³ water tank over one week

Figure 10 presents the weekly flow data for the Yozgat Municipality Toki 1000 m³ Water Tank. According to the graph, at 04:47 on April 6, 2019, the flow rate was recorded at 7.29 m³/h, with similar low values observed at other low points. The significantly low flow rate can be attributed to the recent completion of infrastructure works and the maintenance of storage tanks and other equipment, contributing to a low water loss rate and unauthorized use.

The graph also indicates that an average of 5 m³/h of water was used between April 1-5, 2019, while the average usage increased to 10 m³/h between April 6-9, 2019. Additionally, it was observed that at 10:53 on April 6, 2019, the flow rate reached 36.70 m³/h. These data suggest that an extra five m³/h of water was supplied to the system during April 6-9, 2019. Upon investigating the cause of this abnormal consumption, it was determined that it resulted from a burst in the drinking water line.

C. Standard Water Balance Table Method

The SWB table recommended by the International Water Association (IWA) is a method used to analyze water losses and usage within water distribution systems. This table helps balance the inputs and outputs of the system and accurately categorize water losses. By identifying inefficiencies in water management, the IWA water balance table enables more efficient use of water resources. The SWB table includes the following parameters (Farley et al., 2008):

Table II. Standard water balance table

System Input Volume	Authorized Consumption	Billed Authorised Consumption	Billed Metered Consumption	Revenue Water
		Unbilled Authorised Consumption	Billed Unmetered Consumption	
Water Losses		Administrative Losses	Unbilled Metered Consumption	Non-Revenue Water (NRW)
			Unbilled Unmetered Consumption	
		Physical Losses	Unauthorized Consumption	
			Customer Meter Inaccuracies and Data Handling Errors	
		Leakage on Transmission and Distribution Mains		
		Leakage and Overflows at Utility’s Storage Tanks		
		Leakage on Service Connections up to the Point Customer Use		

- System Input Volume: The volume of water entering main reservoirs from pumping stations after disinfection

(treatment), measured by inlet and outlet flow meters.

- **Billed Metered Consumption:** Recorded water bills for consumers registered in the subscriber system of local water and sewerage authorities based on actual consumption.
- **Billed Unmetered Consumption:** Consumption quantities calculated by local authorities based on standard usage estimates for cases where direct measurement is not conducted.
- **Billed Authorized Consumption:** Water consumption provided to a specific subscriber or group within a predetermined permit or quota set by local authorities.
- **Unbilled Authorized Consumption:** Authorized but unbilled water consumption (e.g., for mosques, parks, gardens, government institutions), measured or estimated as permitted by local authorities.
- **Unbilled Metered Consumption:** Measured water usage for locations with a registered subscriber and meter but unbilled by the authority (e.g., neighborhood fountains).
- **Unbilled Unmetered Consumption:** Authorized but unmeasured and unbilled consumption by local authorities (e.g., parks and gardens), estimated based on usage patterns.
- **Revenue Water:** The total of billed metered and unmetered consumption by local authorities.
- **Non-Revenue Water (NRW):** The volume calculated by subtracting revenue water from the system input volume; this quantity also represents water losses.
- **Authorized Consumption:** Metered, regularly monitored, and billed water consumption managed by local authorities.
- **Water Losses:** The amount calculated by subtracting authorized consumption from the system input volume, representing the sum of administrative and physical losses.
- **Unauthorized Consumption:** Water used through unauthorized connections or faulty meters without local authority knowledge, estimated when detected.
- **Customer Meter Inaccuracies and Data Handling Errors:** Losses due to human errors or inaccuracies caused by old or malfunctioning meters.
- **Administrative Losses:** The sum of unauthorized consumption and customer meter inaccuracies.
- **Physical Losses:** The amount derived by subtracting administrative losses from total water losses in the system.
- **Leakage and Overflows at Utility's Storage Tanks:** Water is lost due to leaks in utility-owned storage tanks or overflow caused by monitoring system issues.
- **Leakage on Transmission and Distribution Mains and Service Connections:** Physical losses excluding leaks and overflows from storage tanks, focusing on main transmission, distribution lines, and service connections.

III. RESULTS AND DISCUSSION

This section analyzes the data obtained from the active SCADA system based on the SWB table method. In this context, the data from the last five years were evaluated. Additionally, the data obtained between 2015 and 2019, prior to the installation of the SCADA system, and the comprehensive data obtained between 2019 and 2023, after the SCADA system was installed, were examined. Physical losses significantly affect water losses in the network; however, other factors exist. At this point, losses and leakages can be detected easily in the SWB table. The difference between the amount of water entering the system and the amount of water leaving through flow meters reveals the water loss. While calculating the water loss amounts for the Yozgat province system, the loss-leakage amount was determined by subtracting the accrued water amount from the amount of water entering the system between 2019 and 2023. Table III shows the water produced, billed, and unbilled between 2019 and 2023 and the water loss rates (YOSKİ).

Table III. The quantities of produced and billed water from 2019 to 2023

Years	Number of subscribers	System input volume (m ³)	Billed water volume (m ³)	Unbilled water volume (m ³)	Water loss (%)
2019	34,032	9,980,520	4,616,777	613,089	47.6
2020	34,699	9,395,875	3,715,388	540,000	54.71
2021	35,939	9,592,238	3,085,615	700,000	60.53
2022	36,682	8,873,849	5,113,459	177,481	31.36
2023	37,877	11,603,312	4,841,976	700,000	46.21

Since the data before 2019 belong to the pre-installation period, it is unavailable in the SCADA system. The losses and leakages of the pumping, storage, and drinking water network in Yozgat province between 2019 and 2023 were examined using the SCADA system. Based on the data obtained from SCADA, it was determined that there was a significant amount of loss and leakage in Yozgat province, as well as a lack of maintenance in the storage and pumping centers. These issues resulted in substantial economic losses, corresponding to approximately 60% of the income over the last four years. Consequently, Yozgat Municipality initiated renewal works in all pumping centers, storage facilities, and network systems in 2022, and these efforts are still ongoing. A significant economic gain is targeted as a result of this initiative. Since no SCADA system existed before 2019, the exact amount of economic loss could not be measured. In 2019, the SCADA system recorded all data using flow meters at the inlet and outlet storage facilities. Table IV shows the annual consumption amounts in 2023 according to subscriber types (T.C. Yozgat Municipality, 2023).

Table IV. The 2023 annual consumption volumes by subscriber type

Subscriber information	Number of subscribers	System input volume (m ³ /yıl)		Billed amount (TL/year)
		Paid	Free	
Official institutions	218	1,196,985		15,368,374.77
Commercial establishments	2,597	306,080		3,717,824.41
Residential areas	34,862	3,271,508		26,953,110.67
Parks, gardens, and wcs			650,000	
Construction sites	176	65,485		1,510,445.84
Dormitories	24	1,918		23,538.81
Total	37,877	4,841,976	650,000	47,573,294.50

Table V presents the SWB data for the years 2019 to 2023.

Table V. Data from the Standard Water Balance Table for the years 2019-2023

Year	2019	2020	2021	2022	2023	Unit
Number of subscribers	34,032	34,699	35,939	36,682	37,877	Person
System input volume	9,980,520	9,395,875	9,592,238	8,873,849	11,603,312	m ³ /yıl
Billed metered consumption	4,569,587	3,715,388	3,085,615	4,189,371	4,841,976	m ³ /yıl
Percentage	45.79	39.54	32.17	47.21	41.73	%
Billed unmetered consumption	47,190	0	0	924,088	0	m ³ /yıl

Percentage	0.47	0.00	0.00	10.41	0.00	%
Billed authorized consumption	4,616,777	3,715,388	3,085,615	5,113,459	4,841,976	m ³ /yıl
Percentage	46.26	39.54	32.17	57.62	41.73	%
Revenue water	4,616,777	3,715,388	3,085,615	5,113,459	4,841,976	m ³ /yıl
Percentage	46.26	39.54	32.17	57.62	41.73	%
Non-revenue water (NRW)	5,363,743	5,680,487	6,506,623	3,760,606	1,401,100	m ³ /yıl
Percentage	53.74	60.46	67.83	42.38	12.08	%
Unbilled metered consumption	114,063	0	0	800,000	700,000	m ³ /yıl
Percentage	1.14	0.00	0.00	9.02	6.03	%
Unbilled unmetered consumption	499,026	540,000	700,000	177,481	700,000	m ³ /yıl
Percentage	5.00	5.75	7.30	2.00	6.03	%
Unbilled authorized consumption	613,089	540,000	700,000	977,481	1,400,000	m ³ /yıl
Percentage	6.14	5.75	7.30	11.02	12.07	%
Authorized consumption	5,229,866	4,255,388	3,785,615	6,090,940	6,241,976	m ³ /yıl
Percentage	52.40	45.29	39.47	68.64	53.79	%
Water losses	4,750,654	5,140,487	5,806,623	2,782,909	5,361,336	m ³ /yıl
Percentage	47.60	54.71	60.53	31.36	46.21	%
Unauthorized consumption	1,247,565	1,174,484	1,475,650	177,481	0	m ³ /yıl
Percentage	13	12	15	2	0	%
Customer meter inaccuracies and data handling errors	456,959	432,211	428,645	5000	100	m ³ /yıl
Percentage	4.58	4.60	4.47	0.06	0.00	%
Administrative losses	1,704,524	1,606,695	1,904,295	182,481	100	m ³ /yıl
Percentage	17.08	17.10	19.85	2.06	0.00	%
Physical losses	3,046,130	3,533,792	3,902,328	2,600,644	1000	m ³ /yıl
Percentage	30.52	37.61	40.68	29.31	0.01	%
Leakage and overflows at utility's storage tanks	99,805	93,958	95,527	102,000	500	m ³ /yıl
Percentage	1.00	1.00	1.00	1.15	0.00	%
Leakage on trans. and dist. mains and service connections	2,946,325	3,439,834	3,806,801	2,498,644	500	m ³ /yıl
Percentage	29.52	36.61	39.69	28.16	0,00	%

According to the SWB table, the annual billed volume of measured consumption amounts to an average of 41.28% of the total volume of water supplied into the system over the past five years. The unmeasured consumption data for Yozgat, recorded through the SCADA system, only covers 2019 and 2022. As managed by YOSKİ, authorized billed water consumption represents consumption permitted through a subscription and meter registration, which is allowed with or without quotas. The table displays the five-year percentage of billed authorized water consumption relative to the total water input into the system.

Revenue-generating water volume is the most critical component of the SWB table, as it shows the income generated relative to the volume of water supplied. From 2019 to 2023, the average revenue-generating water volume is 4,274,643 m³/year, accounting for 43.46% of the system's total input. The highest revenue (5,113,459 m³/year) was recorded in 2022, prompting Yozgat Municipality to initiate comprehensive infrastructure and renewal efforts to increase this figure further. Non-revenue water (NRW) is another essential parameter, representing the financial impact of lost and unaccounted-for water throughout the entire Yozgat municipal network and reservoirs. However, NRW is not limited to physical losses; unauthorized non-billed water usage also constitutes a large proportion of NRW. Over the last five years, the average NRW rate is calculated to be 47.29%, with a steady decline observed since 2021.

Unbilled metered consumption encompasses usage in public parks, gardens, religious sites, etc., documented by the municipality yet not billed. Nevertheless, the SCADA system records the water volume consumed. Unbilled

unmetered consumption, on the other hand, covers water used for public services like maintenance and fire hydrants. According to the SWB table, unbilled authorized consumption has steadily increased since SCADA's installation in 2019, with a five-year average of 846,114 m³/year. The highest authorized consumption was recorded in 2023 at 1,400,000 m³.

The amount of authorized consumption between 2019 and 2023 has not shown consistent trends. An increase in authorized consumption suggests economic efficiency. According to the table, the water loss data for Yozgat from 2019 to 2023 highlights an urgent need for infrastructure and reservoir maintenance and repair. In light of this, Yozgat Municipality intensified its infrastructure renewal efforts in 2022.

The unauthorized water consumption values in the SWB table are approximate due to potential undetected leaks or malfunctioning meters, which prevent precise assessment. Consequently, unauthorized consumption is estimated based on average consumption at suspected locations. Between 2019 and 2023, unauthorized consumption notably decreased, reaching zero in 2023. SCADA system implementation has enabled effective monitoring of unauthorized consumption across regions, contributing to substantial reductions.

Metering errors, expressed as a percentage of the total volume entering the system, can be reviewed via the SWB table. These errors arise from faulty or outdated meters, improper installation, or human error during readings. The SWB table shows a significant decrease in metering errors following the SCADA installation.

The SWB data further indicates a substantial reduction in administrative losses over the past two years, underscoring the savings achieved through SCADA-enabled monitoring of administrative water losses.

Physical losses include leaks and overflows in reservoirs and losses along supply, distribution, and service lines. From 2019 to 2023, physical losses averaged 2,616,778 m³/year, representing 27.62%. A notable decrease in physical water losses, particularly in 2023, was observed compared to previous years.

Inspections of reservoir leaks and overflows reveal recurring losses, largely due to personnel's inconsistent monitoring of reservoir fill levels. In 2023, significant reductions were achieved through SCADA-controlled sensor monitoring, which mitigates the need for manual oversight. SCADA-based real-time assessments eliminated costs associated with personnel, labor, and transportation previously required for reservoir-level monitoring, providing substantial economic savings.

The SWB data also illustrates that the infrastructure works initiated in 2022 have dramatically reduced the volume of leaks and bursts in supply, distribution, and service connections. Damage from pipe bursts, leaks, and cracks along the network, previously high between 2020 and 2022, has approached zero following extensive renovations since 2022.

All these metrics are measured through the SCADA system. While some parameters are measured precisely, others are estimated. Data collected from SCADA—installed by YOSKİ in 2019 to monitor and control critical parameters such as pH, chlorine, pressure, and especially water losses throughout Yozgat's pumping stations, reservoirs, and drinking water network—has been compiled into annual SWB data packets from 2019 to 2024, enabling easy access to all WMS data. Consequently, the centralized WMS has facilitated real-time monitoring, rapid intervention, and effective problem resolution. The SWB table was developed to enhance water management effectiveness and align with the national policies on water loss management, promoting water, energy, economic efficiency, and conservation.

Table VI presents the volume, unit price, and total cost of water losses from 2019 to 2023. Over these five years, an average water loss of 4,568,401.8 m³ has resulted in a financial loss of 54,024,662.92 TL due to water loss costs. Minimizing this loss would represent a substantial gain for the municipality.

Table VI. Water loss costs by year for Yozgat province

Year	Water loss amount (m ³)	Unit price (TL/ m ³)	Total amount (TL)
2019	4,750,654	1.68	7,981,098.72
2020	5,140,487	1.75	8,995,852.25
2021	5,806,623	2.20	12,774,570.6
2022	2,782,909	2.75	7,652,999.75
2023	5,361,336	3.10	16,620,141.6
Average	4,568,401.8	-	10,804,932.584
Total	22,842,009	-	54,024,662.92

Table VII presents the annual billed and system-output water volumes before SCADA implementation, covering 2015–2019.

Table VII. Water billed and water exiting the system by year in cubic meters

Year/Amount	2015	2016	2017	2018	2019
Billed water volume (m ³ /year)	4815.4	5105.83	4984.72	4322.41	4121.33
System input Volume (m ³ /year)	12,038.50	11,957.45	11,945.18	11,739.31	10,657.70
Percentage (%)	60.01	57.3	58.27	63.18	61.33

Table VIII provides the monthly billed and system-output water volumes, along with loss-leakage rates, for 2019–2023 following the SCADA installation.

The SWB data for 2019–2023 has been analyzed yearly, comparing the total water supplied to the system with revenue-generating and non-revenue water volumes. The data shows no consistent trends in either revenue-generating or non-revenue water volumes. However, with the SCADA system established in 2019, there have been improvements in unauthorized consumption, metering errors, administrative and physical losses, leaks and overflows in reservoirs, and losses along supply, distribution, and service lines. This outcome has provided economic benefits to Yozgat Municipality. A review of the SWB data reveals a notable decline in water losses and leaks between 2019 and 2023. It is anticipated that the active utilisation of SCADA will result in a further reduction in these losses, with the eventual convergence to zero.

Table VIII. Monthly water loss-leakage table for Yozgat province 2019-2023

Year	Month	Water supplied to the city (m ³)	Billed consumption (m ³)	Water loss (%)
2019	January	754,467.00	346,895.00	54.02
	February	899,169.00	377,256.00	58.04
	March	847,824.00	369,785.00	56.38
	April	824,725.00	327,898.00	60.24
	May	765,744.64	454,548.00	40.64
	June	888,714.00	356,499.00	59.89
	July	874,603.51	311,258.00	64.41
	August	811,295.00	328,754.00	59.48
	September	733,543.00	343,719.00	53.14
	October	849,148.00	498,751.00	41.2
	November	833,405.91	467,194.00	43.94
	December	897,881.00	434,220.00	51.64
	Total	9,980,520.06	4,616,777.00	53.59
2020	January	782,467.00	310,276.00	60.35
	February	754,879.00	324,531.00	57.01
	March	718,724.00	311,228.00	56.7
	April	845,729.00	314,522.00	62.81
	May	796,133.64	365,348.00	54.11
	June	806,574.00	324,399.00	59.78
	July	765,503.51	389,488.00	49.12
	August	823,659.00	305,560.00	62.9
	September	754,773.00	390,031.00	48.32
	October	759,146.00	381,467.00	49.75
	November	796,305.91	398,462.00	49.96
	December	791,981.00	434,220.00	45.17
	Total	9,395,875.06	4,249,532.00	54.67
2021	January	769,874.40	220,276.00	71.39

	February	699,253.08	254,531.00	63.6
	March	817,273.99	98,228.00	87.98
	April	776,047.49	237,622.00	69.38
	May	796,133.64	265,348.00	66.67
	June	786,889.94	264,399.00	66.4
	July	865,503.51	309,488.00	64.24
	August	865,381.56	305,560.00	64.69
	September	801,321.95	279,831.00	65.08
	October	827,142.13	301,767.00	63.52
	November	796,305.91	298,462.00	62.52
	December	791,111.00	250,103.00	68.39
	Total	9,592,238.60	3,085,615.00	67.82
2022	January	764,985.00	298,855.00	60.93
	February	734,025.00	245,500.00	66.55
	March	727,735.00	485,932.00	33.23
	April	708,082.00	377,223.00	46.73
	May	706,794.00	376,278.00	46.76
	June	758,308.00	435,499.00	42.57
	July	711,880.00	352,955.00	50.42
	August	739,794.00	441,847.00	40.27
	September	767,734.00	591,056.00	23.01
	October	744,518.00	563,273.00	24.34
	November	724,736.00	492,309.00	32.07
	December	785,258.00	452,732.00	42.35
Total	8,873,849.00	5,113,459.00	42.44	
2023	January	930,193.00	347,766.00	62.61
	February	857,695.00	412,586.00	51.9
	March	953,759.00	347,522.00	63.56
	April	921,119.00	380,635.00	58.68
	May	958,175.00	358,174.00	62.62
	June	951,304.00	314,422.00	66.95
	July	1,022,030.00	586,774.00	42.59
	August	1,069,906.00	367,709.00	65.63
	September	1,030,622.00	411,885.00	60.04
	October	1,049,256.00	518,502.00	50.58
	November	847,854.00	379,045.00	55.29
	December	1,011,399.00	416,956.00	58.77
Total	11,603,312.00	4,841,976.00	58.27	

IV. CONCLUSION

The sustainability of water resources, which hold great importance for various aspects of human life, is crucial. Access to safe water depends on the reliability and cleanliness of storage tanks. Therefore, it is essential to measure sediment levels, water levels, pressure, pH, temperature, chlorine, turbidity, and loss-leakage rates in storage tanks, along with disinfection and treatment processes. To prevent the spread of waterborne diseases, continuous monitoring and adequate disinfection and treatment of water are necessary. This study examined data from water reservoirs and pumping stations in Yozgat Province, enabling real-time monitoring of all stages from the water source to storage tanks and distribution networks via the SCADA system. This system immediately detected any abnormal conditions in the reservoirs and pumping stations. Data was remotely monitored from a central point, resulting in efficient water management for the city. Measurements of parameters such as chlorine, pH, turbidity, and pressure through water sensors ensured prompt maintenance and repairs in reservoirs and other essential locations. Centralized monitoring and management have contributed to personnel, fuel, and time savings. With reduced workload for staff and remote access for managers, trust and responsibility in water management have been enhanced, improving functionality across the water management team through systematic control.

Through real-time monitoring, the loss-leakage rate in central Yozgat was precisely determined. Immediate reporting, archiving of past events, and real-time wired and wireless communication between operators and the field enabled quick responses to malfunctions, increasing user satisfaction. The quality of supplied water was maintained, ensuring that safe water reached end users with minimal loss. The SWB table generated with the data collected in this study

revealed an average 50–60% water loss rate over the past five years. To address this issue, Yozgat Municipality undertook infrastructure improvements in 2022. The positive impact of these efforts was reflected in the SWB table, with the 2023 data showing minimized water loss.

This study sets an example for institutions across Turkey to reduce water losses and increase efficiency in WMS. Institutions should work meticulously on water management, employing advanced technology to accurately collect data, which expert teams should then evaluate and record in the SWB table to identify profit or loss areas. Timely maintenance, repairs, and renewals should be carried out, considering equipment aging due to its lifespan and environmental conditions. Old and malfunctioning meters should be replaced with digital meters, and pressure values that lead to leaks should be controlled via flow meters. This study recommends SCADA usage as a tool for effective water management. The proposed SCADA-based framework has the potential to serve as a model for other municipalities seeking to implement efficient water management strategies, particularly in regions facing water scarcity.

STATEMENT OF CONTRIBUTION RATE

The authors' contribution rates to the study are equal.

CONFLICTS OF INTEREST

They reported that there was no conflict of interest between the authors and their respective institutions.

RESEARCH AND PUBLICATION ETHICS

In the studies carried out within the scope of this article, the rules of research and publication ethics were followed.

ACKNOWLEDGMENT

We extend our gratitude to Yozgat Municipality for providing access to project data, which has offered valuable contributions to the execution of this research.

REFERENCES

- [1] Ahmed, Z. Y. (2024). Reducing Non-Revenue Water. *International Journal of Applied Mathematics, Computational Science and Systems Engineering*, 6, 23-29.
- [2] Alıcı, O. V., & Özasan, K. (2016). *Yerel Yönetimlerde Altyapı Sistemlerinin Sayısallaştırılması ve Su Kayıplarının Önlenmesi. Uluslararası Bilimsel Araştırmalar Dergisi (IBAD)*, 3(1), 204-218.
- [3] Akdemir, M., & Yılmaz, S. (2023). *İçme Suyu Sistemlerinde Sızıntuların Uygulamalı ve Teorik Olarak Karşılaştırılması. İleri Teknolojilerde Çalışmalar Dergisi*, 1(2), 55-66.
- [4] Akdeniz, T., & Muhammetoglu, H. (2023). Türkiye'de Kentsel Su Dağıtım Şebekelerinde İdari Su Kayıplarının Değerlendirilmesi. *Çevre İklim ve Sürdürülebilirlik*, 24(1), 1-6.
- [5] Akıllı, H., & Özasan, R. (2017). Su Kayıplarının Önlenmesinde Teknoloji Kullanımı: Büyükşehir Belediyelerinde Scada Uygulaması. *Süleyman Demirel Üniversitesi İktisadi ve İdari Bilimler Fakültesi Dergisi*, 22(Kayfor 15 Özel Sayısı), 1599-1618.
- [6] Al-Ghamdi, A. S., & Gutub, S. A. (2002). Estimation of Leakage in The Water Distribution Network of The Holy City of Makkah. *Journal of Water Supply: Research and Technology—AQUA*, 51(6), 343-349.
- [7] Aslan, B. (2016). *İçme Suyu Temin ve Dağıtım Sistemlerinde Su Kayıp ve Kaçaklarının Tespiti. Uzmanlık Tezi, İller Bankası AŞ, Ankara*, 88.
- [8] Aydın, D. (2007). *İçmesuyu dağıtım sistemlerinde cbs tabanlı su kalitesi yönetimi (Doktora Tezi, İstanbul Teknik Üniversitesi)*
- [9] Babu, C. G., Jayakar, S. A., Dhanasekar, R., & Kalaiyarasi, M. (2023, April). Quality drinking water distribution system. *In AIP Conference Proceedings (Vol. 2725, No. 1)*. AIP Publishing.
- [10] Başa, Ş., & Kurt, S., (2017). Su ve Kanalizasyon İdarelerinde Akıllı Su Yönetimi Uygulamaları: Tekirdağ Örneği. *Süleyman Demirel Üniversitesi İktisadi ve İdari Bilimler Fakültesi Dergisi*, 22(Kayfor 15 Özel Sayısı), 1519-1532.
- [11] Bulut, O., & Ertugay, N. (2022). Assessing Water Losses in Drinking Water Distribution Systems Using the SCADA System: The Erzincan Case. *Development*, 2, 2, 141-160.

- [12] Brentan, B., Rezende, P., Barros, D., Meirelles, G., Luvizotto Jr, E., & Izquierdo, J. (2021). Cyber-attack detection in water distribution systems based on blind sources separation technique. *Water*, 13(6), 795.
- [13] Cinal, H. (2009). *Basınç yönetimi ile içmesuyu şebeke kayıplarının azaltılması: Sakarya örneği* (Master's thesis, Sakarya Üniversitesi).
- [14] Çelik, A., Kocaman, H., & İnce, H. C. (2016). Sakarya SASKİ Genel Müdürlüğü SCADA ve CBS Entegrasyonu.
- [15] Demir, A. (2001). *Konya içme suyu şebekesinde su kayıplarının belirlenmesi* (Master's thesis, Fen Bilimleri Enstitüsü).
- [16] Dilcan, Ç. C., Çapar, G., Korkmaz, A., İritaş, Ö., Karaaslan, Y., Selek, B., (2018). İçme Suyu Şebekelerinde Görülen Su Kayıplarının Dünyada ve Ülkemizdeki Durumu. *Anahtar Dergisi*, S: 354, 10-18.
- [17] Fan, X., Zhang, X., & Yu, X. B. (2021). Machine learning model and strategy for fast and accurate detection of leaks in water supply network. *Journal of Infrastructure Preservation and Resilience*, 2, 1-21.
- [18] Fırat, M., Yılmaz, S., & Orhan, C. (2021). Su Kayıp Yönetimi İçin Temel Hesaplama Araçlarının Geliştirilmesi ve Temel Su Kayıp Bileşenlerinin Analizi. *Gümüşhane Üniversitesi Fen Bilimleri Dergisi*, 11(2), 405-416.
- [19] Gerger, R., & Aslan, A. (2019). Şanlıurfa İli İçin İçme Suyu Kayıp ve Kaçaklarının Tespiti. *Harran Üniversitesi Mühendislik Dergisi*, 4(2), 26-35.
- [20] Görgülü, M. E. (2022). *Konya ili içme suyu şebekelerinde işletmeden kaynaklı bakım-onarım işlerinin analizi* (Master's thesis, Necmettin Erbakan Üniversitesi Fen Bilimleri Enstitüsü).
- [21] Güçlü, A. (2024). *İçme suyu şebekelerinde oluşan su kayıp ve kaçaklarının SCADA sistemi yardımıyla incelenmesi: Muş ili örneği* (Master's thesis, Lisansüstü Eğitim Enstitüsü).
- [22] Gülaydın, O., (2017). *İçme suyu dağıtım şebekelerinde ekonomik su kayıpları seviyesinin belirlenmesi: Antalya Kaleiçi örneği*.
- [23] Güney, İ., & Selvi, İ. H. (2023). Makine Öğrenmesi Yöntemleriyle Anormal İçme Suyu Tüketimlerinin Tespit Edilmesi ve Tahmin Modellerinin Geliştirilmesi. *Journal of Intelligent Systems: Theory and Applications*, 6(2), 159-173.
- [24] Grigg, N. S. (2024). Water Distribution Systems: Integrated Approaches for Effective Utility Management. *Water*, 16(4), 524.
- [25] Jun, S., & Lansley, K. E. (2023). Comparison of AMI and SCADA Systems for Leak Detection and Localization in Water Distribution Networks. *Journal of Water Resources Planning and Management*, 149(11), 04023061.
- [26] Karaca, Z. (2009). *İçme Suyu Şebeke Sistemlerinde Su Kayıp ve Kaçaklarının Tespiti. Yıldız Teknik Üniversitesi Fen Bilimleri Enstitüsü* (Doctoral dissertation, Yüksek Lisans Tezi, İstanbul).
- [27] Karadirek, I. E., Kaya-Basar, E., & Akdeniz, T. (2024). A study on pipe failure analysis in water distribution systems using logistic regression. *Water Supply*, 24(1), 176-186.
- [28] Karakaya, D., & Toprak, Z. F., (2018). İçme Suyu Şebekelerindeki Su Kayıplarının ZFT Algoritması Kullanılarak Sınıflandırılması. *Su Kaynakları*, 3(2), 22-30.
- [29] Karakuş, C. B., Yıldız, S., & Cerit, O. (2013). The Studies of Water Loss and Reducing The Rate of Loss in Sivas City Potable Water Network. *Selcuk University Journal of Engineering, Science and Technology*.
- [30] Kılıç, R. (2021). Fiziki Kayıpların Azaltılması İçin İzole Alt Bölgelerin Etkin Yönetimi. *Avrupa Bilim ve Teknoloji Dergisi*, (22), 306-315.
- [31] Klosok-Bazan, I., Boguniewicz-Zablocka, J., Suda, A., Łukasiewicz, E., & Anders, D. (2021). Assessment of leakage management in small water supplies using performance indicators. *Environmental Science and Pollution Research*, 28, 41181-41190.
- [32] Köker Gökçöl, E. (2018). *Leakage optimization of water distribution networks by pressure control* [Ph.D.-Doctoral Program]. Middle East Technical University.
- [33] Körpe, M., (2018). *Konya içme suyu şebekesinde su kayıplarının tespiti ve değerlendirilmesi* (Master's thesis, Necmettin Erbakan Üniversitesi Fen Bilimleri Enstitüsü).
- [34] Kurban, R. (2022). Su Temin ve Dağıtım Sistemlerinin Otomasyonunda Endüstri 4.0, Nesnelerin İnterneti, Bulut Bilişim, Makine Öğrenimi ve Optimizasyon Uygulamaları. *Araştırma ve Değerlendirmeler II*, 49-70.
- [35] Ma, X., Li, Y., Zhang, W., Li, X., Shi, Z., Yu, J., ... & Liu, J. (2022). A real-time method to detect the leakage location in urban water distribution networks. *Journal of Water Resources Planning and Management*, 148(12), 04022069.
- [36] Olmuştur, M. M. (2021). *İçme suyu şebekelerinde basınç kırıcı vananın gerçek zamanlı kontrolünün su kayıpları üzerine etkisinin model analizi ve deneysel incelenmesi* (Master's thesis, Sakarya Uygulamalı Bilimler Üniversitesi).
- [37] Özaslan, R. K., & Alıcı, O. V. (2018). Su ve Kanalizasyon İdarelerinin Performans Göstergelerinin Uygulanabilirliğinin Analizi. *Strategic Public Management Journal*, 4(8), 35-51.
- [38] Öztürk, Y., & Abama, H. İ. (2023). Kilis' te Evsel Su Tüketiminin Şebekeden Yapılan Ölçümler ile Saptanması. *Euroasia Journal of Mathematics, Engineering, Natural & Medical Sciences*, 10(29), 120-127.

- [39] Pala, B. (2002). *İçmesuyu şebekelerinde oluşan su kayıplarının belirlenmesi ve kontrolü: Kayseri İli Örneği* (Master's thesis, Fen Bilimleri Enstitüsü).
- [40] Radaković, N., & Šenk, I. (2020). Deep Autoencoder Based Leakage Detection in Water Distribution SCADA Systems. *In Industrial Innovation in Digital Age* (pp. 355-361). Cham: Springer International Publishing.
- [41] Shabangu, T. H., Hamam, Y., & Adedeji, K. B. (2020). Decision support systems for leak control in urban water supply systems: A literature synopsis. *Procedia CIRP*, 90, 579-583.
- [42] Songur, M. (2016). *İçmesuyu şebekelerindeki fiziksel kayıpları önlemeye yönelik Diyarbakır için örnek bir model geliştirilmesi* (Doctoral dissertation, Sakarya Üniversitesi (Turkey)).
- [43] Songur, M., Dabanlı, A., Yılmazel, B., & Kürkçüoğlu, M. A. Ş., (2021). Su Dağıtım Şebekelerindeki Fiziki Kayıpların Önlenmesinde SCADA'nın Önemi: ASKİ Örneği, *Afyon Kocatepe Üniversitesi Fen ve Mühendislik Bilimleri Dergisi*, 21(6), 1424-1433.
- [44] Stătescu, F., Boboc, V., Tatu, G., Sârbu, G. C., Marcoie, N., & Toma, D. (2024, March). Improving pressure monitoring and control in order to reduce water loss in water urban public systems. *In IOP Conference Series: Materials Science and Engineering* (Vol. 1304, No. 1, p. 012031). IOP Publishing.
- [45] SUEN- Türkiye Su Enstitüsü (2017). Büyükşehir Su ve Kanalizasyon İdareleri ile Mukayeseli Değerlendirme Çalışması, *SUEN Yayını, İstanbul*. <https://www.suen.gov.tr/Suen/catdty.aspx?val=168> (19.05.2024 Ziyaret Tarihi)
- [46] Tchórzewska-Cieślak, B., Szpak, D., Żywiec, J., & Roźnowski, M. (2024). The concept of estimating the risk of water losses in the water supply network. *Journal of Environmental Management*, 359, 120965.
- [47] Toprak, S., Koç, A. C., Bacanlı, Ü. G., Dikbaş, F., Fırat, M., & Dizdar, A., (2007a). İçme Suyu Dağıtım Sistemlerindeki Kayıplar, *III. Ulusal Su Mühendisliği Sempozyumu*, 601-609
- [48] Toprak, S., Dikbaş, F., Fırat, M., Koç, A. C., Bacanlı, Ü. G., & Dizdar, A., (2007b). Su Kayıplarının Azaltılması ve Su Dağıtım Sistemlerinin Performanslarının İyileştirilmesi Üzerine Leonardo Da Vinci Projesi: Prowat, *III. Ulusal Su Mühendisliği Sempozyumu*, 611-618.
- [49] Torneyiadzi, H. M., Owusu-Ansah, E., Mohammed, H., & Seidu, R. (2024). Node search space reduction for optimal placement of pressure sensors in water distribution networks for leakage detection. *Alexandria Engineering Journal*, 94, 325-338.
- [50] Tuna, M., Armut, S. (2021). Orta Ölçekli Bir Şehirde Kentsel Su Yönetimi: Amasya İli Merzifon İlçesi Örneği. *Bilecik Şeyh Edebali Üniversitesi Fen Bilimleri Dergisi*, 8(2), 990-1009.
- [51] Tuna, M., Armut, S., & Tombul, M., (2023). İçme Suyu Şebekelerinde Kayıp Kaçak Seviyesinin Belirlenmesi: Merzifon İlçesi Örneği. *Kent Akademisi*, 16(1), 1-17.
- [52] Uçar, A. (2022). Akıllı Kentler ve Su Kullanımı. *Medeniyet Araştırmaları Dergisi*, 7(1), 1-14.
- [53] Vrachimis, S. G., Eliades, D. G., Taormina, R., Kapelan, Z., Ostfeld, A., Liu, S., ... & Polycarpou, M. M. (2022). Battle of the leakage detection and isolation methods. *Journal of Water Resources Planning and Management*, 148(12), 04022068.
- [54] Yıldız, S., & Değirmenci, M. (2010). Sivas Kenti Mevcut İçme Suyu Temini ve Bazı Çözüm Önerileri. *Erciyes Üniversitesi Fen Bilimleri Enstitüsü Fen Bilimleri Dergisi*, 26(2), 125-130.
- [55] Yüksel, İ., Songur, M., & Demirel, İ. H., (2018). Diyarbakır içme suyu şebekesindeki su kayıplarını önlemek için hidrolik yöntem geliştirme. *Dicle Üniversitesi Mühendislik Fakültesi Mühendislik Dergisi*, 9(1), 535-542.



JSTER

JOURNAL OF SCIENTIFIC, TECHNOLOGY AND ENGINEERING RESEARCH

Bilim, Teknoloji ve Mühendislik Araştırmaları Dergisi

ISSN: 2717-8404

EL-CEZERİ

Al-Jazari, known as the world's first control engineer, is known as the founder of cybernetics, which is the basis of computers.

El Cezerî (b. 1136, - d. 1206, Cizre), full name Ebû'l İzz İsmail İbni Rezzaz El Cezerî (الجزري از الرز بن إسماعيل العز أبو) Muslim scientist and engineer who worked in the Golden Age of Islam. Ebû'l İzz El Cezeri, who is considered to have taken the first steps in cybernetics and built and operated the first robot, is thought to have inspired Leonardo da Vinci.

He was born in the Tor neighborhood of Cizre. Al-Jazari, who took his name from the city he lived in, completed his education at the Camia Madrasa, concentrated on the fields of physics and mechanics, and made many principles and inventions.

The oldest known written record about robotics belongs to Cezeri. The automatic machines made by Cezeri, who was the first scientist to work on today's cybernetics and robotics in terms of world science history, constitute the cornerstones of today's mechanical and cybernetic sciences.

"The Book Containing the Utilization of Mechanical Movements in Engineering" (El Câmî-u'l Beyn'el İlmî ve El-Amelî'en Nâfi fî Sinâ'ati'l Hiyel, Arabic: **الْحَيْلُ صِنَاعَةٌ فِي لِنَافِعِ** He put it forward in his work called **لِنَافِعِ فِي صِنَاعَةِ الْحَيْلِ**. In this extraordinary book, in which he shows the principles of use and the possibilities of utilizing more than 50 devices with drawings, Cezeri says that any technical knowledge that is not translated into practice will remain between right and wrong.



Dünyanın ilk kontrol mühendisi olarak bilinen El-Cezeri, bilgisayarların temeli olan sibernetiğin kurucusu olarak tanınır.

El Cezerî (d. 1136, - ö. 1206, Cizre), tam adıyla **Ebû'l İzz İsmail İbni Rezzaz El Cezerî (أبو الجزري الرزاز بن إسماعيل العز)** İslam'ın Altın Çağında çalışmalar yapan Müslüman bilim adamı ve mühendis. Sibernetiğin ilk adımlarını attığı ve ilk robotu yapıp çalıştırdığı kabul edilen Ebû'l İzz El Cezeri'nin Leonardo da Vinci'ye ilham kaynağı olduğu düşünülür.

Cizre'nin Tor mahallesinde doğmuştur. Lakabını yaşadığı şehirden alan El Cezeri, öğrenimini Camia Medresesi'nde tamamlayarak, fizik ve mekanik alanlarında yoğunlaştı ve pek çok ilke ve buluşa imza attı.

Robotikle ilgili bilinen en eski yazılı kayıt, Cezeri'ye âittir Dünya bilim tarihi açısından bugünkü sibernetik ve robot biliminde çalışmalar yapan ilk bilim adamı olan Cezeri'nin yaptığı otomatik makineler günümüz mekanik ve sibernetik bilimlerinin temel taşlarını oluşturmaktadır.

"*Mekanik Hareketlerden Mühendislikte Faydalanmayı İçeren Kitap*" (El Câmî-u'l Beyn'el İlmî ve El-Amelî'en Nâfi fî Sinâ'ati'l Hiyel, Arapça: **لِنَافِعِ فِي صِنَاعَةِ الْحَيْلِ**) adlı eserinde ortaya koydu. 50'den fazla cihazın kullanım esaslarını, yararlanma olanaklarını çizimlerle gösterdiği bu olağanüstü kitapta Cezeri, **tatbikata çevrilmeyen her teknik ilmin, doğru ile yanlış arasında kalacağını** söyler.



<https://dergipark.org.tr/tr/pub/jster>

e-mail : jster.editor@gmail.com